# An Experimental Study of Compaction Band Evolution in an Anisotropic Sandstone

Edward Townend

A thesis submitted to the University of London for the degree of

Doctor of Philosophy

Faculty of Mathematical and Physical Science
University College, London

April, 2008





ProQuest LLC
789 East Eisenhower Parkway
P.O. Box 1346
Ann Arbor, MI 48106-1346

## Abstract

Diemelstadt sandstone is a quartz dominated material of about 23% porosity. It has been characterised as transversely isotropic about the pole to its bedding plane by measuring the anisotropy of pore-fabric using a magnetic susceptibility technique, and by measuring elastic wave velocities as a function of azimuth around orthogonal cores. These measurements indicate an average void-space shape approximating an oblate spheroid with an anisotropy of around 6%. Conventional triaxial experiments were then performed on samples of Diemelstadt sandstone cored in directions normal and parallel to the plane of isotropy (the bedding plane), under effective pressure conditions sufficient to traverse the brittle-ductile regime and to induce failure by the development of discrete compaction bands oriented in planes normal to the maximum compressive stress.

Results show that samples deformed normal to bedding are consistently weaker in the compactive regime than the samples deformed parallel to bedding. This observation is consistent with further measurements which reveal that discrete compaction bands have a more pronounced impact on the evolution of permeability in samples deformed in the direction normal to the bedding plane. However, the permeability reduction in both orientations is dramatic, with the bulk permeability of Diemelstadt sandstone falling by up to four orders of magnitude. Acoustic emission locations show that the velocity of compaction band propagation is less than 0.1 mm $s^{-1}$, and that the seismic b-value response to compaction band inception is consistent with a grain-scale deformation mechanism.

Microstructural observations reveal a more tortuous compaction band trace in samples deformed parallel to bedding, which is consistent with greater strength observed in this direction. Our experimental data validate earlier theoretical predictions from spring network models which also point towards the influence of anisotropy on the morphology of compaction bands.

# Table of Contents

# List of Figures

# List of Tables

## Acknowledgements

I would like to thank the people who made this work possible, and whose input has been central to this investigation. Firstly to my supervisors, Professor Phil Meredith and Doctor Patrick Baud who provided me with guidance on the experimental method, were always keen to discuss approaches and concepts with me, and were available to critique my output.

I would also like to acknowledge the engineering expertise of Neil Hughes, Steve Boon and John Bowles, who were crucial in the design, manufacture and implementation of sophisticated experimental apparatus; which was at once the most frustrating and rewarding aspect of my PhD experience. I am also indebted to past PhD students; to David Eccles and to Phil Benson, who continued to provide insights to aspects of my work post-UCL. I am grateful to NERC, The Royal Society, The British Council and CNRS for providing sponsership, funding and grants for this research.

Finally and mostly, I would not have been able to complete this work without the patient support and encouragement of my family and my friends.

# 1 Introduction

## 1.1 Compaction Bands

Compaction bands are a recently recognised geological structure, first reported in the field by Mollema and Antonelini (1996) who observed tabular features between 0.5 and 1.5 cm wide outcropping in a high-porosity sandstone host. In their purest form, compaction bands exhibit normal compactive strain with zero shear strain, and as such they form a kinematic end-member of the deformation band spectrum (Du Bernard et al., 2002). The discovery of compaction bands in nature has motivated much laboratory work aimed at reproducing these structures under controlled conditions to gain insights into the processes operating during their inception.

Two types of laboratory structure are reported in the literature as analogues to natural compaction bands. Olsson (1999) reports on zones of compaction in sandstone that widen axially during deformation under conventional triaxial conditions, whereas other workers (Klein et al., 2001; Wong et al., 2001; Baud et al., 2004) describe planar compactive structures, intercalated with undamaged host material, which form normal to the maximum compressive stress under confining pressures sufficient to suppress shear localisation. As a result of their distinct morphologies, the two types of compaction band are termed 'diffuse' and 'discrete', respectively. To date, most work has reported on discrete compaction bands and it is this style of compaction band that appears to bear the most resemblance to the structures reported in the field.

The stress states at the onset of compaction localisation are associated with the transitional regime between brittle faulting and cataclastic flow (Wong et al. 2001), with microstructural work (Mollema and Antonelini, 1996; DiGiovanni et al., 2000; Wong et at., 2001) revealing that compaction bands are characterised by pore collapse and interpenetration of grains. This style of deformations leads to a significantly reduced porosity within the band, and as a result

compaction bands were initially suspected to form barriers to fluid flow, thereby having implications for hydrocarbon recovery, groundwater flow and waste disposal. This was later confirmed by experimental work (Vajdova et al., 2004) which demonstrated that compaction bands may reduce the bulk permeability of a host material by several orders of magnitude.

Olsson (1999) first recognised that the conditions allowing for localised compaction could be assessed using the bifurcation approach of Rudnicki and Rice (1975), which was originally developed for predicting the inception of shear bands. However, this approach uses a constitutive model based on a single yield-surface, which later work (Wong et al., 2001) has ruled as being inadequate, since it does not account for the partitioning of damage between the multiple damage mechanisms which operate in the brittle-ductile transition. However, more elaborate constitutive models have been developed (Issen, 2002) which show better agreement with the available experimental data.

## 1.2 Purpose of Investigation

Experimental work has lead to significant advances in the understanding of localised compaction in porous rocks, although to date the vast majority of work has been conducted on rock samples deformed in a direction normal to the bedding plane of the material, thereby inducing compaction bands in a plane parallel to bedding, normal to the maximum compressive stress, $\sigma_1$. This practise has continued despite the majority of natural compaction bands being reported in planes oriented at a high angle to bedding, and has resulted in a paucity of data describing how anisotropy may influence aspects of compaction band properties and evolution. This study, therefore, aims to examine aspects of compaction band development as a function of anisotropy by performing deformation experiments on samples cored in orthogonal directions with respect to the bedding plane. We use Diemelstadt sandstone (a quartz dominated material of 23% porosity) as our experimental material since it is a visibly anisotropic material, and also because previous work (Fortin et al., 2003; Baud et

al., 2004) has shown that it is capable of developing compaction bands within the pressure range attainable by our deformation apparatus.

The experiments reported in this work are performed under a range of effective pressures in order to establish the influence of anisotropy on the failure envelope of Diemelstadt sandstone as deformation evolves from shear localisation in the brittle regime to compaction localisation in the brittle-ductile regime. The influence of compaction bands on bulk permeability are investigated as a function of sample orientation, and the propagation of compaction bands are studied using acoustic emission locations.

## 1.3 Thesis Description

This thesis is organised into 11 chapters. Following this brief introduction, chapters two to four provide some underlying theory and concepts relevant to rock physics and, in particular, to laboratory studies of compaction bands. Chapters five to nine describe the methodology used to generate experimental data, and present the results obtained for this work. The final two chapters are dedicated to an analysis of these results, the conclusions drawn from them and some potential directions for future research.

# 2 Some Principles and Mechanics of Brittle Rock Deformation

## 2.1 Crustal Conditions

### 2.1.1 Structure and Composition

The thickness of the earth's crust varies substantially, being fairly uniformly 5 km in oceanic settings, and averaging around 30 km (but sometimes exceeding 70 km) for continental regions. The vast majority of earth's crust is composed of igneous rocks, the result of molten material from the earth's interior solidifying, although sedimentary rocks cover 70% of continental surface and nearly all of the ocean floor. In essence, this results in a stratified crust, of which the upper part is sedimentary to a thickness of 1 – 2 km and the lower 30 or so km is an igneous, and often metamorphosed, basement.

### 2.1.2 Stresses in the Crust

The origin of forces acting on the earth's crust are a result of thermally driven motion within the mantle. These forces give rise to the deformation of rocks and the evolution of natural structures.

The state of stress in the earth's crust depends on the extent of the area being considered. In a regional context, prevailing stress regimes can be estimated through GPS measurements of strain rates and earthquake focal mechanisms. Regional stress regimes, related to tectonic-scale processes, may show localised deviations from the overall configuration which is, in part, a result of forces acting over the topographical, heterogeneous and partitioned body represented by the earth's crust.

Local stress regimes can be determined directly through in-situ measurements from boreholes, by analysis of borehole breakouts (Haimson and Herrick 1986; Zoback et al. 1986), the use of strain gauges or through overcoring techniques (McGarr and Gay, 1978).

Historical stress regimes, and how they evolved, can be inferred from the orientation and development of geologic structures, in other words through a study of how strain has manifested itself over time.

The World Stress Map Project (WSMP) has created a database of *in situ* stress measurements taken from bore-hole breakouts, hydraulic fractures, style of active faulting, volcanic alignment, seismic focal mechanisms and transform fault azimuths. Analysis (Zoback and Magee, 1991; Wilson, 1993) suggests that most of the data in the WSMP can be explained by appealing to the geometry of plate boundaries and the corresponding body forces resulting from either relative or absolute plate motions.

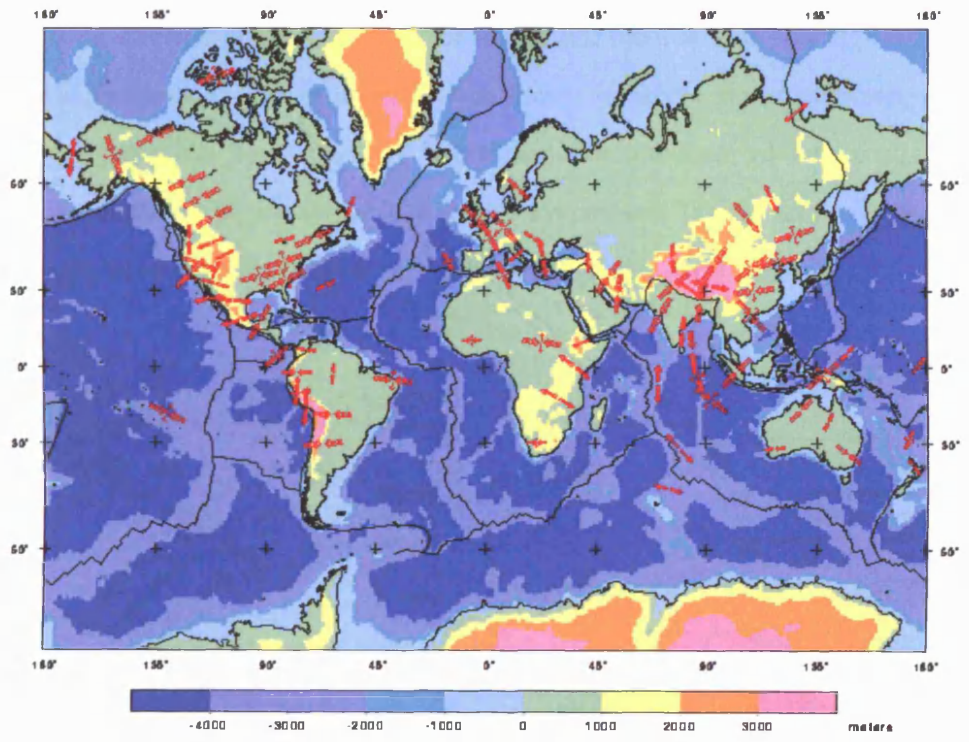


*Fig 2-1. Averaged maximum stress data (red arrows) from the World Stress Map Project. Colour contours represent elevation. From Zoback 1992.*

### 2.1.3 Brittle or Ductile Behaviour

Experimental and field work have demonstrated a rheological layering of the earth's crust, with the brittle upper crust grading into the ductile lower crust across the brittle-ductile transition. Brittle rocks can support a deviatoric stress field, whereas ductile rocks flow under a deviatoric stress field. Although the brittle-ductile transition generally occurs around 10-15 km depth, it does not simply exist at a uniform depth, rather it is determined by the prevalent geothermal gradient and strain rate (Sibson, 1986) – both of which influence the strength of materials deforming by brittle and crystal-plastic processes.

With increasing depth, pressure acts to prohibit the initiation of fractures, resulting in rocks generally being stronger at higher confining pressures and more likely to flow than to fracture. With depth, temperature also increases, which further enhances the ductile behaviour of rocks. These processes are resolved at the brittle-ductile transition; where the strength of brittle upper crustal rocks are determined largely by pressure (depth) and the strength of ductile lower crustal rocks are determined largely by temperature conditions.

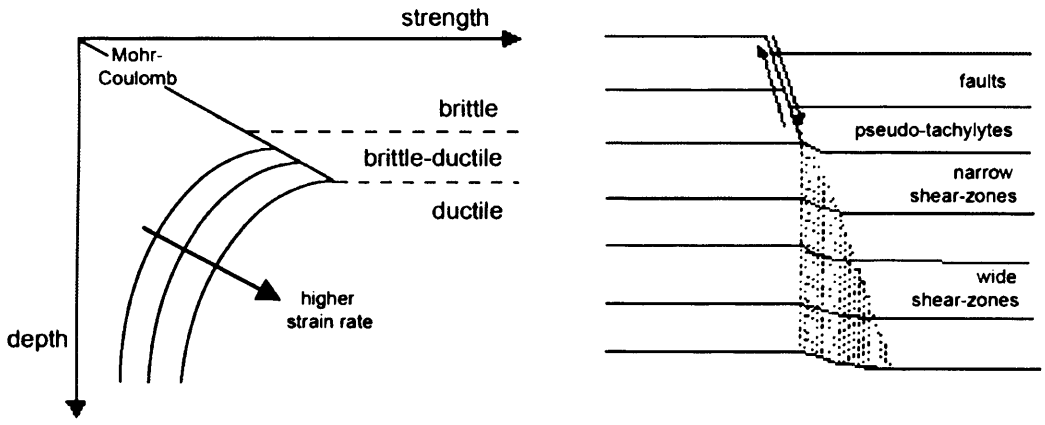


*Fig 2-2. Schematic diagram showing a typical strength profile of the earth's crust (left), and the consequent transition between brittle processes in the upper crust and ductile processes in the lower crust (right)*

In nature, materials possess a combination of elastic, viscous and plastic properties. For such materials, the relationship between stress and strain depends critically on the length of time for which the stress is applied. Rocks are weaker at lower strain rates as slow deformation allows diffusional crystal plastic processes to more closely keep up with the applied stress.

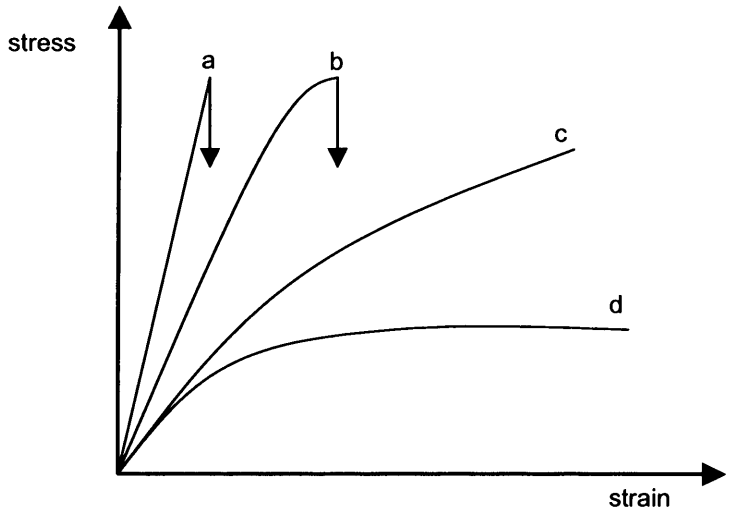


*Fig 2-3. A schematic representation of (a) brittle, (b) semi-brittle, (c) semi-ductile and (d) ductile stress-strain curves.*

## 2.2 Experimental Rock Physics

### 2.2.1 History and Development

To understand the mechanical behaviour of rocks is of importance to many disciplines, and has wider implications than may initially be apparent. Civil engineers, and therefore society, rely on an understanding of the behaviour of rock masses that allow the safe construction of tunnels and dams, for example. Geophysicists have probed the links between the physical properties of sedimentary sequences, such as electrical resistivity and sonic velocity, in order to assess the viability of oil recovery. Hydrogeologists are concerned with how the movement of groundwater, and therefore the leaching of pollutants, is influenced by the regional geology

and by the presence of man-made structures. Laboratory based experiments have allowed scientists to systematically investigate the behaviour of rocks without the difficulty of *in situ* measurement, which necessitate the drilling and manual pumping of fluids into rock masses which interfere with the initial conditions that are part of the study in the first place. Laboratory studies allow a recreation of crustal conditions which can be controlled and designed to elucidate specific scenarios.

Modern equipment for the mechanical testing of rocks is usually triaxial, whereby all three principal stresses are non-zero. There is an important distinction between a conventional-triaxial configuration and a true-triaxial configuration; a conventional-triaxial test (from here on termed 'triaxial') has principal stresses $\sigma_1 > \sigma_2 = \sigma_3$, whereas a true-triaxial test has principal stresses $\sigma_1 > \sigma_2 > \sigma_3$.

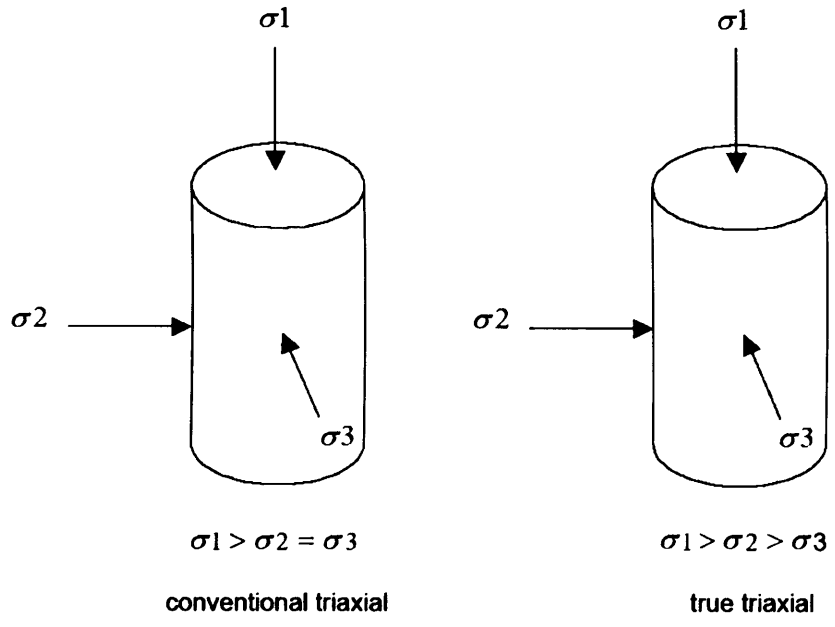


*Fig 2-4. The difference in the principal stress configuration of a conventional-triaxial test (left) and a true-triaxial test (right)*

The pioneering apparatus of von Kármán in 1911 allowed the application of a confining pressure and an independently controlled axial force, and formed the prototype for more sophisticated future deformation rigs. Modern day apparatus typically operates in the 1000 MPa range, and may use a furnace to apply temperature conditions commensurate with those that would exist at the depths being simulated during testing. The advancement of electrical engineering gave rise to servo-controlled systems in the 1970s, whereby the control input is compared to the actual position of the mechanical system as measured by a transducer at the output. Any difference between the actual and desired values (the error signal) is amplified and used to drive the system in the direction necessary to reduce or eliminate the error. This approach has meant that constant conditions of stress or strain can be maintained during testing, despite processes operating during sample deformation that would otherwise act to alter the imposed conditions.

The data from modern triaxial tests comes in raw voltages, the response of transducers to displacements and loads. Through calibration of the load and displacement transducers, meaningful values of axial strain, stress and volumetric change during the course of an experiment can be derived. External apparatus, wholly independent to the deformation rig, is often used to passively monitor phenomena associated with the deformation process, such as acoustic emissions (AE). Modifications to the deformation rig may have to be made (or initially incorporated into the design of the apparatus) in order to accommodate additional measurement devices. Geophysical signals recorded by external devices may also be used to control experimental conditions. In the example of AE, Lockner et al. (1992) used AE hit rate as a feedback to control strain rate, thus effectively slowing down their experiments to study phases of fault growth.

### 2.2.2 Limitations

The use of experimental protocol and data in understanding natural systems have two main limitations. Firstly, the issue of representing geologic-scale rock masses in laboratory scale rock specimens, and secondly the reproduction of geologically realistic conditions and time scales in the laboratory.

A sample of a material of given dimensions may not be representative of that material on a larger scale. When the purpose of investigating processes in laboratory-scale specimens is to throw light on geological-scale processes, the issue of scalability becomes significant. Consequently, the larger the laboratory sample (centimetre scale) is, the more representative it will be of a natural system (meter scale, or greater). As a result, laboratory studies often contribute to the understanding of fundamental micro-scale processes which are thought to operate within natural systems.

Geological processes occur over spatial and temporal scales which are simply, and obviously, not reproducible in laboratory settings. Natural strain rates in orogenic systems may be of the order of $10^{-15}$ $s^{-1}$ (Price, 1975), whereas in the laboratory strain rates are typically $10^{-5}$ $s^{-1}$ with $10^{-8}$ $s^{-1}$ being the lowest realistically achievable. Novel testing procedure (Meredith et al., 2005) has allowed for experiments to be conducted at strain rates as low as $10^{-11}$ $s^{-1}$, but this is by no means a simple, standard, protocol which could easily be adopted. As a result of the discrepancy between natural strain rates and those which can be achieved in laboratories, data must be interpreted with caution before being directly applied to geological scenarios.

## 2.3 The Stress Tensor

Stress is a measure of the distribution of force per unit area. By considering the force acting on a plane of an area in the limits of zero, stress can be defined as a vector property, such that:

$$\sigma = \lim_{A \to 0} \frac{F}{A}$$

where F is the force acting on an area A. To conceptualise stress in 3D, it is useful to consider an elemental cube, such as shown in figure 2-5. The stress at a point, $\sigma_{ij}$, is resolved into components either normal or tangential to the surface they are acting on and can be represented in matrix form as the stress tensor. The stress tensor is fully described by the 9 components shown in figure 2-5. In the absence of body moments, the stress tensor is symmetrical about the leading diagonal, and can therefore be described by 6 components.

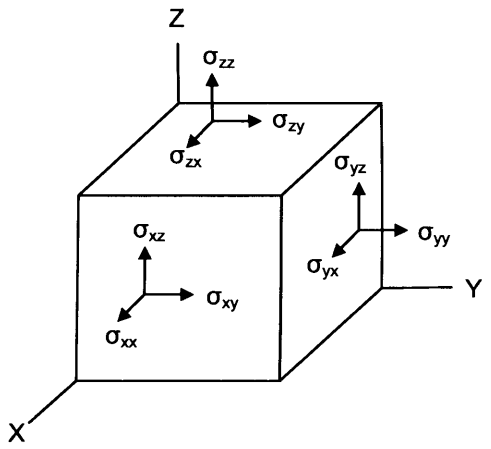


$$\sigma_{ij} = \begin{Bmatrix} \sigma_{xx} & \sigma_{xy} & \sigma_{xz} \\ \sigma_{yx} & \sigma_{yy} & \sigma_{yz} \\ \sigma_{zx} & \sigma_{zy} & \sigma_{zz} \end{Bmatrix}$$

*Fig 2-5. An illustration of the stress components acting on an elemental cube (left), and the corresponding stress matrix (right). Subscripts represent the plane and direction in which the stress is acting i.e. $\sigma_{xz}$ denotes the stress component acting on the plane normal to the x-axis and in the z-direction.*

### 2.3.1 Principal, Isotropic and Deviatoric Stresses

Principal stresses are defined as the normal components of stress acting on planes that have tangential, or shear, components of zero magnitude. Therefore, to represent the system shown in figure 2-5 in terms of principal stresses, a transformation must be applied to the stress tensor that reduces it to a diagonal matrix, termed the principal stress tensor:

$$\sigma_{ij}^{P} = \begin{pmatrix} \sigma_{xx}^{P} & 0 & 0 \\ 0 & \sigma_{yy}^{P} & 0 \\ 0 & 0 & \sigma_{zz}^{P} \end{pmatrix}$$

The principal stresses are the values of the on-diagonal components of the stress matrix. By convention, principal stresses are subscripted according to their magnitude: $\sigma_1 \geq \sigma_2 \geq \sigma_3$.

The stress tensor can also be separated (Ranalli, 1995) into isotropic and deviatoric components, whereby the isotropic component is defined as:

$$\sigma_{ij}^{0} = \frac{1}{3}\sigma_{kk}\delta_{ij}$$

where $\sigma_{kk}$ is the sum of the on-diagonal components of the stress tensor and $\delta_{ij}$ is the Kronecker delta which is equal to one when i = j, and zero when $i \neq j$, with deviatoric stress given by the relationship:

$$\sigma_{ij}' = \sigma_{ij} - \sigma_{ij}^{0}$$

Which allows the stress tensor to be written as the sum of the deviatoric and isotropic components:

$$\sigma_{ij} = \sigma_0 \delta_{ij} + \sigma'_{ij}$$

### 2.3.2 Effective Stress in Fluid Saturated Rock

A natural rock formation is generally saturated at depth, with pore fluid residing within the interconnected pore and crack network. With burial and deformation, the presence of a fluid within a rock gives rise to a pore pressure which may affect the strength of the rock by either mechanical or physico-chemical processes.

Assuming the rock's pore-space is fully saturated, the pore pressure ($P_p$) of the saturating fluid acts against the confining stress ($\sigma_{ij}$) to reduce the effective stress ($\sigma^e_{ij}$) which controls the mechanical properties of the rock.

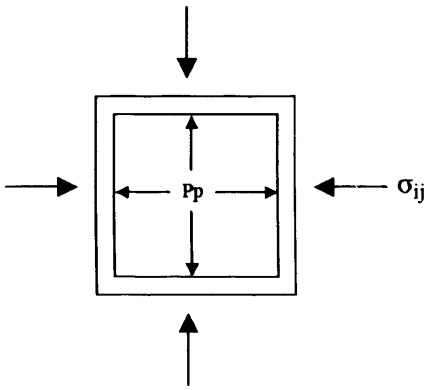


*Fig 2-6. The concept of simple effective stress illustrated by a confining stress ($\sigma_{ij}$) acting on a porous element of pore pressure ($P_p$). This system results in an effective stress of $\sigma_{ij} - P_p$.*

This gives rise the concept of effective stress, defined as

$$\sigma^e_{ij} = \sigma_{ij} - P_p \alpha_{ij}$$

The term $\alpha_{ij}$ is a constitutive relation of poroelasticity called the effective stress coefficient and is unique to a given system. It was introduced by Terzaghi (1936) in order to address the over-simplification that exists if effective stress is calculated simply as:

$$\sigma_{ij}^{e} = \sigma_{ij} - P_p$$

$\alpha_{ij}$ acts to reduce the contribution of the pore fluid in balancing against the confining pressure by taking into account forces such as intergranular stresses which provide resistance to both $P_p$ and $\sigma_{ij}^{e}$. As such, $\alpha_{ij}$ with a value of 1 indicates a matrix which doesn't provide any resistance to pressure. This is an idealised scenario, known as 'simple effective stress', and is unlikely in any natural system although it is often used as standard in experimental work. Deviations from $\alpha_{ij}$=1 may be the result of any combination of compressibility of the pore-fluid, the mechanical strength of the rock matrix or the partial saturation of the pore fabric.

If $\alpha_{ij} \neq 1$, then it is possible to determine the correct value (Nur and Byerlee 1971) through the relationship

$$\alpha_{ij} = 1 - \frac{K}{K_s}$$

where K is the bulk modulus of the rock containing the pores, and $K_s$ is the bulk modulus of the solid component only. In this work, the use of relatively incompressible distilled water as the saturating fluid justifies the assumption of the simple effective stress model.

## 2.4 The Strain Tensor

Strain is a measure of the change in relative configuration of points within a solid, the result of stresses on a body. Just as for infinitesimal stress, infinitesimal strain is a concept introduced to account for discrepancies in strain throughout a body, in other words it describes homogenous strain over a small element of a strained body. Strain, like stress, is described by a second rank tensor which can be resolved into normal and shear components (Ranalli, 1995).

### 2.4.1 Longitudinal Strain

The system illustrated in figure 2-7 shows longitudinal strain in the x-direction, given as:

$$\varepsilon_{xx} = du_x / dx .$$

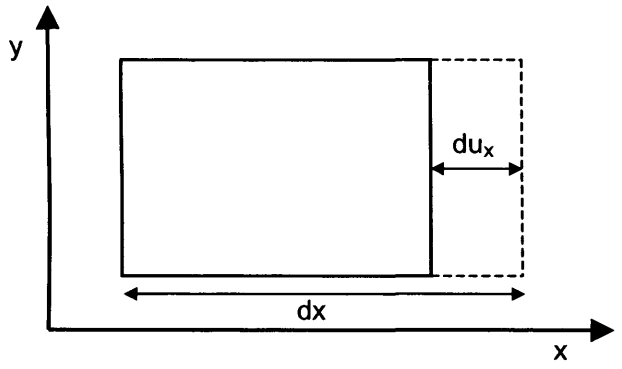


*Fig 2-7. Schematic representation of infinitesimal longitudinal strain in the x-direction*

Considering the same deformation in the y and z-directions, the normal components of the strain matrix can be written as:

$$\varepsilon_{ij} = \begin{pmatrix} \varepsilon_{xx} & 0 & 0 \\ 0 & \varepsilon_{yy} & 0 \\ 0 & 0 & \varepsilon_{zz} \end{pmatrix}$$

### 2.4.2 Shear Strain

Referring to figure 2-8, shear strain is defined as a change in angle and, in the limits of zero, angular deformation assumed to be small so that $\alpha'' \approx \tan\alpha'' = du_x / dy$ and $\alpha' \approx \tan\alpha' = du_y / dx$ with the tensorial shear strain given as the average of the two strains. This gives the relationship:

$$\alpha'' + \alpha' \approx \frac{du_x}{dy} + \frac{du_y}{dx} = 2\varepsilon_{xy}$$

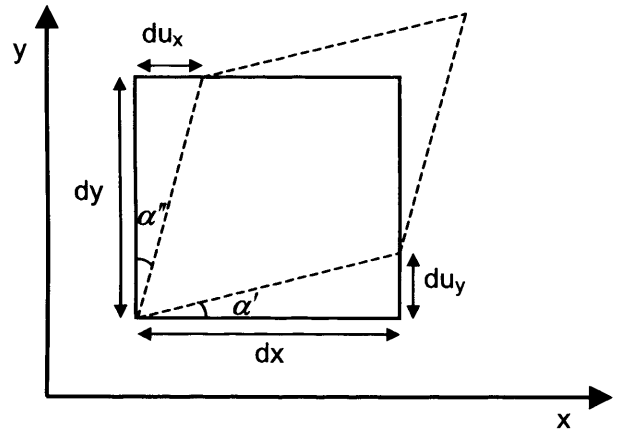


*Fig 2-8. Schematic representation of infinitesimal shear strain in the xy plane*

Considering the shear-strain system in 3D, allows the longitudinal and shear strains to be written together as the strain matrix:

$$\varepsilon_{ij} = \begin{pmatrix} \varepsilon_{xx} & \varepsilon_{xy} & \varepsilon_{xz} \\ \varepsilon_{yx} & \varepsilon_{yy} & \varepsilon_{zz} \\ \varepsilon_{zx} & \varepsilon_{zy} & \varepsilon_{zz} \end{pmatrix} = \begin{pmatrix} du_x/dx & 0.5\left(\frac{du_x}{dy}+\frac{du_y}{dx}\right) & 0.5\left(\frac{du_x}{dz}+\frac{du_z}{dx}\right) \\ 0.5\left(\frac{du_y}{dx}+\frac{du_x}{dy}\right) & du_y/dy & 0.5\left(\frac{du_y}{dz}+\frac{du_z}{dy}\right) \\ 0.5\left(\frac{du_z}{dx}+\frac{du_x}{dz}\right) & 0.5\left(\frac{du_z}{dy}+\frac{du_y}{dz}\right) & du_z/dz \end{pmatrix}$$

This tensor is directly analogous to the stress tensor, and is symmetric about its leading diagonal, allowing it also to be described by 6 components.

## 2.5 Failure

During the loading and stressing of a rock, the manner in which it behaves over short time scales ($<10^5$ s) is reasonably well described by the theory of elasticity (Gueguen and Palciauskas, 1994). For an isotropic material the relationship is given as $\sigma = E\varepsilon$, where the constant $E$ is the Young's modulus, which describes the stiffness of the material. In light of rocks being generally porous and therefore not elastically isotropic, theories of poroelasticity have evolved from classical elasticity theory to more accurately model the behaviour of rocks under stress (see Zimmerman, 1991 for a comprehensive review). However, at elevated temperature, pressure and stress conditions neither elasticity or poroelasticity theory accurately describe rock behaviour. The departure from elastic/poroelastic behaviour during deformation is termed yield, and is a often a precursor to failure. Failure can be thought of as the loss of, or significant departure from, the load bearing capacity of a material which has been stressed beyond its strength limits. In an engineering context, failure can be considered to be when a material is no longer fit for purpose.

### 2.5.1 Mohr Coulomb Fracture Criteria

The 2D state of stress on a plane can be represented on a Mohr circle in terms of the normal ($\sigma_n$) and shear ($\tau$) stresses. Mohr's criterion describes a general condition for shear fracture occurring on a plane when the shear stress reaches a value, $\tau_p$, that is a function of the normal stress on the plane, and of specific material properties. Experimentally, Mohr's criterion has been shown to be the envelope of Mohr circles at failure, which is approximately linear and can be written as the Coulomb criterion:

$$\tau_p = S + \mu' \sigma_n$$

where $S$ and $\mu'$ are material properties termed cohesive strength and internal friction respectively.

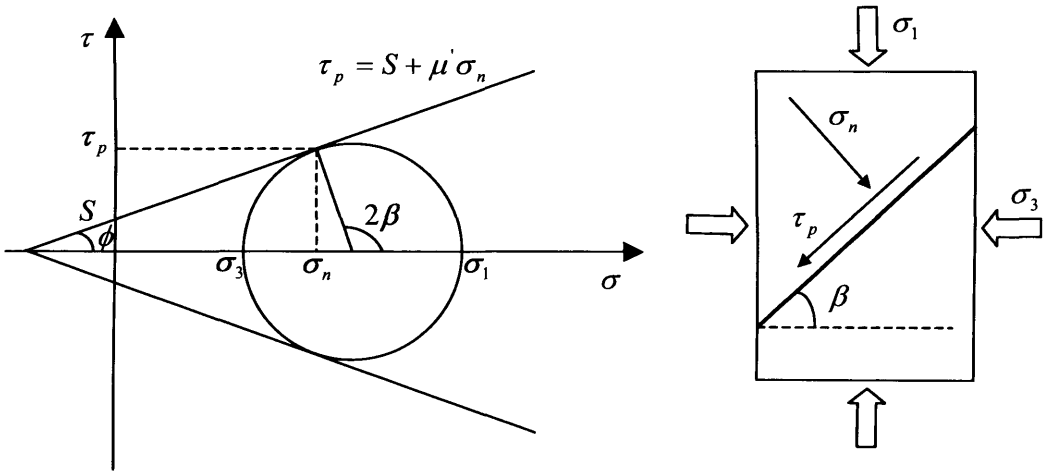


*Fig 2-9. Coulomb criterion for shear fracture, showing a Mohr circle to the left corresponding to the biaxial situation shown to the right*

For the situation shown in figure 2-9, the stress conditions at failure are given by the biaxial stress equations:

$$\sigma_n = \frac{\sigma_1 + \sigma_3}{2} + \frac{\sigma_1 - \sigma_3}{2} \cos 2\beta$$

and

$$\tau_p = \frac{\sigma_1 - \sigma_3}{2} \sin 2\beta$$

The internal friction, $\mu'$, has been shown experimentally to be a decreasing function of normal stress, and therefore the failure envelope in reality is slightly concave towards the $\sigma$-axis leading to greater fracture angles at higher mean stresses (Jaeger and Cook, 1979). Despite limitations such as this, the Coloumb criterion gives an empirically satisfactory account of the brittle shear failure of rocks (Ranalli, 1995).

As discussed in section 2.3.2, the presence of a pore pressure ($P_p$) influences the effective stress of a system, and therefore alters the Mohr circle by shifting it to the left by an amount equal to the pore-pressure. The fluid pressure is deducted from the normal stress components, but not the shear stress components. If this shift in the orientation of the Mohr circle causes contact with the Mohr-envelope, the system will destabilise sufficiently to induce failure.

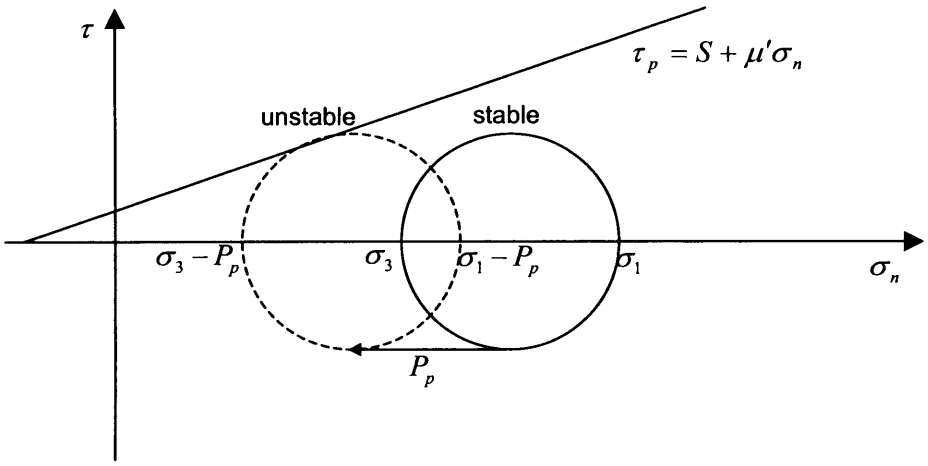


*Fig 2-10. The effect of pore-pressure in positioning the Mohr circle into unstable stress-space*

### 2.5.2 The Plane Griffith Criterion

Whereas the Coulomb criterion is purely empirical, Griffith (1924) developed a biaxial fracture criterion, where materials break in tension as a result of an existing microcrack, based upon thermodynamic principles. This concept relies on sufficient energy being released to provide the necessary surface energy for crack propagation, and concludes that failure takes place when the crack of most favourable orientation reaches a critical value of tensile stress. Figure 2-11 shows the energy partition for the Griffith model of tensile crack propagation, and illustrates the idea that for a crack length greater than that corresponding to the maximum in free energy, the crack will propagate catastrophically.

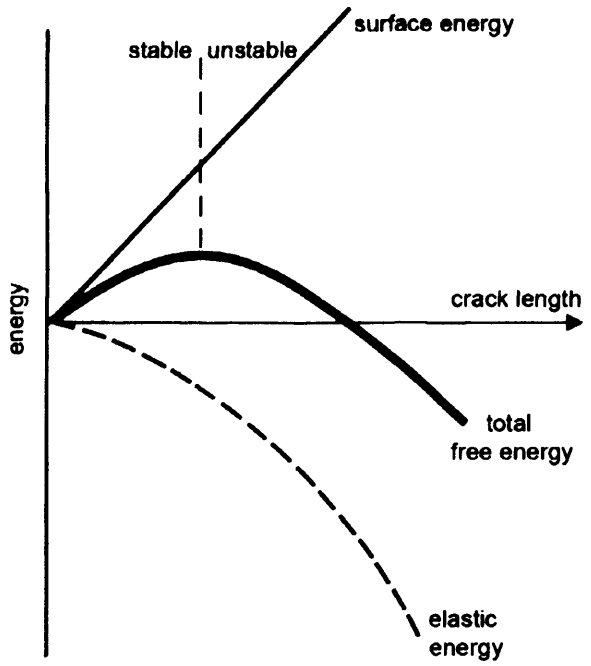


*Fig 2-11. The energy partition for the Griffith model of tensile crack propagation. After Scholz 2002.*

Griffith's theory has been extended empirically (Murrell, 1963) to a 3-dimensional scenario, and other workers (McClintock and Walsh, 1962; Murrell, 1964) have considered the effect of crack closure and the frictional interaction of crack surfaces under high pressure conditions. These extensions of Griffith's theory provides a more accurate description of fracture, because by taking into account the friction acting on crack faces, the influence of some internal physical processes are addressed. However, although the Griffith analysis provides insight into fracture initiation, it does not describe crack interaction and linkage.

### 2.5.3 Damage Mechanics

Models of damage mechanisms describe the effects of crack interaction and coalescence by considering isolated cracks in a homogeneous medium. Cracks initiate at energetically favourable positions, and grow when the stress intensity factor, $K$, exceeds the fracture toughness, $K_c$, of the surrounding medium (Digby and Murrell, 1975).

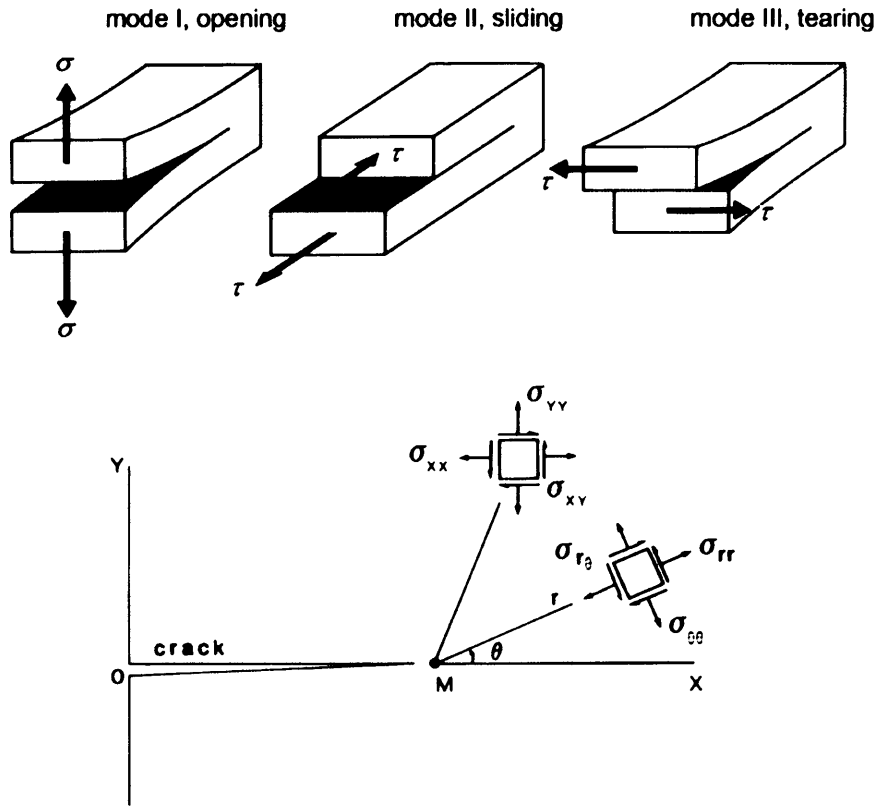


*Fig 2-12. Schematic representation of the three crack propagation modes (above) and a conceptualisation of the stress conditions at the tip of a crack (from Gueguen and Palciauskas, 1994)*

The stress field at a crack tip is given as:

$$\sigma_{ij} = \frac{K}{\sqrt{2\pi r}} f_{ij}(\theta)$$

where $r$ and $\theta$ are the polar co-ordinates of a point, $M$ (see figure 2-12). In the case of homogeneous loading, this gives stress fields for crack modes I, II and III of length 2c as:

$$K_I = \sigma\sqrt{\pi c} \qquad K_{II} = \tau\sqrt{\pi c} \qquad K_{III} = \tau\sqrt{\pi c}$$

For a linear elastic material, a the stress field at the tip of a mixed mode of crack can be determined by summing all modes:

$$\sigma_{ij}^{T} = \sigma_{ij}^{I} + \sigma_{ij}^{II} + \sigma_{ij}^{III}$$

Models considering the effects of elevated confining pressure and temperature suggests that distributed cracking leads to an amplification of the stress intensity factor, $K$, permitting crack growth under relatively low differential stress (e.g. Horrii and Nemat-Nasser, 1985). The time-dependent influence of chemically active fluids on the stress field around crack tips has been considered by Costin (1987), and was found to allow the sub-critical growth at stress intensity factors well below $K_c$.

### 2.5.4 Failure Modes During Triaxial Deformation

Samples that fail under triaxial testing do so in different ways depending on the prevailing pressure and temperature conditions. Rocks generally deform elastically up until about 50% of the peak stress. After this point, crack growth, interaction and coalescence become significant and eventually the rock fails. In studying the mechanical behaviour of rocks, the stress-strain curve for a brittle rock typically shows the form shown in figure 2-13.

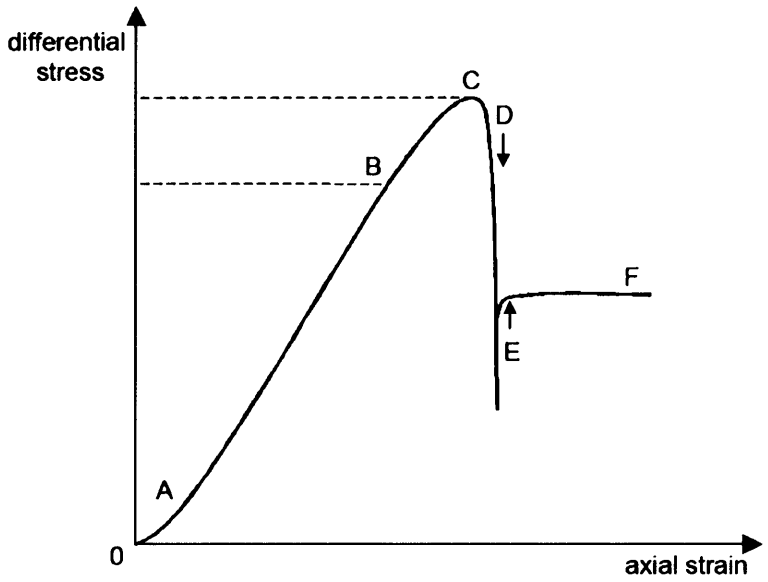


*Fig 2-13. A typical stress-strain curve for a rock undergoing brittle failure (see text for detail).*

Region OA is slightly concave upwards as pre-existing microcracks within the material close in response to an applied differential stress. Following this, region AB is pseudo-linear, demonstrating an elastic response to loading. At point B , the stress-strain curve departs from its pseudo-linear trend as the differential stress becomes sufficient to introduce new damage into the sample. Subsequent deformation is inelastic and permanent, involving the initiation and growth of microcracks leading to the dilation of the sample. Region BC shows a 'roll-over' until the attainment of a peak stress, C. During this period, microcracks start to coalesce and interact. At the point of dynamic failure, D, interacting microcracks form a through-going fault, often leading to a complete loss of cohesion across the fault plane. At this point, the material can no longer support the existing differential stress, and a rapid stress drop is observed. Following this sudden rupture, there is a rebound, E, and frictional sliding along the newly formed fault. Region F of the curve is associated with frictional sliding, and this plateau represents the differential stress required to overcome friction and produce displacement along the fault plane.

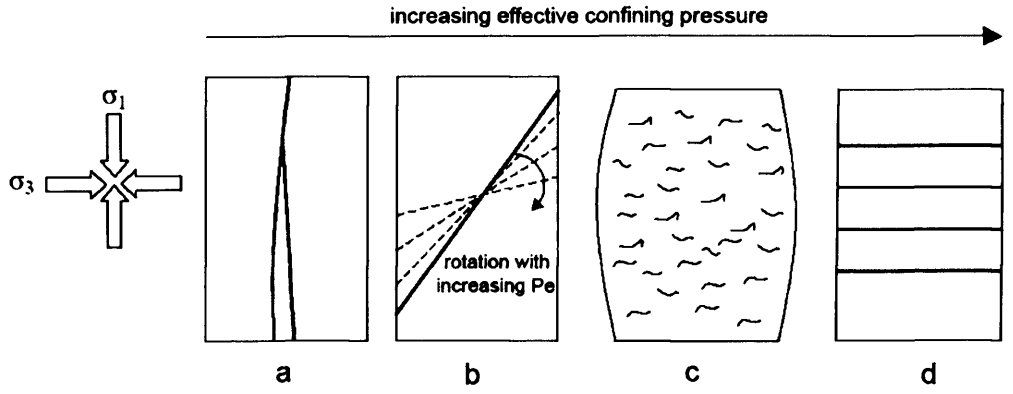


*Fig 2-14. The transition from axial splitting, through faulting, to cataclastic flow and localised compaction as a function of increasing confining pressure.*

Confining pressure plays a key role in the macroscopic failure mode that is observed during triaxial deformation experiments. At low confining pressure, samples fail through axial splitting in a direction parallel to the axis of $\sigma_1$ (fig. 2-14a), at intermediate confining stress, samples fail with the development of a through going fault oriented at about 60° to $\sigma_1$ (fig. 2-14b). With increasing confining stress, the orientation of the fault plane develops at a higher angle to $\sigma_1$ (fig. 2-14b). At sufficiently high confining pressure, overtly frictional processes, such as faulting, are suppressed and the rock deforms by distributed cataclastic flow (fig. 2-14c). In a rock of sufficient porosity, deformation at a high confining pressure can lead to pore-collapse and localised compaction in the form of compaction bands (fig. 2-14d). Since compaction bands are the subject of this thesis, they are discussed in detail in chapter 4.

### 2.5.6 Acoustic Emission and Failure

Acoustic emissions (AE) are elastic waves that result from rapid strain relief in a brittle material, for example during the development of a crack. In the study of rock deformation AE is also termed microseismic activity. During deformation and increasing stress, it has been shown many times that the number of AE hits increases as failure is approached (e.g. Sammonds et al., 1989; Meredith et al., 1990).

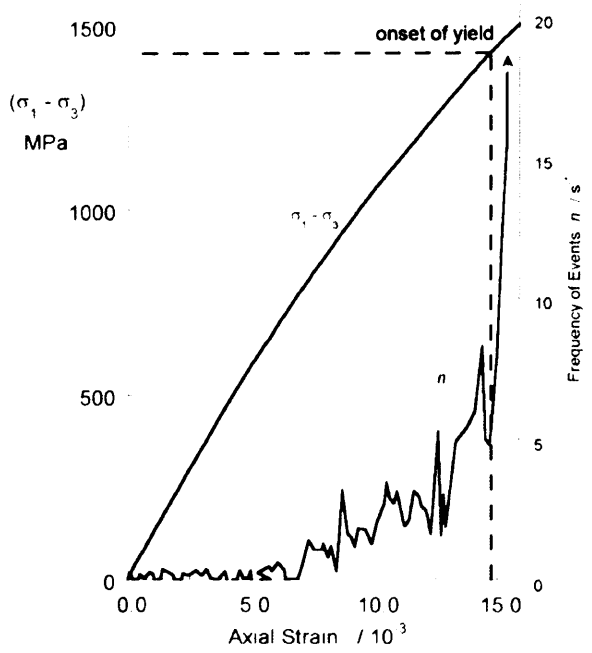


*Fig 2-15. The onset of yield is indicated by a surge in AE activity commensurate with the departure from pseudo-elastic linearity in the stress-strain curve. After Paterson and Wong, 2005.*

These studies, which include uniaxial, biaxial, triaxial and creep deformation, show that the threshold for the onset of AE associated with microfracturing generally occurs at about 70% of the macroscopic fracture stress. This is in agreement with the work of Brace et al. (1966), which asserts that the onset of dilatancy occurs at 65-75% of the peak stress. The cracking which gives rise to AE has been shown to be time-dependent, with activity continuing after a given stress level has been applied and no longer increased. During cyclical straining, it has been observed (Lockner, 1993; Holcomb, 1993) that AE recommences only when the maximum stress of the previous cycles has been exceeded. This is known as the 'Kaiser effect', and suggests that new damage is initiated only at stress levels that the material has not been previously exposed to.

Studies of the frequency distribution of AE events of different magnitudes (Scholz 1968; Sammonds et al., 1992; Lockner 1993, Read et al., 1995) have shown that the frequency of

occurrence of events decreases as their magnitude increases. This phenomenon has previously been found in seismology, and the (Gutenberg-Richter) relationship is given by

$$\log N(M) = a - bM$$

Where N is the number of earthquakes of magnitude M or greater, and a and b are constants. The slope of the log linear frequency-magnitude plot is termed the b-value, and has been shown during brittle fracture tests (Meredith et al., 1990; Sammonds et al., 1992) to decrease to a minimum at the point of peak stress, before recovering post-failure as frictional sliding dominates the deformation sequence. This is in line with theoretical predictions (Main et al., 1989).

By monitoring AE on several transducers located around the specimen being tested, and recording the relative arrival times of events, it is possible to locate the spatial origin of microfractures. The principles of this are similar to the use of global seismic networks in determining the epicentre of earthquakes based on the p-wave first arrival. Such studies have shown (Scholz, 1968; Lockner et al., 1992) that initially AE are distributed throughout the specimen being tested, as failure approaches AE locations become more spatially concentrated; corresponding to the nucleation and coalescence of cracks (fig 2-16). Eventually, macroscopic fracture occurs in the zone of high AE concentration. The accurate location of hypocentres depends on how well known the velocity structure of the deforming rock is, and this is an anisotropic property subject to variation during the course of the experiment as the stressed rock accumulates damage. The work of Lockner (1993) suggests that AE location with an accuracy of 2 mm can be achieved with transducers in the megahertz frequency response range.

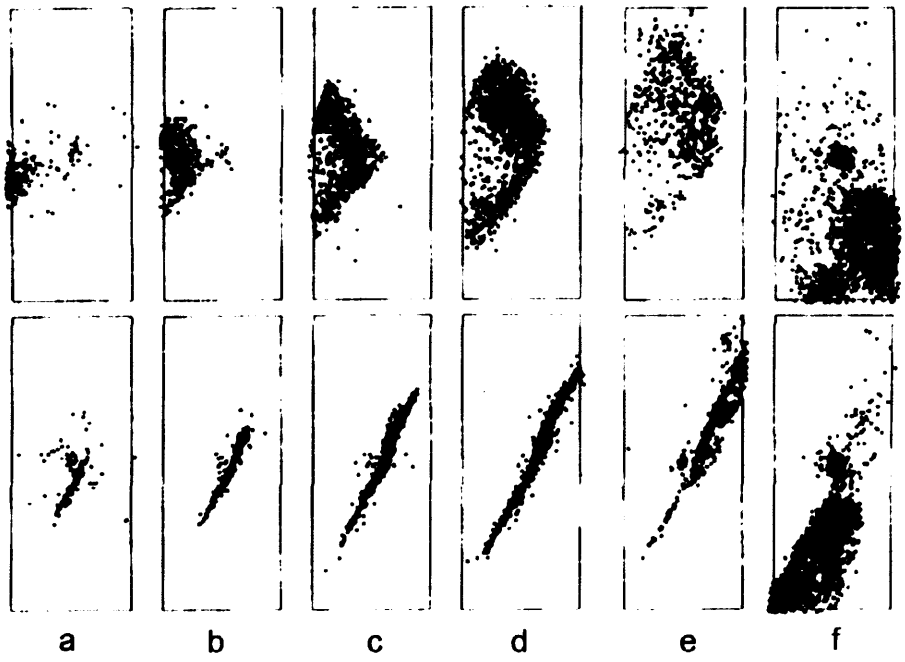


*Fig 2-16. Plot of AE locations showing the development of damage in Westerly granite during triaxial deformation. Top plot is a face-on view of the fault, bottom plot is a view along-strike of the fault. After Lockner et al., 1992.*

### 2.5.7 Permeability and Failure

Permeability describes the ease with which a medium transmits a fluid. It is thought (Brace et al., 1968), in the case of compact rocks, that under initial hydrostatic loading, the applied confining pressure causes elastic closure of pre-existing microcracks within the rock. This leads to a reduction in both porosity and permeability as void space and fluid pathways are reduced. As applied stress is increased, the specimen starts to undergo dilatancy as new damage is introduced, resulting in an increase in porosity and permeability.

For porous rocks, behaviour is less predictable, with some workers observing an increase in permeability before peak stress, and others reporting a decreasing permeability with increasing stress. Experimental data presented by Zhu and Wong (1997) shows that during initial hydrostatic loading, there is a positive correlation between porosity and permeability

change. However, when the onset of dilatancy is reached during triaxial loading, a negative correlation between permeability and porosity change becomes apparent; with permeability continuing to decrease despite an increase in the porosity of the rock. A possible explanation for this is that, during dilatancy, the communition of grains results in the obstruction of fluid pathways leading to a decreased permeability. A full discussion of dilatancy and compaction under differential stress is presented in the context of compaction bands, in chapter 4.

# 3 Anisotropy

## 3.1 Overview

Anisotropy exists when a property varies with the direction in which it is measured. Anisotropy is ubiquitous in rocks, and may be the result of a fabric alignment caused by depositional processes (in sedimentary rocks) or as a result of an inherent anisotropy associated with crystallographic structure (in igneous and metamorphic rocks). Diagenetic processes may add to the anisotropy of a material, by virtue of the fact that when subjected to an anisotropic stress field (e.g. fig 2-1), damage will develop in a preferentially aligned manner (e.g. parallel to $\sigma_1$) leading to a pore-fabric anisotropy which in turn is likely to induce a mechanical (strength) anisotropy.

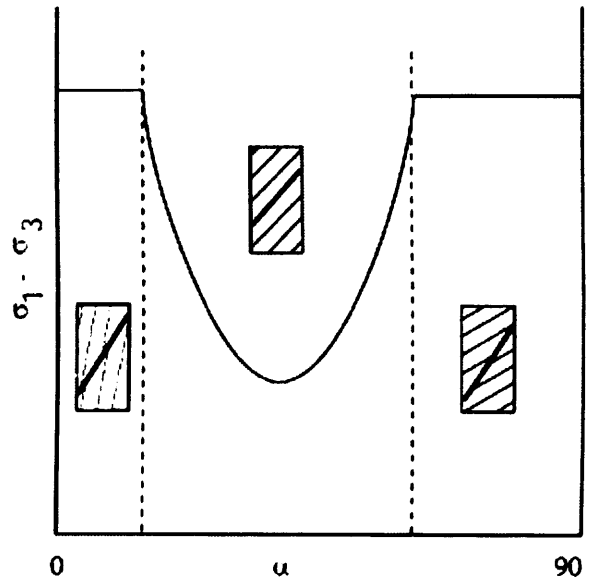


*Fig 3-1. The dependence of the differential stress at failure on the orientation α for the single-plane-of-weakness model of anisotropic rock. From Paterson and Wong, 2005.*

Anisotropy is commonly quantified by measuring one, or preferably several, directionally dependent parameters such as electrical resistivity, magnetic susceptibility, permeability and elasticity (usually via elastic wave velocities). The advantage of using multiple measures of anisotropy comes from the fact that each is sensitive to different material properties. For example, as a result of the high contrast between the stiffness of a rock's matrix and its void-space, the anisotropy of elastic wave velocities is particularly sensitive to the orientation of pores and cracks. The anisotropy of permeability, on the other hand, is sensitive to the connectivity of pores and cracks rather than to the physical distribution of void space in and of itself, although the two may often be coupled. Thus, by measuring a number of material properties, a more fully orbed picture of the nature of a material's anisotropy can be obtained. However, given the substantial time-scales and diverse processes operating in natural systems, rocks may exhibit an overall anisotropy which reflects the contribution of many independent mechanisms superimposed upon one-another. In such cases, it is a non-trivial task to capture the essence of a material's anisotropy.

### 3.1.2 Anisotropy of Pore Fabric

Although porosity is defined as a ratio, and is therefore a scalar quantity, it is important to understand the anisotropic geometric properties of rock void-space because of the influence it has in controlling fluid flow (Bear, 1988), and therefore its relevance to a wide range of issues including resource management and waste disposal (Fetter, 2001). A convenient way of characterising pore-fabric is to assign it an equivalent geometrical shape (e.g. Dullien, 1992) to represent the average orientation of the void-space within the rock. This is illustrated schematically in figure 3-2, where the void-space is represented as an ellipsoid with semi - axes $a > b > c$.

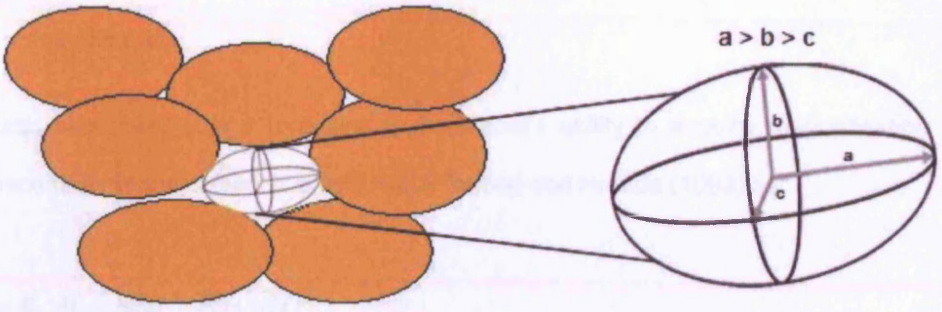


*Fig 3-2. Schematic illustration of the assignment of an ellipsoid as the equivalent void-space. The major, intermediate and minor semi-axes of the ellipsoid are shown as a, b and c, respectively.*

The assignment of an equivalent void-space in this manner is only an approximation of the complexity that exists in nature, but it provides a useful way to visualise and calculate the anisotropy of the pore-fabric. Pore-fabric anisotropy is defined as the relative shape and orientation of the average void-space within the rock, and is calculated as the ratio between the major and minor ellipsoid semi-axes, given as *a/c* for the example shown in figure 3-2. By convention, this is a different calculation to that used in studies of seismic anisotropy, which is calculated as *velocity differential / mean*.

In this study, anisotropy of pore-fabric is quantified by measuring three parameters; magnetic susceptibility, elastic wave velocity and permeability. The methodologies used for each technique are described in detail in chapter 5, with the following sections providing some background theory on the individual properties.

## 3.2 Magnetic Susceptibility

### 3.2.1 Introduction

Magnetic susceptibility is a measure of a material's ability to acquire magnetisation in the presence of a magnetic field. It is defined by Tarling and Hrouda (1993) as:

$$M_i = K_\chi H_i \quad \text{and} \quad J_i = \chi H_i$$

where $M_i$ is the magnetisation per unit volume, $K_x$ is volume susceptibility, $\chi$ is mass susceptibility, $H_i$ is the magnetising field and $J_i$ is the magnetisation per unit mass.

Anisotropy of magnetic susceptibility is therefore the variation of magnetic susceptibility with direction of measurement. As such, magnetic susceptibility can be described in relation to a spatial reference frame and written as:

$$\begin{aligned} M_x &= K_{xx}H_x + K_{xy}H_y + K_{xz}H_z \\ M_y &= K_{yx}H_x + K_{yy}H_y + K_{yz}H_z \\ M_z &= K_{zx}H_x + K_{zy}H_y + K_{zz}H_z \end{aligned}$$

or

$$M = K_{ij}H_j$$

Collinson (1983) considered the relations $K_{xy} = K_{yx}$, $K_{yz} = K_{zy}$ and $K_{zx} = K_{xz}$, which reduces $K_{ij}$ to a symmetrical tensor containing six independent constants. Like all second rank tensors, magnetic susceptibility maps out an ellipsoid in 3D which can be described in terms of the lengths of its semi-axes.

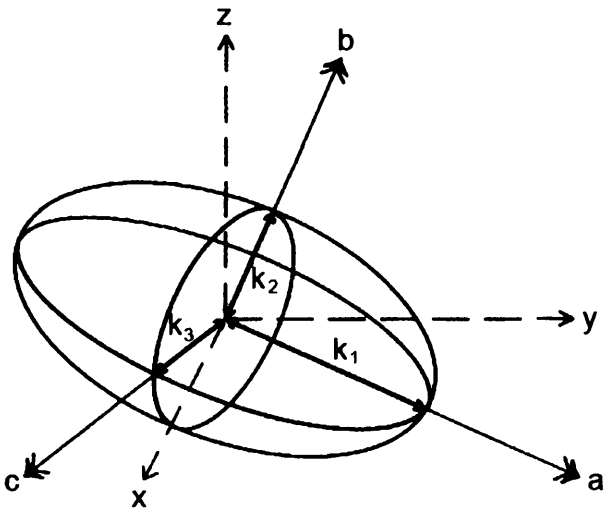


*Fig 3-3. A magnetic susceptibility ellipsoid within a general $O_{xyz}$ co-ordinate frame, with principal susceptibility axes $K_1 > K_2 > K_3$ and principal geometric axes a > b > c. After Tarling and Hrouda, 1993.*

In rock magnetism studies, the susceptibility ellipsoid is generally characterised via three parameters; lineation, foliation and anisotropy. These terms are defined as follows:

Lineation (L) = $K_1 / K_3 = K_{max} / K_{min}$

Foliation (F) = $K_2 / K_3 = K_{int} / K_{min}$

Anisotropy (A) = $K_1 / K_3 = K_{max} / K_{min}$

The lineation and foliation parameters describe the extent to which the magnetic susceptibility ellipsoid is oblate or prolate, with the anisotropy indicating the eccentricity of the ellipsoid with respect to a sphere.

Traditionally, anisotropy of magnetic susceptibility (AMS) measurements are used to provide information on the anisotropy of the rock's matrix. However, a novel technique first developed by Pfleiderer and Halls (1990) is used to apply these principles to the study of pore-fabric anisotropy. This application of AMS is discussed in the following sections.

### 3.2.2 AMS to Quantify Pore Fabric

Many sedimentary rocks are magnetically susceptible as a result of the natural occurrence of magnetic grains within the material matrix, and geologists have been able to take advantage of this by measuring the AMS of samples to determine preferred grain orientations and hence to estimate palaeocurrent directions. Since empty void space cannot contribute to a rock's magnetic susceptibility, the conventional AMS technique can only provide information on the matrix of the material being measured. However, Pfleiderer and Halls (1990) developed a modified approach to AMS measurements which provides information on the anisotropy of void-space.

This application of AMS involves saturating samples with a magnetic ferrofluid suspension so that the void space is filled with a highly susceptible medium. The AMS of the ferrofluid saturated sample is then measured in exactly the same manner as done for dry samples. The resulting anisotropy parameters then represent the superposition of the dry matrix AMS and that of the ferrofluid filled pore-space. Providing the magnetic susceptibility of the ferrofluid is much greater than the susceptibility of the rock's matrix, then the measurements can overwhelmingly be attributed to the rock's pore-fabric. To distinguish between the traditional AMS technique used on dry samples and the more recent technique used on ferrofluid saturated samples, the convention of Benson et al. (2003) is adopted whereby dry AMS measurements are termed mAMS (matrix AMS) and measurements on ferrofluid saturated samples are termed tAMS (total AMS). Sedimentary rocks often have significant porosity and a relatively low native magnetic susceptibility. This makes such materials ideal for this technique because, when saturated with ferrofluid, tAMS >> mAMS, and therefore it can be said that tAMS ~ pAMS (pore-fabric AMS).

### 3.2.3 Equivalent Pore Concept

Experimental work (Pfleiderer and Halls, 1993; Benson et al, 2003) has shown that the direction of the principal axes of magnetic susceptibility from measurements of pAMS are in close agreement with the principal anisotropy directions of the overall void-space. However, the relative magnitudes of the magnetic susceptibility axes often underestimate the anisotropy of the void space as a result of internal opposing magnetisation induced by the applied measuring field, termed the 'demagnetising effect' (Collinson, 1983).

In relation to an ellipsoid such as that shown in figure 3-3, the demagnetising effect means that:

$K_1 / K_2 \neq a / b$

$K_2 / K_3 \neq b / c$

$K_1 / K_3 \neq a / c$

Therefore, the lineation and foliation parameters derived from magnetic susceptibility cannot be taken as being equal to the lineation and foliation of the average void-space. However, Hrouda et al. (2000) have developed an approach known as the 'equivalent pore concept' (EPC) whereby an overall physical void space shape and alignment is modelled so as to produce the same magnetic anisotropy parameters as the measured sample, which, takes into account the demagnetising effect. This allows a direct comparison between the pAMS ellipsoid and the ellipsoid that describes the average void space.

The approach of Hrouda et al. (2000) considers the AMS shape of a ferrofluid filled pore being defined as:

$$L = \frac{K_1}{K_2} = \frac{(1 + k_i N_2)}{(1 + k_i N_1)} \qquad F = \frac{K_2}{K_3} = \frac{(1 + k_i N_3)}{(1 + k_i N_2)} \qquad A = \frac{K_1}{K_3} = \frac{(1 + k_i N_3)}{(1 + k_i N_1)}$$

Where $K_1 > K_2 > K_3$ are the principal susceptibilities, $N_1 > N_2 > N_3$ are the demagnetising factors along these axes, $k_i$ is the intrinsic susceptibility related to measured susceptibility by: $k_m = k_i / (1+N k_i)$, where $k_m$ is the measured ferrofluid susceptibility and $N=1/3$, the demagnetising factor of a sphere. The demagnetisation factors derived as functions of the magnitudes of the axes a > b > c are given by Osborn (1945) as:

$$N_1 = \frac{\cos\varphi\cos\vartheta}{\sin^3\vartheta\sin^2\alpha}\left[F(n,\vartheta) - E(n,\vartheta)\right]$$

$$N_2 = \frac{\cos\varphi\cos\vartheta}{\sin^3\vartheta\sin^2\alpha\cos^2\alpha}\left[E(n,\vartheta) - \cos^2\alpha\,F(n,\vartheta) - \frac{\sin^2\alpha\sin\vartheta\cos\vartheta}{\cos\varphi}\right]$$

$$N_3 = \frac{\cos\varphi\cos\vartheta}{\sin^3\vartheta\cos^2\alpha}\left[\frac{\sin^2\alpha\sin\vartheta\cos\vartheta}{\cos\varphi} - E(n,\vartheta)\right]$$

where: $\cos\vartheta = c/a \qquad (0 \le \vartheta \le \pi/2)$

$$\cos\varphi = b/a \qquad (0 \le \varphi \le \pi/2)$$

$$\sin\alpha = \left\{\frac{1-(b/a)^2}{1-(c/a)^2}\right\}^{\frac{1}{2}} = \frac{\sin\varphi}{\sin\vartheta} = n \qquad (0 \le \alpha \le \pi/2)$$

Where $F(n,\vartheta)$ and $E(n,\vartheta)$ are elliptic integrals of the first and second kind respectively, $n$ is the integral modulus, and $\vartheta$ is the integral amplitude. From this, Hrouda et al. (2000) calculate the magnetic lineation and foliation for given ellipsoid principal axes ratios a/b and b/c. The relationships between magnetic lineation & foliation and the physical void space ratios a/b and b/c are then shown graphically on an equivalent pore concept chart, allowing measured values of L and F to be read off in terms of a/b and b/c.

Jones et al. (2006) tested the EPC using synthetic pores of known dimensions, and found that the EPC did a good job in correcting for the demagnetising effect for high ferrofluid concentrations, but significantly underestimated the required correction for low concentrations. This is an important problem since low ferrofluid concentrations are commonly used when making measurements on high porosity sedimentary rocks. In response to this, the same workers derived an empirical correction factor that allows accurate predictions of void-space anisotropy to be made from the EPC method for measurements made using a range of ferrofluid concentrations. These issues are addressed in the discussions chapter.

## 3.3 Acoustic Velocity

### 3.3.1 Influence of Porosity

Shear waves and compressional waves have velocities ($Vs$ and $Vp$ respectively) which, in the idealised case of an elastic isotropic rock, can be expressed in terms of the elastic constants and density of a medium:

$$Vp = \sqrt{\frac{K + 4/3\mu}{\rho}} \qquad Vs = \sqrt{\frac{\mu}{\rho}}$$

where $\rho$ is density, $K$ is the bulk modulus and $\mu$ the shear modulus of the media.

However, rocks contain porosity which in nature is often saturated, or partially saturated, with a fluid or multiple fluids. This leads to a relationship, proposed by Wyllie et al. (1958), to describe the bulk velocity through a fluid saturated rock as:

$$\frac{1}{Vt} = \frac{\phi}{Vf} + \frac{1-\phi}{Vm}$$

where $Vt$ is the bulk velocity, $Vf$ is the wave velocity in the fluid, $Vm$ is the velocity in the mineral aggregate and $\phi$ is the rock porosity. Elastic wave velocity is therefore very sensitive to the contrast between the densities and 'stiffness' of pore fluids and the rock matrix. As such, oriented measurements of elastic wave velocities can be used to infer something about the relative distribution of void-space to solid matrix as a function of direction. However, at the mineral scale, elastic anisotropy is always the case (Gueguen and Palciauskas, 1994), with, for example, the elastic modulus of quartz differing by as much as 40% along different crystallographic axes (Zimmerman, 1991). Therefore, measurements which seek to attribute velocity anisotropy to the distribution of void-space must ensure that the elastic wavelength is such that its travel time through a rock reflects the effective elastic properties of the 'bulk' sample, rather than the individual properties of minerals phases and grains. To ensure this, it is prudent to take measurements on samples which allow 10 grain diameters per wavelength, and 10 wavelengths per sample length.

### 3.3.2 Anisotropy of Velocity

Measurements of velocity as a function of azimuth around three orthogonal cores can be fitted to an ellipsoid (methodology described in chapter 5), whose principal axes can be described in the same way as introduced for AMS measurements. However, as acoustic velocity is strongly coupled with elasticity, and in the anisotropic situation elasticity is described by a fourth rank tensor, the expression of velocity anisotropy as a ellipsoid (a second rank tensor) is strictly an approximation (Louis et al., 2003). Although approximate, the errors in fitting velocity data to an ellipsoid are generally less than the error involved in P and S-wave measurements (which are about 1% and 2% respectively). Fitting velocity data to an ellipsoid in this way has the advantage of allowing a determination of principal anisotropy directions that can be directly compared to the pAMS data.

## 3.4 Permeability

Permeability is a measure of how easily a material transmits a fluid, it has dimensions of $L^2$ and may be thought of as an effective cross-sectional area for flow. Permeability is a material property that shows vast range in nature, with typical values for geological media easily spanning a dozen orders of magnitude, and values for a given rock type varying by 3 or 4 orders of magnitude (see figure 3-4). As a result of its economic and environmental significance, a great deal of effort has been made to understand the factors controlling the movement of fluids through geological media. A good review is presented by England et al., 1987.

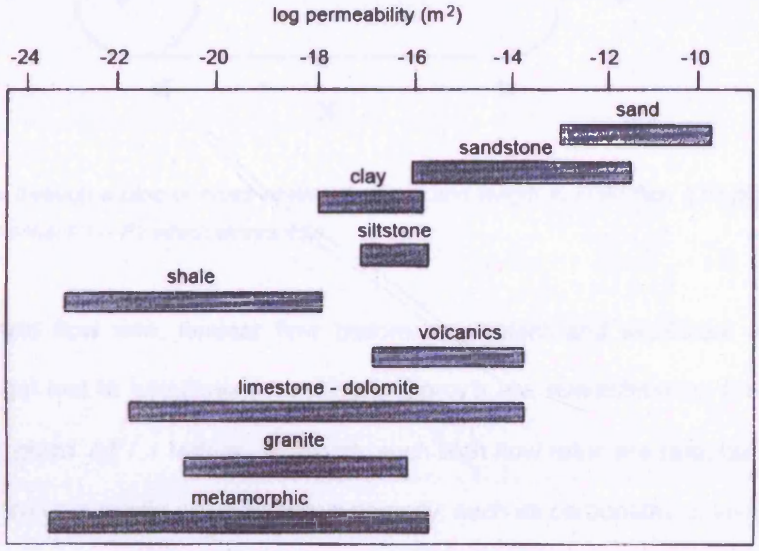


*Fig 3-4. Crustal rocks and their typical permeabilities at 10 MPa effective pressure. (From Brace et al., 1968).*

### 3.4.1 Darcy's Law and its Limits

For the scenario shown in figure 3-5, the empirically derived Darcy's law is used to relate flow rate to permeability, $k$, and can be written as:

$$q = -\frac{k\,\Delta P}{\eta\, x}$$

where $q$ is the fluid flux (volume / time x area), $\eta$ is the fluid viscosity, $x$ is the sample length and $\Delta P$ is the pressure gradient which drives flow.

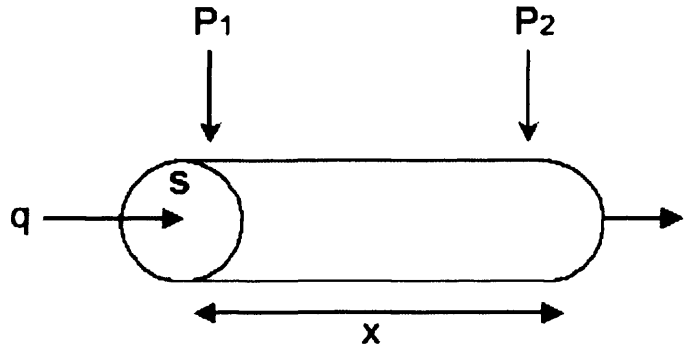


*Fig 3-5. Fluid flow through a pipe of cross-sectional area s and length x. Fluid flux, q, is proportional to the pressure differential P1 – P2 which drives flow.*

Above a threshold flow rate, laminar flow becomes turbulent and significant amounts of energy start to get lost to turbulence, resulting in Darcy's law overestimating the flow rates associated with given $\Delta P / x$ values. In nature, such high flow rates are rare, but may occur near to a well-bore or in media with cavernous porosity such as carbonates or lava flows. The upper boundary for Darcy's law is typically estimated in relation to the Reynold's number, Re, a dimensionless parameter used to identify different flow regimes. The Reynold's number is the ratio of a fluid's inertial to viscous forces, given as:

$$\mathrm{Re} = \rho q L / \mu$$

where $\rho$ is the density of the fluid, $q$ is the fluid flux, $\mu$ is the dynamic viscosity of the fluid and $L$ is a characteristic length. In granular porous media, such as sedimentary rocks, $L$ is

often related to the grain-size distribution, with the transition to non-Darcian flow (laminar to turbulent flow) occurring at Re ~ 5 (Bear, 1979). For a porous-medium/fluid system, where $\rho$ =1000 kg/m$^3$, $\mu$ =1.1 x10$^{-3}$ Pa-sec and the grain size of a coarse sand, $L$, is taken as 0.001 m, it can be shown that Darcy's law would begin to over predict flow rates for $q$ > 5.5 x10$^{-3}$ m/s.

Under very low pressure gradients, Darcy's law may be non-applicable as other modes of mass transport, such as diffusion along a chemical gradient, may act to control the rate of flow, in which case a Darcian approach may underestimate the flow rate associated with a given $\Delta P / x$.

### 3.4.2 Permeability and Porosity

There is usually a strong positive correlation between porosity and permeability, which for well-sorted porous media is often expressed in terms of the Kozeny-Carman relationship:

$$k = \frac{\phi^3}{5 s_0^2 (1-\phi)^2}$$

where $k$ is permeability, $\phi$ is porosity and $s_0$ is the solid surface exposed to the fluid per unit volume of solid material. However, some geologic media may show a negative correlation between porosity and permeability, for example a volcanic tuff which cools rapidly around the edge of the ash-flow may retain its high porosity (around 50%), although the permeability of the material stays relatively low because the pores are not well connected. In contrast, the interior of the flow, which cools slowly, may lose much of its original porosity (reducing to around 5%), but fractures during the process, becoming a welded unit. Potentially, this can lead to an interconnected network that transmits fluids very efficiently, despite a low overall porosity. For example, Winograd (1971) shows that the permeability of a tuff may be 10$^4$ times

higher through the interior than through the top or bottom of the unit, despite respective porosities which might suggest otherwise. This illustrates that there is not a straightforward relationship between porosity and permeability, as ultimately the latter is dependent not on porosity in and of itself, but on the degree to which it is interconnected. This has lead to workers explaining permeability trends using geologically representative pore-scale network models, a procedure which has had a degree of success in predicting porosity/permeability trends consistent with experimental data (e.g. Byrant et al., 1992).

### 3.4.3 Anisotropy and Heterogeneity

Permeability is often anisotropic, with the most significant cause in sedimentary rocks being layering and preferential alignment of minerals and grains (Ingebritsen and Sanford, 1999), which generally leads to greater permeabilities parallel to bedding than normal to bedding. In experimental work when making comparative studies, homogeneity between samples is often assumed, which, when dealing with fluid flow, may be taken to mean that the value of permeability in a given direction is randomly distributed about a mean, or that between representative elemental volumes the permeability in a given direction does not vary.

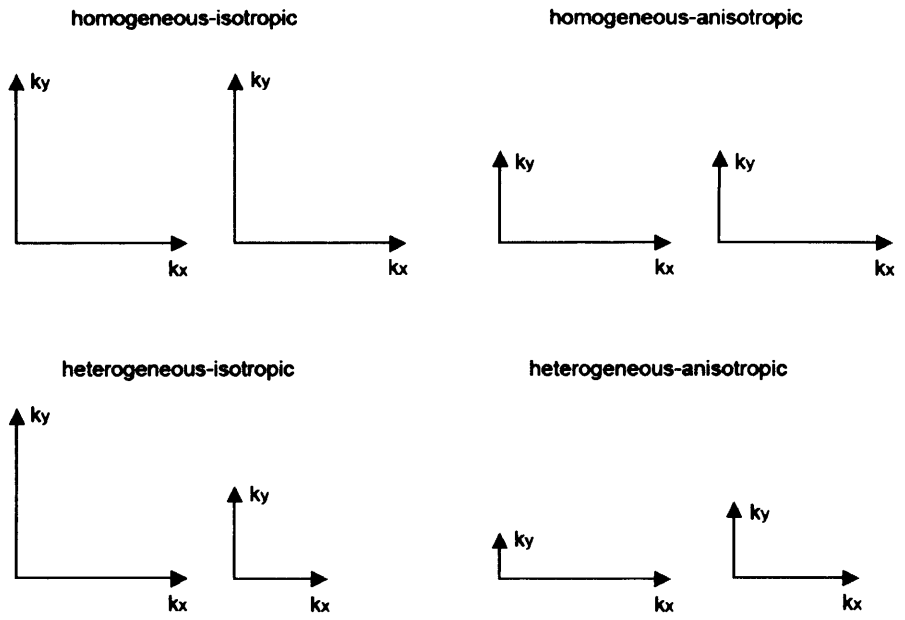


*Fig 3-6. The four combinations of heterogeneity and isotropy showing that in a homogeneous-isotropic medium permeability does not vary ($k_y$=$k_x$) with direction or position. In a homogeneous-anisotropic medium permeability does not vary with position but does vary with direction at a point. In a heterogeneous-isotropic medium permeability varies with position but not with direction, and in heterogeneous-anisotropic medium permeability varies with both position and direction. After Freeze and Cherry (1979).*

### 3.4.4 Permeability as a Tensor

If Darcy's law is separated into three principal components (corresponding to a coordinate frame), then a 3D form of Darcy's law can be written as:

$$q_x = -\frac{1}{\eta}\left(k_{xx}\frac{\partial P}{\partial x} + k_{xy}\frac{\partial P}{\partial y} + k_{xz}\frac{\partial P}{\partial z}\right)$$

$$q_y = -\frac{1}{\eta}\left(k_{yx}\frac{\partial P}{\partial x} + k_{yy}\frac{\partial P}{\partial y} + k_{yz}\frac{\partial P}{\partial z}\right)$$

$$q_z = -\frac{1}{\eta}\left(k_{zx}\frac{\partial P}{\partial x} + k_{zy}\frac{\partial P}{\partial y} + k_{zz}\frac{\partial P}{\partial z}\right)$$

or

$$\begin{pmatrix} q_x \\ q_y \\ q_z \end{pmatrix} = -\frac{1}{\eta}\begin{pmatrix} k_{xx} & k_{xy} & k_{xz} \\ k_{yx} & k_{yy} & k_{yz} \\ k_{zx} & k_{zy} & k_{zz} \end{pmatrix}\begin{pmatrix} \partial P/\partial x \\ \partial P/\partial y \\ \partial P/\partial z \end{pmatrix}$$

which can be simplified to

$$q = -\left(\bar{k}/\eta\right)\nabla P$$

This leads to nine directionally variable coefficients of permeability, but since $\bar{k}(x,y,z)$ is symmetric and has principal directions, the coordinate axes can be aligned with the permeability tensor so that the off-diagonal terms become zero. If measurements of permeability are then taken along the aligned coordinate axes, a calculation of permeability anisotropy, analogous to that used for elastic anisotropy, can be made (*perm differential / mean perm*). However, unlike measurements of AMS and elastic wave velocity (chapter 5 for methodology), which reveal the principal directions, a calculation of permeability anisotropy via the method mentioned above relies on an a priori knowledge of the principal directions ($k_{min}$, $k_{int}$, $k_{max}$). Commonly for sedimentary rocks, the principal axes of permeability are often assumed to be aligned with bedding (Gueguen and Palciauskas, 1994), thus allowing a first order approximation of the directions of measurement necessary to reveal $k_{min}$, $k_{int}$ and $k_{max}$. However, previous work (Benson et al., 2003) has revealed that the principal directions derived from pAMS and velocity anisotropy and closely coincide with the principal directions of permeability. Using pAMS directions as a guide, we are therefore able to measure permeability anisotropy along the principal directions without having to independently establish the complete permeability tensor.

# 4 Compaction in Porous Rock

## 4.1 Field Observations of Compaction Bands

Compaction bands were first identified in the field by Mollema and Antonellini (1996), exposed in outcrops of the Jurassic Navajo sandstone in Utah, an aeolian formation with a porosity of 20-25%. Two morphologically distinct styles of compaction band were reported, firstly a planar 0.5-1.5 cm wide structure that is essentially straight over lengths of 5-10m; and secondly a 0.1-0.5 cm wide structure which has an undulating trace with wavelengths of 1-5 cm and amplitudes on the mm to cm scale. The structures were inferred to have developed within the compressional quadrant of local fault tips, perpendicular to the maximum compressive stress, since they exhibit micro-structural evidence of compaction without any shear offset.

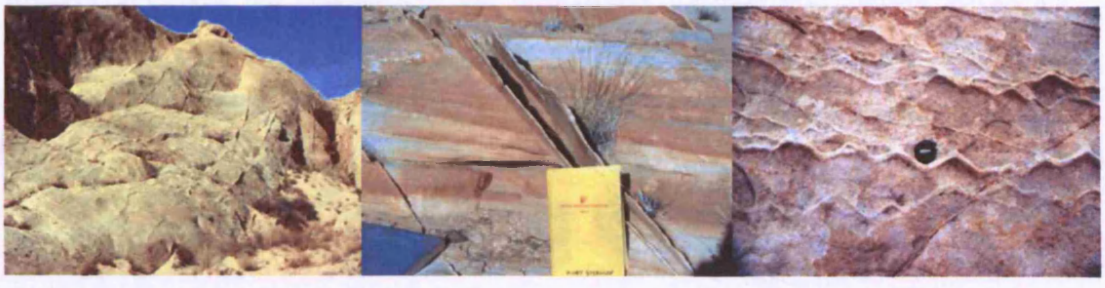

*Fig 4-1. Photos taken by Kurt Sternlof showing compaction bands in Aztec Sandstone, Valley of Fire, Nevada. From left to right, photos illustrate the m scale extent, positive relief and undulating trace which have been reported.*

Microstructural analysis revealed grain interpenetration, and that the porosity within the compaction bands had been reduced to less than a few percent. The fracturing and interpenetration of grains without any shear-offset led Mollema and Antonellini to interpret compaction bands as a structural analogue for mode I closing fractures.

Fieldwork by Sternlof et al. (2004; 2005) led to the identification of arrays of compaction bands, up to 62 m in extent, in the Valley of Fire State Park, Nevada. Unlike the earlier structures reported by Mollema and Antonellini (1996), these appear to be unrelated to local

faults. Field measurements indicate a grossly penny shaped geometry, with aspect ratios of around $5x10^{-4}$. Microscopy reveals uni-directional compaction, accommodating about 10% strain perpendicular to the compaction band trace. Based on their field evidence, Sternlof et al. (2005) concur with Mollema and Antonellini (1996) in conceptualising compaction bands as anticracks, and modelled them as contractile Eshelby inclusions embedded in an infinite medium (see Eshelby, 1957; 1959). This approach suggests that modelling compaction bands in 2D as anticracks accurately represents the 3D Eshelby state of stress generated around an idealised compaction band. As discussed in section 4.4, theoretical models expand on these initial Eshelby assumptions (Rudnicki and Sternlof, 2005; Rudnicki, 2006; Katsman et al., 2006 b).

Compaction bands form an end member of the system proposed by Du Bernard et al., (2002) whereby structures are classified by the predominant displacement gradient across the deformation band. Pure compaction bands do not show any element of macroscopic shear offset, although, of course, it is possible to have compacting shear bands which exhibit shear displacement to a greater or lesser extent.

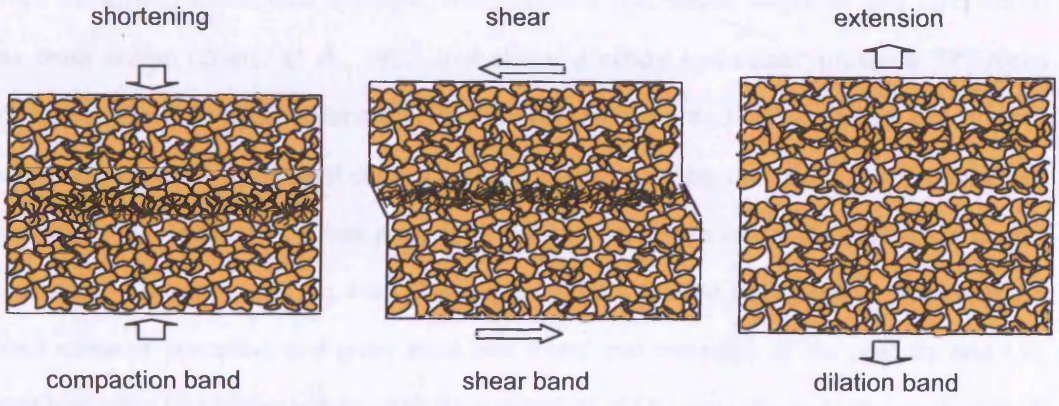


*Fig 4-2. Tripartite classification of deformation bands based on the dominant displacement gradient across the band. (After Du Bernard et al., 2002).*

## 4.2 Volumetric Response to Deformation

The volumetric response of rocks to an applied stress can be described in terms of dilatancy (volume increase) and compaction (volume decrease). Dilatancy has been shown many times to occur prior to macroscopic brittle failure (e.g. Brace et al., 1966) as a result of the formation and coalescence of microcracks under deviatoric stress. In crystalline rocks, where the initial porosity is low and does not play a significant role in the mechanical compaction of the material (Paterson and Wong, 2005), dilatancy is the most commonly observed volumetric response of rocks to triaxial deformation. In high porosity rocks, for example sandstone of porosity greater than 10 %, the volumetric response to triaxial deformation is more complex, as dilatant and compactive mechanisms may both operate. The following paragraphs introduce some concepts concerning the volumetric response of rocks to hydrostatic and triaxial deformation, before lab-developed compaction bands are specifically discussed in section 4.3.

### 4.2.2 Hydrostatic Compaction

Under increasing hydrostatic pressure, rocks show a poroelastic response and compact. It has been shown (Zhang et al., 1990) that above a critical hydrostatic pressure (P*) rocks undergo inelastic compaction and experience grain crushing and pore-collapse, which leads to an acceleration in the rate of compaction. Experimentally, the yield point at P* is observed when there is a marked inflection away from the linear elastic trend of the porosity-reduction vs effective-pressure curve (fig 4-3). Zhang et al. (1990) studied five sandstones, covering a broad range of porosities and grain sizes and found that materials of low porosity and / or small grain size had higher values of P* than materials of high porosity and large grain size. A Hertzian fracture model of grain crushing as a result of contact stresses was proposed by the same authors, and predicts P* values consistent with those determined experimentally (Wong et al., 1997). Their model underscores the primary control that grain size and porosity exert in determining P*, and follows a power law written as:

$$P^* \propto (\phi r)^n$$

where $\phi$ is porosity, $r$ is average grain radius and the exponent $n = -3/2$. The constant of proportionality depends on the material's fracture toughness, elastic modulus and extent of pre-existing damage.

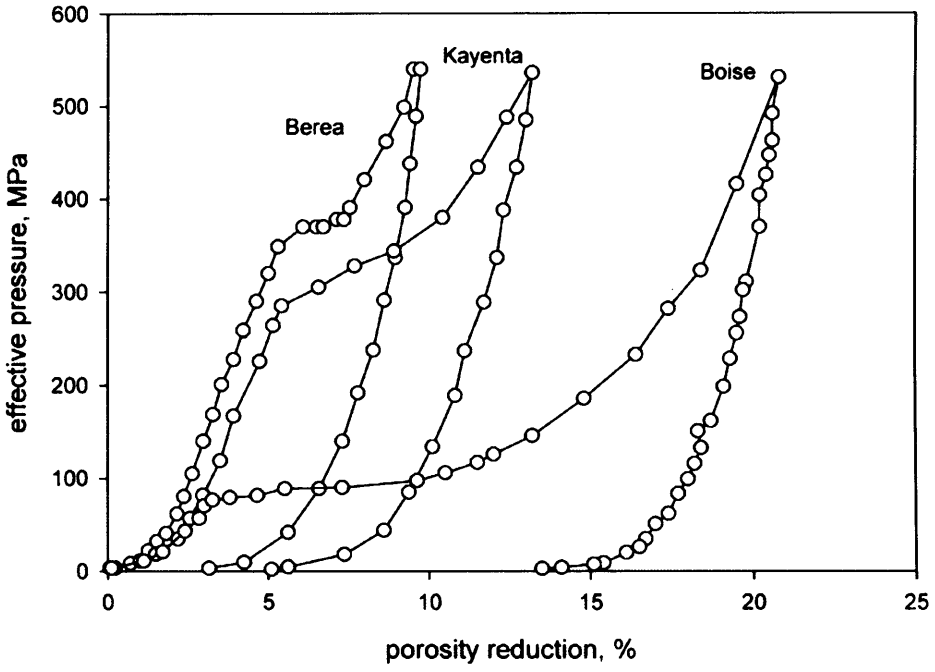


*Fig 4-3. The onset of grain-crushing for three sandstone during hydrostatic loading. The inflections at 75 MPa, 300 MPa and 380 MPa mark the critical stress state P* for Boise, Kayenta and Berea sandstones respectively. (Data from Zhang et al., 1990)*

### 4.2.3 Shear Induced Dilation and Shear Enhanced Compaction

The volumetric behaviour of rock under hydrostatic pressure is relatively straightforward, in as much as it always results in compaction and therefore a reduction in porosity. Under deviatoric stress, behaviour is more complicated, and may result in competing mechanisms of compaction and dilation (Baud et al., 2000). The initiation of microcracks under a deviatoric

stress results in an increase in the volume of a rock sample, and is termed shear-induced dilatancy, with the onset of such behaviour referred to as C'.

In porous rocks, the application of deviatoric stress at sufficiently high confinement often leads to compaction rather than dilation. Such behaviour is termed shear-enhanced compaction (Curran and Carroll, 1979) to distinguish it from the compaction associated with purely hydrostatic pressure. The onset of shear-enhanced compaction is termed C*, and acoustic emission and microstructural observations (Wong et al., 1992; Menendez et al., 1996) show that this regime is characterised by distributed intragranular microcracking and pore-collapse. Intragranular cracking and the subsequent relative movement of fractured grain components is termed cataclastic flow, and it is thought to be a dominant mechanism by which strain is accommodated during shear-enhanced compaction (Wong et al., 1997). For porous (>10%) sandstones, deformation under confining pressures greater than about 60 MPa is often sufficient to promote shear-enhanced compaction over shear-induced dilation. However, the observation of a global reduction in sample porosity does not preclude the possibility that dilatant mechanisms are also operating (Baud et al., 2000), and therefore shear-induced dilation and shear-enhanced compaction should not be viewed as mutually exclusive processes. This idea is discussed later.

Experimentally, C' and C* are determined by comparing the evolution of porosity during triaxial deformation to that measured during purely hydrostatic deformation. It is inferred that any deviation of the triaxial loading path from the hydrostat is the result of the deviatoric component of the effective mean stress. As such, the point at which the triaxial curve shows an enhanced rate of porosity reduction with respect to the hydrostat is inferred as C*. Similarly, C' is inferred if the triaxial curve deviates from the hydrostat in the direction of dilatancy (see figure 4-4). Since both processes involve brittle fracturing, the onset of accelerated AE activity provides a useful tool in constraining C' and C* (e.g. Wong et al., 1997).

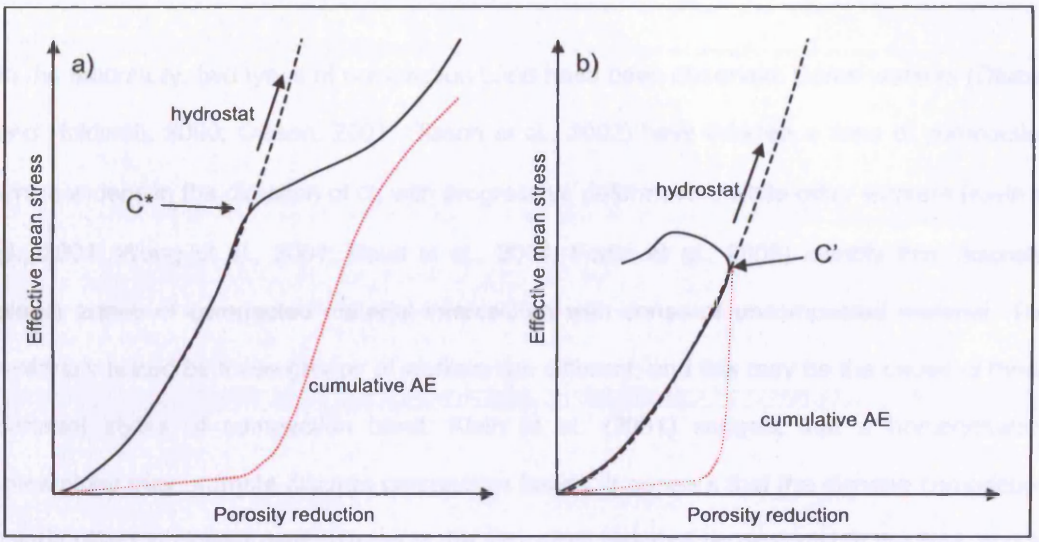


*Fig 4-4. Schematic diagram showing the onset of shear-enhanced compaction (a), and shear-induced dilation (b) in relation to porosity reduction and acoustic emission activity during triaxial loading. Hydrostatic compaction curves are shown as dashed lines (After Wong et al., 1997).*

## 4.3 Laboratory Studies of Localised Compaction

Initially, it was thought that compactant behaviour in high porosity rocks was characterised by homogeneously distributed cataclasis (Handin et al., 1963; Menendez et al., 1996), a process representing the intermediate step in the brittle-ductile transition between shear faults and cataclastic flow for quartzo-feldspathic aggregates (Tullis and Yund, 1992; Hirth and Tullis, 1994). The implication of this idea was that the process of compaction in a porous rock did not involve strain localisation, but rather an even distribution of damage. However, the identification of localised compactive structures in the field, and the subsequent development of such structures in the laboratory (Olsson, 1999; DiGiovanni et al, 2000; Baud et al., 2004), has shown this not to be true. The following paragraphs discuss compaction bands as laboratory-produced structures

### 4.3.1 Diffuse vs. Discrete Compaction Bands

In the laboratory, two types of compaction band have been observed. Some workers (Olsson and Holcomb, 2000; Olsson, 2001; Olsson et al., 2002) have inferred a zone of compaction which widens in the direction of $\sigma_1$ with progressive deformation, while other workers (Klein et al., 2001; Wong et al., 2001; Baud et al., 2004; Fortin et al., 2006) identify thin, discrete, planar zones of compacted material intercalated with zones of uncompacted material. The materials tested by these groups of workers are different, and this may be the cause of these different styles of compaction band. Klein et al. (2001) suggest that a homogeneous mineralogy may promote discrete compaction bands. It appears that the discrete compaction bands offer the closest resemblance to the structures reported by geologist in the field, and to date the majority of laboratory work on compaction bands has focused on this style.

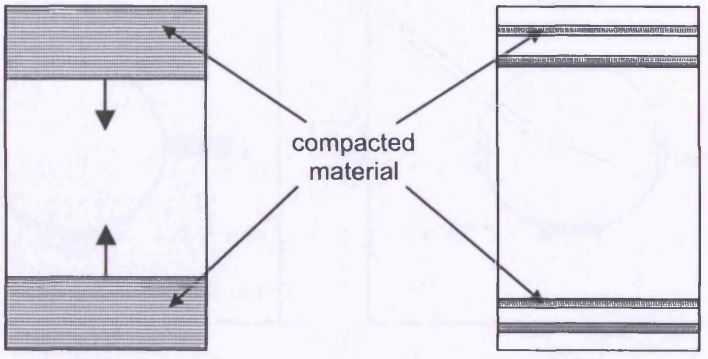


*Fig 4-5. Two types of evolving compaction reported by experimentalists. a) Compacted zone which widens with piston displacement, b) discrete bands, intercalated with undeformed material, which develop with piston displacement. (After Rudnicki, 2002).*

### 4.3.2 Reassessment of Previous Structures

Compaction bands were first identified in the laboratory during axisymmetric compression experiments on Castlegate sandstone (Olsson, 1999), a material of 28% initial porosity. This

led to a reassessment of structures produced during the study of sliding cracks (Lajtai, 1974) and borehole breakouts (Bessinger et al., 1997; Haimson and Song, 1997; 1998).

Lajtai (1974) had produced planar 'narrow crush zones' which showed a compaction of pore-space and which developed in the compressional quadrant at the tips of artificial shear cracks in loaded plaster models. Bessinger et al. (1997) applied uniaxial compression to simulated boreholes drilled through bricks composed of glass beads, finding that in specimens of relatively low Young's modulus and compressive strength, 'non-dilational' fractures developed normal to the compressive stress in orientations consistent with the Kirsch solutions (fig 4-6). In specimens with a higher Young's modulus and strength, more typical dog-ear shaped borehole breakouts were reported.

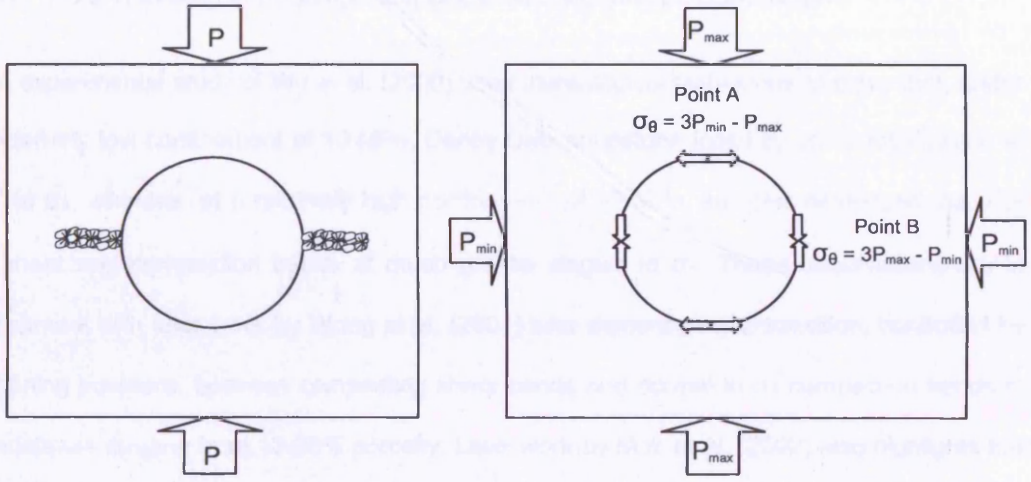


*Fig 4-6. Non-dilational borehole breakouts (left), as reported in the uniaxial experiments of Bessinger (1997), and the 2D Kirsch solutions (right) for the stresses around a circular void, with tensile stress concentration occurring at Point A, and compactive stress concentration occurring at Point B.*

The significance of porosity in controlling the development of compaction bands was demonstrated by Haimson and Song (1997; 1998) who reported on breakout features in Berea sandstone of two porosities. In Berea sandstone of 22% porosity, tabular compactive structures similar to those of Bessinger (1997) formed perpendicular to the maximum

compressive stress, also in locations predicted by the Kirsch solutions; the areas of maximum compressive stress concentration. However, for Berea sandstone of 17% porosity, normal dog-ear shaped borehole breakouts developed. It was noted that porosity is the only significant variable between these two materials, which otherwise have a very similar composition and microstructure. Haimson also reported that during testing, drilling fluid was responsible for flushing out the compacted and loose grains from the compactive bore-hole breakout structures. This observation has implications for sand-production in active oil reservoirs, where boreholes are drilled in formations of sufficient porosity, and may influence the efficiency of hydrocarbon recovery. Such dependence upon porosity for the development of compaction bands is consistent with the fieldwork of Mollema and Antonellini (1996), who reported the structures only in sandstones of porosity greater than 20%.

### 4.3.3 The Transition from Compacting Shear Bands to Compaction Bands

The experimental study of Wu et al. (2000) used stereological techniques to show that, under a relatively low confinement of 10 MPa, Darley Dale sandstone failed by shear localisation at 30° to $\sigma_1$, whereas, at a relatively high confinement of 95 MPa, samples developed mosaics of shear and compaction bands at much greater angles to $\sigma_1$. These observations are in agreement with later work by Wong et al. (2001) who demonstrate a transition, controlled by confining pressure, between compacting shear bands and normal-to-$\sigma_1$ compaction bands in sandstones ranging from 13-28% porosity. Later work by Mair et al. (2002) also highlights the pressure-sensitive nature of deformation band orientation, reporting that the angle between $\sigma_1$ and the resulting deformation band increases systematically with confining pressure. Deformation bands that are oriented normal to $\sigma_1$ and do not show any shear displacement are considered to be 'pure' compaction bands, although there clearly exists a transition over which deformation bands will exhibit compaction and shear to different extents.

Combining brittle peak stress points with the stress values at C*, as demonstrated by Wong et al. (1997), maps out a failure envelope that spans the transition between macroscopic brittle failure and failure by cataclastic flow. Such envelopes have an approximately elliptical form and have been demonstrated in carbonates (Baud et al., 2000) as well as siliciclastic rocks.

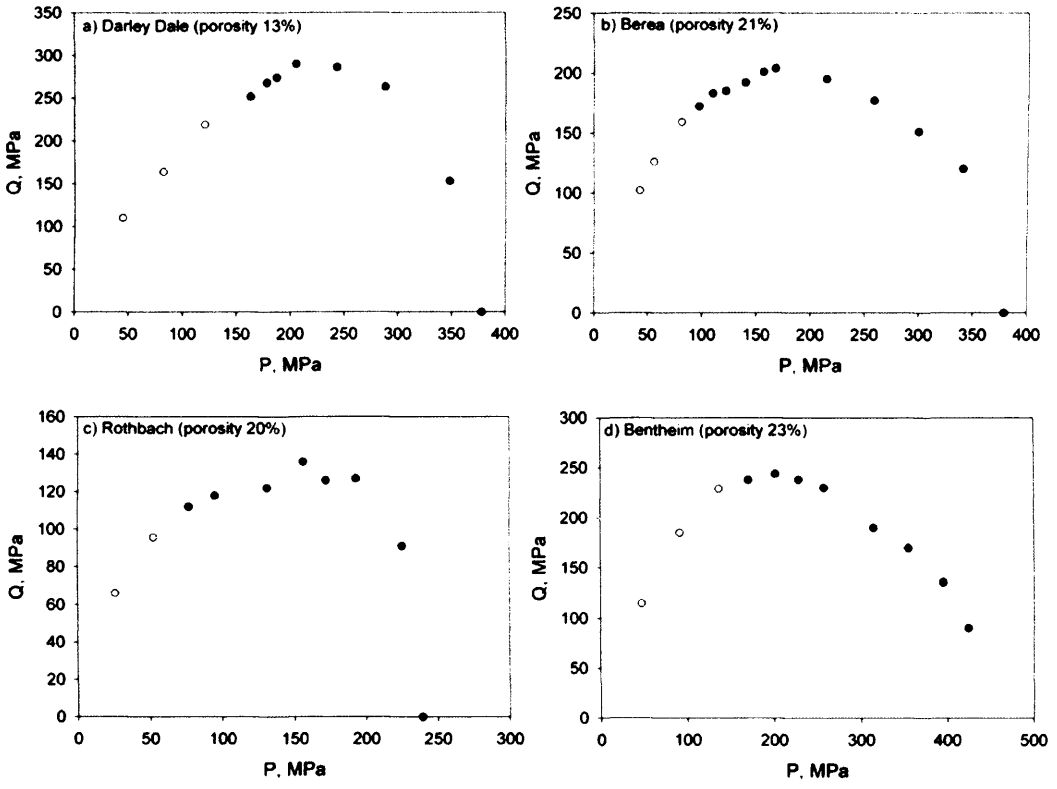


*Fig 4-7. Yield envelopes for four sandstones, covering the transition from shear-induced dilatancy (open symbols) to shear-enhanced compaction (closed symbols). Plotted in P-Q space, where P is the effective mean stress, and Q is the differential stress (Data from Baud et al., 2004). Note that the open symbols show PQ conditions at C' rather than peak stress, although both show a positive correlation with effective mean stress (Wong et al., 1997).*

The right-hand limb of the yield envelopes of the type shown in figure 4-7 show a negative pressure dependency and are anchored by the point that corresponds to P*, the conditions sufficient to induce graining crushing under hydrostatic pressure. Wong et al. (1997) infer that P* acts as a scaling parameter for C*, and suggest that since the Zhang et al. (1990 ) model

for predicting P* is largely dependent on porosity and grain-size, similar microstructural parameters are also likely to influence the extent of the compactive yield envelope.

Figure 4-8 shows a schematic representation in PQ space of the styles of deformation band observed during the transition from shear-induced dilation through to shear-enhanced compaction. The value of P, before the application of Q, represents the hydrostatic confining pressure on top of which a differential stress is superimposed. Since a constant strain rate is applied for and during each experiment, the loading paths leading to inelastic yield can be imagined as straight parallel lines with origins at the initial hydrostatic value of P.

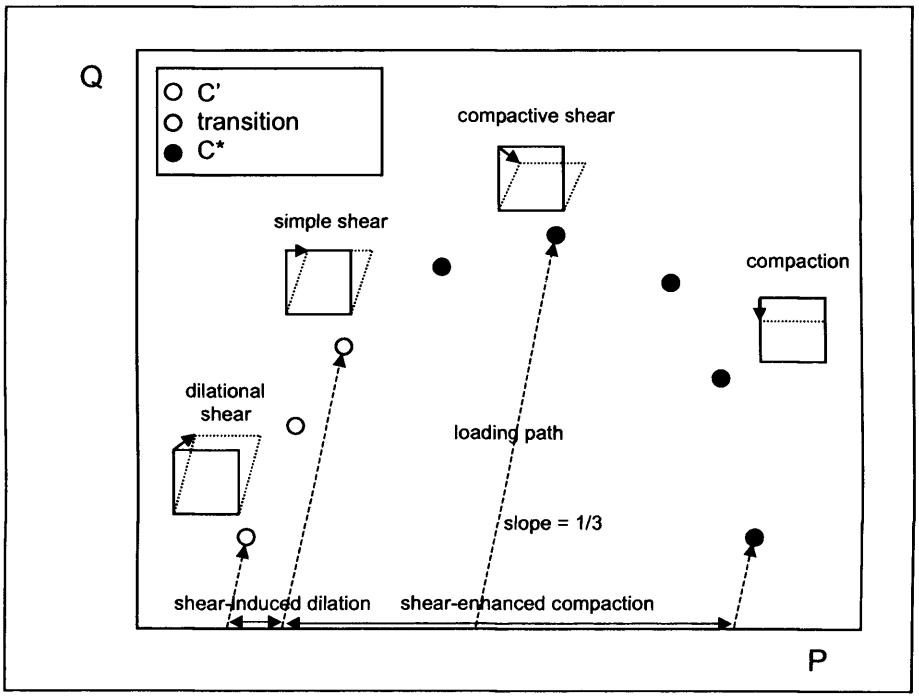


*Fig 4-8. Schematic representation of deformation styles associated with different parts of the elliptical yield envelope.*

Figure 4-8 only reflects the dominant deformation style at the respective yield points. This is important since Baud et al. (2000) demonstrate that at high amounts of strain, shear-enhanced compaction may evolve into shear-induced dilatancy and ultimately shear localisation (figure 4-9). This phenomenon was observed in Solnhofen limestone, a material of

just 3% porosity, and suggests that pore collapse can occur in relatively compact low-porosity materials, and that shear-enhanced compaction may be a transient precursor to dilatant behaviour. This may be significant in considering natural systems where strain can accumulate to very high levels over the course of geological time.

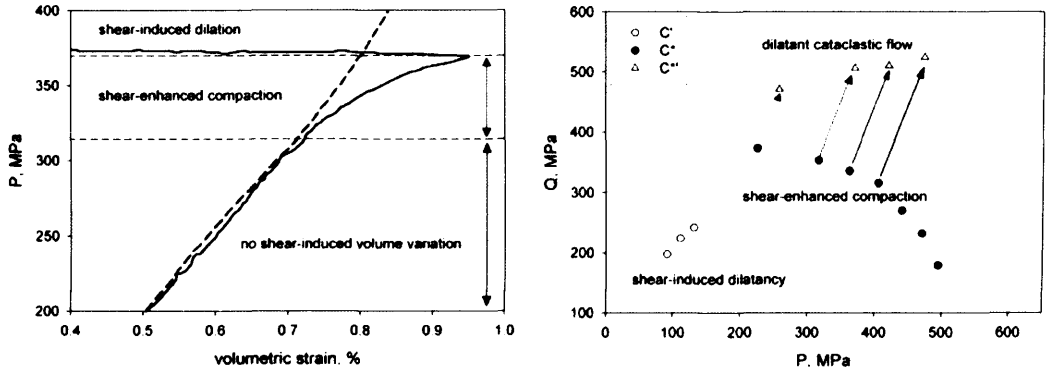


*Fig 4-9. (Left) Transitional behaviour of Solnhofen limestone deformed at 200 MPa effective pressure, with the hydrostat shown for reference as the heavy dashed line. (Right) The evolution of dilatant cataclastic flow from shear-enhanced compaction in P-Q space. C*' marks the transition from shear-enhanced compaction to dilatancy (Data from Baud et al., 2000).*

### 4.3.4 Spatial and Temporal Observations on Compaction Bands

Microstructural characterisation by Wong et al. (2001) of the damage associated with compaction bands shows localised failure involving the partitioning of damage between axial microcracking and pore-collapse with grain crushing. The stress-strain curve during compaction band development has been seen to show an overall strain hardening trend that is punctuated by episodic stress drops and concomitant surges in AE activity (e.g. Klein et al., 2001; Wong et al., 2001; Baud et al., 2004). There is a positive correlation between the number of compaction bands and the cumulative number of stress drops, leading to the inference that the stress drops are caused by the development of compaction bands and the sudden shortening of the sample that results. These observations are in general agreement with the earlier work of Mair et al. (2000), which reports that deformation bands develop

strands of gouge, intercalated with lenses of apparently undeformed material, whose number increase with applied axial strain. If the stress drops and AE surges are the result of individual compaction bands being introduced to the sample, then compaction bands can be inferred to develop during the strain hardening portion of the stress-strain curve (figure 4-10).

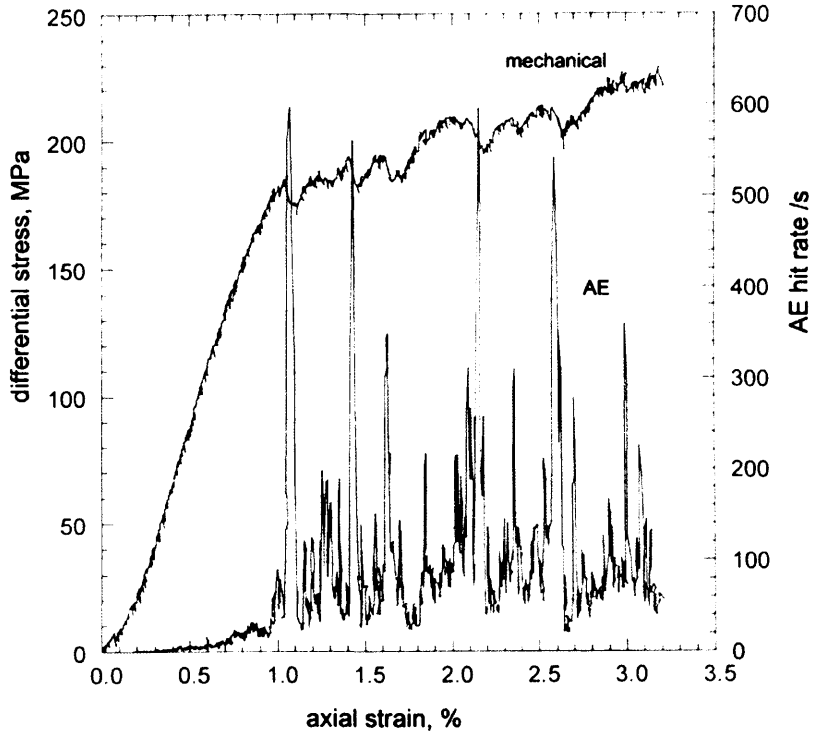


*Fig 4-10. Episodic stress drops and AE surges reported in the literature, and thought to be associated with the development of discrete compaction bands. Data shown is from Betheim sandstone deformed at 300 MPa effective pressure. (From Baud et al., 2004).*

The accumulation of damage during the development of discrete compaction bands, was investigated using microstructural methods by Baud et al., (2004). For the case of highly porous sandstones (~20%), they found that with increasing amounts of axial strain, compaction bands first developed at the ends of the sample and before spreading towards the centre. Compaction bands were found to be pervasive through the sample by about 6% axial strain (see Figure 4-11). In the case of diffuse compaction bands, AE locations measured during triaxial testing of Castlegate sandstone (Olsson and Holcomb 2000; Olsson, 2001)

reveal that compaction localisation originates towards the ends of specimens during the peak and post-peak region of the stress-strain curve and grows as a 'compaction front' through the deforming sample until the entire specimen has been compacted (see figure 4-5). The propagation speed of the diffuse compaction band front was estimated as being roughly an order of magnitude greater than the axial displacement rate.

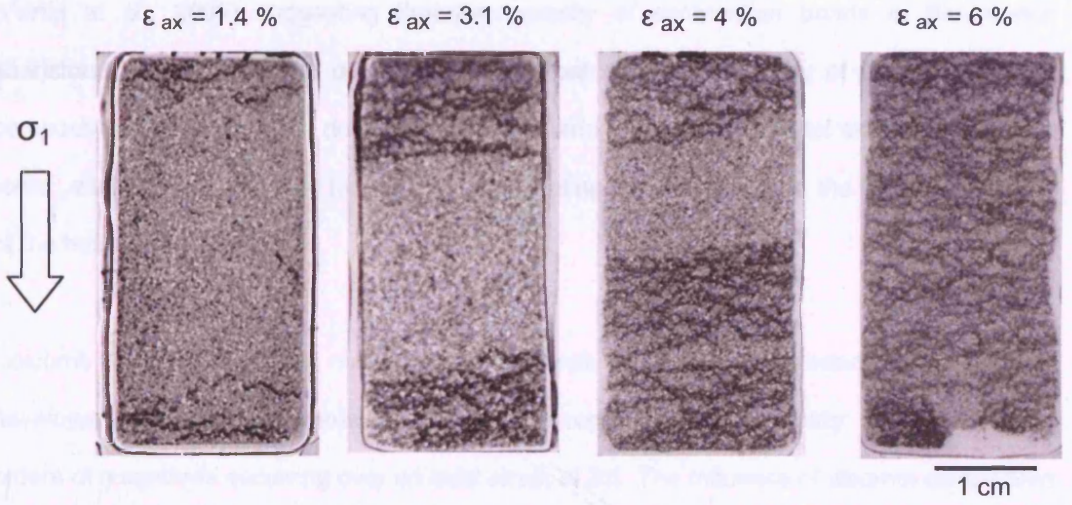


*Fig 4-11. Transmission optical micrographs of Bentheim sandstone samples deformed at 300MPa effective pressure to the levels of axial strain ($\varepsilon_{ax}$) shown. Dark bands are associated with significant comminution, and are interpreted as compaction bands. (From Baud et al., 2004).*

A study on the development of discrete compaction bands was reported by Vajdova and Wong (2003), who used notched samples of Bentheim sandstone to induce local stress and structural heterogeneities to investigate the propagation of compaction bands. They reported that compaction bands initiated at the notches and propagated incrementally as anti-cracks. Inferences from the AE surges observed during testing, and believed to be associated with compaction band growth, led to the conclusion that compaction band propagation velocity was about two orders of magnitude higher than the axial displacement rate, although it was not measured directly. More recently, AE location locations (Fortin et al., 2006) were used to map out the accumulation damage associated with discrete compaction bands. Although the

discrete nature of these structures is clearly shown, this work was not able to discern any dynamic propagation of damage associated with this style of compaction band.

### 4.3.4 Transport Properties of Compaction Bands

Deformation bands associated with compactive volumetric strain and involving cataclastic processes are likely to impact the fluid-flow properties of the host material, with recent work (Fortin et al., 2005) suggesting that the porosity of compaction bands in Bleurswiller sandstone is less than 5%, compared to the host material's porosity of 24%. Given that compaction bands are often documented as occurring in porous material similar to reservoir rocks, attention has naturally focused on investigating their influence on the bulk permeability of the host material.

Holcomb and Olsson (2003) measured the permeability of Castlegate sandstone during the development of diffuse compaction bands, and recorded a permeability reduction of two orders of magnitude occurring over an axial strain of 2%. The influence of discrete compaction bands was investigated by Vajdova et al. (2004) who used Bentheim sandstone (porosity of 23%) as their test material. They identified three regimes of permeability evolution associated with compaction localisation; an initially moderate reduction followed, by a rapid permeability drop of about an order of magnitude at the point of C*, followed by a more gradual decay (see figure 4-12).

By modelling compaction bands as low permeability layers embedded in a non-damaged host rock, the effective permeability, $k_{eff}$, of a sample containing compaction bands was described as:

$$k_{eff} = \frac{k_m}{\left(n\frac{l}{L}\right)\left(\frac{k_m}{k_{cb}} - 1\right) + 1}$$

where $k_m$ is the permeability of the undeformed host, $k_{cb}$ is the permeability within a compaction band, $n$ is the number of compaction bands and $l/L$ is the ratio of the width of a compaction band ($l$) to the sample length ($L$). They demonstrate that the use of a layered media model is fits their data well if the permeability within a compaction band is assumed to be reduced with respect to the host rock by a factor of 40-400.

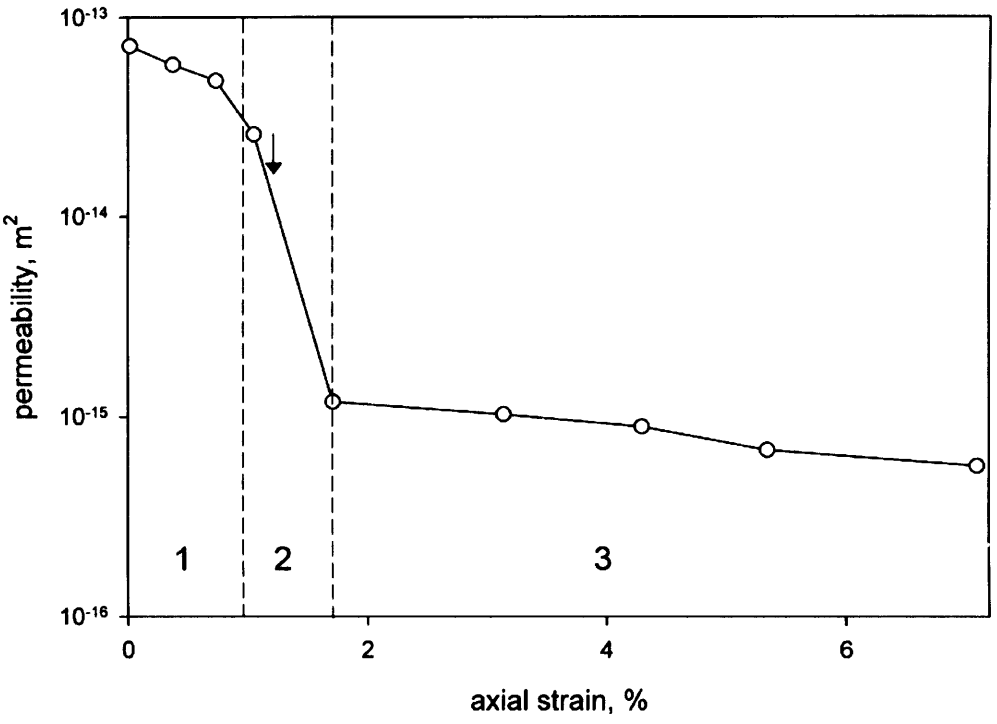


*Fig 4-12. Permeability as a function of axial strain in Bentheim sandstone deformed at an effective pressure of 300 MPa. Three regimes of permeability evolution are shown, with the solid arrow indicating C*. (Data from Vajdova et al., 2004).*

The permeability contrast between host rock and compaction band was also investigated by Fortin et al. (2005), who used a statistical physics approach based on the method of Gueguen and Dienes (1989). They showed that, in a material of sufficient porosity, pre-compaction band permeability was controlled by pore-volume, with the closure of microcracks having a

negligible effect. This allows the permeability of the undeformed rock matrix, $k_m$, to be modelled as a network of intersecting tubes or capillaries, written as:

$$k_m = \frac{1}{32} f \bar{r}^2 \phi$$

where $\phi$ is porosity, $\bar{r}$ is the mean capillary radius and $f$ is the connectivity factor (assumed to be 1 for high porosity rocks). Substituting the relevant data suggests an average pore radius of about 1 μm. Given that the microstructure within a compaction band is composed of fractured grain fragments, a fracture permeability model was used to represent compaction band permeability, $k_{cb}$, as:

$$k_{cb} = \frac{2}{15} f \overline{w}^2 \overline{\zeta} \rho$$

where $\rho$ is the crack density, $\overline{\zeta}$ is the average crack aspect ratio and $\overline{w}$ is the average crack aperture. By assuming that compaction bands are fully connected and fully fractured such that $f$ = 1 and $\rho$ = 1, and that $\overline{w} \approx \bar{r} \approx 1$ μm, the ratio $k_m / k_{cb}$ is shown to scale as:

$$\frac{k_m}{k_{cb}} \approx \frac{\phi}{\overline{\zeta}}$$

Given that the aspect ratio of cracks is commonly in the range $10^{-2} < \zeta < 10^{-4}$, Fortin et al. (2005) showed that the permeability within a compaction band is reduced by a factor of 6 – 600 with respect to the host material. This theoretical range is in general agreement with that used by Vajdova et al. (2004), and therefore suggests that the layered media model is suitable for describing the permeability influence of discrete compaction bands.

## 4.4 Modelling Compaction Bands

### 4.4.1 Bifurcation Analysis

In an attempt to understand the stress conditions and constitutive relationships that lead to the development of compaction bands, Olsson (1999) recognised that the approach Rudnicki and Rice (1975) used to study the inception of shear bands could also be applied to compaction bands. This approach seeks to define conditions for which the constitutive description of homogeneous deformation allows non-uniform deformation in a planar band as an alternative to further homogeneous deformation, that is to say that the inception of compaction bands can be addressed as a bifurcation from homogeneous deformation (Rudnicki, 2002).

According to the theory of Rice and Rudnicki (1975), strain localisation is an instability in the constitutive relation for inelastic homogeneous deformation. Hence, the localisation conditions and predictions of band orientation given by this analysis are influenced by the choice of constitutive model. Issen and Rudnicki (2000) used a single surface model to produce a failure map and derive the general conditions for the inception of compaction bands as:

$$\beta + \mu < -\sqrt{3}$$

Where $\beta$ is the dilatancy factor, which may be positive or negative, representing dilatancy or compaction respectively, and is given by:

$$\beta = -\sqrt{3}\left(d\varepsilon_V^P / d\varepsilon_L^P\right)/\left(3 - d\varepsilon_V^P / d\varepsilon_L^P\right)$$

Where $d\varepsilon_V^P / d\varepsilon_L^P$ denotes the ratio between increments of plastic volumetric and axial strains. $\mu$ is an internal friction coefficient which characterises the pressure dependence of the yield stress, and for axisymmetric compression is described as (Wong et al., 1997):

$$\mu = (dQ / dP)/\sqrt{3}$$

where $Q$ denotes differential stress and $P$ denotes effective mean stress.

However, laboratory constraints (Wong et al. 2001) of $-\sqrt{3/2} < \beta < 0$ mean that for the condition $\beta + \mu < -\sqrt{3/2}$ to be satisfied, the parameter $\mu$ must be $< -\sqrt{3/2}$. Which is not in agreement with the measured values of Wong et al. 2001, which show that for samples that develop compaction bands $\mu > -\sqrt{3/2}$ (figure 4-14).

Wong et al. (2001) explain this discrepancy by suggesting that because localised failure generally occurs in the transitional regime between shear and compaction, damage is partitioned between at least two mechanisms and a constitutive model which uses just one yield-surface is fundamentally inadequate. As a result of these shortcomings, Issen (2002) proposed a two yield-surface model where the second surface is characterised by a pressure-sensitivity factor $\mu_2$, and the plastic component of deformation is characterised by a dilatancy factor, $\beta_2$, and a bulk hardening modulus, $k$. The two yield-surface model is depicted in $\tau - \sigma$ space, where $\sigma$ is the mean stress and $\tau$ is the second invariant of deviatoric stress, (figure 4-13).

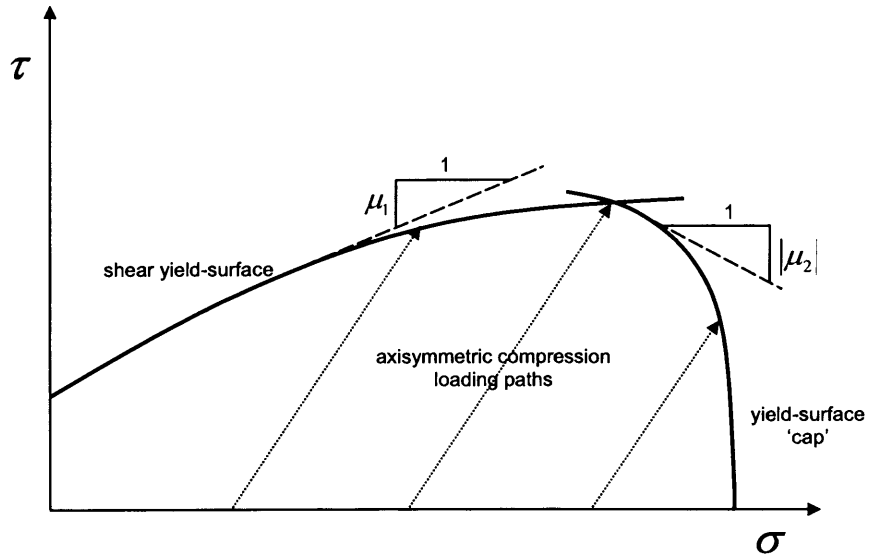


*Fig 4-13: The two-surface yield model, comprising a shear yield-surface and a yield-surface cap, proposed by Issen (2002).*

In this model, the shear yield-surface corresponds to a dilatant frictional damage mechanism, and the second yield-surface is a cap corresponding to a compactive damage mechanism. Wong et al. (2001) showed that experimental results fall within the wide range of $\mu_2$ and $\beta_2$ predictions made by the two yield-surface model for localisation on the plateau portion of a stress-strain curve (fig 4-15).

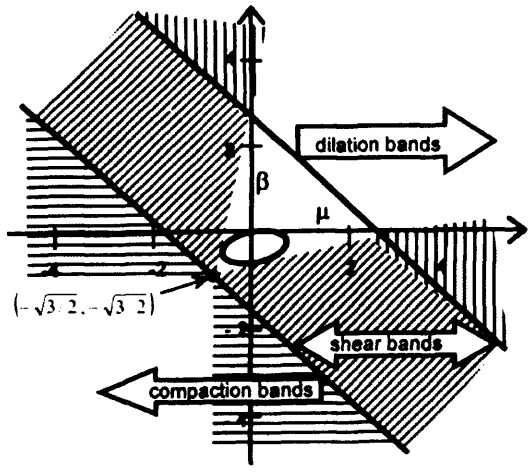


*Fig 4-14. Failure mode map derived from bifurcation analysis of a constitutive model with one yield-surface. Failure modes are separated by diagonal lines* $\beta + \mu = -\sqrt{3}$ *and* $\beta + \mu = \sqrt{3}(2-\nu)/(1+\nu)$, *where* $\nu$ *is Poisson's ratio. For each mode, shaded areas represent localisation during strain hardening and clear areas represent localisation during strain softening. The oval shows the data range from samples that failed by compaction bands and high-angle shear bands. From Wong et al., (2001).*

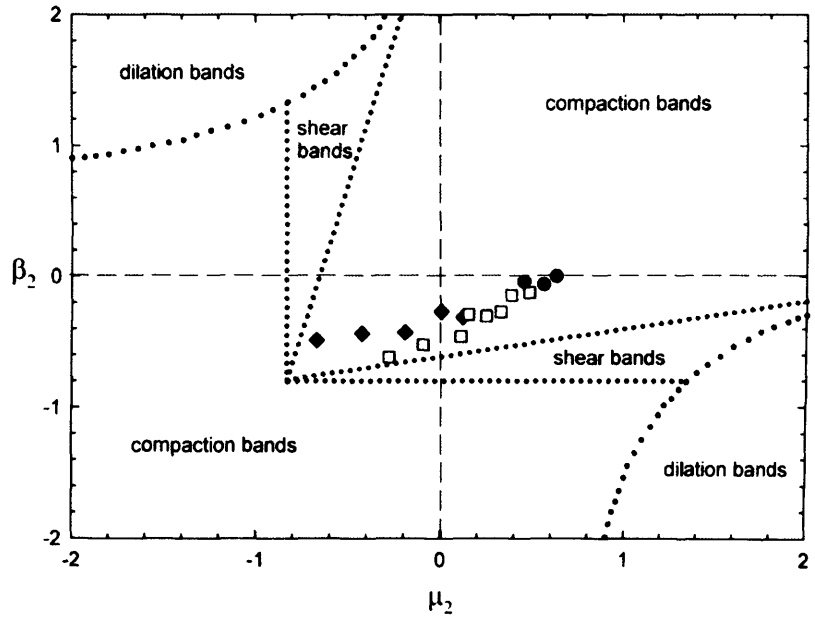


*Fig 4-15. Failure mode map derived from bifurcation analysis of a constitutive model with two yield surfaces (from Issen 2000). Analysis is for* $(\mu_1 - \mu_2)(\beta_1 - \beta_2) > 0$ *and* $k = 0$. *Constitutive parameters for Bentheim (diamonds), Berea (squares) and Darley Dale (circles) sandstones, which all developed compaction bands or high-angle shear bands. From Wong et al., (2001).*

### 4.4.2 Network Modelling

Katsman et al. (2005) developed a 2D spring-network numerical model to investigate the role of inhomogeneities, disorder and boundary conditions in the development of compaction bands. Disorder and heterogeneities were incorporated into this model by use of a Gaussian probability distribution of compressive stress thresholds among the springs, where compaction via grain crushing and pore collapse were represented by a change in the elastic properties and equilibrium length of each element upon which stress exceeded its assigned compressive threshold.

It was found that in the absence of disorder, compaction bands develop in a discrete manner. With increasing disorder, compaction becomes more homogeneous, and with a large degree of disorder, diffuse compaction bands were observed to develop. These results offer some parallels to what has previously been observed in the laboratory, namely the development of a homogenous compaction front (cf. Olsson, 2001) and the opposite situation of discrete compaction bands (cf. Klein et al., 2001) intercalated with undamaged material.

For the modelled scenario, the development of either discrete compaction bands or diffuse compaction bands was shown to be the result of competition between stress concentrations produced by elastic mismatch ( $K_{bc}$ ) and disorder ( $D$ ), where:

$$K_{bc} = \frac{E^{bc}}{E} \quad \text{and} \quad D = \left| \frac{\Delta F_0^{cr}}{\overline{F}_0^{cr}} \right|$$

where $E^{bc}$ is the Young's modulus of the boundary springs, $E$ is the Young's modulus of the internal springs of the lattice, $\Delta F_0^{cr}$ is the half-width of the stress threshold distribution and $\overline{F}_0^{cr}$ is the centred value of the distribution (see Katsman et al. 2005 for full model algorithm

and description). In the absence of disorder, compaction nucleation is seen to be dominated by the large values of $K_{bc}$ which promotes the development of discrete compaction bands. Larger values of $D$ promote the diffuse mode of compaction bands, with distributed cataclastic flow observed at the greatest values of $D$.

Compaction bands are often described as analogues to closing mode 1 anticracks, however, further application of the spring network model by Katsman et al. (2006 a) suggests that the stress concentrations at the tips of compaction bands is independent of the compaction band length, and that, in contrast to mode 1 cracks, compaction bands formed by normal stress-induced processes will maintain a constant and not an accelerating planar growth rate. These ideas are developed further by Katsman et al. (2006 b) to provide an analytical solution for the stress around a 2D compaction band using the 'transformation problem' of Eshelby (see Eshelby, 1957). They show that the results from the spring network model are in good agreement with the solution to Eshelby's transformation problem, and that the stress fields around compaction bands and edge-dislocations are similar; allowing compaction bands to be accurately described as anti-dislocations.

Discrete element modelling by Wang et al. (2006), in which rock was modelled as a bonded assembly of circular disks of seven different radius distributions, was used to investigate the affects of grain-scale heterogeneities. Results are in basic agreement with Katsman et al. (2005), in that discrete compaction bands are observed in a homogeneous assembly. Both of these numerical results support the early suggestion of Klein (2001) which attributed the preferential development of discrete compaction bands over diffuse compaction bands in Bentheim sandstone to the material's relatively homogeneous mineralogy (95% quartz).

### 4.4.3 Micromechanical Modelling

Based on existing field measurements, Rudnicki (2006) modelled compaction bands as thin ellipsoidal heterogeneities embedded within a matrix of different elastic modulus, assumed to be infinite in extent. His work attempts to understand the stress states inside the compaction band, and at the compaction band tip, in order to shed some light on the process of compaction band propagation. The underlying model is that compaction band propagation can be expected to occur when the energy released per unit advance of the compaction band ($G_{band}$) is equal to some critical value ($G_{crit}$) that reflects the resistance of the material to compaction (Rudnicki and Sternlof, 2005).

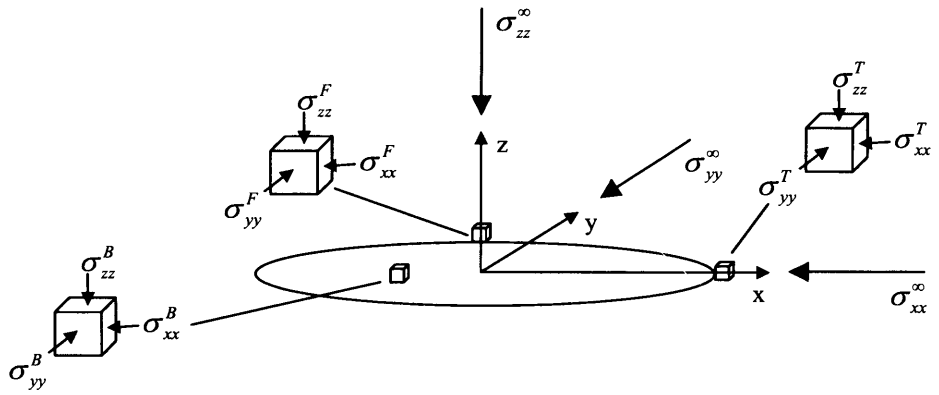


*Fig 4-16. Model of a compaction band as an axisymmetric ellipsoidal inclusion, showing far-field stresses $\sigma^{\infty}_{ij}$, stresses in the band $\sigma^{B}_{ij}$, stresses at the band tip and stresses at the band flank $\sigma^{F}_{ij}$. (From Rudnicki, 2006).*

Rudnicki calculates the ratio of compressive stress at the band tip to compressive stress in the far-field as being of the order of 10 –100. This ratio is observed not to vary significantly with elastic mismatch between the compaction band and the matrix, and thus Rudnicki concludes that elastic mismatch is unlikely to be a factor in the extension of a compaction band. The energy release model for compaction band propagation proposed by Rudnicki and Sternlof (2005) is given as the product of the far-field stress and the inelastic compactive

strain: $G_{band} = \sigma \varepsilon^P h$, where $G_{band}$ is the energy release per unit growth of compaction band, $\sigma$ is the compactive far-field stress, $\varepsilon^P$ is the inelastic compactive strain within the band and $h$ is the thickness of the band. $G_{band}$ must meet a critical quantity for compaction band propagation, i.e. for propagation: $G_{band} \geq G_{crit}$.

Material parameters based on the compaction bands within the Aztec sandstone give an estimate of $G_{band}$ as 10 – 60 kJ/m$^{-2}$, and suggest that $G_{crit}$ must have been at least equal to $G_{band}$ at the end of propagation, or else the compaction band would not have stopped growing (Rudnicki and Sternlof, 2005). The estimated range of $G_{crit}$ is in agreement with the compaction energies of 16 kJ/m$^{-2}$ - 40 kJ/m$^{-2}$ inferred from axisymmetric compression tests (Vajdova and Wong, 2003; Tembe et al. 2006).

# 5 Methods and Equipment for Material Characterisation

This chapter discusses the methodologies of the ambient and elevated hydrostatic pressure measurements made on Diemelstadt sandstone. Ambient pressure methodologies are described for measurements of pAMS (anisotropy of magnetic susceptibility of pore-space) and anisotropy of elastic-wave velocity. Elevated pressure methodologies are described for measurements of elastic-wave velocity, permeability, and porosity reduction. These techniques are employed to try to quantify the nature and extent of the material's anisotropy in order to help inform the triaxial suite of experiments, both in terms of experimental design and to add explanatory scope to the results.

The measurements and techniques used to characterise Diemelstadt sandstone all involve the use of sophisticated apparatus, particularly so for the measurements made at elevated pressure. Certain modifications were made to the apparatus in order to improve the facility of conducting the experiments and/or to improve the quality of the data, and in some instances new designs were implemented, and so these aspects of the methodology are also discussed in this chapter. Associated with any type of measurement is error, which may result from any combination of the sensitivity of the instrument being used (for example, the accuracy of a displacement transducer) or from certain subjective aspects of experimental work (for example, picking the arrival time of a P-wave). The sources of error in this work, and the steps taken to ensure data is as reliable as possible are discussed. The specific calibrations performed on the various pressure and displacement transducers integral to the hydrostatic cell are presented, along those performed on the triaxial system, in chapter 7.

## 5.1 Sample Material

The blocks of sandstone used in this study were quarried in a town called Diemelstadt, in the German state of Hesse. Diemelstadt sandstone was chosen for this investigation because it has been shown (e.g. Fortin et al., 2003) to be a material capable of developing compaction

bands, and because it exhibits anisotropy. Its anisotropy can be confirmed by eye, evidenced by meso-scale bedding sub-parallel to the xy plane (see figure 5-1).

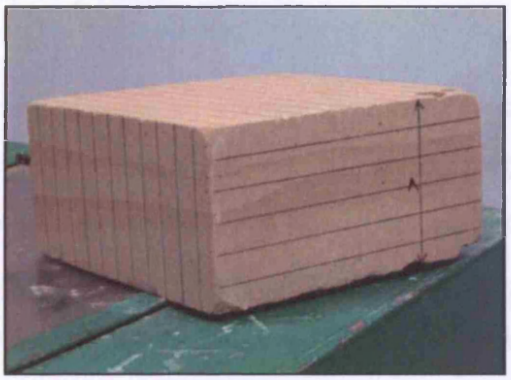

*Fig 5-1. Block of Diemelstadt sandstone, with reference coordinates shown. Meso-scale bedding can be seen running in a sub-horizontal plane.*

Four blocks of Diemelstadt sandstone, cut adjacent to one another from the quarry, were used in this study, and the anisotropy of the pore-fabric was characterised by using AMS techniques and measurements of elastic wave velocities (as described later in this chapter).

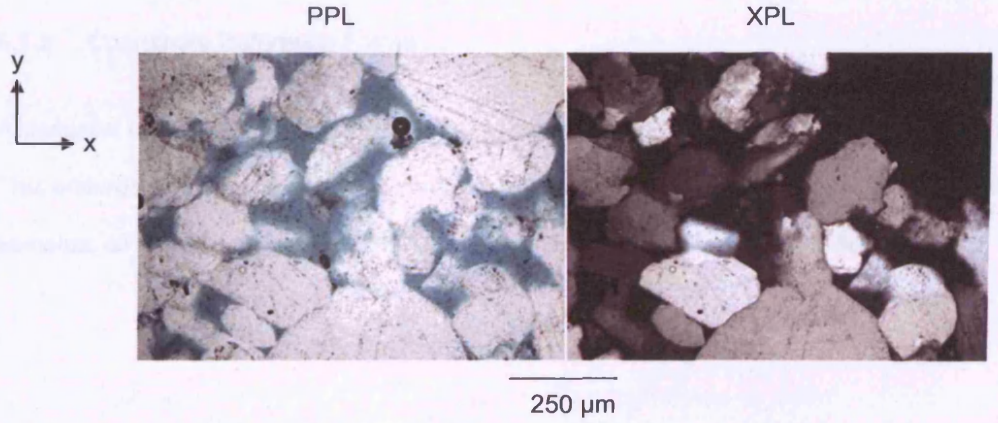


*Fig 5-2. Transmitted-light micrographs of Diemelstadt sandstone in the xy plane under plane-polarised light (PPL) and cross-polarised light (XPL).*

Diemelstadt sandstone is a quartz-dominant sandstone of 23% porosity. Its average grain radius is 150 µm and there are occasional lithic clasts of poly-crystalline quartz, with a long

axis of up to 500 μm. The grain contacts are generally of the point variety, although there are also some sutured contacts. Grains show evidence of quartz cement overgrowths, with ghost edges of the original crystal faces being visible.

Hematite staining around the edges of grains is responsible for picking out the bedding seen in hand-specimen, it is inferred that this staining is post early diagenesis (i.e. after cement formation) because there is no staining around grains where contacts occur. Chlorite is a common alteration product of Fe/Mg rich minerals such as pyroxenes, amphiboles and biotites, although it is not clear whether its modest occurrence in Diemelstadt sandstone is primary or secondary. The textural maturity of Diemelstadt sandstone suggests a fluvial origin.

| Mineralogy | Observations | Comments |
|---|---|---|
| Quartz, ~70%<br>Lithics, ~10%<br>Feldspars, ~10%<br>Chlorite, <5%<br>Muscovite mica, <5%<br>Opaques, <5% | Uniform and undulose extinction<br><br>Plagioclase and microcline<br>Exhibits 'book cleavage'<br>Prismatic habit | Sub-rounded grains, moderately sorted, average radius of 150 μm. Mostly point contacts, occasionally sutured. |

*Table 5-1. A summary of the petrology of Diemelstadt sandstone*

### 5.1.2 Coordinate Reference Frame

A common coordinate frame of reference was adopted during the preparation of all samples. This ensures that directional measurements made using different techniques, and on different samples, all have a common datum. This convention is illustrated below in figure 5-3.

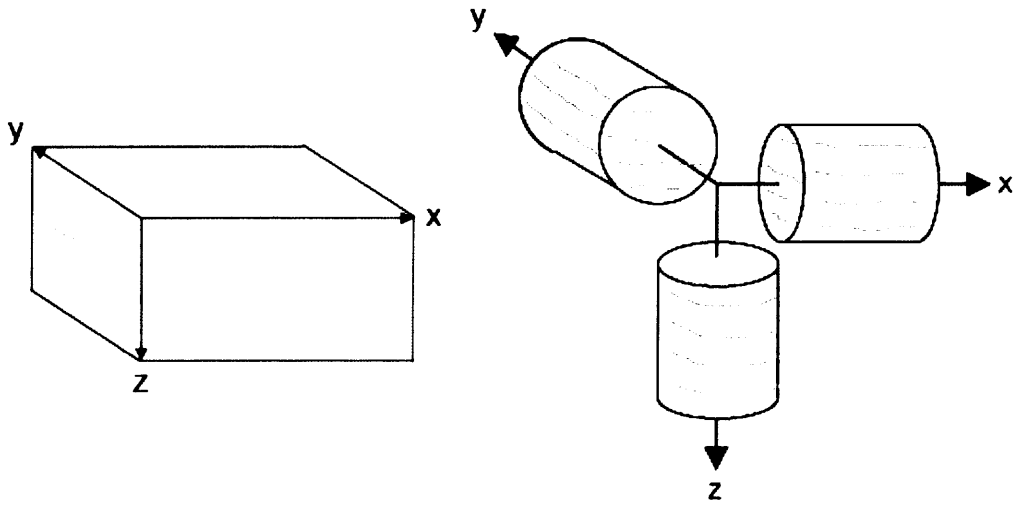


*Fig 5-3. (Left) Diemelstadt block assigned orthogonal axes X, Y and Z. (Right) Coring directions drilled to coincide with coordinate frame axes. Cross-bedding indicated by stripes.*

## 5.2 Measurements of Anisotropy of Magnetic Susceptibility (AMS)

### 5.2.1 Sample Preparation

Cylindrical samples were prepared to have a length/diameter ratio of 0.88. This is the standard geometry used in palaeomagnetic studies since it minimises the shape dependent demagnetising effect observed in samples with a high intensity of magnetisation (Pfleiderer and Halls, 1990; Tarling and Hrouda, 1993). To prepare such samples, cylindrical cores were prepared to 25 mm diameter and 22 mm length, with each core oriented relative to the co-ordinate reference frame shown in figure 5-3. Following measurements of mAMS, tAMS was evaluated using the same sample cores which were this time saturated with a EMG-905 ferrofluid, diluted by a factor of 20 with the carrier-fluid Multipar H, which was necessary to keep the bulk susceptibility of the saturated rock samples within the range measurable by the susceptibility bridge. Samples were saturated by immersion under a vacuum for 12 hours, after which the samples were wrapped in cling-film and the ends capped using discs of thin plastic. Finally, samples were encased in lengths of heat-shrink tubing which contracted

around the samples, sealing them from ferrofluid leaks. The intrinsic susceptibility of the of 5% ferrofluid is 0.1 SI, and describes the susceptibility of a material in the absence of any demagnetising effects.

### 5.2.2 Apparatus and Measurement

The susceptibility-bridge, manufactured by AGICO Instruments, has a pick-up unit containing magnetic field coils, an electronic control and measurement unit, and a PC for control and data logging. The instrument is fitted with highly accurate $6^{th}$ - order compensated solenoids, which produce and measure the magnetic field using an inductivity bridge principle.

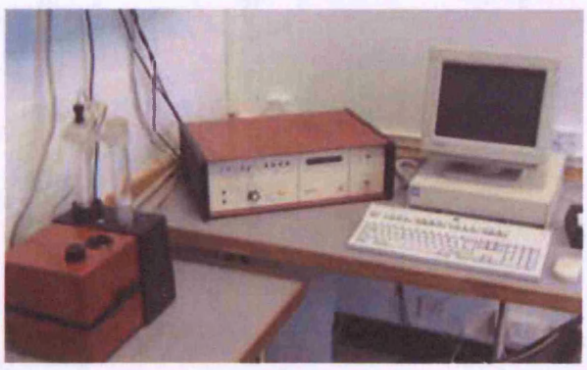

*Fig 5-4. Photo of the AMS kit, showing the KLY-2 pickup unit (left), the electronic bridge / measurement unit (centre) and the data logging PC (right)*

To determine AMS, samples are placed in the pick-up unit where magnetic susceptibility is measured in 15 orientations by rotating the sample into five different positions for each of the three planes of the co-ordinate reference frame. These orientations are shown in figure 5-5, and it can be seen that positions 1-5 rotate the XZ plane through five directions, positions 6-10 rotate the YZ plane through five directions and positions 11-15 rotate plane XY through five directions. The 15 directional measurements are fitted to an ellipsoid using a least-squares method (Jelinek, 1978), which allows the calculation of the six independent components of the susceptibility tensor, and the principal directions of the ellipsoid axes. There is redundancy in the measurement directions shown in figure 5-5, with several positions being the same in 3D

space, allowing the standard deviation of the fitted ellipsoid to be derived. Only ellipsoids with a relative standard deviation equal to or less than 2.5 % are accepted as valid.

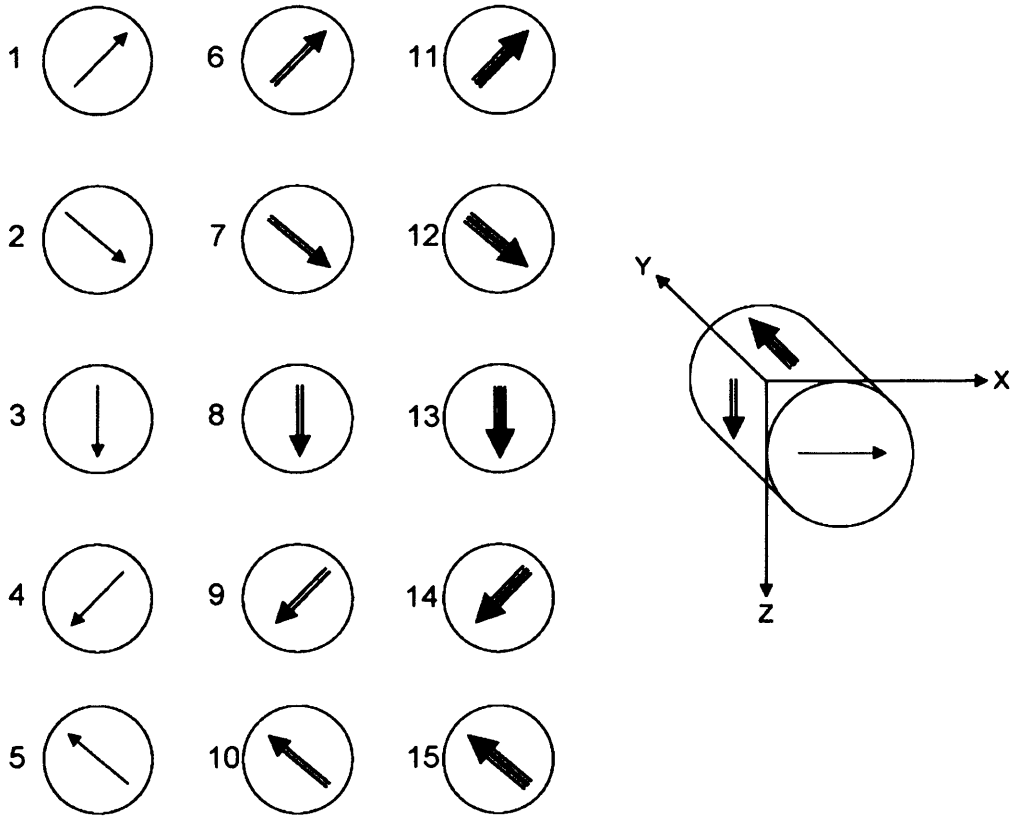


*Fig 5-5. (Left) the 15 orientations in which magnetic susceptibility is measured. The arrows correspond to those shown in the sample co-ordinate frame (right), and each of the three sample planes is rotated through five directions. The susceptibility measurements are then fitted to an ellipsoidal surface, which describes the AMS principal directions in terms of magnitude and orientation.*

## 5.3 Measurements of Elastic Wave Anisotropy

P and S-wave travel times were measured as a function of azimuth at 10° increments across the diameter of 38.1 mm cylindrical cores in each of the 3 orthogonal directions (a trio of x, y and z axis cores being termed a core-set), under dry and water-saturated conditions. In order

to ensure a representative dataset was generated, velocity measurements were taken around 6 core-sets.

### 5.3.1 Apparatus and Method

A new apparatus was designed and built to improve the quality and facility of ambient-condition measurements of elastic wave velocity (figure 5.6). This system improves on a previous design by incorporating a spring loaded piston directly above the transducer mounts. This provides a flush contact and a constant contact force between the rock sample and the transducers during sequential measurements. The design also incorporates a 'groove and indent' system that allows the sample to be rotated in precise 10° increments.

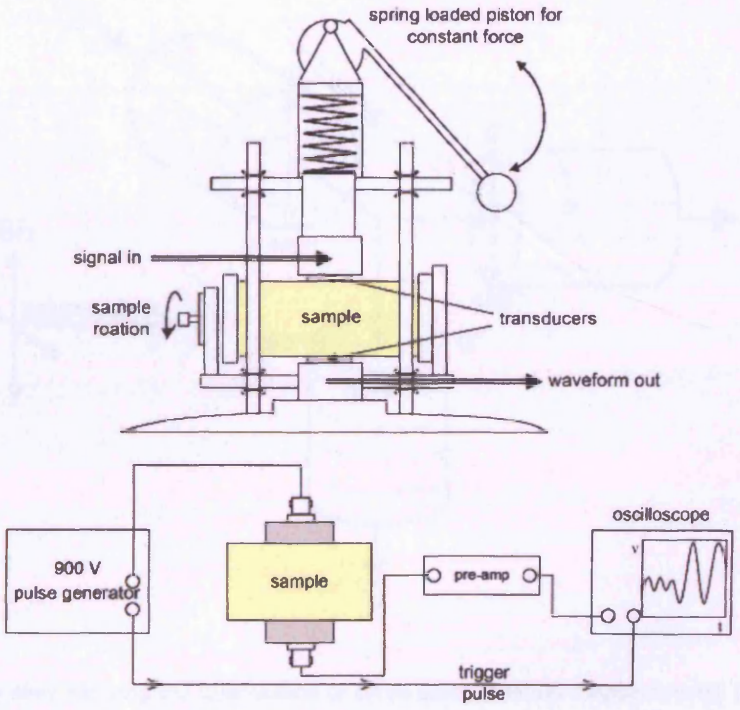


*Fig 5-6. Radial velocity measurement jig (above) and operating principles (below). A cylindrical rock sample is rotated about its central axis in 10° increments, allowing a velocity to be calculated at each azimuth via a pulse-and-receive technique. A calibration (detailed below) is used to correct the travel-time for time-of-flight through circuitry.*

Elastic waves are generated and detected using sets of Panametrics A303S-SU P-wave and V153-RB S-wave transducers, both types of transducer being of 1 MHz central frequency. P and S-waves were generated by exciting the relevant transducers using a 900 volt pulser/receiver (DPR300, JSR Ultrasonics), and the resulting waveforms were displayed and recorded using a HP Agilent Infiniium Oscilloscope.

Samples cored along each axis of the reference frame shown in figure 5-7 had P and S-wave measurements taken at each 10° rotation increment about the sample's central axis. Samples were rotated in the directions indicated, with the first measurement on each core taken at the relevant 0° datum.

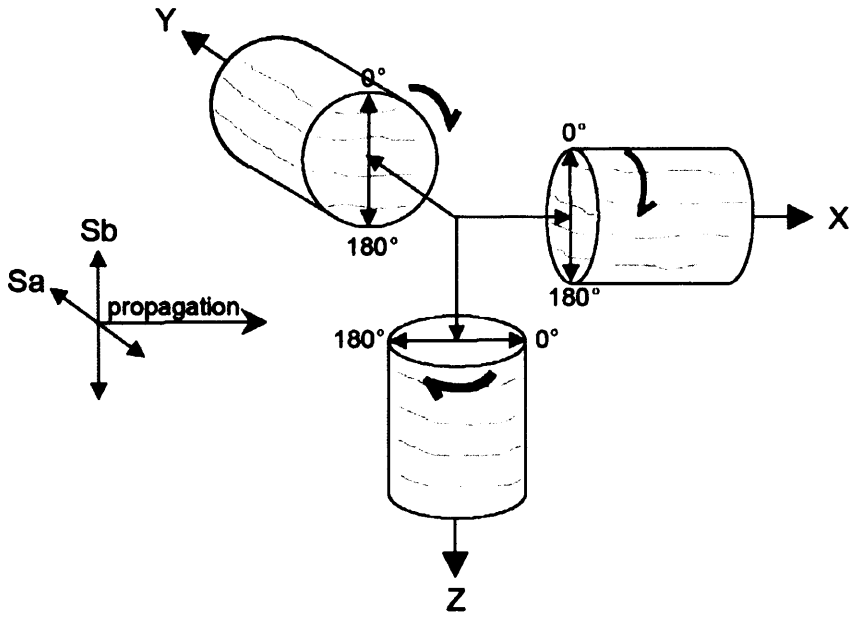


*Fig 5-7. Coring axes showing the orientations of cores during velocity measurements. Arrows to the left indicate the relationship between s-wave polarisation plane and material cross-bedding plane. For z-axis cores, Sa and Sb modes are consistent with changing azimuth, although this is not the case of x and y-axis cores (see section 5.3.3).*

Using the waveform displayed on the oscilloscope, time-of-flight measurements of P and S waves across the 38.1 mm diameter of the rock sample were made. These measurements were then converted to velocities by the simple relationship:

$$v = \frac{sample\ diameter}{corrected\ time\ of\ flight}$$

In order to eliminate the time-of-flight through the apparatus circuitry and transducer contact wear-plates, a correction was applied by performing a pulse-and-receive with the two transducers in direct contact with one another. The travel times for P and S waves through the circuitry and wear-plates alone were measured as 0.15 μs and 0.25 μs respectively. These times were then deducted from the time-of-flights measured through the circuitry plus rock sample to yield the travel-time through the rock sample alone.

Of these radial measurements on orthogonal cores, there is a degree of redundancy in the data in as much as some measurements share common directions. For example, a measurement at 180° azimuth around the axis ($Z_{180}$ ) shares the same direction as a measurement at $Y_{270}$. This redundancy allows a levelling procedure to be performed which corrects for the non-reproducibility of measurements made from sample to sample; the procedure is fully discussed in section 6.2.

### 5.3.2 Picking P and S-wave Arrivals

To generate a clear signal, one which is as unambiguous as possible, 256 waveforms were stacked and averaged. This procedure dramatically increases the signal-to-noise ratio, and allows a greater level of confidence in accurately identifying the arrival times of P and S-waves.

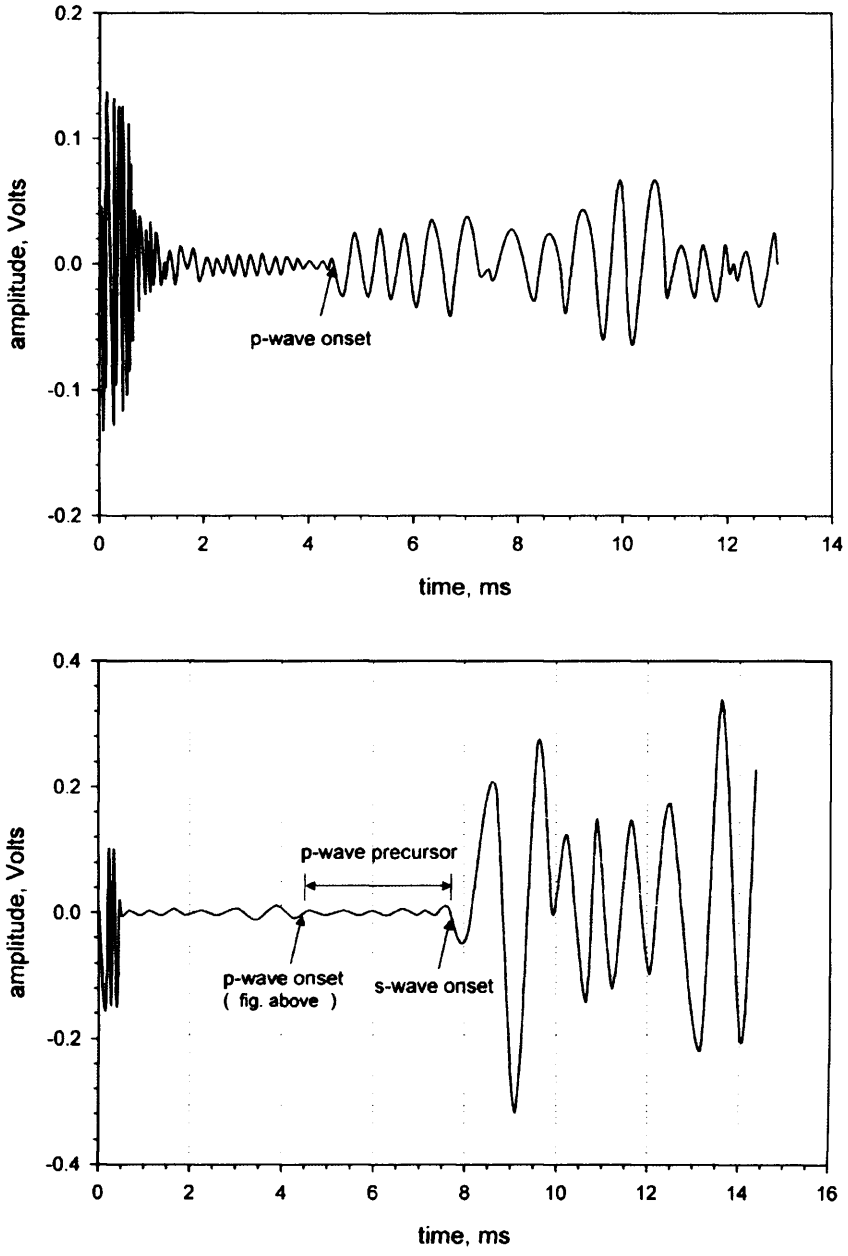


*Fig 5-8. P and S-wave onsets (shown top and bottom, respectively) and their picks.*

P-wave onset is determined independently to S-wave onset by using a dedicated P-wave transducer. Provided a clear signal, P-wave picking is a relatively unambiguous and straightforward process. Picking S-wave onsets is a trickier process because shear mode transducer crystals inherently produce a P-wave component, and therefore the interpretation of an S-wave onset has to take into account the associated P-wave signal.

When using elastic wave velocities to characterise anisotropy, internal consistency between successive measurements is arguably the most important aspect of the technique. This is because anisotropy is determined by relative variations in elastic velocity as a function of azimuth, rather than by the absolute magnitude of bulk velocity measurements. With this in mind, elastic wave measurements on each core-set were made in one sitting so as to eliminate the subjectivity associated with making a given set of measurements.

### 5.3.3 S-wave Polarisation

Since S-waves are polarised, and because Diemelstadt sandstone exhibits cross- bedding, which may induce S-wave splitting, it is necessary to consider the geometric relationship between the plane of S-wave polarisation and any plane of material isotropy. Sa polarisation is defined as the S-wave measurement in which both the direction of wave propagation and polarisation are in the xy plane (i.e. the plane of the material's cross-bedding); Sb polarisation is defined as the S-wave measurement for which the direction of S-wave propagation is in the xy plane, but where the plane of polarisation of the S-wave is normal to the xy plane.

In the instance of these measurements, the plane of S-wave polarisation with respect to the reference xy plane changes with each successive 10° rotation. This is such that, as shown in figure 5-7, the plane of S-wave polarisation with respect to sample orientation is meaningless in the 0° and 180° positions for the x and y-axis cores. In contrast, for the x and y-axis cores, the 90° and 270° positions are the only orientations for which the S-wave polarisations have a

definitive meaning. In the case of z-axis cores, the plane of S-wave polarisation with respect to bedding is always distinct because the rotation axis is normal to the xy plane.

## 5.4 Characterisation at Elevated Hydrostatic Pressure

### 5.4.1 Equipment Overview

The hydrostatic cell is shown schematically in figure 5-9, and is used for making steady-state permeability measurements, contemporaneously with axial P and S-wave velocities and measurements of pore volume change.

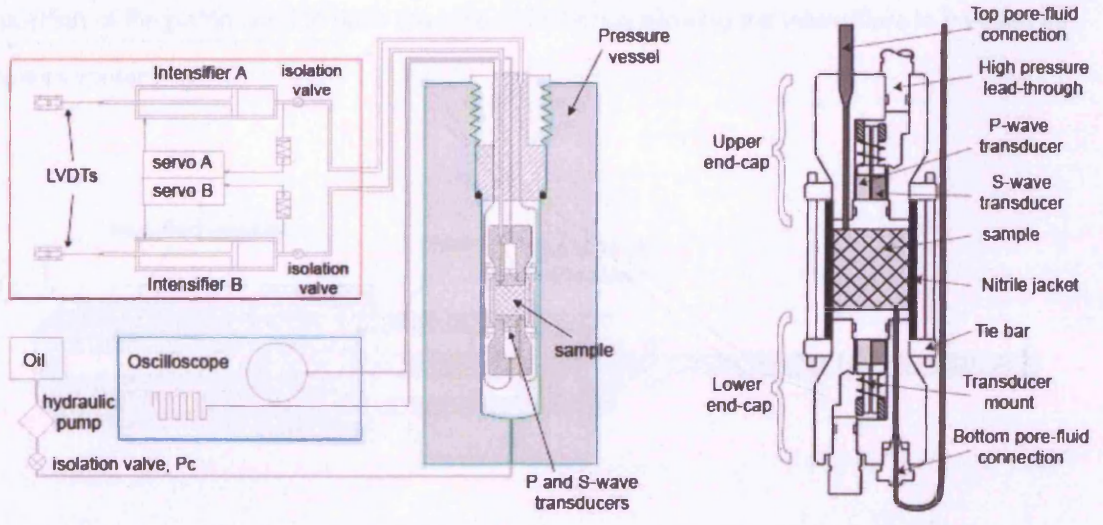


*Fig 5-9. Schematic overview of Hydrostatic Pressure Vessel (left). The intensifier system (red), pulse generator and receiver (blue) and the vessel itself (green) are shown. Sample assembly within the vessel shown in detail to the right.*

Confining pressures of up to 300 MPa are applied by means of a hydraulic pump, which drives a silicone-oil confining medium into the vessel. Pore pressure is applied to the sample ends through use of two servo-controlled pore fluid intensifiers, each is independently controlled and capable of generating up to 70 MPa of pore-pressure. Internal P and S-wave piezoelectric transducers, fitted behind the sample end-caps, are attached to a pulse

generator and oscilloscope and allow the measurement of elastic wave velocities along the sample axis at any point during an experiment.

### 5.4.2 Servo-Controlled Pore Fluid Intensifiers

Two identical hydraulic intensifiers are used to provide pore-pressure to the rock sample within the pressure vessel, one connected to the top of the sample and the other to the bottom. Each intensifier has an internal volume of 45 $cm^3$, and is servo-controlled via analogue electrical feedback from an external pressure transducer. This system allows the intensifiers to maintain constant (to within 5 kPa) pressures within their range of 1.5 – 70 MPa. Each intensifier is fitted with an integral displacement transducer (LVDT) which monitors the position of the piston used to drive the pore-fluid, hence allowing the intensifiers to be used as volumometers.

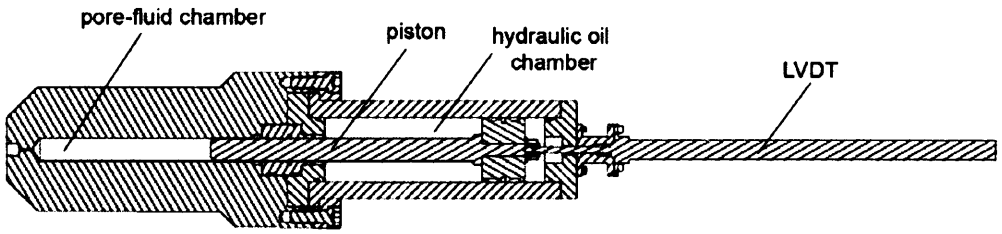


*Fig 5-10. A cross-section through a pore-fluid intensifier*

Pore fluid is evenly applied to the upper and lower sample surfaces by use of spreader plates, with concentric ring etchings, housed in the end-caps of the apparatus (see figure 5-11). Since both the upstream and downstream intensifiers are independently controlled, it is possible to set a constant pore-pressure differential across the sample. This provides the basis for making steady-state measurements of permeability (Jones and Meredith, 1998), where the rate of fluid flow, the applied pressure gradient and the sample dimensions are related through Darcy's Law (see section 5.5.4).

### 5.4.3 Acoustic Transducer Assembly

The piezoelectric transducer assemblies are housed within each end-cap, behind the pore-fluid spreader plates mentioned above. Each assembly is comprised of two PZT crystals of 1 MHz central frequency, one P mode and one S mode, as shown below.

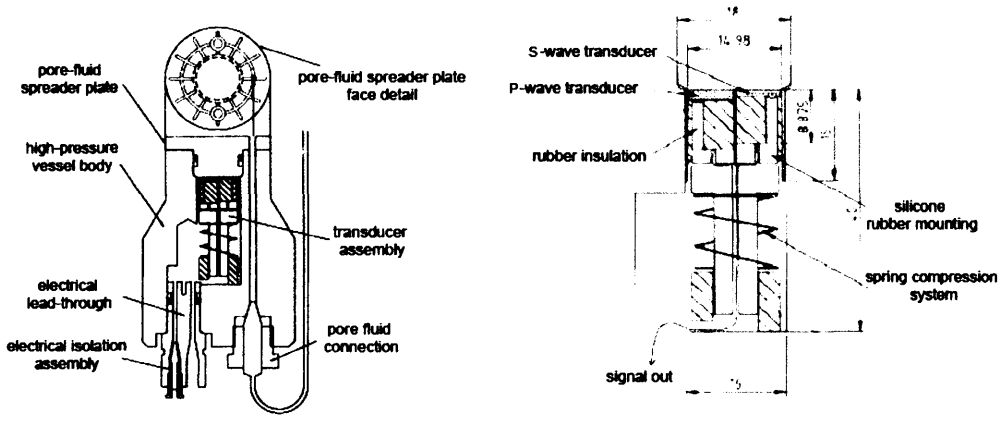


*Fig 5-11. End cap detail (left) housing transducer assembly and spreader plate. Transducer assembly is shown in detail to the right. Dimensions are in mm.*

### 5.4.4 Data Acquisition and Lead Through Design

A lead-through design first implemented by Clint (1999) is used to allow data to be reliably measured under high pressure conditions. An exploded diagram of this design is shown in figure 5-12. Coaxial wires were soldered to the ends of the conductor pin, which were electrically isolated from the plug by use of a cone and insulator component made from the high strength polymer ULTEM. The initial seal is provided by tightening a hollow screw over the ULTEM sheathed conductor pin, forcing the cone against a machined shoulder within the plug. When this system is pressurised during the course of an experiment, the conductor pin and ULTEM cone is forced further against the machined shoulder within the plug, producing a seal capable of maintaining its integrity at pressures of up to 400 MPa. Each plug is designed

to house three conductor pins, and the plug itself seals by way of an o-ring and PTFE (a synthetic fluoropolymer) backing ring arrangement.

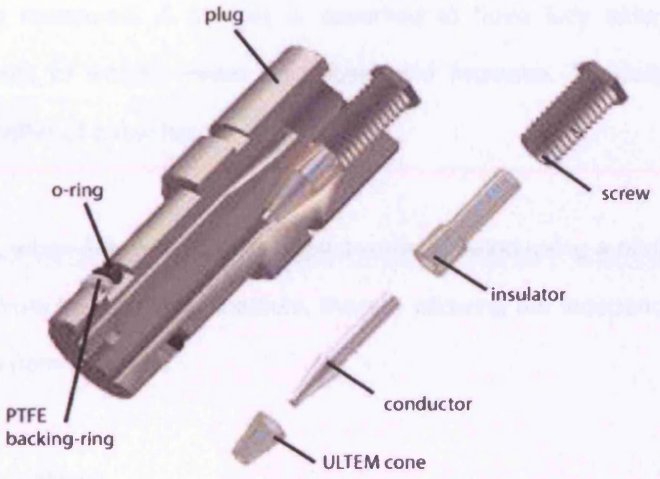


*Fig 5-12. Lead-through plug used to relay electrical wiring from within the pressure vessel to the data-logging kit. This design was used for both the hydrostatic and triaxial pressure vessels.*

## 5.5 Measurements Under Hydrostatic Pressure

Using the apparatus detailed in the preceding sections, measurements were taken of changes in P and S-wave velocity, porosity and permeability, all as a function of increasing hydrostatic pressure. The effective pressure range covered in these measurements extends from 5 - 250 MPa, with stepwise increases of 5 MPa made until Pe = 20 MPa followed by 10 MPa increments until Pe = 250 MPa. The following sections detail the protocol used to make these measurements.

### 5.5.1 Sample Preparation

For experiments run in the hydrostatic pressure cell, right circular cores of 38.1 mm diameter and 40 mm length were prepared along the z and x-axes of the common co-ordinate reference frame (figs 5-3, 5-7). The sample ends were ground flat and parallel to one another

using a diamond impregnated grinding wheel. The individual connected porosity of each sample was determined using a gravimetric technique, whereby the dry weight of the sample is measured, and then, following immersion in distilled water under a vacuum, the saturated weight of the sample is measured. A sample is assumed to have fully saturated when consecutive measurements of weight reveal no subsequent increase. Typically, samples would saturate within a matter of a few hours.

Prior to the start of a test, when fully saturated, samples were jacketed using a nitrile sleeve in order to isolate the rock from the confining medium, thereby allowing the independent control of confining pressure and pore pressure.

### 5.5.2 Initial Pressure Conditions

Because of the presence of a sample jacket, it was necessary to apply a confining pressure to the sample before the application of a pore pressure. Further, it was necessary to ensure that Pc > Pp at all times. This is because even a modest pore-pressure applied to an insufficiently confined sample would breach the seal of the jacket and contaminate the confining medium (silicone oil) with the pore fluid (distilled water). This would waste the volume of silicone oil contaminated, and, over the long term, potentially damage the apparatus through rusting. Therefore, an initial confining pressure of 10 MPa was applied to the sample, with 5 MPa pore-pressure applied concurrently with the final 5 MPa of confinement. This ensured that the sample was not exposed to any effective pressure greater than 5 MPa at any point. These were the starting conditions of each experiment performed in the hydrostatic cell. From this point, pore-pressure was maintained at 5 MPa whilst confining pressure was increased systematically by the increments mentioned earlier.

### 5.5.3 P and S-wave Measurements

At each effective pressure interval, the arrival times of P and S-waves were discerned. As with velocity measurements taken under ambient conditions, a correction is applied to the hydrostatic travel times to adjust for the time-of-flight through the necessary circuitry and 30 mm of hardened steel associated with the hydrostatic system (see figure 5-11). To perform this calibration, a simple time-of-flight measurement was made with the pulsing and receiving transducer assemblies in direct contact with one another. The resulting off-sets (5.40 μs for P-waves, 9.50 μs for S-waves) were then applied to each velocity measurement taken. A correction was also applied to adjust for the effects of sample shortening during hydrostatic loading (described in section 7.4.2).

### 5.5.4 Permeability Measurements

Under hydrostatic conditions, flow rate was measured using a steady-state method (see figure 5-13), whereby a known pore-pressure gradient is applied along the length of a sample of known dimensions. A pore-pressure differential of 0.5 MPa was applied to ensure a pore-pressure gradient no greater than 10% of the total pore-pressure. This approach is adopted to limit the effects of establishing a significant effective confining-pressure gradient across the length of the sample.

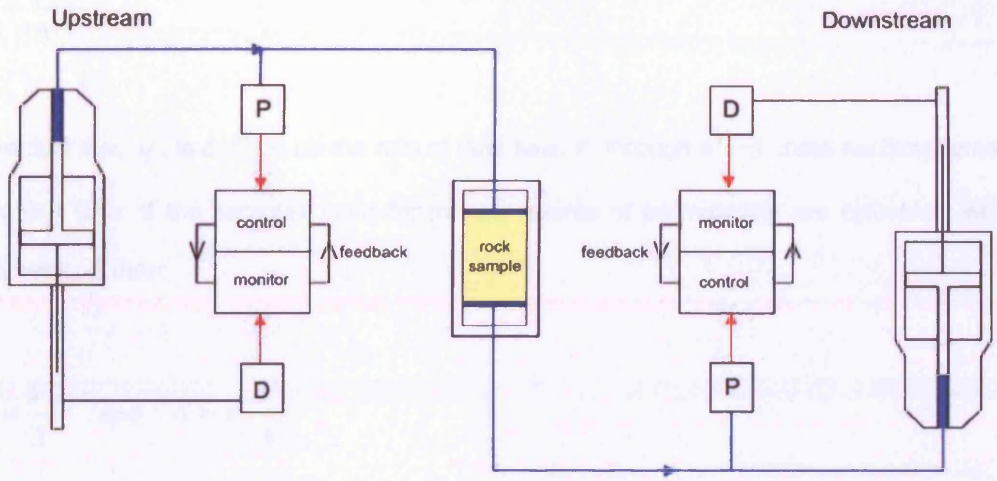


*Fig 5-13. Principle of steady state flow, after Jones and Meredith (1998). A rock sample is subjected to elevated hydrostatic pressure while two independently controlled pore-pressure intensifiers apply a constant and known pore-pressure (P) gradient across the sample length. The resulting fluid flow is measured as a function of time by the integrated displacement transducers (D) of the pore-fluid intensifiers.*

It is also necessary to keep the applied pore-pressure gradient at modest levels because otherwise a) the pore-fluid intensifiers may run out of stroke before a steady-state flow regime is established, and b) if the flow rate is too great, then a turbulent flow regime may develop resulting in Darcy's law being non-applicable to the measurements.

The co-efficient of permeability, $k$, can be related to the applied pressure gradient, $\Delta P$, through Darcy's law:

$$q = -\frac{k\,\Delta P}{\eta\, x}$$

where $q$ is the fluid flux, $\eta$ is the fluid viscosity and $x$ is the sample length. Re-arranging the relationship for $k$ gives:

$$k = \frac{q\eta\, x}{\Delta P}$$

The fluid flux, $q$, is defined as the rate of fluid flow, $V$, through a unit cross-sectional area, $S$, per unit time. If the samples used for measurements of permeability are cylindrical with a diameter, $d$, then:

$$q = \frac{V}{S} \quad \text{and} \quad S = \pi\frac{d^2}{4}$$

allowing permeability to be written as:

$$k = \frac{V\ 4\eta x}{\Delta P\ \pi d^2}$$

Since all measurements of permeability are performed at elevated pressure, a correction is applied to adjust sample dimensions for the shortening associated with hydrostatic loading (see section 7.4.2).

### 5.5.5 Pore Volumometry

At the point of each increment increase in confining pressure, the rock sample compresses an amount in reaction. Under hydrostatic conditions, this compression is the result of microcrack and pore closure, and can be measured by the contemporaneous change in piston displacement of the intensifier controlling the pore-pressure. As such, the piston displacement represents the amount of pore fluid expelled in order to maintain a constant pore pressure. Therefore, a pore volume change associated with each successive increase in effective pressure can be measured and recorded directly off the data log in real time. Figure 5-14

illustrates the steps involved in making contemporaneous measurements of pore-volume change and permeability.

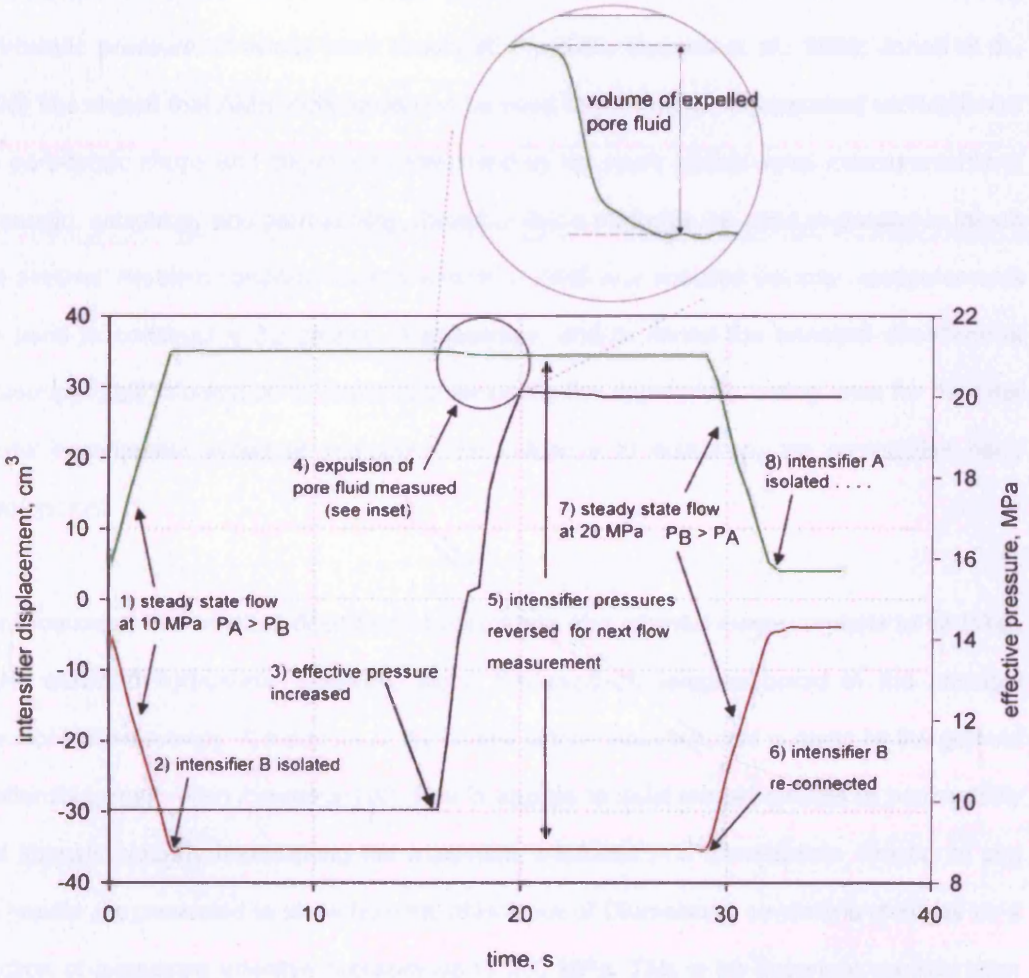


*Fig 5-14. Fluid flow expressed as intensifiers displacement against time during the application of a 0.5 MPa pressure differential across a sample of Diemelstadt sandstone (1). A 10 MPa increase in effective pressure (3) results in a measurable change in the sample's pore volume (4), before another measurement of permeability is made under the new, higher, effective pressure conditions (8).*

# 6 Results of Material Characterisation

Results are presented of measurements designed to characterise the anisotropy of Diemelstadt sandstone under ambient conditions and under conditions of increasing hydrostatic pressure. Previous work (Louis et al., 2003, Benson et al., 2003; Jones et al., 2006) has shown that AMS techniques can be used to provide an independent verification of the pore-fabric shape and alignment determined by the more conventional measurements of ultrasonic anisotropy and permeability, therefore these methods are used in parallel to inform one another. Ambient condition measurements of AMS and acoustic velocity measurements are used to construct a 3D picture of anisotropy, and to reveal the principal directions of anisotropy. This information is useful in determining the appropriate coring axes for the later triaxial experiments aimed at examining the influence of anisotropy on compaction band development.

Identification of the principal directions of anisotropy also allowed measurements to be taken under elevated hydrostatic pressure, along the axes of samples cored in the principal directions of anisotropy. A measure of anisotropy is then possible, and is given by the general relationship, *max – min / mean x 100*. This is applied to axial measurements of permeability and acoustic velocity taken along the maximum, minimum and intermediate directions, and the results are presented to show how the anisotropy of Diemelstadt sandstone changes as a function of increasing effective pressure up to 250 MPa. This is an important consideration because the triaxial experiments of this study necessarily involve elevated pressure, and therefore any insight on the anisotropy of Diemelstadt sandstone at elevated pressure is a useful addition to the ambient pressure character of the material.

## 6.1 Anisotropy of Magnetic Susceptibility

As discussed in section 5.2, conventional measurements of AMS are conducted on dry samples of rock with the aim of measuring the anisotropy of magnetic susceptibility of the material's matrix (termed mAMS). By repeating the same measurements on samples saturated with a magnetically susceptible ferrofluid, the AMS of both the matrix (mAMS) and the ferrofluid filled pore-space (pAMS) can be assessed.

The principle of mAMS relies on there being a magnetic fabric to the rock, caused by the presence of magnetically susceptible minerals within the rock matrix. Diemelstadt sandstone does not have a naturally strong magnetic susceptibility, so that when the AMS of a ferrofluid saturated sample is measured, the resulting principal anisotropy axes overwhelmingly reflect the geometry of the pore fabric. Therefore it can be said that in the case of Diemelstadt sandstone (mAMS ~ 10 $x10^{-6}$ SI, tAMS ~ 20,000 $x10^{-6}$ SI) that measurements of tAMS are a very close proxy for pAMS. As a result of the virtually non-existent native magnetic fabric of Diemelstadt sandstone, not too much emphasis is placed on the measurements derived from mAMS data as it cannot be certain to what extent the measurements accurately represent the material. However, the data is presented for the sake of completion.

To ensure an accurate representation of global pore-fabric anisotropy, a total of 22 samples were cored from different areas of the sandstone block and measured in the magnetic susceptibility bridge. The principal axes of mAMS and tAMS (~pAMS) are plotted on stereographic projections in figure 6-1, which are oriented to the reference frame defined in section 5.1.2, which provides a convenient way of visualising the directional measurements. The average orientation of the mAMS and pAMS principal axes are summarised in table 6-1.

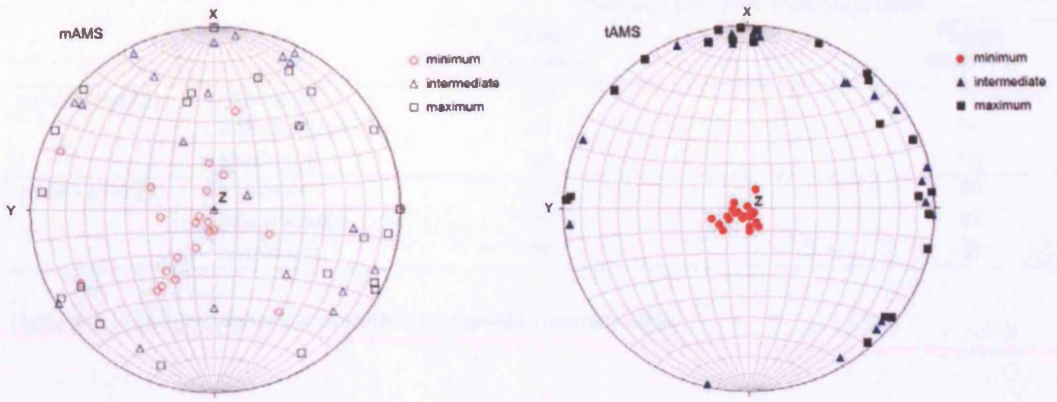


*Fig 6-1. Stereographic projection of mAMS (left, open symbols) and tAMS ~pAMS (right, filled symbols). Minimum principal axes are represented as red circles, intermediate as blue triangles and maximum as black squares.*

For measurements of mAMS, the data very loosely shows two populations. A minimum direction aligned around the z-axis, and the intermediate and maximum directions distributed sub-parallel to the x and y-axis.

Measurements of pAMS show a tight cluster of minima aligned with the z-axis, and the intermediate and maximum directions oriented at about 90° to the minimum, sub-parallel to the x and y-axis. Measurements of pAMS show no obvious distinction between the intermediate and maximum directions, which appear quite evenly distributed along a common plane. The minimum directions are on average 5° off-set from the z-axis, and the intermediate and maximum directions are on average 12° and 9° sub-parallel to the XY plane, respectively. These offsets are approximately equal to the dip of the cross-bedding observed in hand-specimens of Diemelstadt, which suggests that the pore-fabric geometry is controlled by the cross-bedding fabric.

| | | Average principal anisotropy axes | |
|---|---|---|---|
| | | Trend (degrees) | Plunge (degrees) |
| mAMS (n=22) | Minimum | 226 | 77 |
| | Intermediate | 21 | 54 |
| | Maximum | 55 | 53 |
| pAMS (n=22) | Minimum | 225 | 85 |
| | Intermediate | 40 | 12 |
| | Maximum | 34 | 9 |

*Table 6-1. Average orientation of mAMS and pAMS principal axes.*

### 6.1.1 Fabric Anisotropy

The ellipsoids generated though AMS techniques not only can be described in terms of the principal axes' orientations, but also their magnitudes. This allows the shape of the ellipsoid to be defined by considering the length ratios of the principal axes. For this analysis, two parameters are considered; lineation (L) and foliation (F). Lineation is defined as the ratio of the maximum principal axis to the intermediate principal axis, and foliation is defined as the ratio of the intermediate principal axis to the minimum principal axis. For ellipsoids, the lineation and foliation reflect the extent to which the overall shape is oblate or prolate, respectively.

The lineation and foliation parameters can be displayed using the method of Flinn (1962), which allows the relative contribution of lineation and foliation to be visualised, therefore providing an graphical representation of the degree to which pore-fabric is oblate or prolate (figure 6-2).

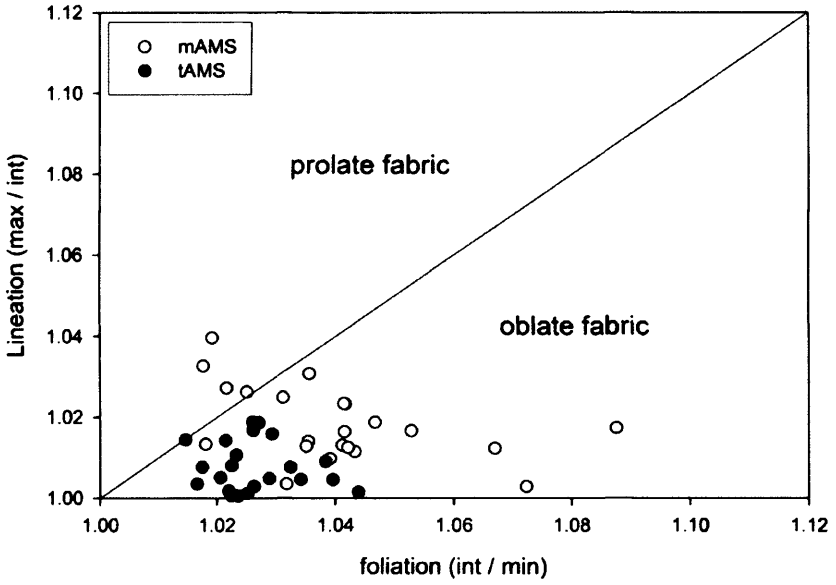


*Fig 6-2. Flinn diagram for mAMS ellipsoids (open symbols) and tAMS~pAMS ellipsoids (closed symbols).*

The Flinn plots show a statistically oblate pore-fabric, which is typically to be expected in sedimentary rocks as a result of the processes of deposition and compaction. Although this oblate fabric is clear in both plots, it is more evident in the pAMS data. A calculation of anisotropy, based on the magnitudes of principal axes is given simply by the formula:

$$\frac{\max - \min}{mean} \; x\,100$$

This measure of anisotropy is commonly used when describing the anisotropy of elastic wave velocity through a material. When applied to the AMS data, anisotropies of 5.7% and 3.4% are shown for mAMS and pAMS, respectively (table 6-2).

| AMS (n=22) | Bulk susceptibility ($10^{-6}$ SI) | Principal axis length (normalised to bulk susceptibility) | | | Anisotropy parameters | | |
|---|---|---|---|---|---|---|---|
| | | Minimum | Intermediate | Maximum | F | L | A, % |
| mAMS | | | | | | | |
| Average | 13 | 0.968 | 1.007 | 1.025 | 1.040 | 1.018 | 5.7 |
| St. Dev. | 4 | 0.010 | 0.007 | 0.005 | 0.018 | 0.009 | 1.4 |
| Minimum | 6 | 0.939 | 0.993 | 1.013 | 1.018 | 1.003 | 3.1 |
| Maximum | 19 | 0.984 | 1.022 | 1.039 | 1.088 | 1.040 | 10.0 |
| pAMS | | | | | | | |
| Average | 19934 | 0.980 | 1.006 | 1.014 | 1.026 | 1.008 | 3.4 |
| St. Dev. | 700 | 0.005 | 0.003 | 0.004 | 0.007 | 0.006 | 0.9 |
| Minimum | 18960 | 0.971 | 1.000 | 1.008 | 1.015 | 1.000 | 2.0 |
| Maximum | 21170 | 0.988 | 1.014 | 1.021 | 1.044 | 1.019 | 4.6 |

*Table 6-2. Summary of mAMS and pAMS data. Parameters F, L and A correspond to foliation, lineation and anisotropy, respectively.*

## 6.2 Elastic Wave Velocity

Elastic wave velocities are particularly sensitive to void space as a result of the significant contrast between the stiffness of the rock matrix and the pore fluid occupying the void space, which in nature may be a gas, liquid or a combination of both. Measurements of elastic wave velocity may therefore be used as a proxy for measuring void-space geometry. For this study, P and S-wave velocities were measured as a function of azimuth around orthogonal core-sets of Diemelstadt sandstone under dry and water saturated conditions according to the method described in section 5.3. These data are presented as 2D plots showing velocity variation with azimuth within specific planes (figures 6-4 and 6-5). However, by using the method of Louis et al. (2003), data from 3 complementary cores (between them showing velocity variation with azimuth in all three planes XY, XZ and YZ) may be used to construct velocity ellipsoids which can in turn be described in 3D in terms of principal directions. This method allows stereonets to be plotted to visualise the directional measurements in the same manner as for the AMS measurements. It should be noted, however, that because an ellipsoid describes a second-rank tensor and elasticity is described by a fourth-rank tensor, the fitting of velocity data in this manner is strictly an approximation (Louis et al., 2003; Benson et al., 2003).

Before velocity data taken in different 2D planes can be used to describe velocity structure in 3D, it is necessary to employ a levelling technique to ensure that complementary velocity data collected from three orthogonal planes are treated in comparable way. To this end, the assumption is made that velocity measurements taken in the same direction should be equal, irrespective of the fact that they are taken on different cores. Given that orthogonal core-sets are prepared in close proximity to one another, this is a reasonable assumption to make. For example, for the schematic core-set illustrated in figure 6-3, it can be seen that the velocity along the x-axis may be determined either by a measurement at 90° azimuth on the y-axis core, or by a measurement at 0° azimuth on the z-axis core. Similarly, the velocity along the y-axis may be determined either by a measurement at 90° azimuth on the x-axis core, or by a measurement at 90° azimuth on the z-axis core. Any independent velocity measurements taken in the same direction are as equally valid as one another, and therefore the discrepancies between such measurements are treated in such a way as to 'level' the difference observed between measurements taken in the same direction albeit on different cores.

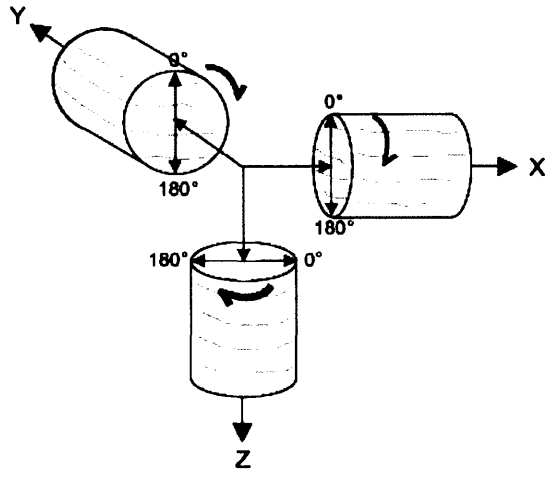


*Fig 6-3. A schematic core-set showing the reference axes and orientations used to make radial velocity measurements.*

This technique is performed by treating the velocity measurement taken at 180° azimuth on the z-axis core ($z_{180}$) as a datum. The mismatch in measured velocity between $z_{180}$ and the directionally co-incident measurement at $y_{270}$ is calculated, and the percentage offset is then applied to all azimuthal data around the y-axis core to bring the $z_{180}$ and $y_{270}$ measurements into agreement. The process is repeated for the directionally co-incident velocity measurements at $y_{180}$ and $x_{180}$, with the mismatch offset being applied to all data around the x-axis core. Finally, the mismatch between the directionally co-incident measurements at $x_{90}$ and $z_{90}$ is evaluated. However, any resulting offset, if applied to the z-axis data, would alter the datum at $z_{180}$ and therefore lead to an infinite regress. To avoid this, the final velocity mismatch is distributed equally between all data points levelled up to this point. The offsets produced by this levelling technique are very subtle, at the most 2% of the measured velocity, and are within the error associated with taking the measurement.

Velocity data is presented in figures 6-4 and 6-5 for Diemelstadt sandstone under dry and water saturated conditions, respectively. For dry data, a clear variation with azimuth can be seen for P-wave velocity with anisotropy being greatest in the XZ plane, followed by the YZ plane. Velocity variation within the XY plane is lowest. The same general trend is observed for S-wave velocities, although difference in variation between the XZ and YZ planes is much less pronounced, to the extent where there is no discernable difference. Both modes of S-wave were measured (Sa and Sb, as described in section 5.3.3), although there appears to be no distinction in their velocities as measured in this material. In the XZ and YZ planes, both P and S-wave velocities show minimum values at around 0° and 180°, and maximum values at around 90° and 270°. Within the XY plane, the azimuthal distribution of maximums and minimums are observed at 0° and 180°, and 90° and 270°, respectively. The elastic anisotropy is greatest in the XZ plane at approximately 7% for P-waves and 5% for S-waves. Within the XY plane, anisotropy is least, at approximately 1.5% for both P and S-waves (table 6-3).

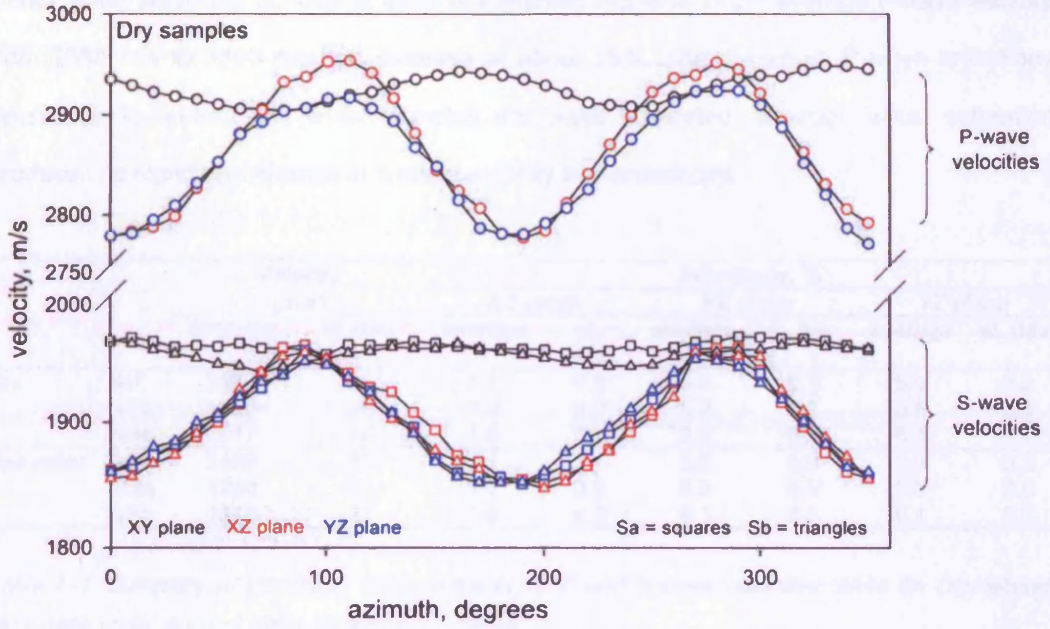


*Fig 6-4. Elastic wave velocity variation with azimuth for Diemelstadt sandstone under dry conditions*

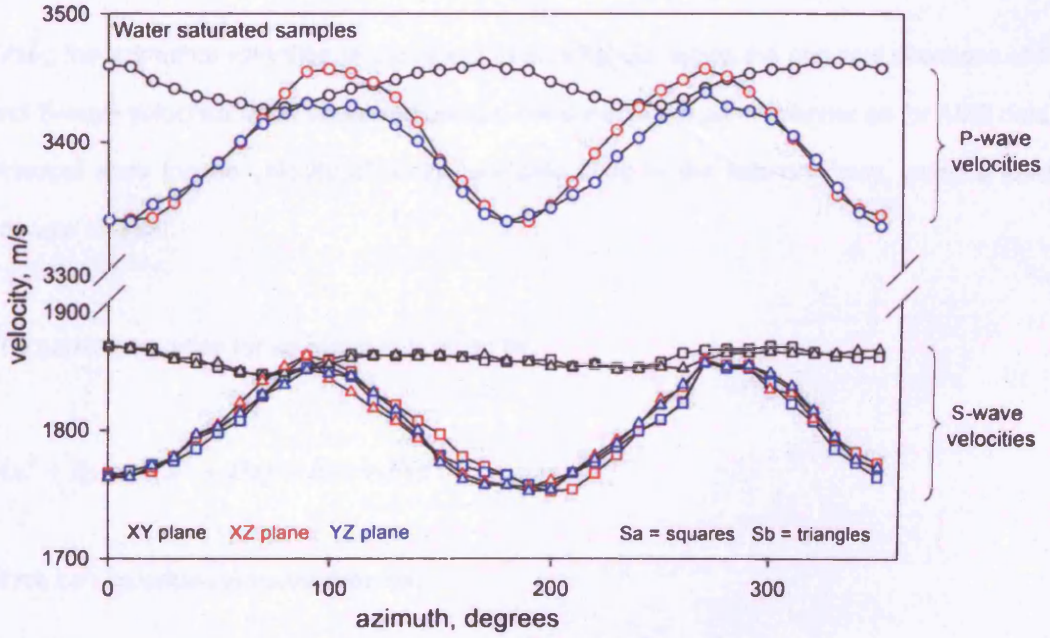


*Fig 6-5. Elastic wave velocity variation with azimuth for Diemelstadt sandstone under water saturated conditions*

Under water saturated conditions there is a marked increase in the average P-wave velocity from 2880 m/s to 3400 m/s, an increase of about 18%. The maximum P-wave anisotropy decreases to around 4% when samples are water saturated, although water saturation produces no significant change in S-wave velocity and anisotropy.

| | | Velocity (m/s) | | Anisotropy, % | | | | | |
|---|---|---|---|---|---|---|---|---|---|
| | | | | XY plane | | XZ plane | | YZ plane | |
| | | average | st. dev. | average | st. dev. | average | st. dev. | average | st. dev. |
| Dry | vP | 2882 | 44 | 1.7 | 0.2 | 6.9 | 0.1 | 5.5 | 0.2 |
| | vSa | 1920 | 25 | 1.0 | 0.2 | 5.2 | 0.2 | 5.6 | 0.3 |
| | vSb | 1917 | 26 | 1.5 | 0.2 | 5.3 | 0.3 | 5.4 | 0.2 |
| Saturated | vP | 3409 | 30 | 1.4 | 0.1 | 3.8 | 0.2 | 3.0 | 0.2 |
| | vSa | 1820 | 25 | 1.6 | 0.2 | 6.3 | 0.5 | 6.3 | 0.6 |
| | vSb | 1819 | 25 | 1.6 | 0.3 | 6.1 | 0.3 | 6.1 | 0.2 |

*Table 6-3. Summary of laboratory measurements of P and S-wave velocities taken on Diemelstadt sandstone under dry and water saturated conditions.*

### 6.2.1 Velocity data in 3D

Fitting the azimuthal velocities of a core-set to an ellipsoid allows the principal directions of P and S-wave velocities to be visualised using a stereonet in the same manner as for AMS data. Principal axes for the velocity ellipsoids are calculated in the following way, using a least squares method:

The general equation for an ellipsoid is given by:

$$Ax^2 + By^2 + Cz^2 + Dxy + Exz + Fyz = 1$$

which can be written in matrix form as:

$$(x\ y\ z)\cdot\begin{pmatrix} A & D/2 & E/2 \\ D/2 & B & F/2 \\ E/2 & F/2 & C \end{pmatrix}\cdot\begin{pmatrix} x \\ y \\ z \end{pmatrix} = 1$$

where A, B, C, D, E, F are parameters which describe the magnitude and direction of the principal axes in x, y, z Cartesian space.

To estimate the six parameters needed to define the ellipsoid, the least squares system for a number, $k$, of velocity measurements, $\vec{V}$, with direction, given by the unit vector $\vec{u}_i\,(l_i, m_i, n_i)$, written as:

$$\begin{pmatrix} l_1^2 & m_1^2 & n_1^2 & l_1 m_1 & l_1 n_1 & m_1 n_1 \\ \vdots & \vdots & \vdots & \vdots & \vdots & \vdots \\ l_k^2 & m_k^2 & n_k^2 & l_k y_k & l_k n_k & m_k n_k \end{pmatrix} \cdot \begin{pmatrix} A \\ B \\ C \\ D \\ E \\ F \end{pmatrix} = \begin{pmatrix} 1/V_1^2 \\ \vdots \\ 1/V_k^2 \end{pmatrix}$$

Defining the left-hand-side matrix as $Q$, the parameter vector as $P$, and the inverse squared velocity vector as $W$, the least squares solution for $P$ is estimated by:

$$P = ({}^{t}Q \cdot Q)^{-1} \cdot ({}^{t}Q \cdot W)$$

The parameters in P are then solved to give, as eigenvalues and eigenvectors, the magnitudes and orientations of the three principal axes of the velocity ellipsoid. These orientations are plotted on stereonets in figure 6-6.

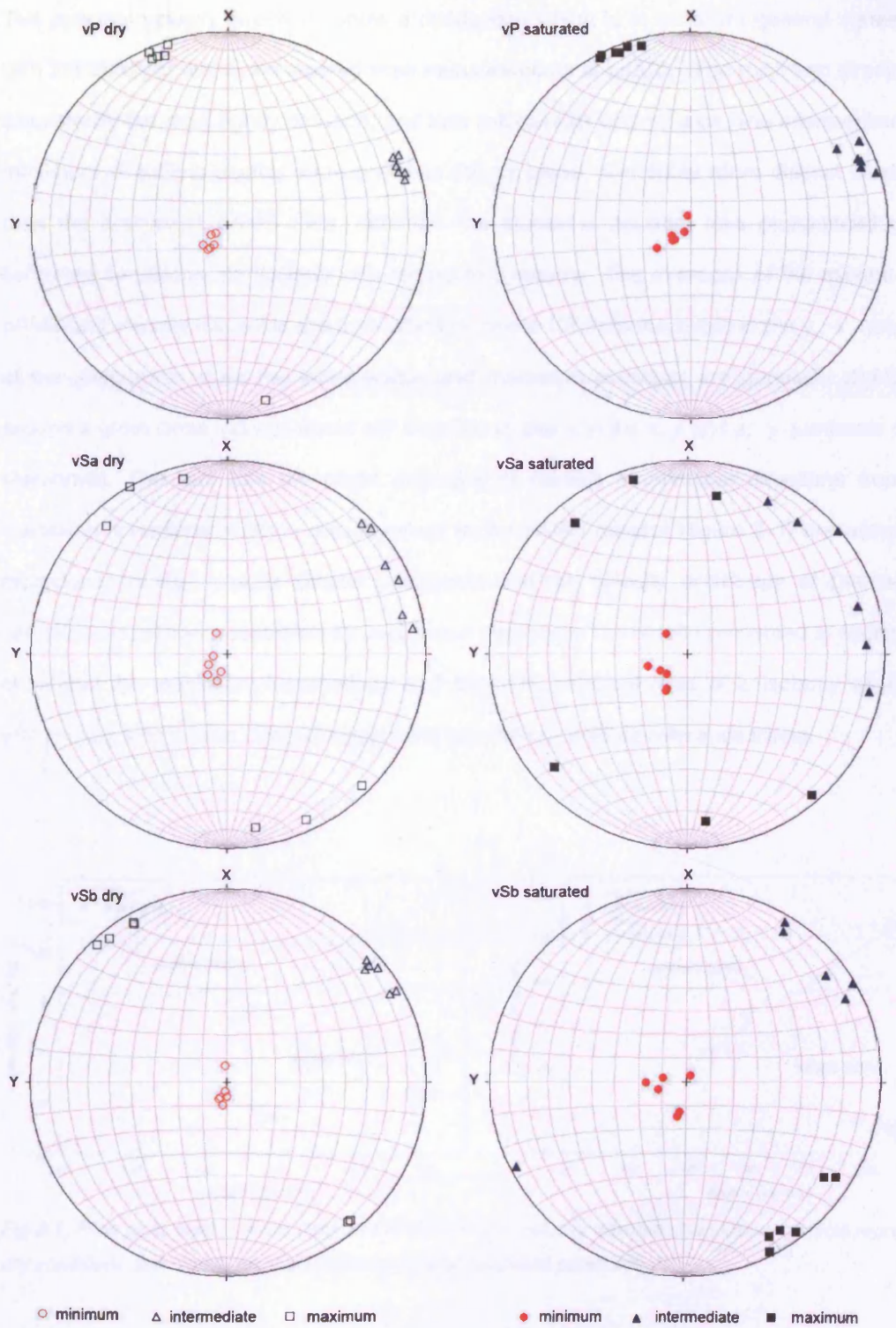


*Fig 6-6. Stereonets showing the principal directions for P and S-wave velocities under dry (open symbols) and water saturated (closed symbols) conditions.*

The principal velocity directions show a distribution which is in excellent general agreement with the principal directions derived from measurements of pAMS. The minimum direction is consistently the most tightly grouped, and falls sub-parallel to the z-axis. The intermediate and maximum directions scatter sub-parallel to the xy plane, and show more distinct clustering than the equivalent pAMS data, although the clustering appears less pronounced under saturated conditions, particularly with regard to S-waves. The averages of the minima from pAMS and velocity ellipsoids are both offset by about 10° from the z-axis in the y, -x quadrant of the stereonets, while the intermediate and maximum averages are generally distributed around a great circle inclined about 10° from the xy plane in the x, y and x, -y quadrants of the stereonets. The fact that the slight and distinct off-sets in principal directions from the Cartesian co-ordinates which are observed in the pAMS dataset (figure 6-1) are accurately reproduced in the velocity dataset suggests that the velocity anisotropy of Diemelstadt sandstone is primarily controlled by void space geometry. The results presented in section 6.2 show that the maximum, intermediate and minimum principal axes of anisotropy align well with the x, y and z axes, respectively, of the general co-ordinate reference frame.

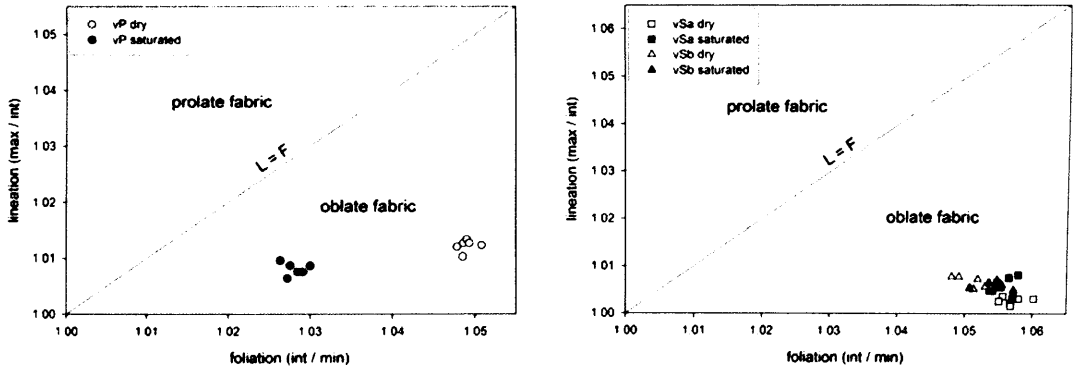


*Fig 6-7. Flinn plots from P-wave (left) and S-wave (right) velocity ellipsoid data. Open symbols represent dry conditions and closed symbols represent water saturated conditions.*

The magnitudes of the principal axes of the velocity ellipsoids are used to construct Flinn plots of lineation against foliation, the same in principle to those used to display the AMS ellipsoid data. The lineation and foliation parameters of the velocity Flinn plots are shown in figure 6-7 and summarised in table 6-5.

Both pAMS and velocity measurements indicate pore-fabric anisotropy with a minimum principal direction oriented sub-parallel to the z-axis of the general co-ordinate frame used in this study. pAMS data show the intermediate and maximum principal directions to be scattered interchangeably about a plane sub-parallel to the xy plane of the general co-ordinate frame, whereas velocity measurements show a clearly distinct grouping between intermediate and maximum principal directions. However this is not necessarily a contradiction. The difference may arise from the fact that each technique is sensitive to different parameters. pAMS measurements are sensitive to the ferrofluid-filled porosity whereas velocity measurements are very sensitive to any elastic discontinuity, caused for example by a microcrack or a pore throat. If it is assumed that the greatest contribution to bulk porosity is pores rather than pore-throats and microcracks, then pAMS measurements will more overtly reflect the influence of pores than the influence of microcracks or pore-throats of a comparatively low volume. In the case of acoustic velocity measurements, an alignment of pore-throats or microcracks, caused by palaeocurrents or diagenesis in an anisotropic stress field, are likely to be revealed as a result of the methods sensitivity to this parameter. The hydrostatic results discussed in the following sections are used to help inform the picture of anisotropy revealed by the ambient pressure data.

| vP | | Average principal anisotropy axes | | |
|---|---|---|---|---|
| | | Velocity (m/s) | Trend (degrees) | Plunge (degrees) |
| Dry | Minimum | 2779 | 225 | 80 |
| | Intermediate | 2916 | 71 | 10 |
| | Maximum | 2948 | 340 | 3 |
| Saturated | Minimum | 3338 | 249 | 81 |
| | Intermediate | 3431 | 67 | 8 |
| | Maximum | 3461 | 338 | 3 |
| **vSa** | | **Average principal anisotropy axes** | | |
| | | Velocity (m/s) | Trend (degrees) | Plunge (degrees) |
| Dry | Minimum | 1849 | 242 | 81 |
| | Intermediate | 1954 | 63 | 7 |
| | Maximum | 1959 | 152 | 1 |
| Saturated | Minimum | 1751 | 241 | 75 |
| | Intermediate | 1849 | 63 | 9 |
| | Maximum | 1860 | 293 | 4 |
| **vSb** | | **Average principal anisotropy axes** | | |
| | | Velocity (m/s) | Trend (degrees) | Plunge (degrees) |
| Dry | Minimum | 1851 | 220 | 83 |
| | Intermediate | 1945 | 54 | 7 |
| | Maximum | 1959 | 322 | 7 |
| Saturated | Minimum | 1753 | 203 | 78 |
| | Intermediate | 1848 | 50 | 5 |
| | Maximum | 1859 | 140 | 8 |

*Table 6-4. Summary of the principal axes for P and S-wave velocity ellipsoids under dry and water saturated conditions.*

| | | Velocity (m/s) | | Ratios of velocity ellipsoid principal axes | | | | | |
|---|---|---|---|---|---|---|---|---|---|
| | | | | Foliation ($V_{int}$ / $V_{min}$) | | Lineation ($V_{max}$ / $V_{int}$) | | Anisotropy, % ($V_{max}$-$V_{min}$ / $V_{mean}$) | |
| | | average | st. dev. | average | st. dev. | average | st. dev. | average | st. dev. |
| Dry | vP | 2882 | 2.2 | 1.05 | 0.001 | 1.01 | 0.001 | 5.9 | 0.16 |
| | vSa | 1921 | 1.8 | 1.06 | 0.002 | 1.00 | 0.001 | 5.8 | 0.19 |
| | vSb | 1913 | 2.0 | 1.05 | 0.002 | 1.01 | 0.001 | 5.6 | 0.14 |
| Saturated | vP | 3409 | 2.9 | 1.03 | 0.001 | 1.01 | 0.001 | 3.6 | 0.16 |
| | vSa | 1820 | 3.2 | 1.06 | 0.002 | 1.01 | 0.002 | 6.0 | 0.28 |
| | vSb | 1820 | 2.5 | 1.05 | 0.002 | 1.01 | 0.001 | 5.8 | 0.21 |

*Table 6-5. Summary of anisotropy parameters from velocity ellipsoids*

## 6.3 Results of Hydrostatic Experiments

In light of the results discussed in sections 6.1 and 6.2, the z, y and x-axes of the general co-ordinate frame used in this study have been shown to be respectively co-incident with the minimum, intermediate and maximum principal directions of pore-fabric anisotropy. Therefore measurements of acoustic velocity and permeability taken along z, y and x-axis cores are used to determine the anisotropy of the sample material at increasing levels of hydrostatic pressure, with anisotropy quantified by the general relationship *(parameter max – parameter min) / parameter mean*. The hydrostatic vessel allows contemporaneous measurements of elastic wave velocity, permeability and porosity change. Experiments were performed on two individual samples cored in each principal direction at effective pressures in the range 5 – 250 MPa; results are presented for individual cores and also as averages for each orientation.

### 6.3.1 Elastic Wave Velocity

Data showing P and S-wave velocities at increasing hydrostatic pressure are shown in fig 6-8. For P-waves, velocities are greatest along the x axis and least along the z-axis. Velocity along the y-axis is closer to that along the x-axis than the z-axis. Velocities along all axes show an increase as a result of hydrostatic loading, with the greatest rate occurring during the over the first 30 MPa of applied pressure. During subsequent loading, velocities continue to increase at a relatively steady rate, which starts to decrease after around 150 MPa effective pressure. S-wave velocities show a similar trend to the P-wave velocities, with maximum velocity change occurring during the initial application of hydrostatic pressure. The minimum and maximum velocities converge slightly during the course of hydrostatic loading, the difference between them becoming less. However, after about 30 MPa, the intermediate velocity starts to diverge slightly from the maximum although remaining much more similar in magnitude to the maximum than the minimum. The plots of these data before averaging suggest that, with the possible exception of S-waves, at elevated pressure the trend Vx > Vy >

Vz can be observed between axes without being obscured by any influence of sample variability.

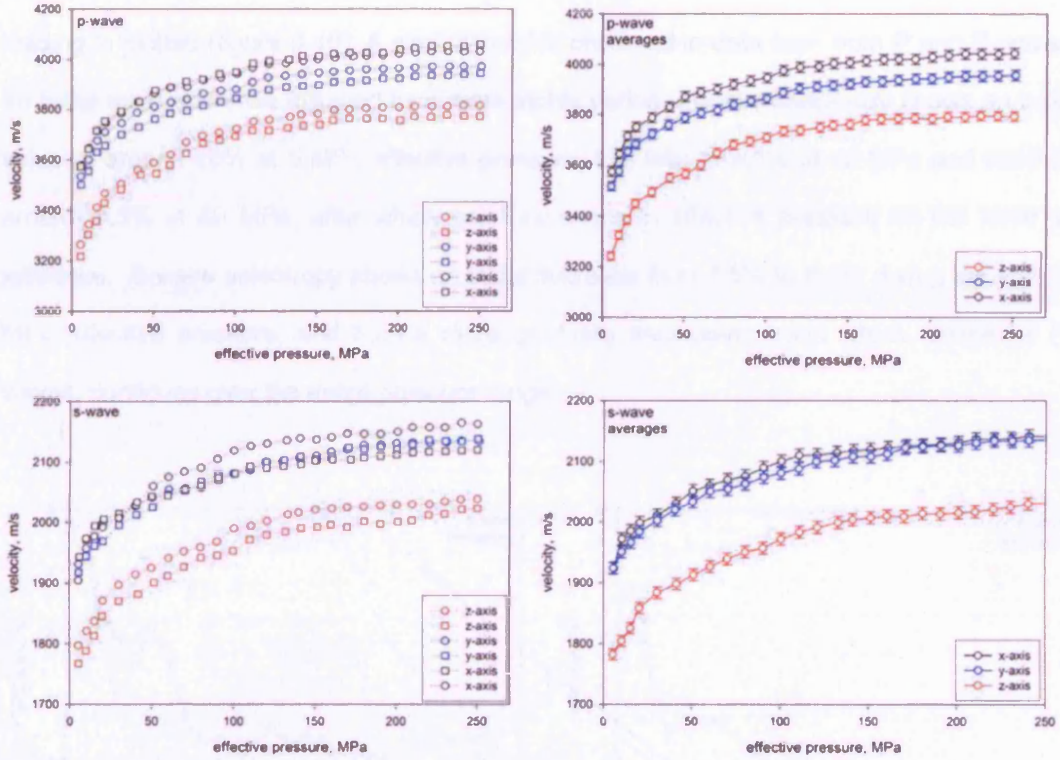


*Fig 6-8. Variation of P-wave (top) and S-wave (bottom) velocity along the x, y and z axes as a result of increasing hydrostatic pressure. Individual results are to the left (dotted lines), and averaged results with 5% error bars are to the right (solid lines). 10 MPa pore pressure was applied during these experiments.*

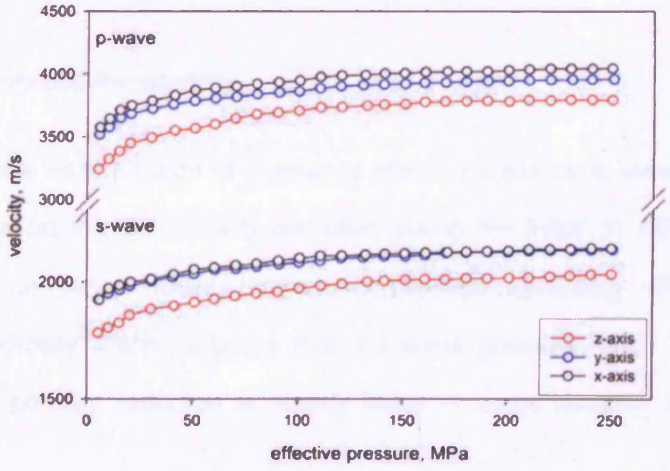


*Fig 6-9. Average P and S-wave velocities as a function of effective pressure along the z, y and x-axes.*

By taking the z-axis as the direction of minimum velocity and the x-axis as the direction of maximum velocity and applying the formula *max-min / mean x 100* to each data point over the hydrostatic pressure range, the change in elastic wave anisotropy during hydrostatic loading is plotted (figure 6-10). A similar trend is observed in data from both P and S-waves; an initial rapid decrease followed by a more stable period. P-wave anisotropy shows an initial value of around 10% at 5 MPa effective pressure, this falls to 7.5% at 40 MPa and reaches around 6.5% at 80 MPa, after which point increases in effective pressure do not have an influence. S-wave anisotropy shows an initial decrease from 7.5% to 6.5% during the first 30 MPa effective pressure, and then a more gradually decreasing trend which, unlike for P-waves, continues over the entire pressure range.

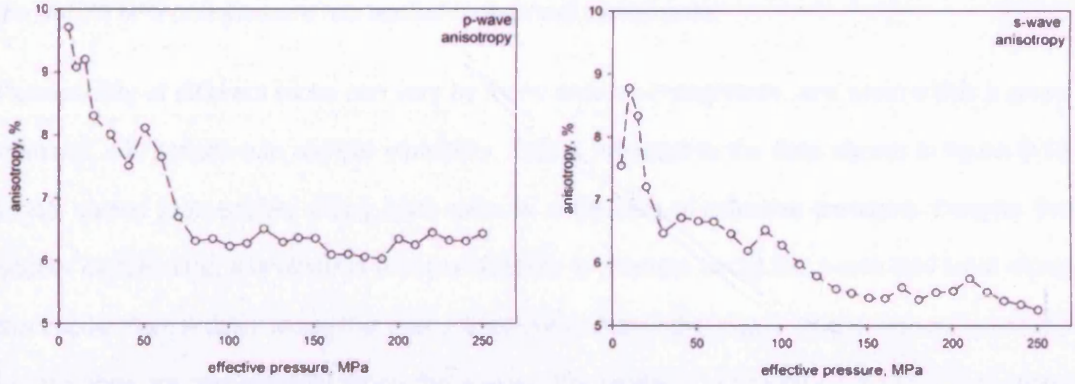


*Fig 6-10. Variation in elastic anisotropy as a function of hydrostatic pressure as expressed by P-wave velocity (left) and S-wave velocity (right).*

### 6.3.2 Porosity and Permeability

Porosity change as a function of increasing effective pressure is shown in figure 6-11. The data shows a rapid initial porosity reduction during the initial 30 MPa effective pressure, followed by an almost linear relationship between increasing effective pressure and decreasing porosity which continues over the entire pressure range. The normalised data suggest that porosity reduction is slightly lower in z-axis samples that for x and y-axis

samples. The averaged data shows a porosity reduction of 2.75 percentage points over the entire pressure range, corresponding to a relative decrease of about 11%.

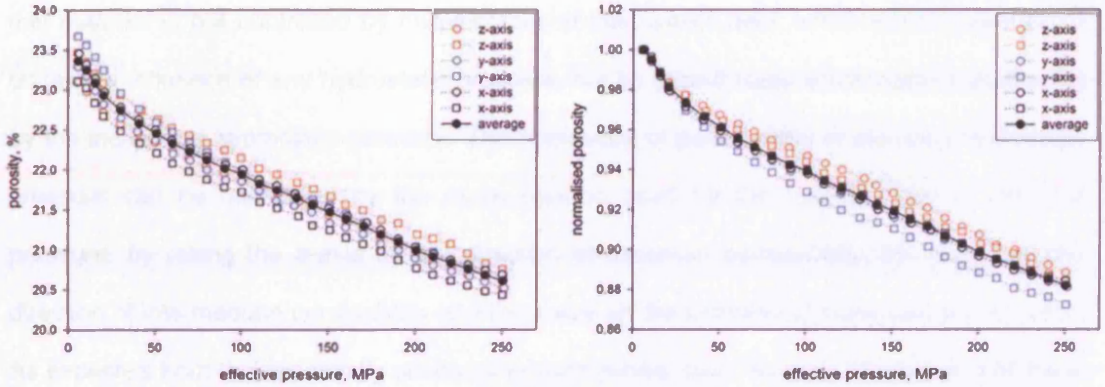


*Fig 6-11. Porosity change as a function of hydrostatic pressure (left) and normalised to the average sample porosity (right), the error associated with these measurements is within the symbol size used in the plot. 10 MPa pore pressure was applied during these experiments.*

Permeability of different rocks can vary by many orders of magnitude, and even within a given material, it is sensitive to sample variability. This is reflected in the data shown in figure 6-12 which shows permeability along each axis as a function of effective pressure. Despite the scatter on the data, it is obvious that permeability is greatest along the x-axis and least along the z-axis. Permeability along the y-axis is similar to that of the x-axis, and is also substantially greater than the permeability along the z-axis. Permeability is typically 1.4 x10 $^{-12}$ m$^2$ along the x-axis, 1.3x10$^{-12}$ m$^2$ along the y-axis and 0.9 x10$^{-12}$ m$^2$ along the z-axis.

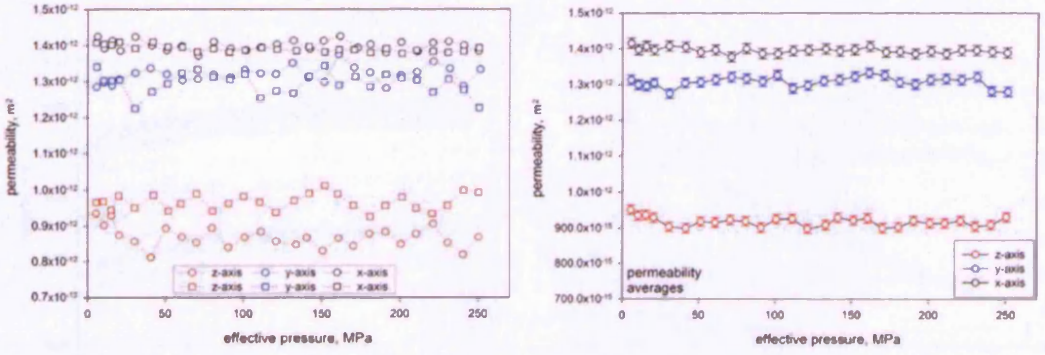


*Fig 6-12. Permeability change along the x, y and z axes as a function of increasing hydrostatic pressure. Averaged data with 10% error bars are shown to the right. 10 MPa pore pressure was applied during these experiments.*

The data show that permeability does not vary significantly as a function of hydrostatic pressure within the range considered, but remains essentially constant despite the continuously decreasing sample porosity. This suggests that the connectivity of pore-space in this material is not controlled by micro-cracks of low aspect ratio, which would easily close under the influence of any hydrostatic pressure, but by pore-throats which remain unaffected by the increasing hydrostatic pressure. The anisotropy of permeability at elevated hydrostatic pressure can be calculated by the same method used for the velocity data at elevated pressure, by taking the z-axis as the direction of minimum permeability, the y-axis as the direction of intermediate permeability and the x-axis as the direction of maximum permeability. As expected from the essentially unchanging permeability data, figure 6-13 reveals that there is no appreciable change in permeability anisotropy under increasing hydrostatic pressure.

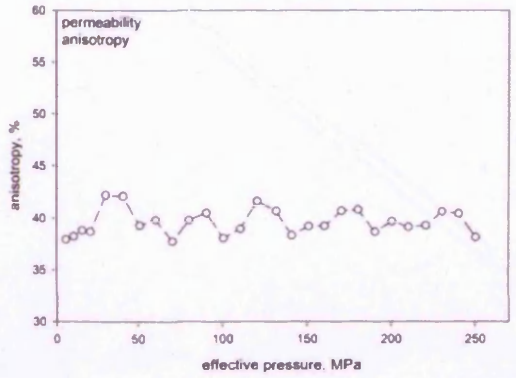


*Fig 6-13. Variation in anisotropy of permeability as a function of increasing hydrostatic pressure.*

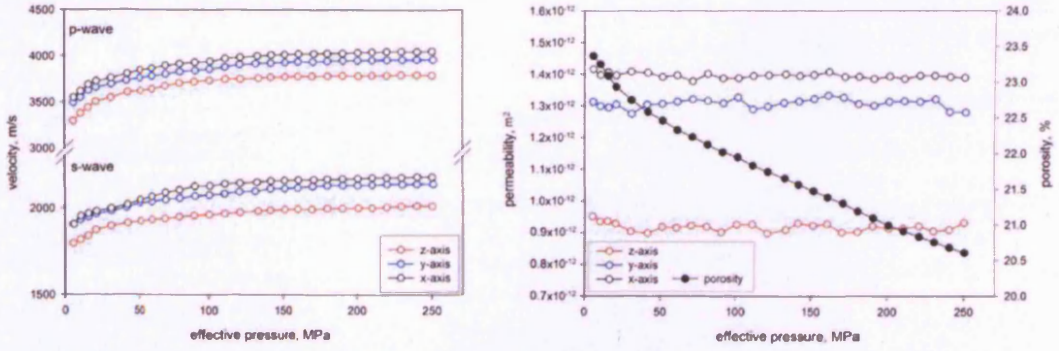


*Fig 6-14. Summary plots showing all the averaged data of P and S-wave velocity variation (left) and porosity and permeability variation (right) with increasing hydrostatic pressure.*

The hydrostatic results are consistent with the ambient pressure results, showing that the velocities along the y and x-axes are greater than the velocities along the z-axis. Permeability is also greater along the y and x-axes, than along the z-axis. Acoustic velocity data show that the anisotropy of Diemelstadt sandstone decreases during the application of hydrostatic pressure, although never to below 5%. This shows that the anisotropy of the material is not removed by relatively high effective pressures, and that the existence of anisotropy remains a valid assumption for when the material is tested triaxially under elevated pressure conditions. The hydrostatic pressure range used for these experiments resulted in elastic behaviour, and was not sufficient to induce grain crushing (P*), which occurs at a hydrostatic pressure greater than can be achieved by the hydrostatic pressure vessel used in this study.

# 7 Methods and Equipment for Triaxial Experiments

Three suites of triaxial experiments were performed to examine aspects of compaction band development as a function of anisotropy in Diemelstadt sandstone. As discussed in chapter 4, it is known that compaction bands develop in a plane normal to the direction of $\sigma_1$. Results presented in chapter 6 show that Diemelstadt sandstone is essentially transversely isotropic about the z-axis, with the maximum and intermediate principal directions of anisotropy approximately equal to one another. Therefore, comparative experiments were carried out on samples cored along the z and x-axes, coinciding with the minimum and maximum principal directions of anisotropy, in order to investigate the influence anisotropy may have on the development of compaction bands. The alignment of principal stresses in the triaxial configuration, with respect to the anisotropy of the experimental material, is shown schematically in figure 7-1.

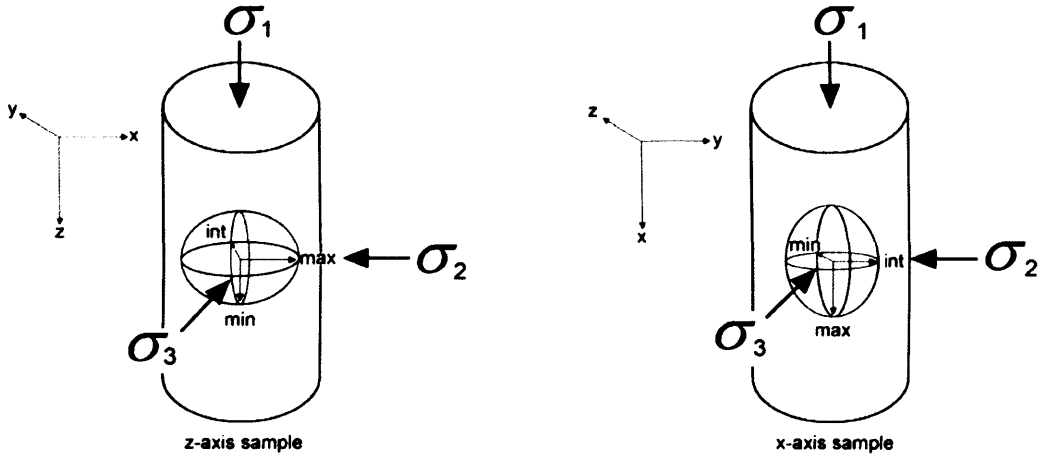


*Fig 7-1. The sample orientations used in the triaxial experiments of this study. Left, a z-axis sample with $\sigma_1$ normal to the material's plane of isotropy, Right, an x-axis sample with $\sigma_1$ parallel to the material's plane of isotropy. $\sigma_1 > \sigma_2 = \sigma_3$, and according to results presented in chapter 6 principal directions of anisotropy max > int ~ min.*

Firstly, axial deformation experiments were performed across a range of effective confining pressures to establish the yield envelope of the material in PQ space (as defined in chapter 4), and to discern the stress conditions necessary to induce compaction bands. This was followed by experiments, at appropriate effective pressures, to measure the change in bulk permeability of the sandstone at axial strain increments during the formation of compaction bands. Finally, experiments were performed using acoustic emission locations to track the spatio-temporal evolution of compaction bands.

This chapter discusses the apparatus and techniques used to conduct these experiments. As mentioned in chapter 5, experiments at elevated pressure require sophisticated equipment, even more so when pressure conditions are non-hydrostatic. Therefore, this chapter also provides details on design aspects which make experiments of this nature possible. The calibration of all pressure and displacement transducers is discussed, along with the sources of potential experimental error.

## 7.1 Equipment Overview

The apparatus is shown schematically in figures 7-2 and 7-3, and is able to simulate crustal stress conditions found down to about 15 km depth. Based on a design by Sammonds et al. (1991), and known through convention as a triaxial configuration, it is possible to generate axial stresses of up to 1.2 GPa and confining pressures ($\sigma_2 = \sigma_3$) of up to 400 MPa. The triaxial cell incorporates a pressure-balanced ram system, which allows the initial application of hydrostatic pressure to all surfaces of the sample under test before the application of a differential stress by the loading ram. Pore pressure is applied by coupling the hydrostatic pressure vessel's intensifier system with the triaxial deformation cell to provide independent control of pore-pressure at both ends of the sample under test, allowing measurements of permeability during triaxial deformation experiments, as described later in section 7.2.

The apparatus can be operated in either load control or extension control, which acts to maintain a constant axial stress or a constant axial strain rate respectively. It is also possible to lock the actuator in place at any time during an experiment, essentially pausing the applied deformation process. These various modes are achieved by using electronic feedback signals from linear variable differential transducers (LVDTs) to control the rate of advance of the actuator. Samples under test in this apparatus are jacketed with a nitrile sleeve, specially designed to accommodate up to 12 piezoelectric crystals which were used, in this study, to record acoustic emission activity.

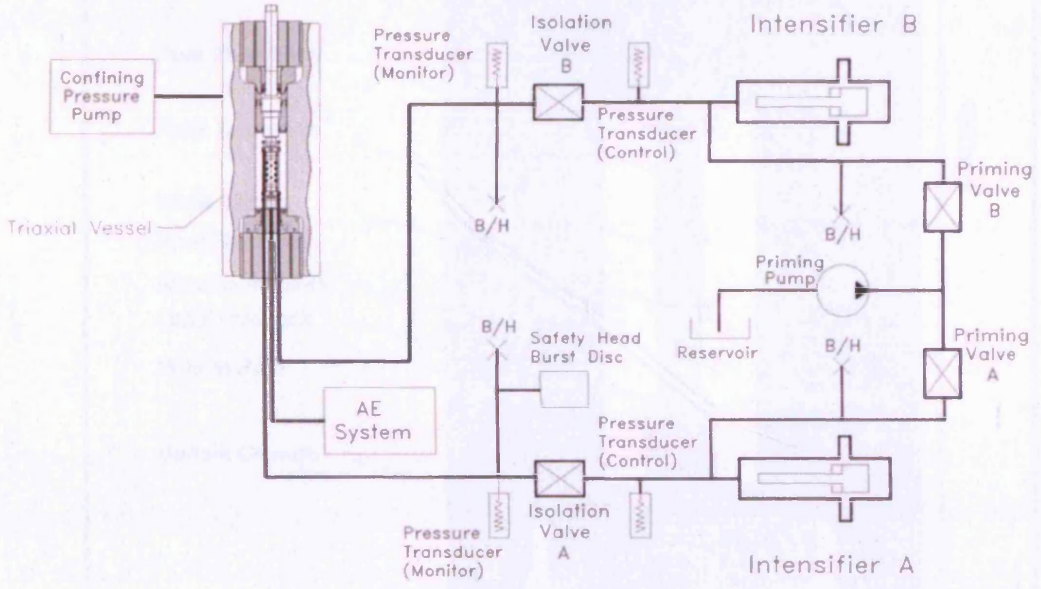


*Fig 7-2. Schematic representation of the triaxial set-up coupled with the hydrostatic vessel's dual intensifier system, and an acoustic emission (AE) facility.*

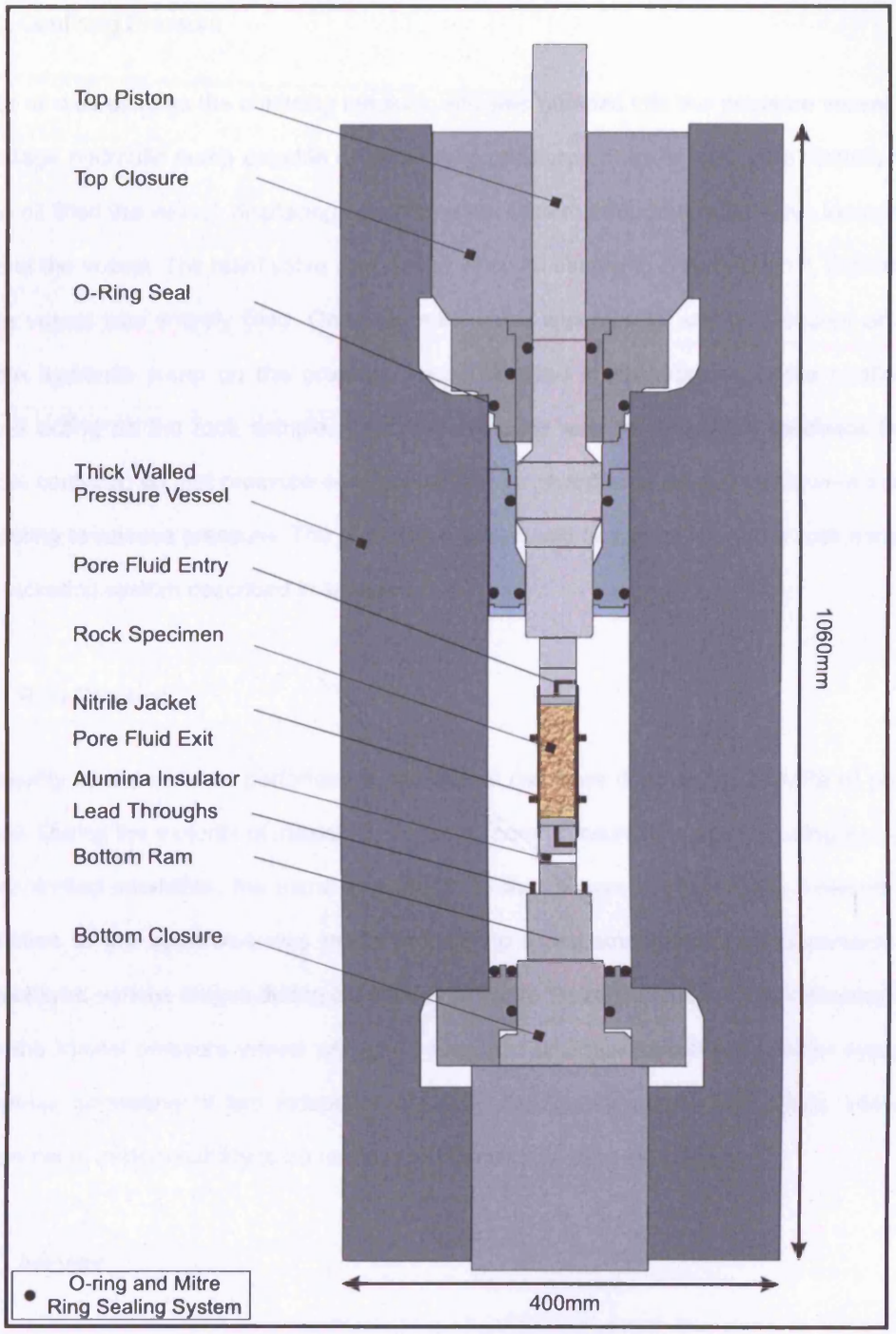


*Fig 7-3. Schematic diagram showing detail of the triaxial deformation cell. The vessel seals through an extensive o-ring and mitre ring system (illustrated). Displacement readings are compensated for machine distortion to give a true measurement of sample strain.*

### 7.1.1 Confining Pressure

Silicone oil was used as the confining medium, and was pumped into the pressure vessel via a two-stage hydraulic pump capable of generating pressures of up to 400 MPa. Initially the silicone oil filled the vessel, displacing all air from the system through a relief valve located at the top of the vessel. The relief valve was closed when oil started to flow through it, indicating that the vessel was entirely filled. Once the relief valve was closed, any subsequent action from the hydraulic pump on the pressure vessel resulted in an increase in the confining pressure acting on the rock sample. Confining pressure was controlled via feedback from electrical contacts, so that pressure conditions could be maintained even if there were some leaks acting to release pressure. The confining medium was separated from the rock sample by the jacketing system described in section 7.2.2.

### 7.1.2 Pore Pressure

The majority of experiments performed in the triaxial cell were done using 20 MPa of pore-pressure. During the majority of triaxial experiments, pore pressure was applied using a single servo-controlled intensifier, the same in principle to that shown in figure 5-10. However, a modification to the apparatus was made in order to make steady-state measurements of permeability at various stages during triaxial deformation. To achieve this, it was necessary to couple the triaxial pressure vessel with the hydrostatic pressure vessel's intensifier system. This set-up, consisting of two independently controlled pore-pressure intensifiers, allowed measurements of permeability to be made using the steady-state method.

### 7.1.3 Actuator

The actuator controls the piston of the ram which applies the axial stress to the sample within the pressure vessel. Using a ramp generator, the actuator can be set to advance the position of the ram at a constant rate, thereby applying a constant axial strain rate to the rock sample; or it can be set to maintain a constant load, thereby applying a constant axial stress to the

rock sample. Control is achieved by the continual referencing of electronic feedback from two LVDTs, which are in contact with the ram, to a programmed signal. The experiments performed in this study were under extension control, that is to say they were performed at conditions of constant axial strain rate ($10^{-5}$ $s^{-1}$).

## 7.2 Measurements Under Triaxial Stress

The majority of experiments performed during this study were under triaxial stress conditions. Tests were performed at a range of effective pressures in order to traverse the brittle / ductile transition, and the applied axial strain rate was consistently $10^{-5}$ $s^{-1}$. This strain rate, although many orders of magnitude greater than those of natural systems, allows experiments to be performed over the course of one day, and therefore makes it feasible for the operator to interact with the experiment as and when required (for example, in making measurements of permeability).

### 7.2.1 Sample Preparation

Cylindrical samples of 40 mm diameter were cored using a diamond sintered coring drill. These cores were then ground to a length of 100 mm using a diamond impregnated grinding wheel, the ends of each sample were prepared to be flat and parallel to one another to within 0.01 mm. The connected porosity of each sample was measured using a gravimetric technique.

### 7.2.2 Sample Jacketing and Insert Modifications

Once saturated, samples were placed in the centre of the rubber jacket (shown in figure 7-3) so that the locations of all the transducer crystals with respect to the jacketed sample were known. Pore fluid spreader caps, similar to the one shown in figure 5-11, were placed on the top and bottom surfaces of the rock sample along with compression rings designed to provide

an initial seal as the jacketed sample is placed over the bottom ram prior to the start of an experiment.

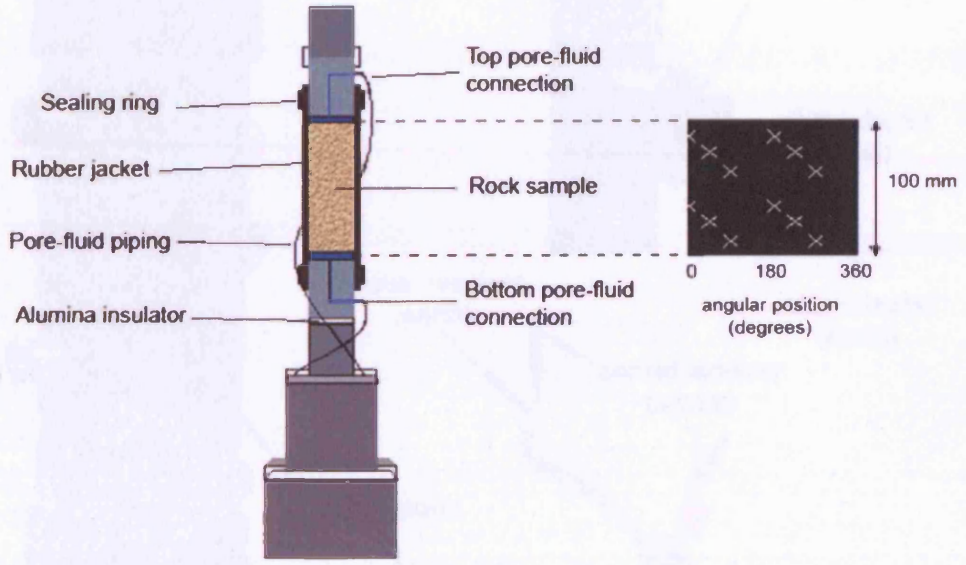


*Fig 7-4. Triaxial sample assembly (left) and map-view of sample jacket with PZT transducer locations (right). Although there are 12 potential transducer locations, the Vallen AE System has only 10 channels and therefore can receive data from only 10 PZT transducers.*

12 ports located around the sample jacket are designed to house steel inserts which contact the rock sample at one end, and to which piezoelectric transducers may be attached at the other end. The steel inserts act as wave-guides allowing acoustic emissions, related to mechanical processes occurring within rock sample, to be transmitted to the transducers and then digitised and recorded. To produce as high a signal-to-noise ratio as possible, the steel inserts have a concave surface which conforms to the curvature of a 40 mm diameter rock specimen, allowing the greatest possible contact area.

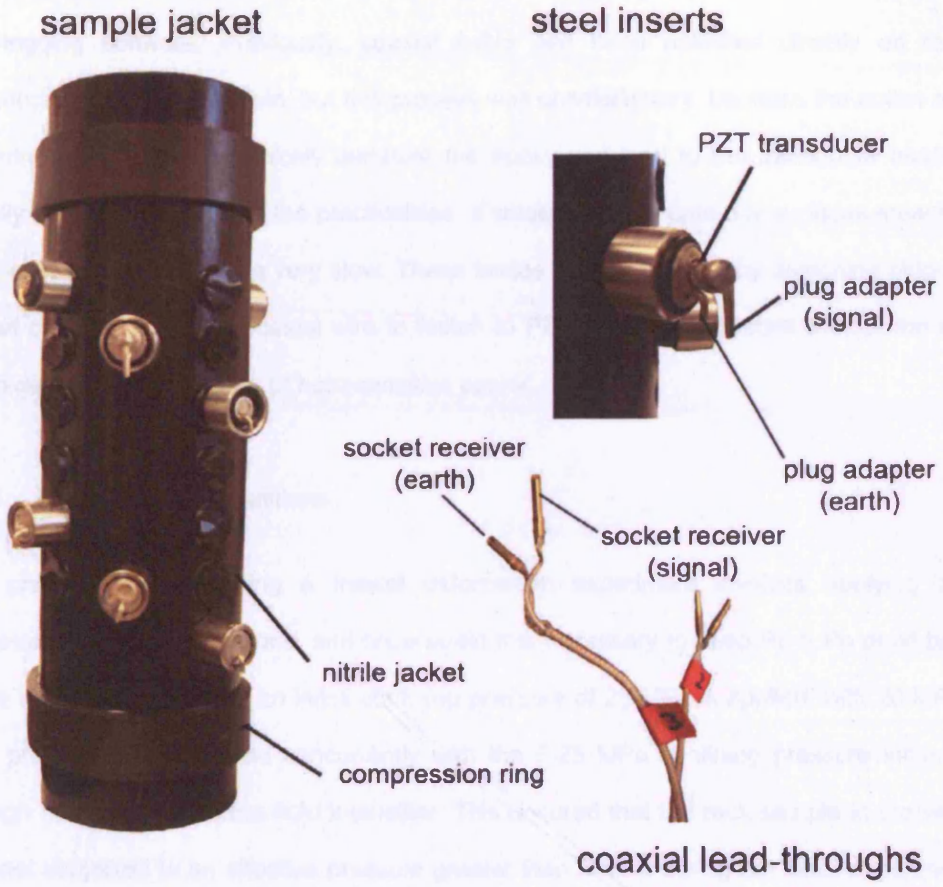


*Fig 7-5. The Nitrile jacketing system used during triaxial deformation experiments (left) and the modified PZT transducer mounts and lead-through connectors used to acquire data (right).*

Cylindrical piezoelectric PZT-5B crystals 3mm in diameter and of 1 MHz central frequency, with gold lapping on their flat surfaces were mounted onto the steel inserts using a silver-loaded epoxy to allow the transmission of an electrical signal. These steel inserts with mounted PTZ crystals were then placed in the specially designed jacket ports with a stainless steel cuff placed around the port to provide an initial compression seal prior to the application of hydrostatic pressure. Subsequent hydrostatic (confining) pressure ensured that the seal between the jacket and the insert was maintained during experiments.

A new design was implemented in transmitting data from the piezoelectric transducers to the data-logging software. Previously, coaxial cable had been soldered directly on to the transducer and to an earth pin, but this process was unsatisfactory because the action of the soldering iron would very quickly denature the epoxy and lead to the transducer assembly literally falling apart. Further, the practicalities of soldering wires onto oily surfaces meant that the experimental set-up was very slow. These issues were overcome by designing plug-and-socket connectors for the coaxial wire to fasten to PZT transducer crystals without the need for soldering in the presence of heat-sensitive epoxy.

### 7.2.3 Initial Pressure Conditions

The protocol for performing a triaxial deformation experiment involves applying initial hydrostatic pressure conditions, and once again it is necessary to keep Pc > Pp at all times. In the triaxial configuration, an initial confining pressure of 25 MPa is applied, with 20 MPa of pore pressure being applied concurrently with the 5-25 MPa confining pressure increment through use of a single pore-fluid intensifier. This ensured that the rock sample in the vessel was not subjected to an effective pressure greater than 5 MPa during the initial experimental set-up.

Triaxial experiments were performed at a range of effective pressures, and once the initial hydrostatic conditions (Pc = 25 MPa, Pp = 20 MPa) had been established, the confining pressure within the vessel was increased incrementally until the desired effective pressure for any particular experiment was reached. During this period of incrementally increasing effective pressure, the displacement transducer of the pore-fluid intensifier was used to record the pore volume change of the sample as it was hydrostatically loaded. Once the correct effective pressure was reached, the vessel was left for about an hour while the system equilibrated.

### 7.2.4 Axial Stress and Strain

Once the system had equilibrated under its hydrostatic starting conditions, a triaxial experiment was ready to start and a differential stress was superimposed over the hydrostatically held sample. The servo-controlled actuator was used to apply a compressive force to the sample end, the absolute value of which was measured using an external load cell. Load was converted to axial stress by considering the area of the sample over which the load is applied. A hemispherical seat is placed between the loading actuator and the upper ram assembly to correct for any slight misalignment of the loading train components. The rate of the actuator's advance was pre-programmed, and determined the axial strain rate applied to the rock sample. Displacement of the actuator was recorded using the averaged output of a pair of LVDTs situated between the pressure vessel and the top crosshead.

### 7.2.5 Pore Volumometry

The intensifier system used to apply pore-pressure is capable of generating a maximum of 70 MPa, and the integral LVDTs fitted in the intensifiers allow pore-volume changes to be monitored during an experiment. In the hydrostatic set-up, pore volume change is measured as a response to a discrete increase in the hydrostatic confining pressure. During the application of a differential stress, pore-volume change is measured as an evolving property driven by the action of the advancing ram. The action of a differential stress may cause the rock sample's pore volume to increase (dilation) or decrease (compaction). By expressing the pore-fluid intensifier's displacement as a percentage of the volume of the rock sample under test, a measure of the sample's porosity change in percentage points can be made.

### 7.2.6 Permeability

Permeability measurements during triaxial deformation experiments were made at increments of 0.25% axial strain. The principle of steady-state flow was adopted, although there are

additional complications when making these measurement at various states of triaxial deformation.

In order to measure permeability at discrete intervals during triaxial deformation, it was necessary to stop the advancing ram so that any intensifier displacement could be attributed to the applied pore-pressure differential across the sample and not to the action of the advancing ram deforming the sample and forcing pore-fluid from it. Once the advancing ram had been stopped, the system was allowed to equilibrate before the pore-fluid intensifiers were set to have a 0.5 MPa pressure differential. After the respective pressures had been set, the previously isolated downstream pore-fluid intensifier was connected and the resulting fluid flow measured as a function of time. Once steady state flow had been established, the downstream intensifier was isolated, stopping flow, and the ram was re-started and the sample allowed to deform by a further 0.25% axial strain before a subsequent permeability measurement was made. This process is summarised in figure 7-6.

During triaxial deformation, the axial length of a sample changes directly as a result of axial strain. It was therefore necessary to correct the sample's length by an amount equal to the cumulative axial displacement at the point of the permeability measurement. These data are readily available from the LVDTs used to regulate axial strain. A correction was also applied to adjust for sample shortening resulting from the application of initial hydrostatic pressure conditions.

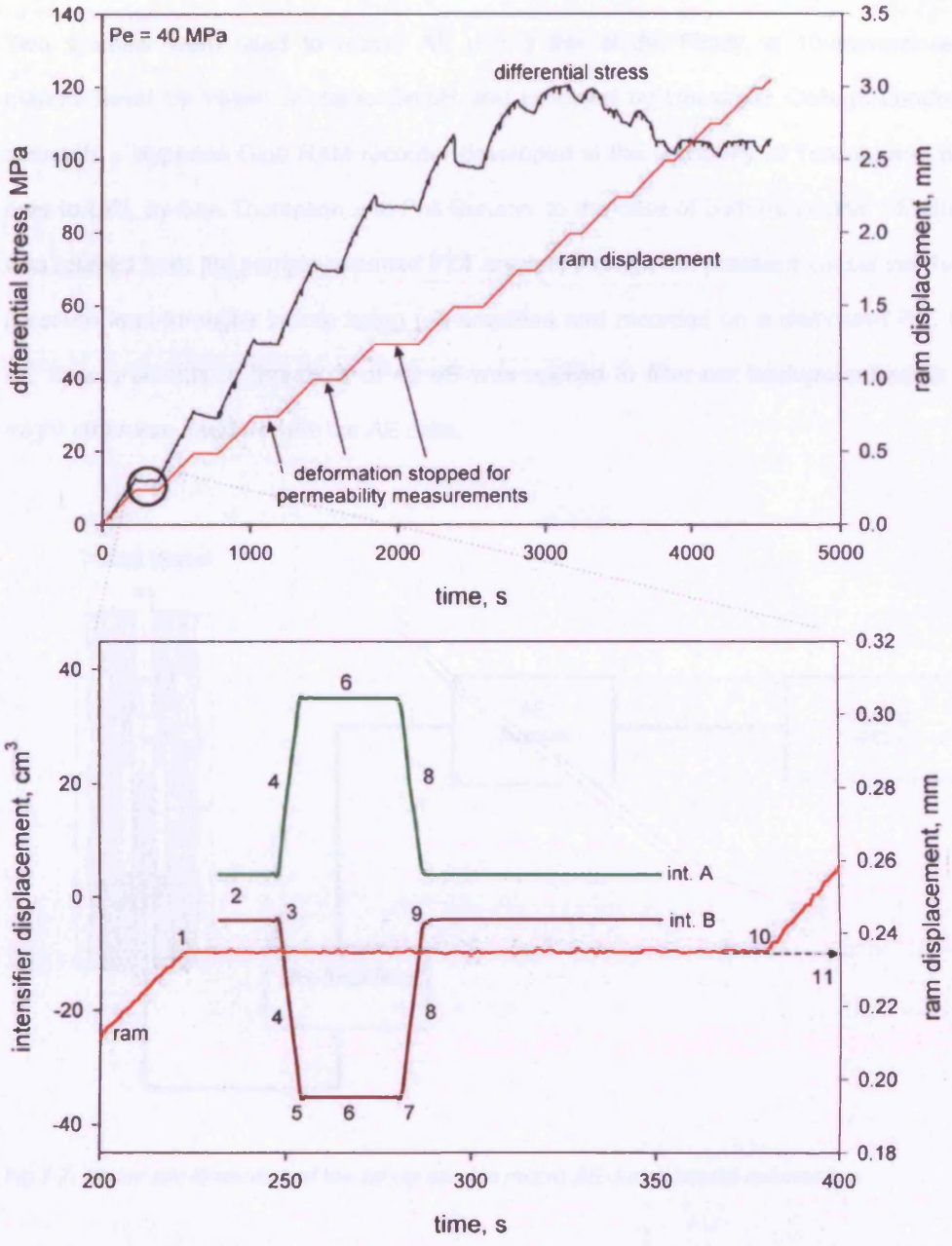


*Fig 7-6. Technique of permeability measurement (lower) during the course of a triaxial deformation experiment (upper) of Diemelstadt sandstone at 40 MPa effective pressure. 1) Deformation halted 2) Pressure differential set 3) Downstream isolation value opened 4) Steady state flow established 5) Downstream isolation valve closed 6) Pressure differential reversed 7) Downstream isolation value opened 8) Steady state flow established 9) Downstream isolation valve closed 10) Deformation re-started 11) Sample length correction recorded.*

## 7.3 Acoustic Emission Logging

Two systems were used to record AE during this study. Firstly, a 10-channel recorder manufactured by Vallen Systeme GmbH and procured by University College London, and secondly a Hyperion Giga RAM recorder developed at the university of Toronto and brought over to UCL by Ben Thompson and Phil Benson. In the case of both respective AE kits, data was relayed from the sample-mounted PZT crystals through the pressure vessel via the high-pressure lead-throughs before being pre-amplified and recorded on a dedicated PC. During AE measurements, a threshold of 40 dB was applied to filter out background noise which might otherwise interfere with the AE data.

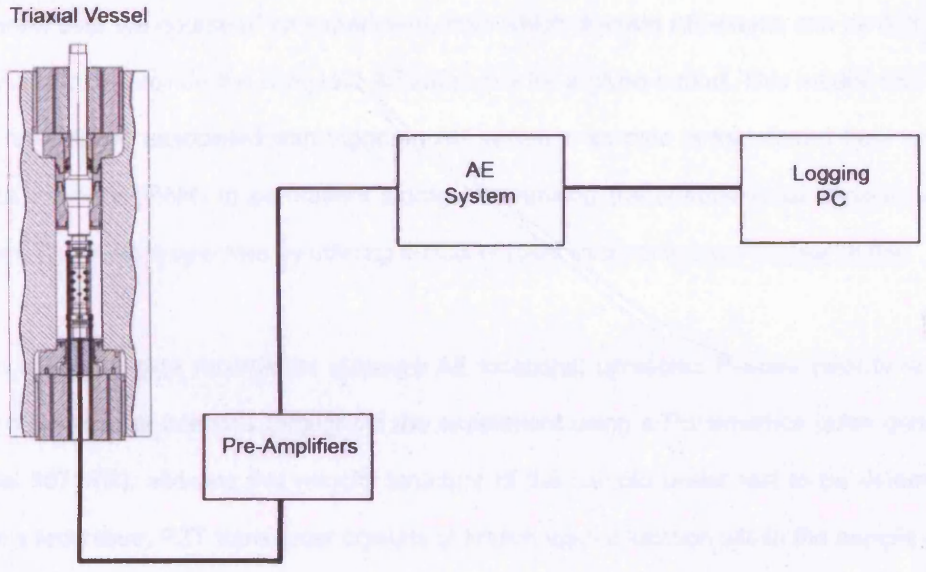


*Fig 7-7. Schematic illustration of the set-up used to record AE during triaxial deformation*

### 7.3.1 Vallen Systeme

A Vallen AMSY4 Acoustic Emission System was used to record AE events through a maximum of 10 channels during triaxial deformation. The AE signal was amplified by 40 dB gain by Vallen AEP3 pre-amps before being recorded to disk. This system has 8 parametric channels which were utilised to record mechanical data, pore-fluid pressure and pore-fluid volumometry onto the same data file as the AE output.

### 7.3.2 Hyperion Giga RAM recorder for AE locations

The 'Giga' recorder was used to measure all AE locations, and has the advantage over conventional AE recording systems in that it is able to record a continuous ultrasonic waveform over the course of an experiment, from which discrete AE events can be extracted, or harvested, to provide the complete AE catalogue for a given period. This means that there is no 'downtime', associated with triggered AE systems, as data is transferred from random access memory (RAM) to permanent storage; increasing the observational capacity of the system. The system operates by utilising 40 GB of RAM as a continuous circular buffer.

When using the giga recorder to measure AE locations, ultrasonic P-wave velocity surveys were conducted at intervals throughout the experiment using a Panametrics pulse generator (model 5072PR), allowing the velocity structure of the sample under test to be determined. For this technique, PZT transducer crystals of known spatial location within the sample jacket were used as sources and receivers, and ultrasonic travel times measured along known ray-paths. A 3D velocity structure, produced through inversion of these travel times, was used to calculate velocity anisotropy to inform the AE location algorithm. First arrivals were picked using an automated routine, and a Simplex algorithm was used for source locations. Typically, around 30,000 AE events were located during each test. However, to ensure accuracy, these located events were filtered so that only those recorded independently on at least 6

transducers and with a location error of less than 2 mm were considered. This resulted in about 10,000 'high quality' AE locations being recorded over the duration of each test.

Although the Giga recorder is a 16 channel system, the number of AE channels available to use during any given experiment was limited to a maximum of 12 by the design of the sample jacketing system. During experiments, each AE channel was connected to a Physical Acoustic Corp. (PAC) pre-amplifier where 40 dB of gain was applied to the signal in order to optimise the signal-to-noise ratio. Software developed by Applied Seismology Consultants (InSite, ASC) was used to visualise waveforms and pick first arrivals. For a full description of the Giga RAM recorder, and of the techniques used to harvest discrete AE events and to determine hypocentre locations, see Thompson (2006).

A Matlab routine (Smith, 2007) based on the maximum likelihood method of Aki (1965) was used to return a $b$-value from the Gutenberg-Richter relationship:

$$\log N(M) = a - bM$$

Where $N$ is the number of AE events of magnitude $M$ or greater, and $a$ and $b$ are constants for the given data-set. By considering the frequency-magnitude relationships of AE events occurring within a rolling window of 200 seconds, the change in $b$-value was measured over the course of the experiment.

## 7.4 Calibrations and Errors

### 7.4.1 Transducer Calibrations and Errors

It is necessary to accurately calibrate a range of displacement and pressure transducers in order to reduce the uncertainty in measurements of pore-volume change, pore-pressure, confining pressure, axial strain and axial load. The calibrations relate a known input (e.g.

pressure, displacement) to a transducer output in volts. Once the calibration relationships are known, then their descriptions are entered directly into the logging software. The plots of the calibrations are shown in figure 7-8.

Pressure transducer calibrations are performed using a Budenberg 'dead-weight' system, whereby accurately known weights are balanced on a hydraulic piston which provides a known and precise pressure to any given pressure transducer to which the system is attached. This process allows transducer output to be measured as a function of applied pressure and, by repeating the measurements at a range of input pressures, it is possible to determine a linear regression of the input/output relationship of the transducers. This procedure was used to calibrate the confining pressure transducer, and the pressure transducers used in the pore-fluid intensifiers.

LVDTs which measure ram displacement, and therefore axial strain, are calibrated using a micrometer head, whereby a precise displacement is applied to an LVDT and the output voltage resulting from that displacement is recorded. Using this technique, the relationship between applied displacement and voltage output can be determined for each of the two LVDTs, with the average of both being used as the control signal.

In order to calibrate the pore-fluid intensifiers as volumometers, it was necessary to measure the volume of fluid displaced by each intensifier over its entire range along with the commensurate change in output voltage from the integral LVDTs. Doing this reveals a relationship of 0.22 $V/cm^3$ and 0.25 $V/cm^3$ for intensifiers A and B respectively.

The load cell within the triaxial pressure vessel is calibrated using a proving ring. Using this method, the servo-controlled actuator applies a load to the proving ring, which deforms to a specific extent for a given load. The load cell's output voltage as a function of a known load is

therefore measurable, and the process is repeated to achieve a linear regression from which axial stress may be calculated.

The absolute accuracy of transducers and other measurement systems are summarised below.

| *Variable* | *Absolute Uncertainty, +/-* |
|---|---|
| Confining Pressure | 0.01 MPa |
| Pore Pressure | 0.005 MPa |
| LVDT Displacement | 0.001 mm |
| Sample Dimensions | 0.01 mm |
| Sample Mass | 0.005 g |

*Table 7-1. Some physical variables and their uncertainties*

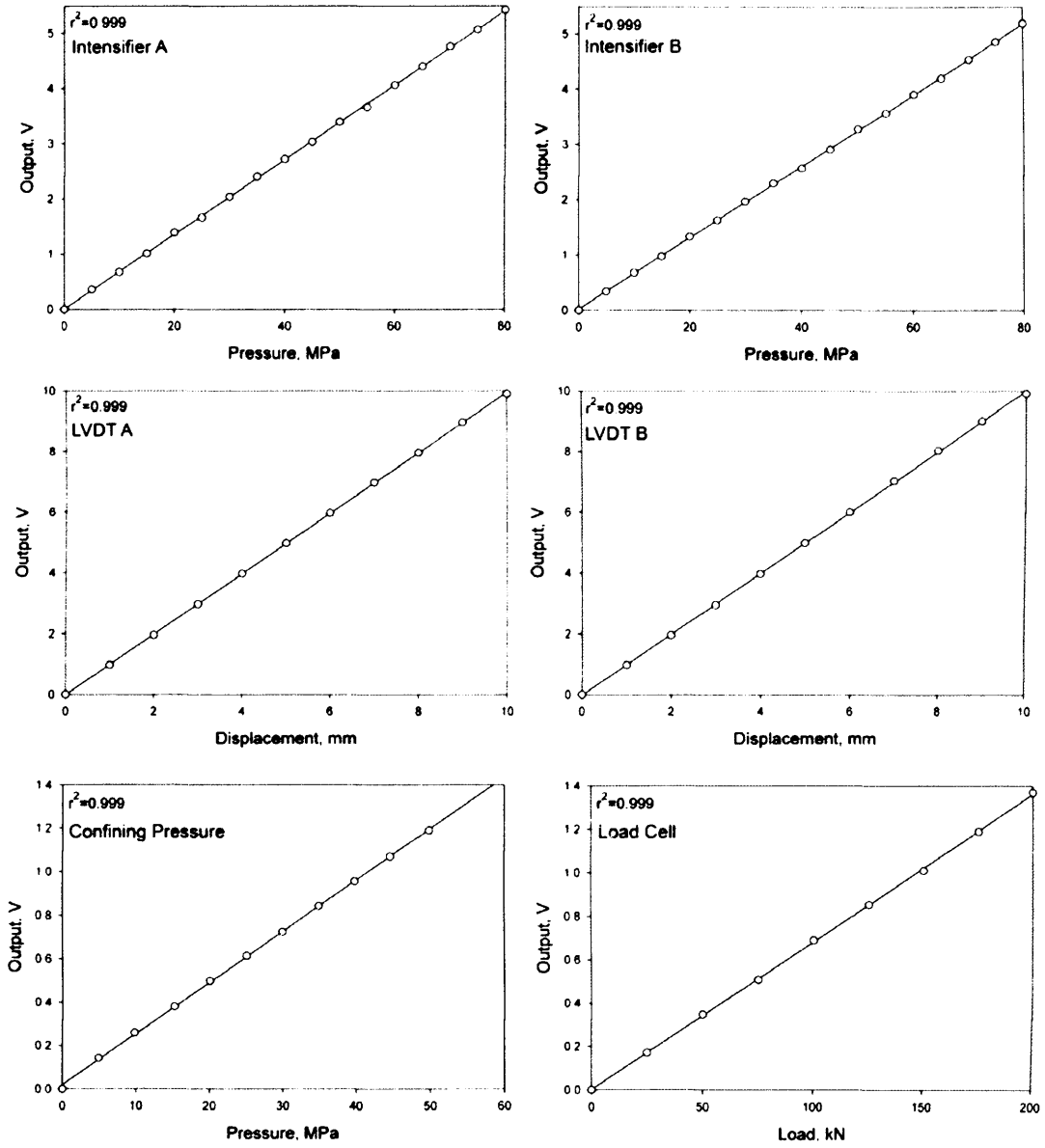


*Fig 7-8. Calibration plots of all transducer systems used in this study. From top: the Intensifiers A and B which provide the pore-pressure to samples in both the hydrostatic and triaxial vessels; the LVDTs A and B which record ram extension and, through a control-loop, regulate strain rate; the Confining Pressure transducer which records the pressure within the hydrostatic and triaxial vessels; the Load Cell, which records the axial load applied to a sample, which is then converted to axial stress. The coefficient of determination ($r^2$) is shown for each regression.*

### 7.4.2 Sample Length Correction

During an experiment, a sample will react to any applied pressure conditions by shortening. This effect has implications for calculations based sample dimensions, for example, elastic velocities, which are calculated based on the elastic wave's travel time over a known distance. The hydrostatic cell is unable to quantify the degree of such shortening, however the triaxial cell is also able to operate in hydrostatic mode and, through the use of its displacement transducers, provide the necessary data on sample shortening. To determine sample shortening, 100 mm sample lengths were prepared for the triaxial cell, which were then hydrostatically loaded to 250 MPa with the resulting shortening measured by two independent LVDTs. Shortening was then normalised to the sample's original length, allowing the calculation of a co-efficient ($-6.99 \times 10^{-5}$) which describes the sample shortening per MPa of effective pressure per mm of sample. Length corrections were then applied to all calculations of elastic wave velocity and permeability. The data from the shortening calibration is shown in figure 7-9. Although the shortening trend deviates very subtly from being a straight line, the amount of error accumulated by applying a straight line fit is very small and most likely within the noise of other measurements and sample variability.

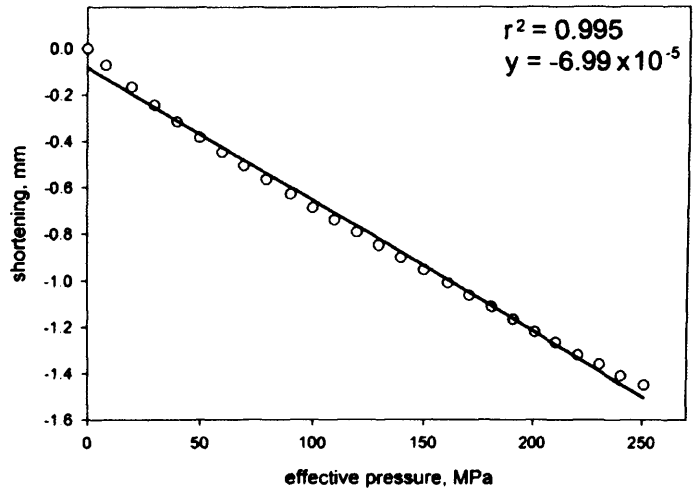


*Fig. 7-9. Shortening associated with loading over the hydrostatic effective pressure range 0-250 MPa*

Assuming isotropy, the bulk modulus of the material can be estimated as being about $1.6x10^4$ MPa, a value an order of magnitude larger than that of the Young's modulus as extracted from triaxial stress-strain data (reported on p.161). This difference may be the result of a slight misalignment of the pressure vessel's loading train, leading to the estimated bulk modulus also reflecting a spurious component of machine distortion. It is likely that the reported Young's modulus is accurate, since it is later seen to be consistent over a number of experiments.

### 7.4.3 Porosity Change Correction

Measurements of pore-volume change rely on the displacement measured by the intensifier controlling pore-pressure. Since, when establishing initial pressure conditions, an initial confining pressure of 5 MPa is applied before the application of any pore-pressure (to maintain Pc >Pp), there can be no measurement of pore-volume change during the initial 0-5 MPa effective pressure increment. This problem is addressed by initially assuming the sample porosity at 5 MPa to be equal to the gravimetrically measured porosity at ambient conditions. Porosity change is then plotted as a function of effective pressure, with curve fitting software used to extrapolate the trend back to 0 MPa effective pressure. The mismatch between the extrapolated porosity at 0 MPa and the measured porosity at 0 MPa is then evaluated and an offset applied to the porosity change data-set.

# 8 Results of Triaxial Experiments

This chapter presents the results of triaxial experiments to show the delineation of the yield envelope of Diemelstadt sandstone in PQ space, and to show the bulk permeability evolution of samples during compaction banding. Firstly, the behaviour of Diemelstadt sandstone during triaxial deformation under a range of effective confining pressures is presented. These data show that generally, for an axial strain rate of $10^{-5}$ $s^{-1}$, Diemelstadt sandstone undergoes shear-enhanced compaction when Pe > 40 MPa, and develops discrete compaction bands when Pe > 100 MPa. Data showing the evolution of bulk permeability during triaxial deformation is then presented; the experimental conditions being such that both the effects of shear-enhanced compaction leading to macroscopic faulting and shear-enhanced compaction leading to compaction banding are evidenced. Microstructural data showing the condition of Diemelstadt at stages of increasing deformation within the compaction band regime are also presented. The graphed data are presented in complementary pairs; with each experiment performed on a z-axis sample having an 'opposite number' for the x-axis, allowing a side-by-side comparison without the clutter of multiple curves on the same axes. The results of triaxial experiments showing AE locations are presented separately in chapter 9.

## 8.1 Mechanical Data

As discussed in chapter 4, previous workers have expressed inelastic behaviour of porous sandstones through the use of failure envelopes in PQ space. Since the mechanical behaviour of materials depends on constitutive relationships, the extent of a failure envelope in stress space is unique for any given rock. Therefore, experiments were necessary to establish the yield-cap of the material used in this study.

Data was obtained by deforming complementary z and x-axis samples at a constant axial-strain rate of $10^{-5}$ $s^{-1}$, under a range of effective pressures (10 – 210 MPa). During these tests, pore-pressure was maintained at 20 MPa and acoustic emissions were recorded throughout.

By examining the mechanical and acoustic data from each experiment, the onset of shear-induced dilation (C'), in the brittle faulting regime, and the onset of shear-enhanced compaction (C*), in the compaction band regime, were determined. The stress states at C' and C* are described in terms of the effective mean stress (P) and the differential stress (Q), and then used to construct yield-caps in PQ space.

### 8.1.1 General Features of Triaxial Data

Under relatively low effective pressures (<40 MPa), as a result of an applied differential stress, samples exhibit dilatant behaviour and ultimately fail by the development of a through-going fault. At higher effective pressures (>100 MPa), samples develop compaction bands oriented essentially normal to $\sigma_1$. During deformation at intermediate effective pressure conditions, samples fail by a combination of high angle (to $\sigma_1$) compacting shear bands and compaction bands oriented sub-normal to $\sigma_1$.

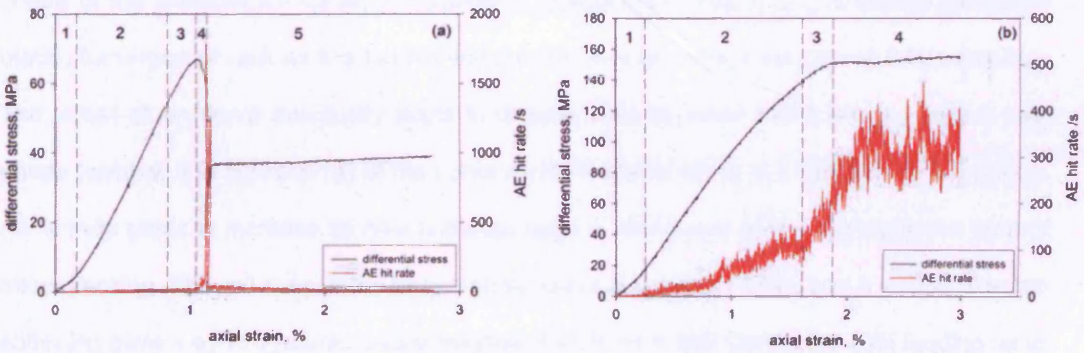


*Fig 8-1. Some generic features of the dilatant (a) and compactive (b) stress-strain curves and AE response as seen in samples deformed at effective pressures of 10 MPa and 110 MPa, respectively. In (a) 5 phases can be identified: 1) Bedding-in 2) elastic loading transitioning to yield and C'. 3) The growth of new cracks, and a commensurate acceleration in AE activity. 4) Strain softening leading to crack coalescence and dynamic failure punctuated by a spike in AE activity. 5) Slip on the newly formed fault plane. In (b) 4 phases can be identified: 1) Bedding-in 2) Pseudo-elastic loading transitioning to the onset of shear-enhanced compaction (C*) and accelerating AE activity. 3) Yielding and 'roll-over'. 4) The plateau where further strain is accommodated at a constant level of stress, AE surges often appear.*

The evolution of differential stress and the AE activity associated with dilation or compaction all share a number of common features which are highlighted in the representative data shown in figure 8-1. During initial application of differential stress at low effective pressures, there is a clear bedding-in period (window 1 in figure 8-1) of relatively low, but increasing, Young's modulus. Bedding-in results from the alignment of components in the loading train of the triaxial machine, coupled with the closure (partial or otherwise) of pre-existing microcracks and pores, during the initial application of differential stress. Therefore, this part of the stress-strain curve reflects a combination of material properties of the sample, and of the deformation apparatus.

Initial AE activity is minimal and is a reflection of the fact that there is no significant new damage being introduced to the sample. An inflection in the stress-curve leads into the next phase of loading (window 2 in figure 8-1a) where the stiffened material shows an approximately elastic-linear behaviour, with each increment increase in axial strain resulting in a commensurate increase in the differential stress supported by the sample. Again, during this phase of the stress-strain curve, AE activity is typically low (<30 hits/s) reflecting the quasi-elastic behaviour of rock as it is loaded without the development of significant brittle damage. The stress-strain curve eventually starts to deviate from its linear trend, which marks a new phase (window 3 in figure 8-1a) of the curve as the material starts to yield. During this period, AE activity starts to increase as new brittle damage is introduced to the sample in the form of microcracking. The roll-over of the stress-strain curve is relatively brief, and a period of strain softening gives way to dynamic failure (window 4 in figure 8-1a). During the time leading up to dynamic failure, there is an acceleration in AE activity culminating at the point where the sample develops a through-going fault. Following failure (window 5 in figure 8-1a), there is a period where the sample under test supports a steady differential stress, representing the force necessary to overcome friction during slip along the recently developed fault plane. During this portion of the stress-strain curve, AE activity decreases to a low level, as further

axial displacement is now accommodated by slip along the fault plane rather than by the development of new damage.

During deformation at higher effective pressures, there is also an initial bedding period (window 1 in figure 8-1b) with very little AE activity associated with it. The next period of loading (window 2 in figure 8-1b) shows noticeably less linear-elastic character than in samples deformed at lower effective pressures, with the stress-strain curve taking a concave-downwards form as AE activity intensifies steadily. At the onset of shear-enhanced compaction (window 3 in figure 8-1b) AE activity starts to accelerate significantly, sometimes in pulses and other times steadily to a maximum (for contrast, see AE patterns following C* in figure 8-6). Following C*, and during the period of intensifying AE activity, the stress-strain curve rolls-over as the sample yields. Following the roll-over, the stress-strain curve typically shows a plateau (window 4 in figure 8-1b) during which time there are surges of AE activity. With continued axial strain, the sample may also show a degree of strain hardening.

During experiments, the change in sample porosity ($\Delta\varphi$) was measured by using the pore-pressure control intensifier as a volumometer. Initially it is necessary to hydrostatically pressurise samples to the starting effective pressure conditions of each experiment. During this period of hydrostatic loading, the data showing porosity change against effective mean stress (P = Pe = Pc – Pp, for hydrostatic conditions), was recorded for each experiment and termed the 'hydrostat'. Porosity change was also recorded during the subsequent 'triaxial' component of each experiment. The porosity change data from both hydrostatic and triaxial loading are combined and plotted against effective mean stress to show the relative rates of dilation and compaction during deformation.

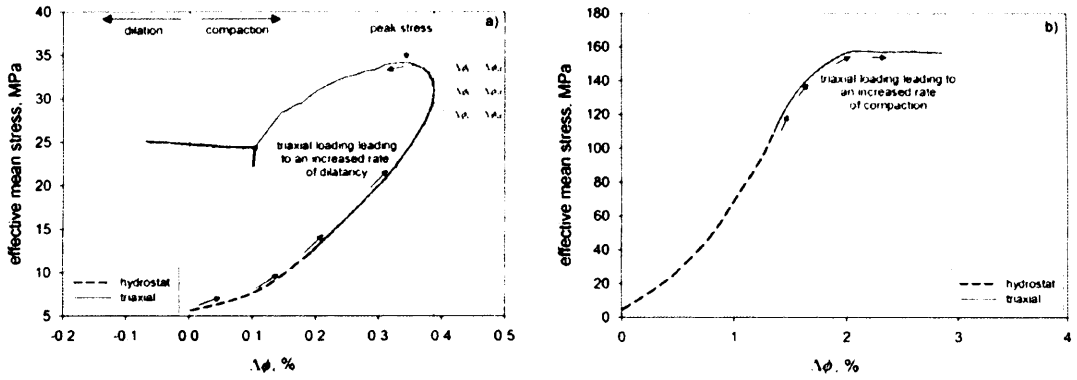


*Fig 8-2 a) Typical features of porosity change during dilatant triaxial deformation under relatively low effective pressure (10 MPa). The processes of compaction and dilation do not act in isolation, and the relative contribution of each is reflected by the evolving gradient of the curve. b) Typical features of porosity change during a compactive triaxial deformation under relatively high effective pressure (110 MPa). Unlike for relatively low Pe, the compactive process becomes more dominant over the course of deformation.*

Figure 8-2 shows a comparison of some of the generic features of the porosity change plots resulting from deformation under relatively low effective pressures, leading to dilatant brittle faulting, and deformation under relatively high effective pressures, leading to localised compaction. During hydrostatic loading samples undergo compaction resulting in porosity reduction (denoted as a positive $\Delta\phi$ trend). During triaxial loading at a relatively low effective pressure (figure 8-2a), $\Delta\phi$ proceeds at an approximately linear rate, after which the rate of porosity reduction starts to decrease which is reflected by a increase in the gradient of the $\Delta\phi$ curve. Upon further deformation, the sense of porosity change reverses, and the sample starts to dilate at a greater rate than it is compacting ($\Delta\phi_c < \Delta\phi_d$). During the transition between net compactive behaviour and net dilatant behaviour, the rate of compaction and dilation balance one another ($\Delta\phi_c = \Delta\phi_d$), reflected by the vertical portion of the curve. The point of dynamic failure is characterised by a period of sudden and dramatic sample dilation, as the development of a through-going fault leads to a net increase in the sample's porosity. Prior to dynamic failure, the picking of C' can be constrained by identifying a significant deviation in the trend of $\Delta\phi$. This is discussed in more detail in section 8.1.2.

In contrast to figure 8-2a, figure 8-2b shows the hydrostatic porosity change up to a higher effective pressure, and the subsequent $\Delta\phi$ evolution as a result of the application of differential stress. During triaxial deformation the rate of porosity reduction increases, reflected in the convex-upwards form of the $\Delta\phi$ curve. Unlike for samples deformed under relatively low effective pressures, samples deformed under relatively high effective pressure do not show an increasing dominance of dilatancy and as such there is no inflexion towards a negative $\Delta\phi$. Ultimately, the sample reaches an effective mean stress, in this case around 160 MPa, where any further action on the sample results in porosity reduction without any increase in effective mean stress.

### 8.1.2 Picking C'

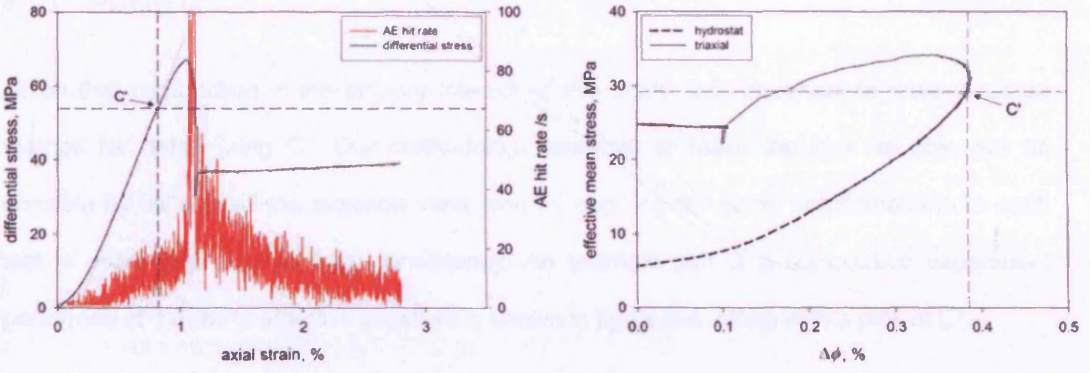


*Fig 8-3. Illustration of how C' is picked. Data shown is from a z-axis sample of Diemelstadt deformed at 10 MPa effective pressure using an axial strain rate of $10^{-5}$ $s^{-1}$. C' is constrained by considering AE activity and stress-strain relationships (left) and pore-fluid volumometry (right).*

During dilatant tests, at low effective pressure, the stress-strain curves deviate only subtly from quasi-linearity as peak stress is approached. This makes picking C' somewhat difficult because, unlike in picking the compactive analogue C* for high effective-pressure compactive tests, there is no notable period of yielding to delineate the onset of shear-induced dilatancy. This is highlighted in figure 8-3, where the stress-strain curve shows only a slight deviation

from linearity (shown by dotted line) at C'. AE activity can be used to an extent to pick C', but acoustic activity was found to be modest during deformation at low effective pressures where C' is observed (except at the point of dynamic failure). Therefore pore volumometry, which is a sensitive indicator of the relative contributions of dilatant and compactive mechanisms, was relied on to constrain where on the stress-strain curve dilatancy started to feature significantly. During experiments involving dynamic failure, a large contrast in the AE hit rate was observed between initial loading and the point of dynamic failure (see, for example, fig 8-1a), with the AE hit rate routinely reaching values greater than 1000 hits per second. In these instances, plotting the entire range of AE data would mask the change in hit rate leading up to, and following, C'. In order to address this, figure 8-5 shows only the lower range of AE hit rate data for experiments involving dynamic failure.

### 8.1.3 Picking C*

Given that compaction is the primary interest of this study, it is important to have a robust method for determining C*. Our methodology attempts to make the pick as objective as possible by utilising all the available data, and by applying the same considerations to each test in order to ensure internal consistency. An example plot of a compactive experiment performed at 110 MPa effective pressure is shown in figure 8-4, along with a pick of C*.

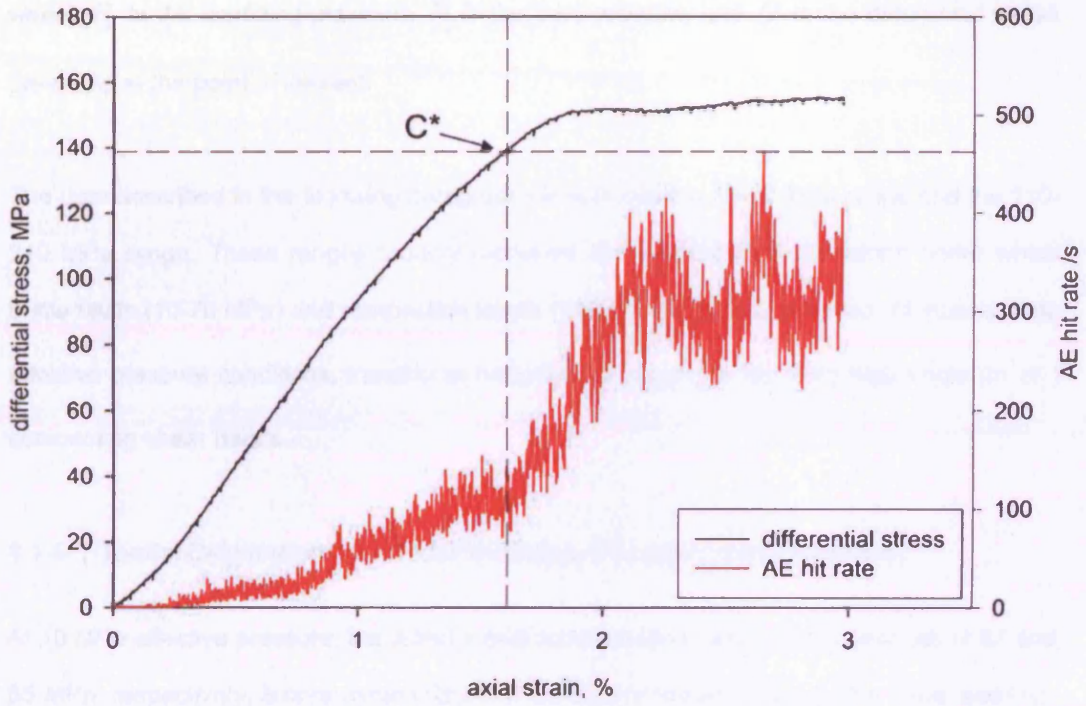


*Fig 8-4. Illustration of how C* is picked from the data showing compactive deformation of a sample at relatively high effective pressure (110 MPa). C* is largely constrained by the acceleration in AE activity which results from the brittle processes associated with shear-enhanced compaction.*

In the example shown in figure 8-4, C* is picked at a differential stress of 140 MPa, at a point on the stress-strain curve that coincides with the start of intensifying AE activity. The non-linear nature of the stress strain curves of samples deformed at high effective pressures makes picking C* on the basis of sample yielding ambiguous. Previous studies have shown that C* is characterised by the proliferation of brittle microcracking, on this basis the onset of significant AE activity is taken to be indicative of C*.

The effective mean stress, $P$, acting on the sample at the point of C* (or at any other point) is given through the relationship:

$$P = \frac{3P_c + Q}{3} - P_P$$

where $P_c$ is the confining-pressure, $P_p$ is the pore-pressure and $Q$ is the differential stress prevailing at the point of interest.

The data described in the following paragraphs is split into the 10-70 MPa range and the 110-210 MPa range. These ranges broadly represent the experimental conditions under which brittle faults (10-70 MPa) and compaction bands (110-210 MPa) are observed. At intermediate effective pressure conditions, transitional behaviour is observed, involving high-angle (to $\sigma_1$) compacting shear bands.

### 8.1.4 Triaxial Deformation, 10 – 70 MPa Effective Pressure Range (figure 8-5)

At 10 MPa effective pressure, the z and x-axis samples attain similar peak stresses of 67 and 65 MPa, respectively, before dynamic failure. During the loading phase, after initial bedding-in, the z-axis sample shows a quasi-linear stress-strain relationship which develops up until 52 MPa differential stress. At this point the material starts to yield and, following a period of strain hardening, the sample reaches its peak stress after 1% axial strain and then rapidly strain softens before dynamic failure at 1.15% axial strain. The yield point at 52 MPa differential stress is interpreted as C' as it coincides with an inflexion in the AE hit rate, which continues to accelerate towards the point of dynamic failure, indicating the development of new microcracks. Pore volume data (shown in figure 8-8) also confirms the onset of significant dilatancy at this point. At 10 MPa effective pressure the x-axis sample also shows an initial quasi-linear relationship between differential stress and axial strain. This trend continues until 48 MPa of differential stress, after which the sample starts to yield, the AE hit rate accelerates and the pore-volumometry (figure 8-8) indicates the onset of dilation. This point, at 0.8% axial strain, is taken as C' and leads into a period of strain hardening before peak stress is reached after 1.2% axial strain. Strain softening gives way to dynamic failure at 1.3% axial strain. At 10 MPa effective pressure, both z and x-axis samples failed by macroscopic brittle fracture, as seen in figure 8-7. It is notable that the z-axis sample develops a very steep fault, almost

parallel (10°) to the sample axis, and as such could be considered axial splitting. The x-axis sample develops a fault which is more inclined to the direction of maximum compression (30°), although a bifurcation of the fault can be identified which trends sub-parallel to the sample axis. For both z and x-axis orientations, the fault plane developed at the point of dynamic failure requires 35 MPa differential stress to drive slip.

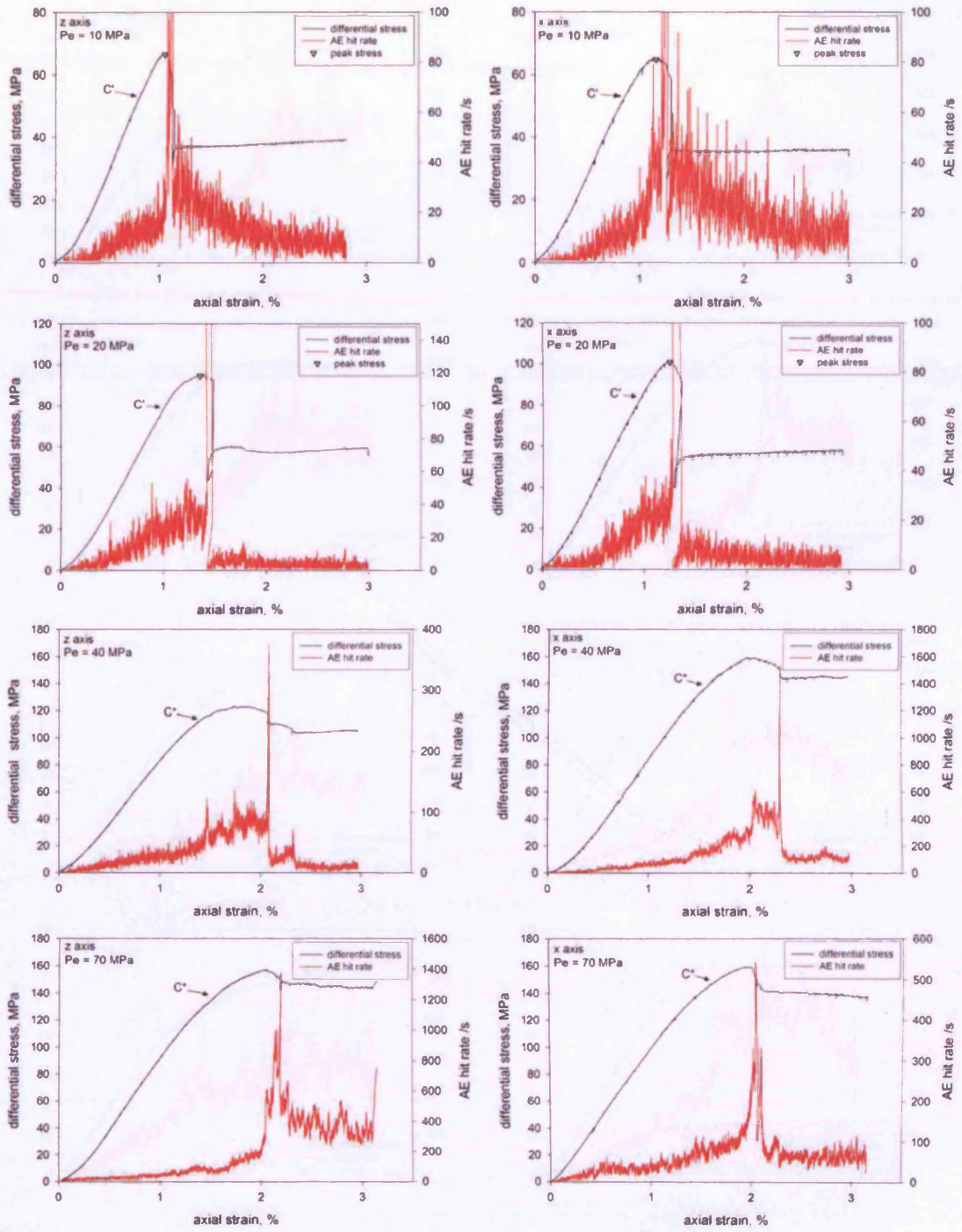


*Fig 8-5. The differential stress - axial strain curves and AE hit rate data for z and x-axis samples deformed in the 10 – 70 MPa effective pressure range. Complementary sample orientations deformed under common effective pressure conditions are shown side-by-side.*

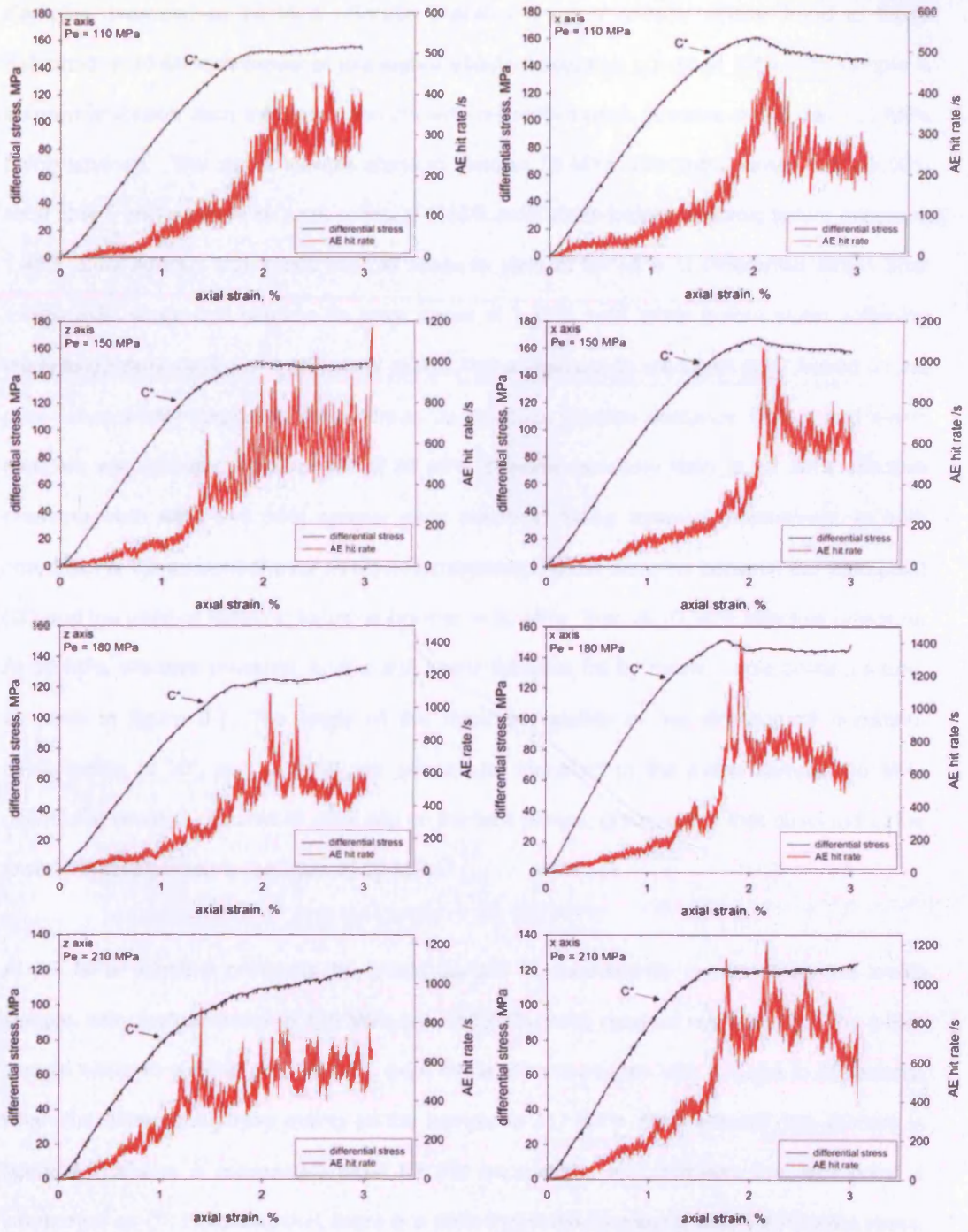


*Fig 8-6. The differential stress - axial strain curves and AE hit rate data for z and x-axis samples deformed in the 110 – 210 MPa effective pressure range. Complementary sample orientations deformed under common effective pressure conditions are shown side-by-side.*

Samples deformed at 20 MPa effective pressure show a broadly similar trend to those deformed at 10 MPa, however at this higher effective pressure condition the z-axis sample is somewhat weaker than the x-axis sample with respective peak stresses of 95 and 101 MPa being attained. The z-axis sample starts to yield at 78 MPa differential stress, after 1.00% axial strain, and reaches its peak stress at 1.38% axial strain before dynamic failure occurs at 1.48% axial strain. The x-axis sample starts to yield at 84 MPa of differential stress after 1.00% axial strain and reaches its peak stress at 1.25% axial strain before strain softening leads to dynamic failure at 1.37% axial strain. These yield points are taken as C' based on the pore-volumometry response, which shows an inflection towards dilatancy. Both z and x-axis samples are considerably stronger at 20 MPa effective pressure than at 10 MPa effective pressure, with 40% and 55% greater peak stresses being attained respectively. In both orientations, the amount of axial strain accommodated by the samples between the yield point (C') and the point of dynamic failure is greater at 20 MPa than at 10 MPa effective pressure. At 20 MPa effective pressure, both z and x-axis samples fail by macroscopic brittle fracture, as seen in figure 8-7. The angle of the fractures relative to the direction of maximum compression is 30°, and a conjugate set can be identified in the x-axis sample. 55 MPa differential stress is required to drive slip on the fault planes; greater than that observed at the lower effective pressure condition of 10 MPa.

At 40 MPa effective pressure the z-axis sample is substantially weaker than the x-axis sample, with peak stresses of 125 MPa and 160 MPa being reached respectively. The z-axis sample starts to yield at around 1.4% axial strain, commensurate with a surge in AE activity, when the differential stress acting on the sample is 117 MPa. Pore volume data (shown in figure 8-8) shows a compactive trend for this experiment, and therefore the yield point is interpreted as C*. Following this, there is a period of strain hardening until 1.80% axial strain, after which the sample starts to soften until a stress drop indicates brittle failure at 2.05% axial strain. This is followed by a further period of strain softening until a less pronounced stress drop at 2.35% axial strain. Both of these stress drops are punctuated by a spike in AE activity,

after which the differential stress supported by the sample remains steady at 105 MPa. The x-axis sample starts to yield at 1.60% axial strain, at a differential stress of 140 MPa, with the AE rate increasing notably from this point. Pore volume data shows the dominance of compaction, and therefore this yield point is interpreted as C*. Following C*, there is an extended period of strain hardening until 2.00% axial strain at which point the sample softens until 2.30% axial strain at which point a stress drop and AE spike indicate brittle failure. After the stress drop, differential stress remains steady at 145 MPa. Both sample orientations show extended periods of strain hardening between C* and peak stress, occurring over an approximately 0.5% axial strain increment. In both sample orientations, the stress drops following strain softening are relatively modest at about 10 MPa, this is in contrast to the stress drops observed under 10 and 20 MPa effective pressures which are around 30 MPa. Post-deformation examination reveals that the z-axis sample failed by a 35° macroscopic fracture and the development of some localised compaction structures at the top of the sample which show little or no shear offset in hand specimen. The x-axis sample, on the macroscopic scale, developed a high-angle (55° to direction of maximum compression) compacting shear band which branches into two limbs parallel to one another, the compactive structures evident at the top of the z-axis sample are lacking in the x-axis sample.

At 70 MPa effective pressure, z and x-axis samples are of similar strength, reaching peak stresses of 158 MPa and 160 MPa respectively. The z-axis sample reaches C* at around 1.5% axial strain while supporting 135 MPa of differential stress, this point being delineated by an acceleration in the AE hit rate. A period of strain hardening leads to the peak stress at 2.00% axial strain, after which strain softening leads to a 5 MPa stress drop at 2.20% axial strain. Following this stress drop, the differential stress supported by the sample remains steady at 145 MPa. During the post-peak region of the stress strain curve, there are two discernable surges in AE activity peaking at 2.55 and 2.80% axial strain. Unlike with previous AE surges, there is no dramatic reflection of the acoustic activity in the stress-strain curve, although two subtle (<2 MPa) stress drops can be identified. The x-axis sample reaches C* at

around 1.6% axial strain, while supporting a differential stress of 152 MPa. After a period of strain hardening, peak stress is reached at 2.00% axial strain and there immediately follows three small stress drops (<10 MPa) occurring in rapid succession, each accompanied by an AE spike. The post-peak region of the stress-strain curve is relatively steady, and, similar to the z-axis sample, a small AE surge and associated stress perturbation can be identified at 2.20% axial strain. Under 70 MPa effective pressure conditions, both z and x-axis samples developed mosaics of high-angle (>50°) to $\sigma_1$ compacting shear bands. The structures seen here have less definition than the shear structures seen at 40 MPa effective pressure conditions, and appear similar to the compactive structures observed at the top end of the z-axis sample deformed at 40 MPa. It is notable that the x-axis sample appears to have sustained less damage than the z-axis sample.

### 8.1.5 Triaxial Deformation, 110 – 210 MPa Effective Pressure Range (figure 8-6)

At 110 MPa effective pressure conditions, z-axis samples are weaker than x-axis samples with peak stresses of 158 MPa and 162 MPa being attained respectively. However, the z-axis sample only attains this peak stress value following a subtle period of strain hardening which occurs after the roll-over in the stress-strain curve. In contrast, the x-axis sample attains its peak stress at the crest of the stress-strain roll-over, and shows a post-peak region characterised by strain softening. The z-axis sample reaches C* after 1.6% axial strain, at a differential stress of 140 MPa. Following this, the stress-strain curve essentially plateaus after 1.85% axial strain and gradually strain hardens throughout the remainder of the experiment. During this plateau region of the stress-strain curve, there are three discernable surges in AE activity, peaking at approximately equal intervals around 2.2%, 2.6% and 3% axial strain. Although the rising limb of the final AE surge is clearly visible, its peak is curtailed by the end of the experiment. The x-axis sample reaches C* after 1.7% axial strain, at a differential stress of 155 MPa. As with the z-axis sample, C* in the x-axis sample is delineated by a notable inflection in the AE hit rate. Following C*, peak stress is reached at 2.00% axial strain

and a period of strain softening follows. Initially, strain softening is relatively pronounced and occurs during the peak rate of AE activity, however, at 2.25% axial strain there is a break in the slope of the strain-strain curve trend after which strain softening proceeds at a more modest rate. During this portion of the stress-strain curve, AE activity remains relatively constant without the clear surges observed in the z-axis sample. During deformation at 110 MPa effective pressure, the z-axis sample developed localised compaction bands oriented in the plane 90° to the direction of $\sigma_1$. The x-axis sample, however, developed a compacting shear band oriented at 50° to $\sigma_1$. This structure is somewhat diffuse, being about 7 mm thick normal to its plane, unlike the faults with clearly defined surfaces seen at lower effective pressures. Both samples appear to be relatively intact towards the middle of the core length, with damage being concentrated in the end thirds.

Under effective pressure conditions of 150 MPa, the z-axis sample is again weaker than the x-axis sample with peak stresses of 150 MPa and 168 MPa being recorded. The z-axis sample reaches C* at around 1.2% axial strain while supporting 122 MPa of differential stress. Following this, there is an extended period of strain hardening until 1.85% axial strain when the stress-strain curve plateaus. During the plateau region of the curve, there is quite a lot of noise on the AE hit rate, although four AE surges can be identified peaking at approximately equal intervals at 2.00%, 2.30%, 2.55% and 2.85% axial strain. The x-axis sample reaches C* at around 1.6% axial strain and 146 MPa differential stress, strain hardening leads into the peak stress at the crest of the stress-strain roll-over at around 2% axial strain. As with the samples deformed at 110 MPa effective pressure, the z-axis sample shows a subtle degree of strain hardening at high axial strains whereas the x-axis sample shows a clear strain softening trend during the post-peak region of the curve. The x-axis sample shows five AE surges during the post-peak region, and, unlike in previous cases, they appear not to occur at regularly spaced intervals. Post deformation examination of the samples show that z-axis core developed discrete compaction bands which are pervasive throughout the sample length. The x-axis core also shows discrete compaction bands, although in hand-section they appear less

continuous and more tortuous than their z-axis counterparts. The x-axis sample also appears not to have accommodated any inelastic strain in the top third of the core.

At 180 MPa effective pressure conditions the z-axis sample is again weaker than the x-axis sample with peak stresses of 135 MPa and 152 MPa being attained, respectively. However, the peak stress reached in the z-axis sample occurs only after significant strain hardening at 3% axial strain whereas the x-axis sample reaches its peak stress at the crest of the stress-strain roll-over. The z-axis sample reaches C* after 1.5% axial strain, at a differential stress of 109 MPa, coinciding with an acceleration in AE activity. Following C*, the sample undergoes strain hardening for the remainder of the test, at least seven AE surges can be identified during the post C* portion of the experiment. These surges occur at roughly equal axial strain intervals of 0.2%, with the most intense AE activity occurring during the 2.00 – 2.40% axial strain increment. There are several perturbations of the stress-strain curve which appear to coincide with the AE surges, although there are no sudden stress drops similar to those observed at lower effective pressure conditions. During the final strain increment of 2.50 – 3.00%, AE activity is relatively subdued and this coincides with the most pronounced period of strain hardening. The x-axis sample reaches C* at 1.25% axial strain, supporting a differential stress of 126 MPa. After this initial yield, the sample continues to strain harden until 1.80% axial strain at which point the peak stress is reached. Following this, the sample strain softens in two notable stages at 1.80% and 1.95% axial strain; both of these phases of strain softening are associated with surges in AE activity. During the post peak region of the stress-strain curve, following the mentioned periods of strain softening, the AE rate remains steady before starting to decrease after 2.50% axial strain. Post-deformation examination shows discrete compaction bands in both samples, although the normal-to-$\sigma_1$ structures in the z-axis sample appear more defined and planar than the compaction bands seen in the x-axis sample which are often oriented sub-normal to $\sigma_1$.

Under the highest effective pressure conditions of 210 MPa, data from the z-axis sample shows the same general form as for the 150 MPa z-axis sample; that is to say that after reaching C* at 1.10% axial strain and 80 MPa the material strain hardens for the remainder of the test attaining a peak stress of 120 MPa. During the post C* region of the stress strain curve, at least 10 surges in AE activity can be identified. These occur at regular intervals of approximately 0.2% axial strain, after the sample has accommodated 1.80% axial strain, and appear to be of more-or-less equal intensity. The x-axis sample is stronger than the z-axis sample, reaching C* at 103 MPa after being deformed to 1.20% axial strain and reaching a peak stress of 124 MPa at the crest of the stress-strain roll-over at 1.65% axial strain. Following this, the sample strain softens slightly before forming a plateau at 120 MPa differential stress and strain hardening during the final 0.25% axial strain. During the post-peak region of the experiment, there are five clearly identifiable AE surges which peak at approximately 0.3% axial strain intervals. These surges are of roughly equal intensity except for the final two which occur during the strain hardening part of the stress-strain curve. Post-deformation examination of the samples reveals compaction bands that are pervasive throughout the length of each core. The z-axis sample shows compaction bands which are more planar and well defined than those seen in the x-axis which show an anastomosing geometry. Again, the z-axis compaction bands appear to be consistently oriented at 90° to the direction of $\sigma_1$, whereas the x-axis compaction bands are more tortuous and generally trend sub-normal to the direction of maximum compression.

The Young's modulus of Diemelstadt sandstone can be extracted from the linear portion of the triaxial stress-strain relationships discussed above, and is found to fall between $6x10^3$ - $8x10^3$ MPa. These values are consistent with those reported for other high-porosity (around 20%) cemented sandstones containing a similar fraction of clay minerals (e.g. Zhu et al., 1997).

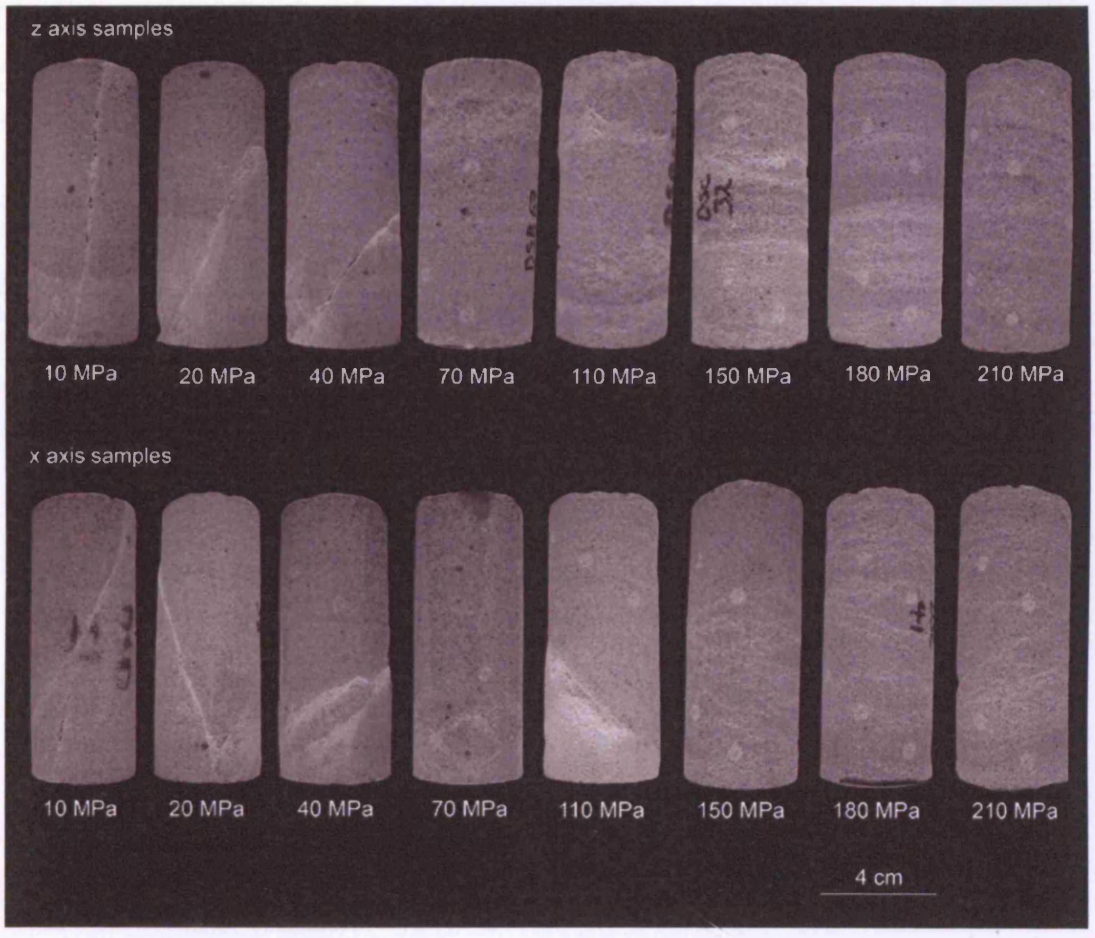


*Fig 8-7. Post-deformation photograph of the z and x-axis samples after deformation to 3% axial strain. The yield data from these experiments were used to establish the yield-cap. The effective pressure condition of each experiment is shown.*

| Pe | z-axis | | | x-axis | | |
|---|---|---|---|---|---|---|
| | Q at C' | P at C' | Q peak | Q at C' | P at C' | Q peak |
| 10 | 52 | 29 | 67 | 51 | 29 | 63 |
| 20 | 78 | 47 | 95 | 84 | 49 | 100 |

*Table 8-1. Mechanical data for samples that failed by dilatant brittle fracture, all figures in MPa.*

| Pe | z-axis | | | x-axis | | |
|---|---|---|---|---|---|---|
| | Q at C* | P at C* | Q peak | Q at C* | P at C* | Q peak |
| 40 | 117 | 79 | 125 | 140 | 86 | 160 |
| 70 | 135 | 115 | 158 | 152 | 120 | 160 |
| 110 | 140 | 154 | | 155 | 159 | |
| 150 | 122 | 190 | | 146 | 198 | |
| 180 | 109 | 218 | | 126 | 221 | |
| 210 | 90 | 237 | | 103 | 243 | |

*Table 8-2. Mechanical data for samples that failed by compaction bands, peak differential stresses of samples failing by compacting shear bands are also shown. All figures in MPa.*

### 8.1.6 Porosity Evolution, 10 –70 MPa Effective Pressure Range (fig 8-10)

Figures 8-8 and 8-9 overleaf show the evolution of porosity during initial hydrostatic loading (dashed lines), and during triaxial deformation (solid lines) plotted as porosity change ($\Delta\phi$) against effective mean stress (P). The form of the $\Delta\phi$-P curves show the relative contribution of dilatant and compactive processes during the course of each experiment (see figure 8-2).

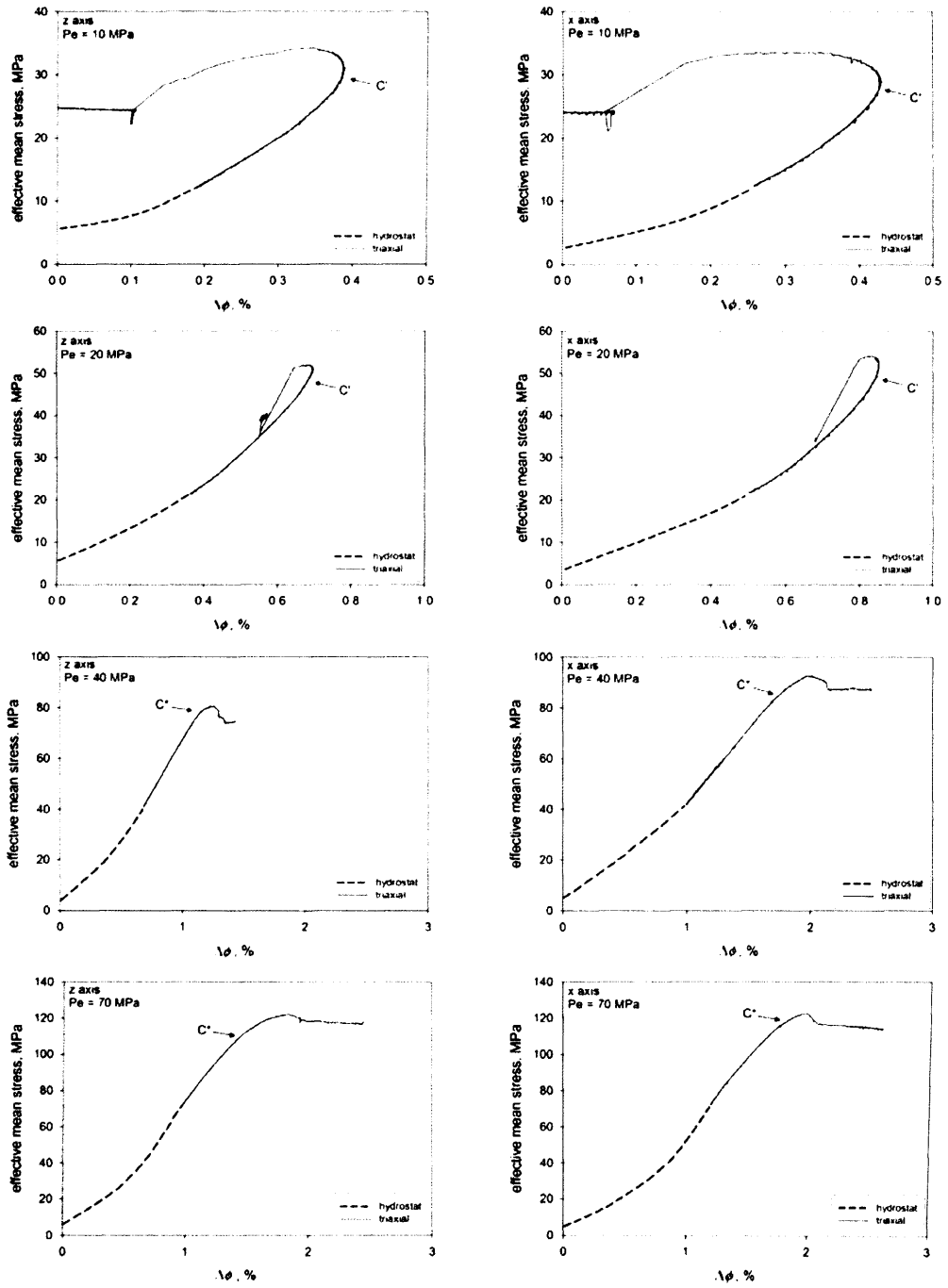


*Fig 8-8. The evolution of porosity during triaxial deformation of z and x-axis samples under effective pressure conditions in the range of 10 – 70 MPa. Complementary sample orientations deformed under common effective pressure conditions are shown side-by-side.*

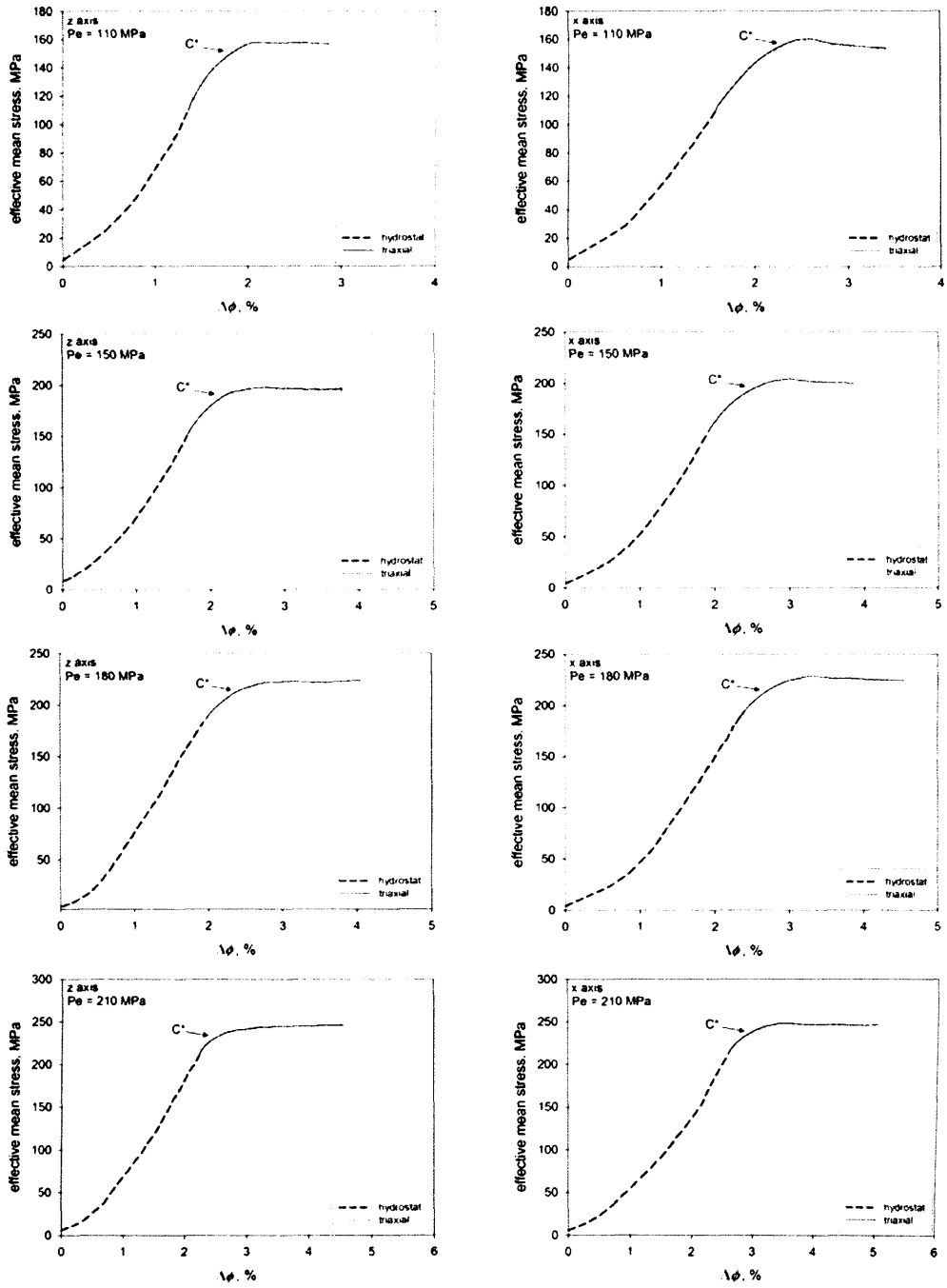


*Fig 8-9. The evolution of porosity during triaxial deformation of z and x-axis samples under effective pressure conditions in the range of 110 – 210 MPa. Complementary sample orientations deformed under common effective pressure conditions are shown side-by-side.*

During hydrostatic loading to 10 MPa effective pressure, the z and x-axis samples compact by 0.20% and 0.26%, respectively. Under effective pressure conditions of 10 MPa, application of a differential stress on both z and x-axis samples initially results in further compaction. The initial gradients of the curves continually increase giving rise to their concave upwards form during the early stages of loading. This reflects the increasing contribution of dilatant mechanisms relative to compactive mechanisms during the application of differential stress. At the onset of shear induced dilation (C'), which in both samples occurs at 29 MPa effective mean stress, there starts a significant reversal in the trend of the $\Delta\phi$-P curves. This reflects an acceleration in the rate of dilatancy as the samples approach peak stress and dynamic failure. At C', the z and x-axis samples have undergone 0.20% and 0.16% porosity reduction, respectively, during triaxial loading.

A similar overall trend in porosity evolution is observed in the samples deformed at 20 MPa as at 10 MPa. After the application of 20 MPa hydrostatic effective pressure, z and x-axis samples had compacted by 0.36% and 0.52%, respectively. In both z and x-axis samples, an initial period of net compaction results from the application of differential stress, with the $\Delta\phi$-P curve taking a concave upwards form which reflects the increasing influence of dilatant mechanisms on the sample volumes. The z-axis sample reaches C' at an effective mean stress of 47 MPa and the x-axis sample reaches C' at effective mean stress of 49 MPa, at which point samples have undergone 0.31% and 0.33% porosity reduction, respectively, during the triaxial phase of the experiments.

Hydrostatic loading to 40 MPa effective pressure results in a 0.68% and 0.85% porosity reduction in z and x-axis samples respectively. Unlike the experiments performed at lower effective pressures, during triaxial loading at 40 MPa effective pressure, samples undergo shear enhanced compaction and there is no period of deformation where the rate of dilatancy overtakes that of compaction. The z-axis sample reaches C* at 79 MPa effective

mean stress, after compacting by 0.45% as a result of triaxial loading, whereas the x-axis sample compacts by 0.90% reaching C* at 86 MPa effective mean stress.

Samples hydrostatically loaded to 70 MPa effective pressure compact by 0.98% and 1.22% in the z and x orientations respectively. Following the application of differential stress, the z-axis sample compacts a further 0.50% before reaching C* at 115 MPa effective mean stress. The x-axis sample reaches C* at 120 MPa effective mean stress, after compacting an additional 0.60% during the course of triaxial loading. Following C*, samples show an acceleration in the rate of compaction, with the z-axis sample undergoing a further 1.0% porosity reduction over only a 10 MPa increase in effective mean stress. Similarly, following C*, the x-axis sample undergoes a 0.8% porosity reduction over a 5 MPa effective pressure increase.

### 8.1.7 Porosity Evolution, 110 – 210 MPa Effective Pressure Range (figure 8-9)

During hydrostatic loading to 110 MPa effective pressure, z-axis sample undergoes 1.36% porosity reduction compared to 1.58% in the x-axis sample. Upon the application of differential stress, C* is reached at 154 MPa (z-axis) and 159 MPa (x-axis) effective mean stress, at which point the porosity reduction as a result of triaxial loading is 0.40% and 0.70% respectively. Following C*, porosity reduction accelerates without requiring a significant increase in the effective mean stress acting on the samples.

Samples hydrostatically loaded to 150 MPa effective pressure undergo a porosity reduction of 1.70% and 1.97% for the z and x-axis orientations respectively. Following the application of differential stress, the z-axis sample reaches C* after a further 0.55% porosity reduction at an effective mean stress of 190 MPa. The x-axis sample reaches C* at 198 MPa effective mean stress, after a 0.60% porosity reduction resulting from triaxial loading. Following C*, porosity reduction continues as the samples are unable to support any significant increase in effective mean stress.

During hydrostatic loading to 180 MPa effective pressure, z and x-axis samples undergo 1.96% and 2.27% porosity reduction respectively. Following this, the application of a differential stress leads to C* at 218 and 221 MPa effective mean stress for the z and x-axis samples respectively. At C*, as a result of triaxial loading, the z and x-axis samples have undergone 0.45% and 0.35% porosity reduction respectively. As has been observed in previous experiments, porosity reduction accelerates significantly after C*.

Hydrostatic loading to 210 MPa effective pressure results in a porosity reduction of 2.24% and 2.58% for z and x-axis samples respectively. Following triaxial loading, for the z-axis sample, C* is reached at 237 MPa effective mean stress after an additional 0.30% porosity reduction. The x-axis sample reaches C* at 243 MPa effective mean stress, having undergone 0.40% porosity reduction as a result of triaxial loading.

| **Pe** | **z-axis** | | | **x-axis** | | |
|---|---|---|---|---|---|---|
| (MPa) | Δφ at Pe | Δφ at C' | Δφ at C* | Δφ at Pe | Δφ at C' | Δφ at C* |
| 10 | 0.20 | 0.39 | | 0.26 | 0.43 | |
| 20 | 0.36 | 0.67 | | 0.52 | 0.86 | |
| 40 | 0.68 | | 1.17 | 0.85 | | 1.76 |
| 70 | 0.98 | | 1.56 | 1.22 | | 1.88 |
| 110 | 1.36 | | 1.92 | 1.58 | | 2.43 |
| 150 | 1.70 | | 2.20 | 1.97 | | 2.66 |
| 180 | 1.96 | | 2.73 | 2.27 | | 2.87 |
| 210 | 2.24 | | 2.68 | 2.58 | | 3.12 |

*Table 8-3. Porosity reduction data in percentage points from the start of hydrostatic loading, at Pe (effective pressure condition at start of triaxial loading), C' or C*.*

### 8.1.8 Grain Crushing Pressure

As discussed in section 4.2, at a sufficiently high hydrostatic pressure a sandstone will reach its grain crushing pressure (P*). The value assigned to P* acts to anchor the yield-cap, and is determined by monitoring the effect of an increasing effective pressure on the porosity reduction of a sample. The point where an incremental effective pressure increase has a dramatic effect on the measured amount of porosity reduction is taken as being the onset of grain-crushing leading to pore-collapse therefore an accelerating porosity reduction. Figure 8-10 shows the complete hydrostats of both z and x-axis sample cores. These data show that the onset of grain-crushing in z and x-axis samples occurs at 310 and 308 MPa effective pressure, respectively, with effective pressures above this threshold leading to increasingly dramatic porosity reduction. These two values of P* are very close to one another, well within the range that might be expected simply as a result of sample variability.

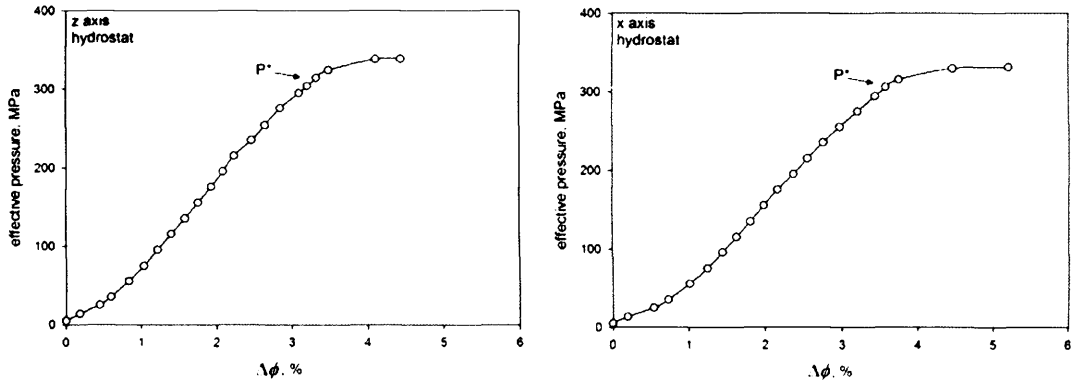


*Fig 8-10. The complete hydrostats for z and x-axis sample cores. The inflexion marked P* is taken to be the onset of grain crushing which results in pore-collapse and an acceleration in porosity reduction.*

During testing to determine P*, there is never any differential stress acting on the sample, and as such the effective pressure is equal to the effective mean stress. Cumulative plots of the triaxial components of the experiments described previously are superimposed on the complete hydrostats for the z and x-axis in figure 8-11 to show the triaxial evolution of dilatancy and compaction with reference to purely hydrostatic loading.

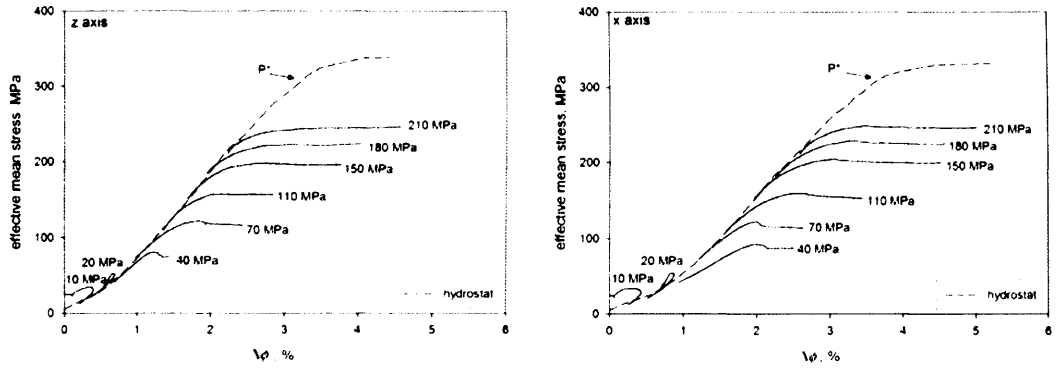


*Fig 8-11. The triaxial components of experiments performed in the 10-210 MPa effective pressure range superimposed on the complete hydrostats for z-axis samples (left) and x-axis samples (right).*

### 8.1.9 Yield-Surface Construction

The values of C', C* and P* can now be plotted to define a yield surface which delineates the extent of Diemelstadt's elastic behaviour in PQ space for deformation in the z and x-directions (figure 8-12). The surface maps out an approximately elliptical form and shows that the strength of the material initially increases with increasing effective pressure conditions until the trend reverses to complete the downward limb of the envelope, culminating with the grain crushing pressure (P*) occurring at 310 MPa effective pressure. The yield-cap of x-axis samples extends to greater differential stresses, reflecting the greater strength of these samples under deviatoric stress. The lateral extent of the x-axis yield-cap is the same as for the z-axis samples, reflecting the essentially equal strength of z and x-axis samples under hydrostatic load.

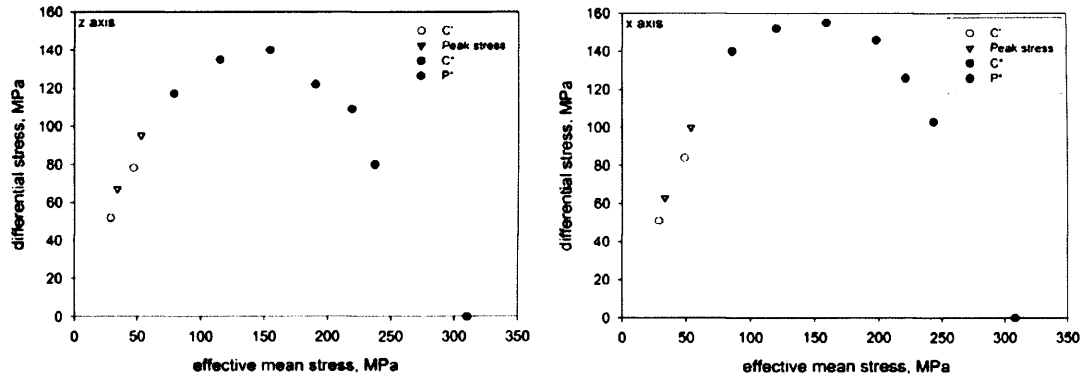


*Fig 8-12. Plot of C', C* and P* for z and x-axis samples in PQ space. Peak stresses for samples that failed by dilatant brittle faulting are also shown. This composite plot maps out a yield-cap which show the stress-states where Diemelstadt sandstone starts to deviate from quasi-elastic behaviour.*

## 8.2 Permeability Data

Measurements of permeability were taken at 0.25% axial strain increments during the deformation of z and x-axis samples over a 40 – 100 MPa confining pressure range. Figure 8-13 highlights some of the general trends observed during permeability evolution, and the complete data-set is shown in figure 8-18.

### 8.2.1 General Features of Permeability Data

During initial deviatoric loading, samples show a period of gradual permeability reduction (window 1 in figure 8-13) during which permeability may fall by a factor of 2 or so. This period may continue until beyond 1% axial strain, and is followed by a dramatic increase in permeability reduction, typically over several orders of magnitude, which coincides with the onset of shear-enhanced compaction (window 2 in figure 8-13). Typically the period of initial permeability reduction which precedes C* is more prolonged in x-axis samples than in z-axis samples. The duration of window 2, or the duration of the large permeability drop associated with C*, also appears to be more prolonged in x-axis samples; sometimes occurring in distinct steps or occurring relatively steadily over a relatively large (1%) axial strain increment. The permeability reduction associated with C* typically slows down notably by 1.5-2% axial strain,

at a phase of the experiment where the stress-strain curve has rolled over and is either flat or is showing signs of strain hardening (window 3 in figure 8-13). During window 3, permeability generally continues to fall steadily with increasing axial strain.

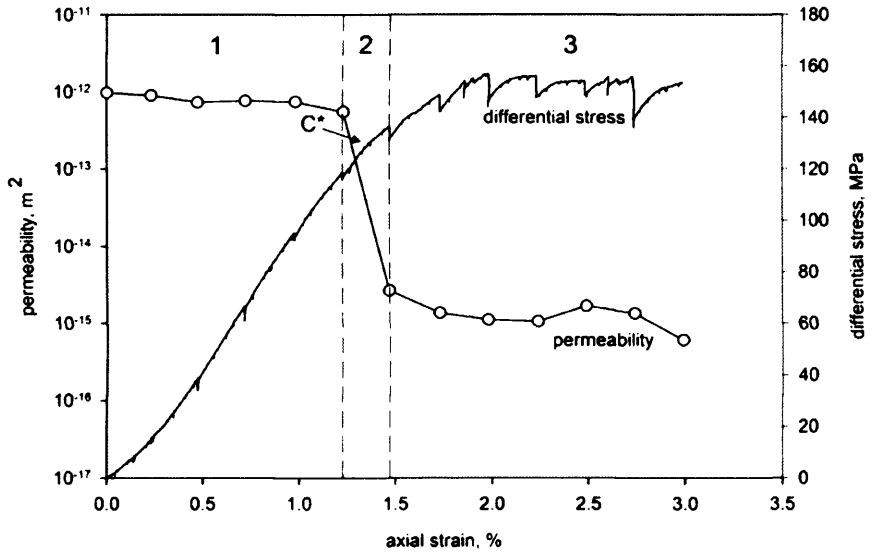


*Fig 8-13. Some general features of permeability evolution during shear-enhanced compaction in a z-axis sample deformed at 100 MPa effective pressure. The stress decrements are associated with sample relaxation during individual permeability measurements, as axial strain was held constant.*

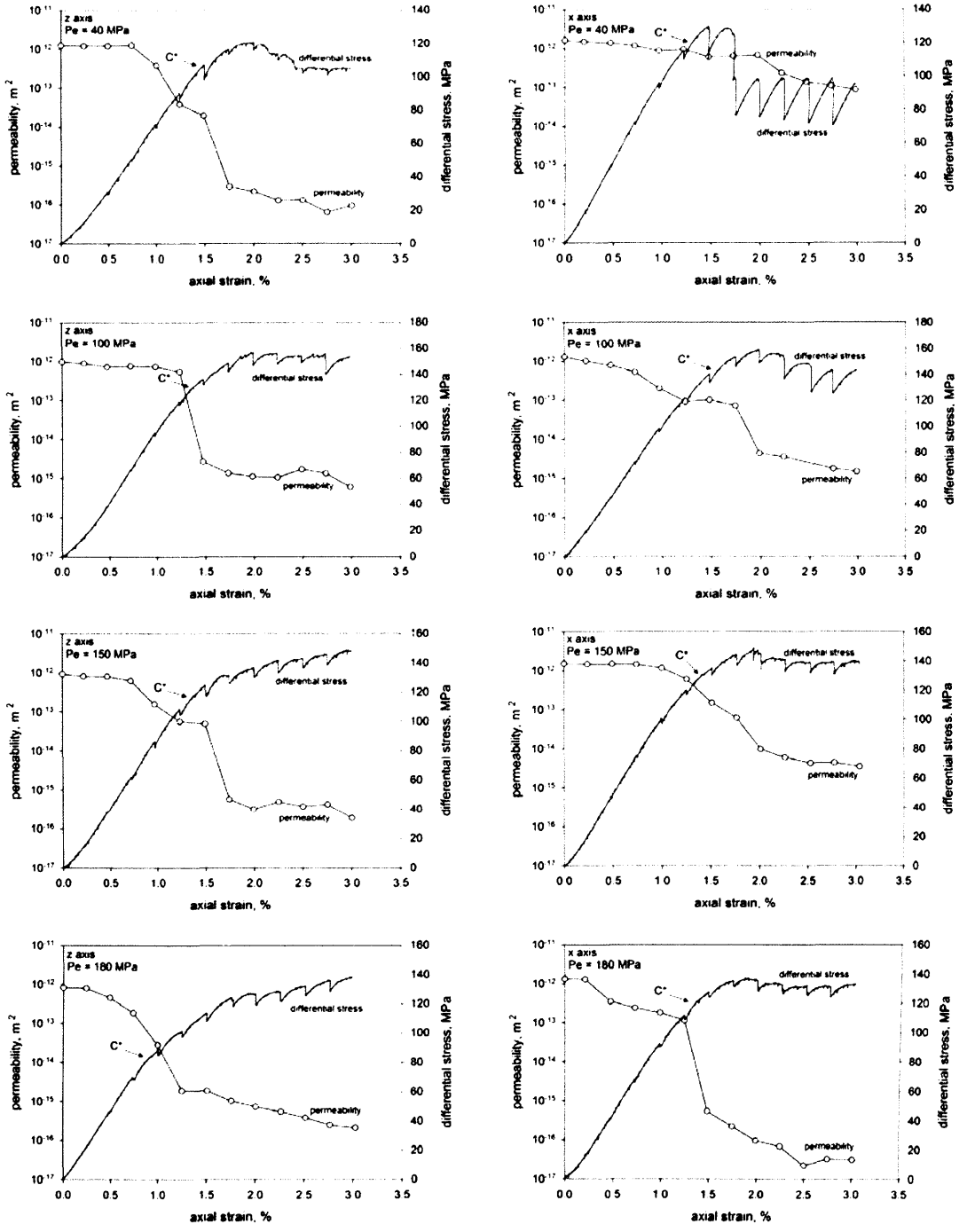


*Fig 8-14. Permeability and differential stress evolution as a function of increasing axial strain during deformation under a range of effective pressures. Complementary sample orientations deformed under common effective pressure conditions are shown side-by-side.*

### 8.2.2 Permeability Evolution During Deformation at Pe = 40 MPa

During deformation at 40 MPa effective pressure, both sample orientations show an initial period of permeability reduction, presumably as a result of the closure of microcracks and pores upon the application of differential stress. The z-axis sample has an initial permeability of $1.2 \times 10^{-12}$ $m^2$, which falls by 4% during the first 0.50% axial strain increment. Following this, there is a period of dramatic reduction as permeability falls by almost two orders of magnitude to $1.9 \times 10^{-14}$ $m^2$ by 1.50% axial strain. This permeability reduction is observed to occur over a period of the experiment that coincides with the pick for the onset of shear enhanced compaction, although there is also a significant permeability reduction before this point. Following C*, which occurs around 1.50% axial strain, there is a another period of permeability reduction of an additional two orders of magnitude which sees permeability fall to just $2.9 \times 10^{-16}$ $m^2$ by 1.75% axial strain. Increasing the amount of axial strain produces a further reduction in permeability, however the changes are less dramatic than those previously described. Between 1.75% and 3.00% axial strain, permeability is reduced by approximately a factor of 3, with final a permeability measured as $9.5 \times 10^{-17}$ $m^2$. Post-deformation examination of the sample reveals that it failed by the development of conjugate shear bands. The x-axis sample deformed under 40 MPa of effective pressure shows a more gradual permeability evolution than the z-axis sample. A 12% reduction occurs during the 0.00 – 0.50% axial strain increment, with permeability falling from $1.6 \times 10^{-12}$ $m^2$ to $1.4 \times 10^{-12}$ $m^2$. Permeability continues to fall during the course of deformation, and between 1.25-1.50% axial strain there is a 40% reduction in permeability to $5.9 \times 10^{-13}$ $m^2$ which occurs at approximately the same point on the stress=strain curve as C*. Following C*, permeability remains steady up to 2.00% axial strain. This phase of steady permeability is associated with the roll-over of the stress-strain which precedes dynamic failure at 1.75% axial strain, and may be the result of balance between the competing mechanisms of crack growth (acting to increase permeability) and porosity compaction (acting to decrease permeability). Following dynamic failure, further deformation results in permeability being reduced by a factor of three to $2.3 \times 10^{-13}$ $m^2$ at 2.25%

axial strain. Permeability continues to fall during the post-peak region of the stress-strain curve, finishing at $8.6x10^{-14}$ $m^2$ by 3.00% axial strain.

### 8.2.3 Permeability Evolution During Deformation at Pe = 100 MPa

At the substantially higher effective pressure of 100 MPa, z-axis permeability is initially $9.8x10^{-13}$ $m^2$ and falls by around 25% during the first 1% axial strain. Following this, there is a further 25% reduction in permeability to $5.5x10^{-13}$ $m^2$ as the reaches 1.25% axial strain. C* is picked at 1.30% axial strain, around which time there permeability is reduced by over two orders of magnitude to $2.7x10^{-15}$ $m^2$. This is followed by a more modest period of permeability reduction where between 1.50 and 3.00% axial strain, permeability is reduced by a factor of 2; resulting in a final permeability of $6.1x10^{-16}$ $m^2$. The x-axis sample deformed under 100 MPa effective pressure immediately undergoes a reduction in permeability, falling by 25% from $1.3x10^{-12}$ $m^2$ to $1x10^{-12}$ $m^2$ over the first 0.25% axial strain increment. This trend accelerates during further deformation with permeability falling by an order of magnitude to $9.2x10^{-14}$ $m^2$ at 1.25% axial strain. C* is picked at around 1.5% axial strain, during which time permeability remains relatively steady. This steady trend gives way to another order-of-magnitude permeability reduction between 1.75 and 2.00% axial strain. This is followed by a more gradual period of reduction during the 2.00-3.00% axial strain increment which sees permeability fall by around 65% to $1.5x10^{-15}$ $m^2$. This final phase of permeability reduction occurs after the sample under test has attained its peak stress, during the plateau region of the stress-strain curve.

### 8.2.4 Permeability Evolution During Deformation at Pe = 150 MPa

At effective pressure conditions of 150 MPa, permeability along the z cores remains relatively steady during the initial 0.50% of axial strain, although further deformation results in a 25% permeability reduction to $6.2x10^{-13}$ $m^2$ by 0.75% axial strain. A decreasing permeability trend continues through subsequent measurements made at 1.00 and 1.25% axial strain, before stabilising at around $5.3x10^{-14}$ $m^2$ during the 1.25 – 1.50% axial strain increment. This period

of stable permeability is short-lived, and during the 1.50 – 1.75% axial strain increment there is a reduction by two orders of magnitude to $5.8x10^{-16}$ $m^2$. The axial strain increment over which this large permeability drop is recorded occurs just after the pick of C* on the stress-strain curve, after which the sample undergoes significant strain hardening. Subsequent measurements of made between 2.00 – 2.75% axial strain show permeability to be relatively steady, around $4x10^{-16}$ $m^2$, with no discernable trend as a result of increasing axial strain. In contrast to the z-axis sample, permeability of the x-axis sample remains relatively steady throughout the initial 0.00 – 0.75% axial strain increment, only falling by 5% compared to 30% for the z-axis sample. Following this, there is a continuous and significant reduction in permeability during the 0.75 – 2.00% axial strain increment, where permeability falls by over two orders of magnitude from $1.5x10^{-12}$ $m^2$ to $9.8x10^{-15}$ $m^2$. C* is picked around 1.25% axial strain, near the start of this phase of permeability reduction. By this point, at 2.00% axial strain, the x-axis sample has reached its peak stress, and during the stress-strain plateau, over the 2.00-3.00% axial strain increment, there is continued permeability reduction at substantially lower rate. By 3.00% axial strain, sample permeability has been reduced to $3.5x10^{-15}$ $m^2$ .

### 8.2.5 Permeability Evolution During Deformation at Pe = 180 MPa

During deformation of the z-axis core at 180 MPa effective pressure, z-axis permeability remains steady between 0.00 - 0.25% axial strain, falling by over two orders of magnitude from $8x10^{-13}$ $m^2$ to $1.9x10^{-15}$ $m^2$ during the 0.25-1.25% axial strain increment. C* is picked from the mechanical data at being around 0.8% axial strain, in between measurements made at 0.75 and 1.00% axial strain which reveal a permeability reduction of 85%. Permeability remains steady during the 1.25 – 1.50% increment before being reduced by almost a factor of two, to $1x10^{-15}$ $m^2$, by 1.75% axial strain. During successive measurements made between 1.75 – 3.00% axial strain, permeability is reduced each time by 25-30% resulting in a final sample permeability of $2.1x10^{-16}$ $m^2$. As with the z-axis sample deformed at 150 MPa effective pressure, this sample shows significant strain hardening after C* that continues throughout

the experiment. Permeability evolution in the x-axis sample is broadly similar to that of the z-axis sample, in that a permeability reduction is first obvious after at the measurement taken at 0.50% axial strain. However, while the z-axis sample then undergoes further rapid permeability reduction, the x-axis sample does not show significant permeability reduction until at least 1.25% axial strain; at which point it falls by several orders of magnitude from $1.1x10^{-13}$ $m^2$ to $5.4x10^{-16}$ $m^2$ over just a 0.25% axial strain increment. In the x-axis sample, C* is observed to coincide with the permeability drop and occurs at around 1.30% axial strain. Following C*, permeability continues to fall, before stabilising after 2.50% axial strain at around $2.8x10^{-17}$ $m^2$.

## 8.3 Microstructural Observations

Figures 8-15 and 8-16 show thin-sections of compaction bands which have developed in the z-axis samples and x-axis sample, respectively, during deformation at Pe = 150 MPa. Each figure shows samples that have been deformed by increasing amounts, up to 4.5% axial strain.

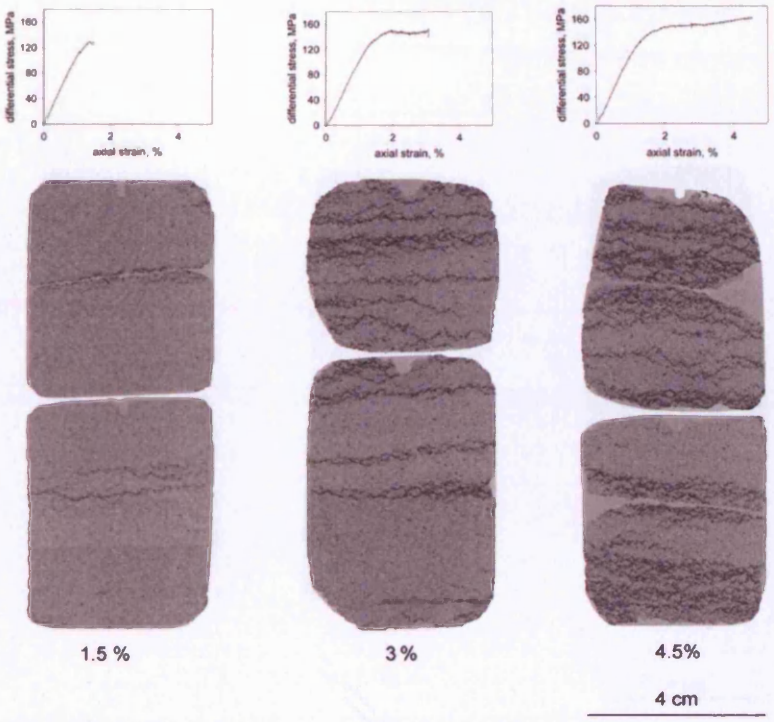


*Fig 8-15. Progressive development of compaction bands in z-axis samples deformed at Pe = 150 MPa to 1.5%, 3% and 4.5% axial strain (left to right).*

There is quite a striking contrast between the structures observed in the two orientations. From the overviews presented in figures 8-15 and 8-16, z-axis compaction bands appear relatively linear and continuous across the width of the sample, whereas the x-axis compaction bands show a greater tortuosity and less lateral continuity. Although by 4.5% axial strain compaction bands are more or less pervasive through both samples, at 3% axial strain z-axis sample appear to have sustained more extensive damage than their x-axis counterpart. It can be seen that, in the z-axis sample, compaction bands have developed through about $2/3^{rds}$ of the sample length, whereas in the x-axis sample, damage is confined to approximately $1/3^{rd}$ of the sample length.

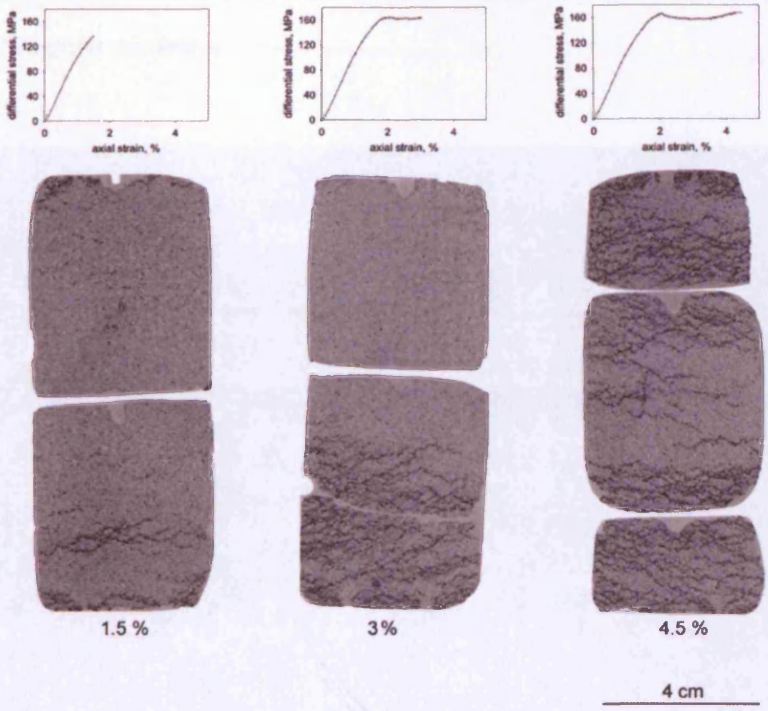


*Fig 8-16. Progressive development of compaction bands in x-axis samples deformed at Pe = 150 MPa to 1.5%, 3% and 4.5% axial strain (left to right).*

In both sample orientations, damage appears discrete rather than diffuse, with lenses of undamaged material intercalated with the compaction bands. This is more apparent in the z-axis samples, where there is a distinct spacing between compaction bands, but the structures in the x-axis samples are also clearly discrete.

### 8.3.1 Inside the Compaction Bands

Upon closer inspection, the discrete nature of the compaction bands can be observed, with damage being concentrated within a narrow zone a few mm wide. Outside of this zone, material intact and essentially undamaged relative to the compaction band. Within the compacted zones there are often lenses of undeformed material which underscores an anastomosing nature to compaction bands. Individual compaction bands can be discerned

within the 'compacted zone', and are typically <0.5 mm wide, corresponding to approximately one or two grain diameters.

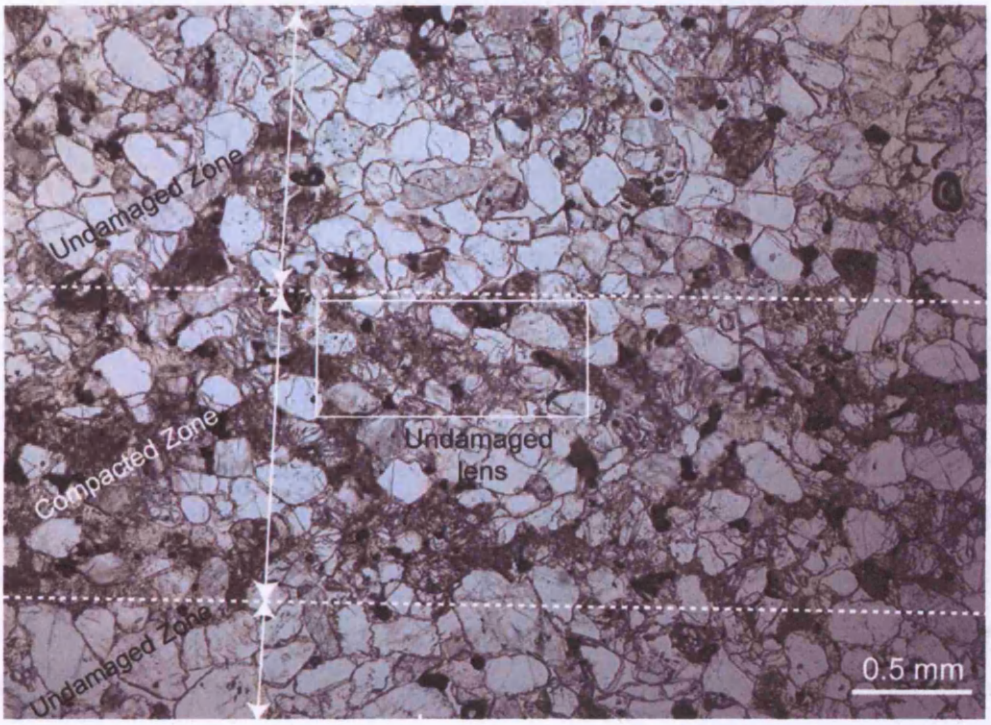


*Fig 8-17. Photo-micrograph showing a discrete compaction band within a z-axis sample, dotted lines delineate zone of compaction. Area within white box shown in detail in figure 8-21. Direction of maximum compressive stress is vertical.*

As shown above, within the compaction bands grain crushing and comminution results in significant porosity reduction as available pore space is infilled with a gouge-like material. Grains that are not entirely disaggregated often show Hertzian cracks emanating from grain contacts

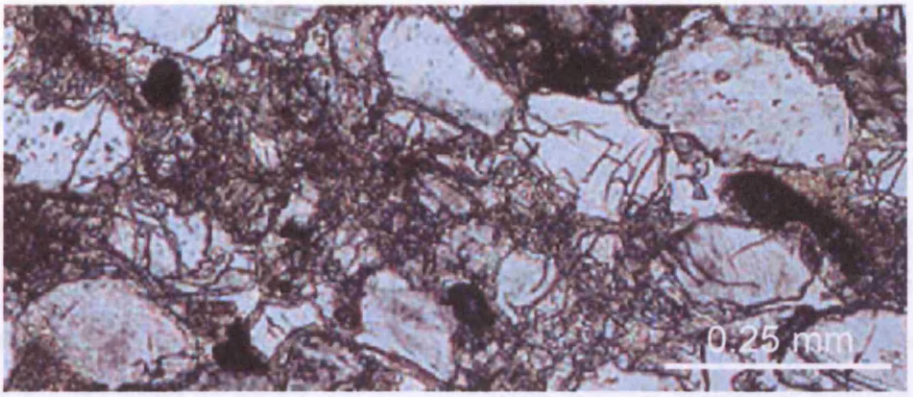


*Fig 8-18. Photo-micrograph showing intensive grain comminution and porosity reduction within a compaction band. Grains which have not been totally crushed show Hertzian cracks across their diameters. Area above shown in context in figure 8-17 Direction of maximum compressive stress is vertical.*

At the grain scale, compaction bands in both sample orientations are tortuous to some extent. However, compaction band tortuosity is more pronounced in x-axis samples than in z-axis samples. This distinction is clearly seen in the overview thin-sections (figures 8-15 and 8-16), and also in post-deformation hand-specimen (figure 8-7). The detailed micrograph of figure 8-19 shows that at the grain-scale, x-axis compaction bands may have 'amplitudes' of several diameters, whereas z-axis compaction bands have a smaller amplitude and appear to be more planar over the same lateral extent.

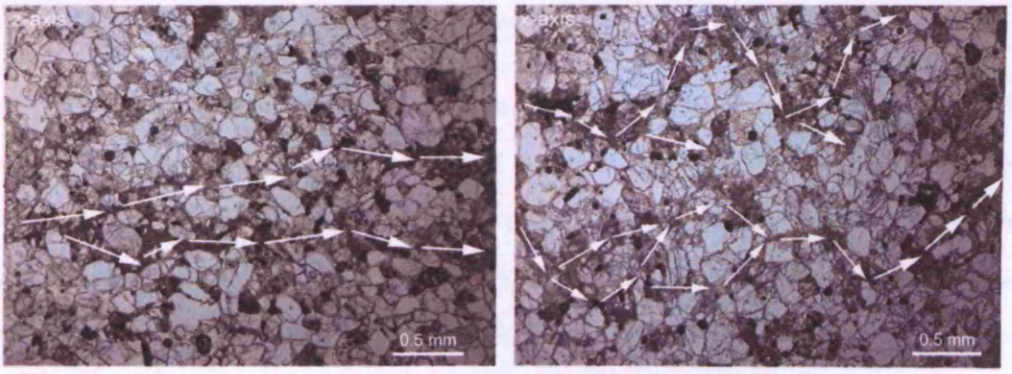


*Fig 8-19. Photo-micrograph showing the typical trace of compaction bands observed in z-axis samples (left) and x-axis samples (right). Direction of maximum compressive stress is vertical.*

# 9 Results of Acoustic Emission Locations

Having established that Diemelstadt fails by the development of compaction bands when deformed triaxially at effective pressures greater than about 100 MPa, pressure conditions of 110 MPa were selected to conduct experiments aimed at measuring the growth of individual compaction bands, through AE locations, in z and x-axis samples. A maximum of 12 channels, listed in table 9-1, were used to record AE. From the magnitude / frequency distribution of located AE events, the seismic b-value response to localised compaction was calculated.

| PZT locality | co-ordinates, mm | | | normalised directional cosines | | |
|---|---|---|---|---|---|---|
| | X | Y | Z | X | Y | Z |
| 1 | -20 | 0 | 12 | -1 | 0 | 0 |
| 2 | -14.1 | -14.1 | 24.5 | -0.705 | -0.705 | 0 |
| 3 | 0 | -20 | 37 | 0 | -1 | 0 |
| 4 | -20 | 0 | 62 | -1 | 0 | 0 |
| 5 | -14.1 | -14.1 | 74.5 | -0.705 | -0.705 | 0 |
| 6 | 0 | -20 | 87 | 0 | -1 | 0 |
| 7 | 20 | 0 | 12 | 1 | 0 | 0 |
| 8 | 14.1 | 14.1 | 24.5 | 0.705 | 0.705 | 0 |
| 9 | 0 | 20 | 37 | 0 | 1 | 0 |
| 10 | 20 | 0 | 62 | 1 | 0 | 0 |
| 11 | 14.1 | 14.1 | 74.5 | 0.705 | 0.705 | 0 |
| 12 | 0 | 20 | 87 | 0 | 1 | 0 |

*Table 9-1. PZT localities relative to the xyz co-ordinate frame used in this study.*

## 9.1 Compaction Band Growth (z-axis sample)

A z-axis sample was hydrostatically loaded to 110 MPa effective pressure conditions before an axial strain rate of $10^{-5}$ $s^{-1}$ was applied and the sample deformed to 3.5% axial strain. The P-wave anisotropy of the sample was characterised at hydrostatic pressure, before the application of any differential stress, using a pulse and receive technique to measure travel times along the 14 ray-paths illustrated and listed in figure 9-1. These data were inverted and plotted to represent the velocity structure of the material on a stereonet. The P-wave anisotropy derived from the hydrostatic velocity surveys was incorporated into the AE location algorithm. Following the characterisation of velocity structure at hydrostatic conditions, further

velocity surveys were conducted at intervals during axial loading. However, it was found that during the post-processing of AE data, changing the velocity structure of the material to reflect the influence of deviatoric stress was time intensive and resulted in minimal location improvements.

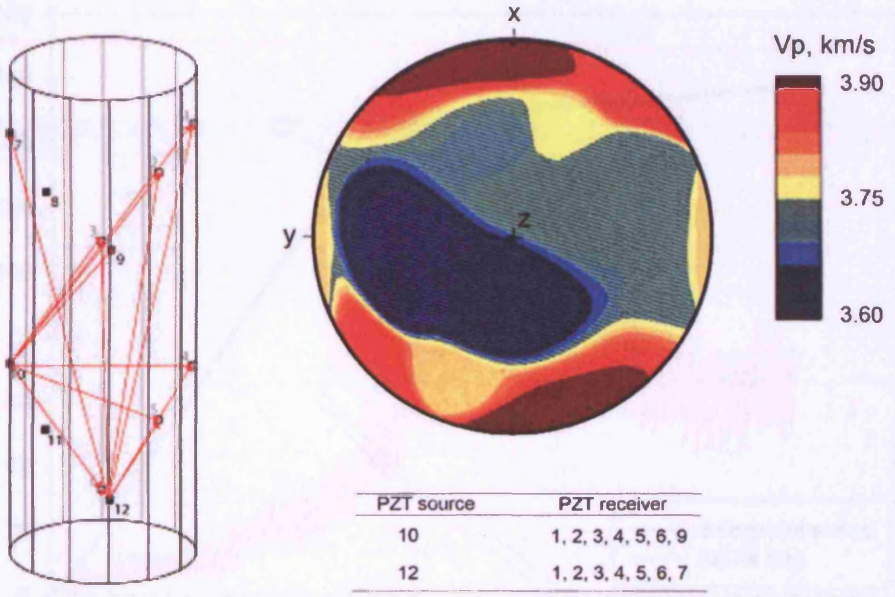


| PZT source | PZT receiver |
|---|---|
| 10 | 1, 2, 3, 4, 5, 6, 9 |
| 12 | 1, 2, 3, 4, 5, 6, 7 |

*Fig 9-1. The ray-paths used (left) to construct a velocity structure stereonet (right) of the z-axis sample at 110 MPa hydrostatic effective pressure. Table lists source and receiver localities.*

As seen on the stereonet, the p-wave anisotropy is approximately 8%, with the minimum velocity in the direction sub-normal to the XY plane. The intermediate and maximum velocities are distributed along a common great circle, sub-parallel to the XY plane.

### 9.1.2 Mechanical Data

The stress-strain curve and AE hit rate during this experiment is shown in figure 9-2, along with the time-window during which compaction band growth was observed. The sample reaches C* at around 135 MPa differential stress after 1.5% axial strain, at which point the AE hit rate begins to increase markedly. The stress-strain curve levels out by 2% axial strain, with

the AE hit rate peaking shortly after. Following this, the sample underwent strain hardening for the remainder of the experiment, reaching a peak stress of 158 MPa while the AE hit rate decreased steadily to a relatively constant value by 3% axial strain.

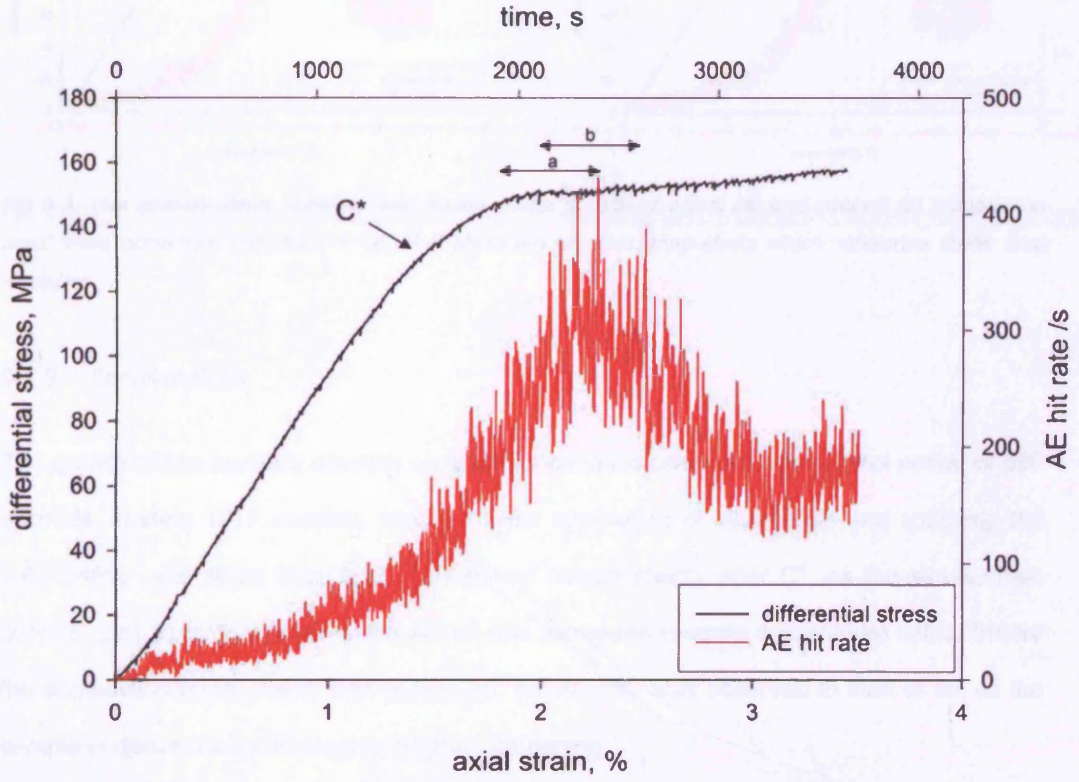


*Figure 9-2. Stress-strain curve and AE hit rate for a z-axis sample deformed to 3.5% axial strain under 110 MPa effective pressure and at an axial strain rate of $10^{-5}$ $s^{-1}$. C* marks the onset of shear enhanced compaction and the double-headed arrows marked a) and b) indicate the periods during which the first and second discrete compaction bands were observed to develop, respectively..*

Two spatially discrete compaction bands were observed to nucleate and propagate during this experiment. Although spatially discrete, the growth of both compaction bands was observed to overlap temporally as illustrated in figure 9-3. Each compaction band nucleated and propagated across the sample over about a 400 second period, allowing their individual growth to be captured by plotting the AE locations occurring during four back-to-back 125 second time-windows. Figure 9-4 shows the relationship between these time-windows and the mechanical data.

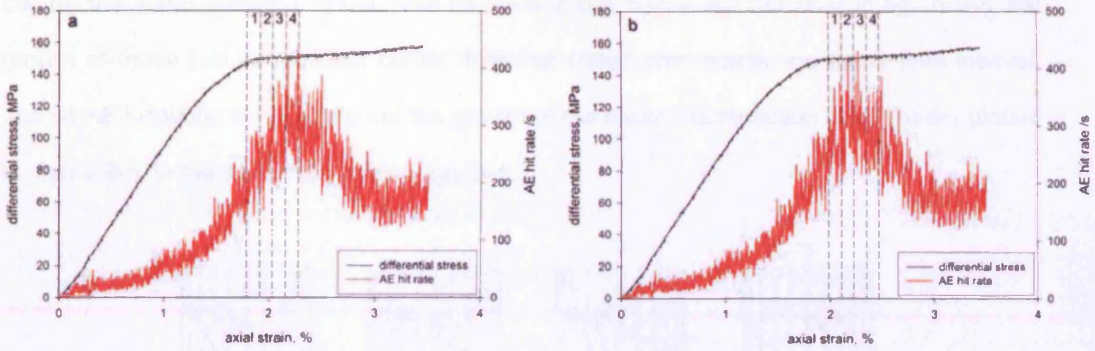


*Fig 9-3. The time-windows, labelled 1-4, during which growth of a first (a) and second (b) compaction band were observed. Figures 9-4 and 9-5 show AE location snap-shots which reference these time windows.*

### 9.1.3 Location Data

The growth of two spatially discrete compaction bands is observed over a total period of 680 seconds, starting 1917 seconds after the initial application of axial strain and spanning the 1.80-2.46% axial strain increment. This period occurs shortly after C*, as the stress-strain curve begins to plateau and as the AE hit rate increases towards a maximum value. Before the compaction band growth had completed, the AE rate was observed to start to fall as the sample underwent a subtle degree of strain hardening.

Over the duration of the entire experiment, some 31,000 events were located. However, to ensure accuracy, these events are filtered so that only those recorded independently on at least 6 transducers with a location error of less than 2 mm are considered. Applying this criteria results in 10,000 'high-quality' locations being made over the duration of the entire experiment. During each period of compaction band growth, over 1,800 high-quality locations were captured.

Growth of the first compaction band (labelled a) is shown in figure 9-4, which plots located AE events as two orthogonal elevations and a plan-view. As well as capturing the complete growth of the first compaction band, the nucleation and partial propagation of the second

compaction band (labelled b) can also be seen in this figure. As indicated in figure 9-3, the growth of these two compaction bands does not occur over exactly the same time interval, and so AE locations centred around the growth of the second compaction band (b) are plotted in figure 9-5, in the same format as figure 9-4.

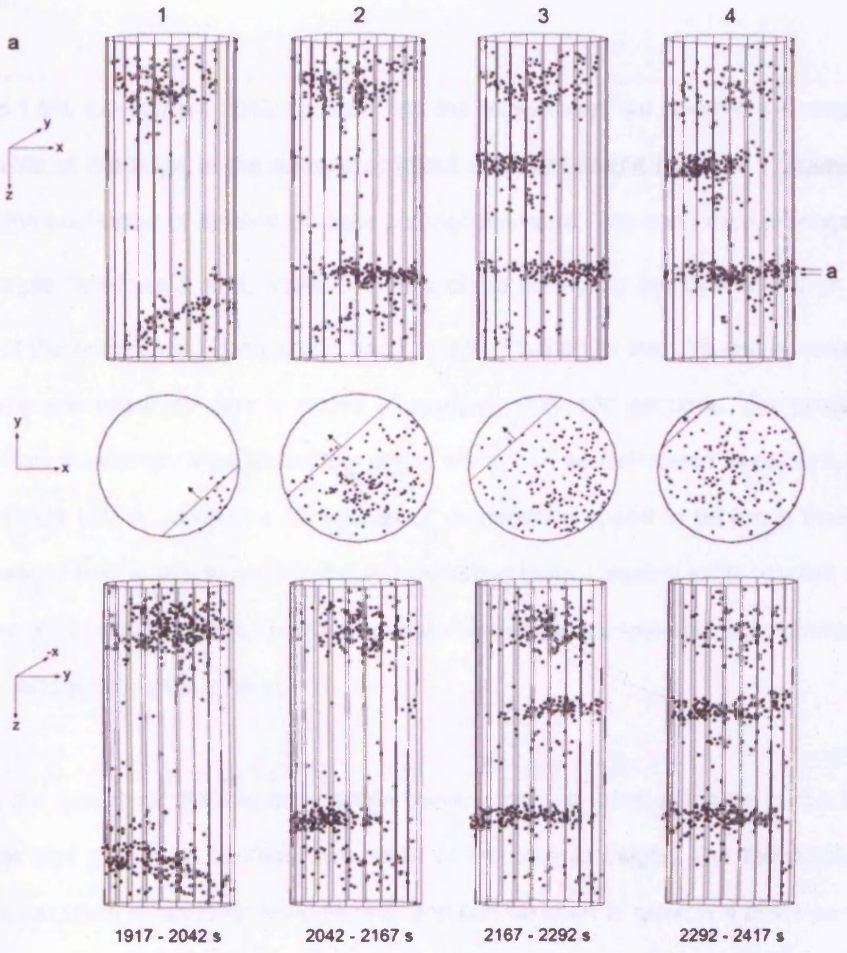


*Fig 9-4. AE locations capturing the nucleation and propagation of the first compaction band, shown as two orthogonal elevations and a plan view. The numbers at the top of the figure correspond to the windows shown in figure 9-4a, with the exact time boundaries marked at the bottom of the figure. The two arrows on the upper right of the figure indicate the extent of the data used for the plan view. The Cartesian axes indicate the orientation of the projections.*

Initially, during axial loading, two zones of relatively diffuse AE activity close to the sample ends can be identified. This may be a result of an end constraint on the sample caused by the

mismatch between the elastic modulus of the rock and that of the steel loading rams. During compactive deformation this leads to enhanced cracking and AE activity at the sample ends. By contrast, it is notable that during dilatant deformation radial constraints of the sample ends leads to reduced cracking and relative seismic quiescence at the sample ends (e.g. Benson et al., 2007).

Around 1.9% axial strain, 2042 seconds into the experiment, we observe a distinct cluster of AE events at the edge of the sample at about one-third height (window 1, figure 9-4). This marks the nucleation of the first discrete compaction band. The band then propagates across the sample (windows 2 to 4, figure 9-4) in a plane normal to the direction of $\sigma_1$. The plan views of the propagating compaction band in figure 9-5 show that the entire cross-section of the sample is traversed over a period of approximately 400 seconds. The propagating AE cluster has a relatively straight leading edge, which can be delineated to capture 95% of the located data points, allowing a calculation of propagation speed to be made through use of the temporal and spatial locations of the compaction band's leading edge (section 9.1.4). The clusters of located AE events which propagate across the sample are approximately 6 mm in vertical extent (along the z-axis).

During the growth of the this compaction band, a second compaction band can be seen to nucleate and propagate at about two-thirds of the sample height. The development of this compaction band is captured in figure 9-5, and can be seen to grow in a plane parallel to the first band, although in the almost opposite direction. Again, the compaction band nucleates at the sample edge, and, as with the first compaction band, the plan-views shown in figure 9-5 shows that the entire cross-section of the sample is traversed over about 400 seconds.

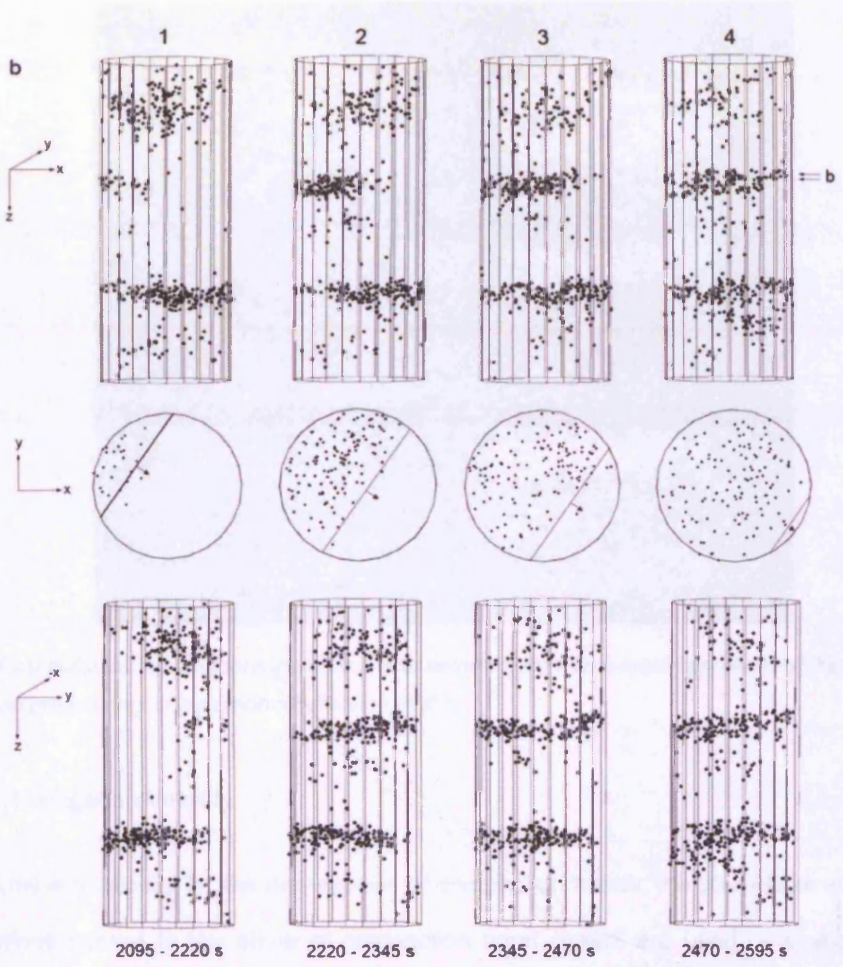


*Fig 9-5. AE locations capturing the nucleation and propagation of the second compaction band, shown as two orthogonal elevations and a plan view. The numbers at the top of the figure correspond to the windows shown in figure 9-3b, with the exact time boundaries marked at the bottom of the figure. The two arrows on the upper right of the figure indicate the extent of the data used for the plan view. The Cartesian axes indicate the orientation of the projections.*

Following the experiment, located AE events were seen to correspond to the visible damage in the z-axis sample. Figure 9-6 shows a superimposition of located AE events over a post-deformation photograph of the sample. The two discrete compaction bands can be identified, as well as the diffuse damage at the sample ends.

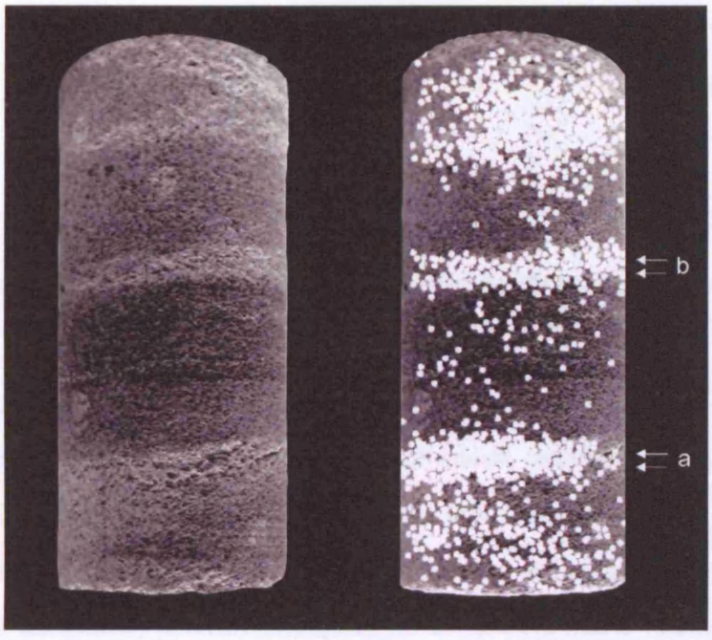


*Fig 9-6. Post-deformation photograph of the z-axis sample (left) with a superimposition of the located AE events captured during compaction localisation (right).*

### 9.1.4 Propagation Velocity

To determine a velocity for the propagation of compaction bands, the plan-views which show AE locations normal to the plane of compaction band growth are used. A spatial scale is plotted perpendicular to the orientation of the leading edge of the AE cluster, indicating the extent of compaction band growth at each time interval. The development of compaction band a) and b) are both examined in this way, as shown in figures 9-7 and 9-8, respectively.


*Fig 9-7. Movement of the first (spatially lower) compaction band's leading edge across the z-axis sample's 40 mm diameter cross-section. In each figure a distance scale is plotted normal to the time-stamped leading edge.*

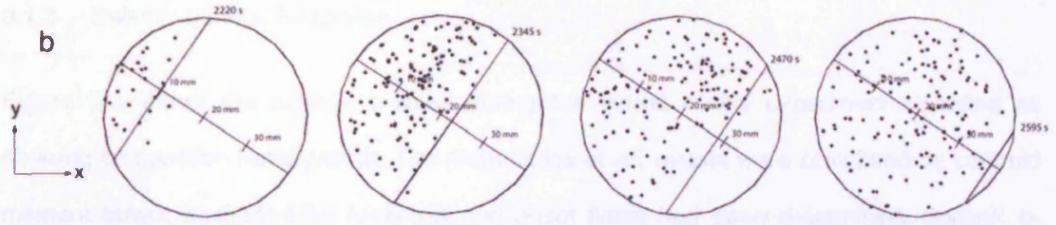


*Fig 9-8. Movement of the second (spatially higher) compaction band's leading edge across the z-axis sample's 40 mm diameter cross-section. In each figure a distance scale is plotted normal to the time-stamped leading edge.*

For both compaction bands, the average propagation speed, calculated simply as distance / time, is around 0.09 mm $s^{-1}$. It is interesting to note that both compaction bands show a similar pattern of evolution in the speed of their growth. The initial stages of development are the most rapid, with compaction band a) propagating at around 0.2 mm $s^{-1}$ during the first 125 seconds of growth and compaction band b) propagating at 0.1 mm $s^{-1}$ over the same initial 125 seconds. Subsequent growth is substantially slower, at 0.03 mm $s^{-1}$ for compaction band a) and 0.05 mm $s^{-1}$ for compaction band b). The rate of growth then appears to increase during the final stages of compaction band development, proceeding at 0.06 mm $s^{-1}$ for compaction band a) and at 0.07 mm $s^{-1}$ for compaction band b).

### 9.1.5 Seismic b-value Response

Figure 9-9 shows the seismic b-value during the period of the experiment identified as showing compaction band growth. The magnitudes of AE events were calculated by centroid moment tensor analysis after locations and onset times had been determined. Seismic b-values were then calculated using a rolling-window of 200 events, which gives a standard error of less than 10%.

As can be seen, during compaction localisation the b-value remains essentially constant (within the standard error) at around 1.6. This suggests that the scale of cracking remains more or less constant during compaction band propagation.

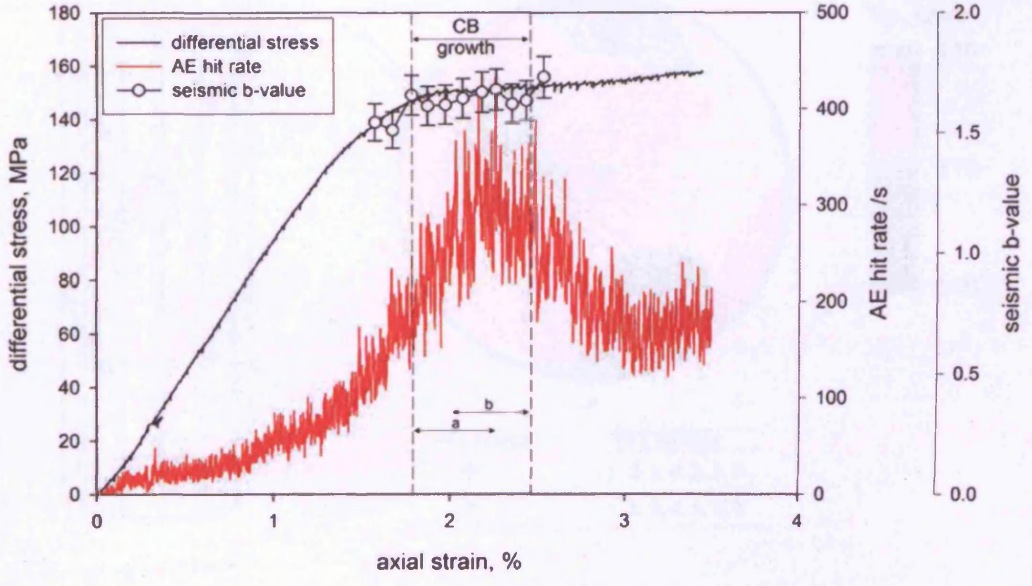


*Fig 9-9. Graph showing the seismic b-value response to the inception of compaction bands during the period indicated by the vertical dashed lines. Double headed arrows a) and b) represent the periods of growth associated with compaction bands a) and b), respectively.*

## 9.2 Compacting Shear Band Localisation (x-axis sample)

In the same manner as for the z-axis sample, an x-axis sample was hydrostatically loaded to 110 MPa effective pressure before an axial strain at a rate of $10^{-5}$ $s^{-1}$ was applied to the sample until it had deformed by 4.5% axial strain. Prior to the application of differential stress, the sample was characterised in terms of its p-wave velocity structure by performing a pulse and receive survey along the ray paths illustrated in figure 9-10, the sample was found to show 8% anisotropy of p-wave velocity. As shown in the stereonet, the x-axis sample has a fast direction approximately parallel to the core-axis, coincident with the orientation of the minimum and intermediate axes of pore-fabric anisotropy.

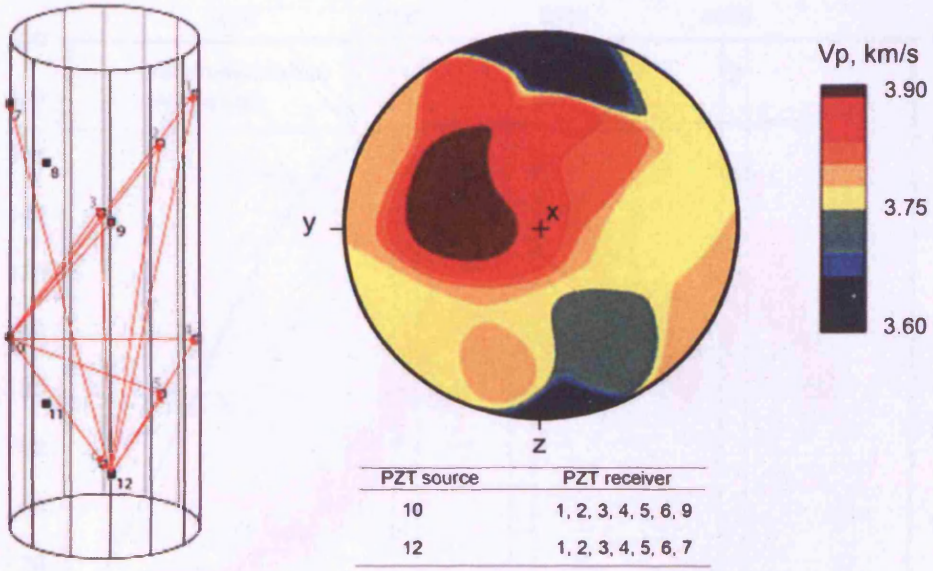


| PZT source | PZT receiver |
|---|---|
| 10 | 1, 2, 3, 4, 5, 6, 9 |
| 12 | 1, 2, 3, 4, 5, 6, 7 |

*Fig 9-10. The ray-paths used (left) to construct a velocity structure stereonet (right) of the x-axis sample at 110 MPa hydrostatic effective pressure. Table lists source and receiver localities.*

### 9.2.1 Mechanical Data

The stress-strain curve of this experiment is shown in figure 9-11, along with the associated AE data. The sample under test reaches C* at about 150 MPa differential stress, at a point where the AE rate starts to increase and the stress-strain curve begins to deviate markedly from being pseudo-linear. Following C*, the stress-strain curve begins to level out, and by 1.9% axial strain the sample under test can no longer support an increasing differential stress, and a peak stress of just over 170 MPa is attained. During this experiment, the AE rate shows three distinct surges of activity, the first beginning at C* and peaking just after 2% axial strain, the second beginning at 2.6% axial strain and peaking at 3.0% axial strain, and the final surge starting at 3.6% axial strain and peaking at 4.1% axial strain.

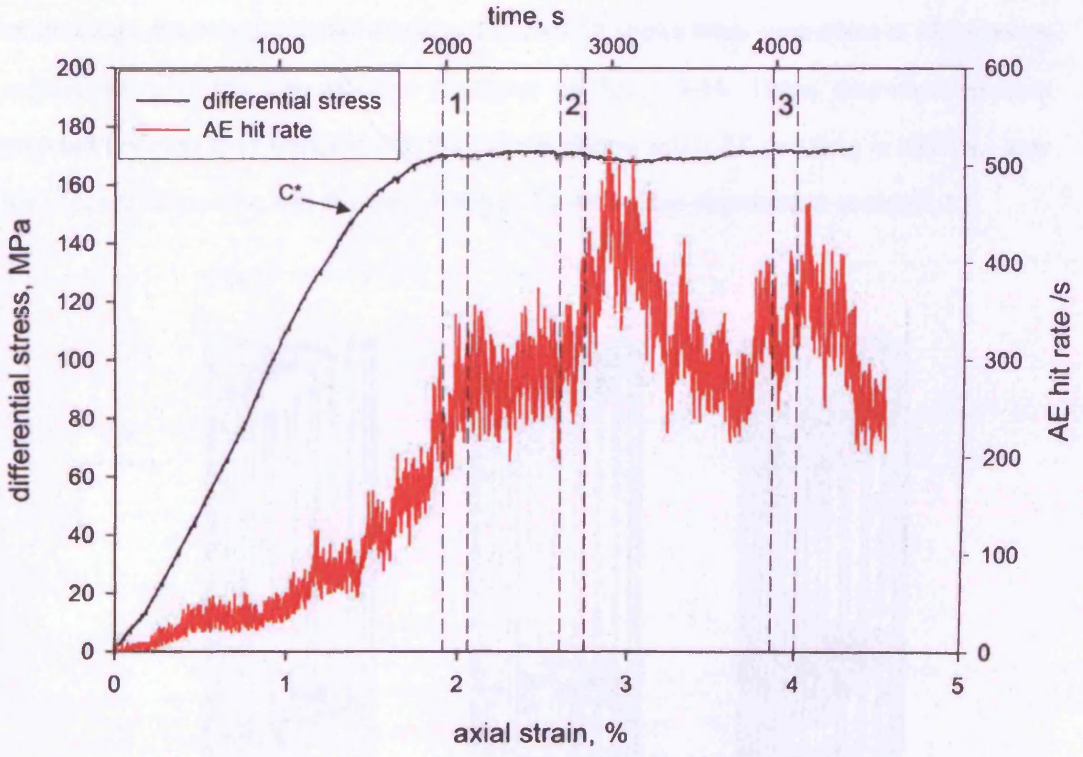


*Figure 9-11. Stress-strain curve and AE hit rate for a x-axis sample deformed to 4.5% axial strain under 110 MPa effective pressure and at an axial strain rate of $10^{-5}$ $s^{-1}$. C* marks the onset of shear enhanced compaction and the time-windows labelled 1, 2 and 3 indicate the periods during which AE locations were most tightly grouped (see text for detail).*

### 9.2.2 Location Data

In contrast to the z-axis sample, where the propagation of two compaction bands was observed in planes normal to $\sigma_1$, the x-axis sample does not show any extensional growth of compaction bands across the sample. Rather, more diffuse groupings of AE events are observed inclined to $\sigma_1$ by about 60°. With increasing axial strain, the inclined AE cluster migrates down the sample axis, remaining parallel to its prior orientation. Although the general form of the AE clusters located in the x-axis sample appear relatively diffuse (in comparison to the AE clusters observed in the z-axis sample), there are periods during loading where the AE clusters becomes more tightly grouped, and organised in more distinct and relatively narrow planes. This suggests that phases of strain localisation are occurring during the development of otherwise diffusely distributed damage. Figure 9-12 shows three snap-shots of AE locations corresponding to the time-windows illustrated on figure 9-11. These time-windows were selected because they coincide with the periods during which AE grouping is tightest, they also appear to coincide with the rising limbs of the AE surges described in section 9.2.1.

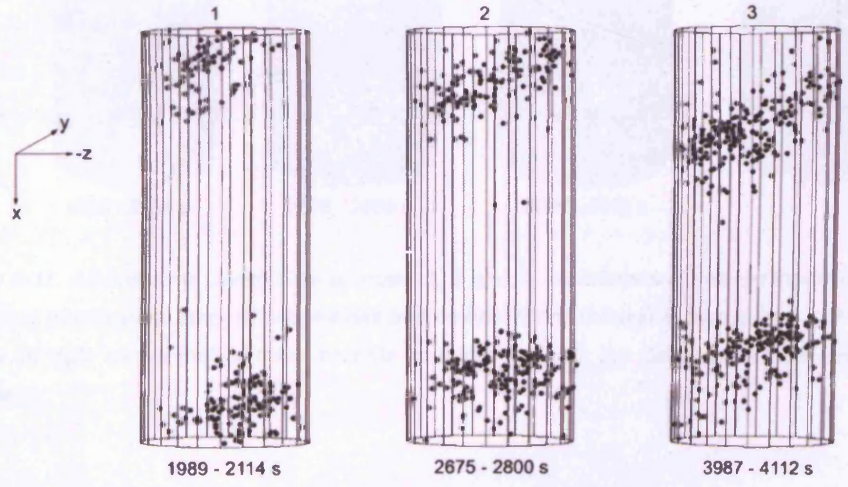


*Figure 9-12. AE locations during the time-windows indicated on figure 9-11. The times at the bottom of the figure are in seconds since the beginning of loading, and represent the boundaries of the time-windows 1, 2 and 3.*

Following the end of the experiment, the sample was recovered and examined for localised damage. Localised damage appears as compacting shear-bands inclined to $\sigma_1$ by about 60°. Although the damage is not oriented normal to $\sigma_1$, there is no macroscopic shear-offset visible across the structures, and therefore they are interpreted as high-angle compaction bands. Three such deformation bands can be identified (labelled a, b and c in figure 9-13), oriented parallel to one another and more or less equally spaced along the sample length. AE locations were found to correlate very well with the orientation of visible damage sustained by the sample, with the best-fit lines of each inclined AE cluster matching up almost perfectly with the three visible structures seen in the sample post-deformation.

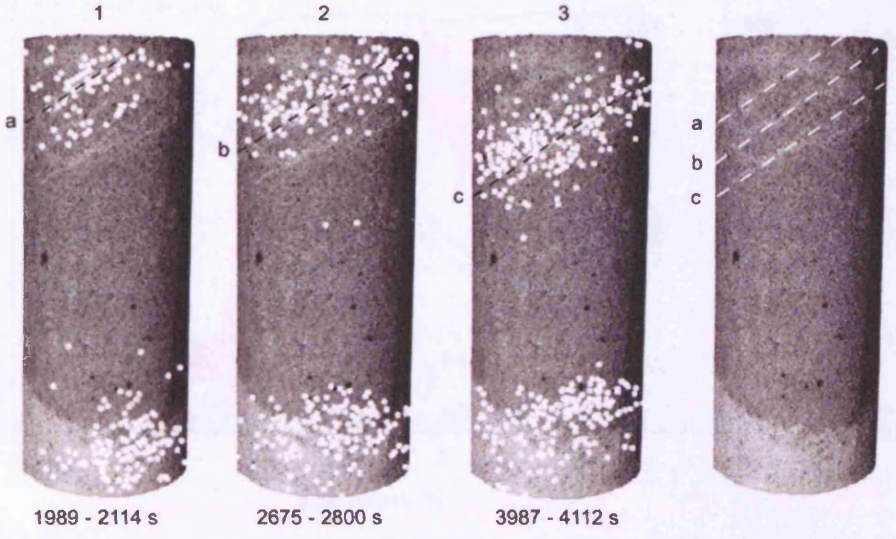


*Figure 9-13. AE locations during time windows 1, 2 and 3 superimposed onto an image of the sample recovered after testing. Each AE cluster has been a best-fit line through it, labelled a b and c. The image on the far right shows that all three best-fits correlate well with the location of visible damage on the sample.*

### 9.2.3 Seismic b-value Response

The seismic b-value of located AE events during the experiment on the x-axis sample are plotted in figure 9-14. In comparison to the b-values plotted during compaction localisation in the z-axis sample, there appears to be more variation during deformation of the x-axis sample, with the b-values falling between 1.4 and 2.2. Although there is no striking trend to the b-value response during deformation of the x-axis sample, there does appear to be a gradual increase in b-value over the course of the experiment.

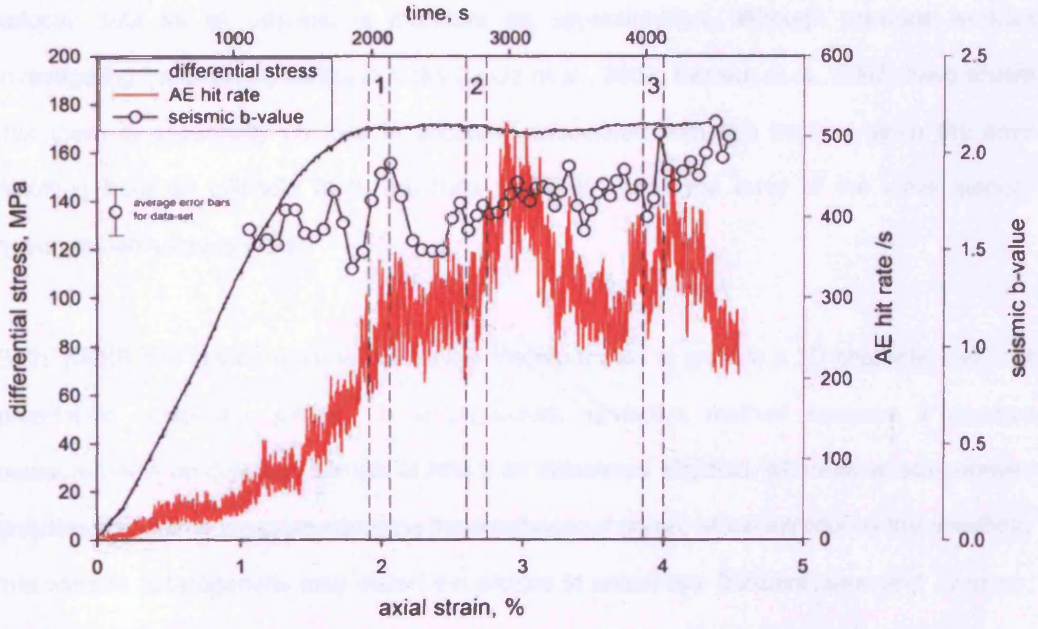


*Figure 9-14. Graph showing the seismic b-value response during the localisation of compaction bands in the x-axis sample. The time-windows 1, 2, 3 are shown for reference along with the average error-bars associated with the data set.*

# 10 Discussion of Results

## 10.1 Anisotropy of Diemelstadt Sandstone

### 10.1.1 Comparisons Between pAMS and Wave Velocity Measurements at Ambient Pressure

Anisotropy of magnetic susceptibility is described by a symmetric second rank tensor, and can therefore be represented as an ellipsoid. The anisotropy of P and S-wave velocity has also been fitted to an ellipsoid, although, as noted in chapter 3, velocity measurements reflect elastic anisotropy which can only be fully described by a fourth rank tensor. Representing the velocity data as an ellipsoid is therefore an approximation, although previous workers investigating transversely isotropic rocks (Louis et al., 2003; Benson et al., 2003) have shown that there is essentially no loss in accuracy associated with this method since the error resulting from an ellipsoid fit to the data (<2%) is within the error of the wave velocity measurements themselves.

Both pAMS and elastic wave velocities are therefore able to provide a 3D characterisation of pore-fabric anisotropy. pAMS is a particularly attractive method because it requires measurements on only one sample to return an anisotropy ellipsoid, whereas velocity derived anisotropy requires measurements on three orthogonal cores, which introduces the possibility that sample heterogeneity may distort the picture of anisotropy (Rasolofosaon and Zinszner, 2003). However, azimuthal measurements around three orthogonal cores incorporates a degree of redundancy by virtue of the fact that several measurements from core to core are in the same direction. The data show that measurements made in the same direction but on different cores are very similar (less than 1% variation), which suggests that Diemelstadt sandstone is relatively homogeneous. Nevertheless, the levelling technique described in section 6.2 was used to account for these small variations, essentially allowing the measurements around three orthogonal cores to be considered as being from the same sample.

The average pore-fabric anisotropy returned from pAMS measurements is 3.4%, which is a lower value than given by the various velocity measurements, which are between 5.6 – 5.9% for dry conditions. It is known that pAMS measurements often underestimate the real, physical void space anisotropy as a result of the demagnetising effect within the magnetic ferrofluid (Collinson, 1983). However, it should also be noted while pAMS reflects only the anisotropy of the porosity, wave velocity measurements reflect the anisotropy of the rock matrix as well as that of the pores. Given that the two methods are sensitive to different parameters, a slight deviation between the two measures is not unexpected.

### 10.1.2 Applying the Equivalent Pore Concept

As noted in section 3.2.3, the demagnetising effect means that the magnitude of the principal susceptibility axes from pAMS cannot be directly equated to the magnitude of the principal void-space axes without a correction first being applied. Hrouda et al. (2000) attempted to link theoretically the measured lineation and foliation parameters from pAMS to an equivalent pore geometry (of axes a>b>c) that would result in the observed lineation and foliations values in the absence of demagnetising effects. Application of the equivalent pore concept to the Diemelstadt sandstone pAMS data is plotted in figure 10-1.

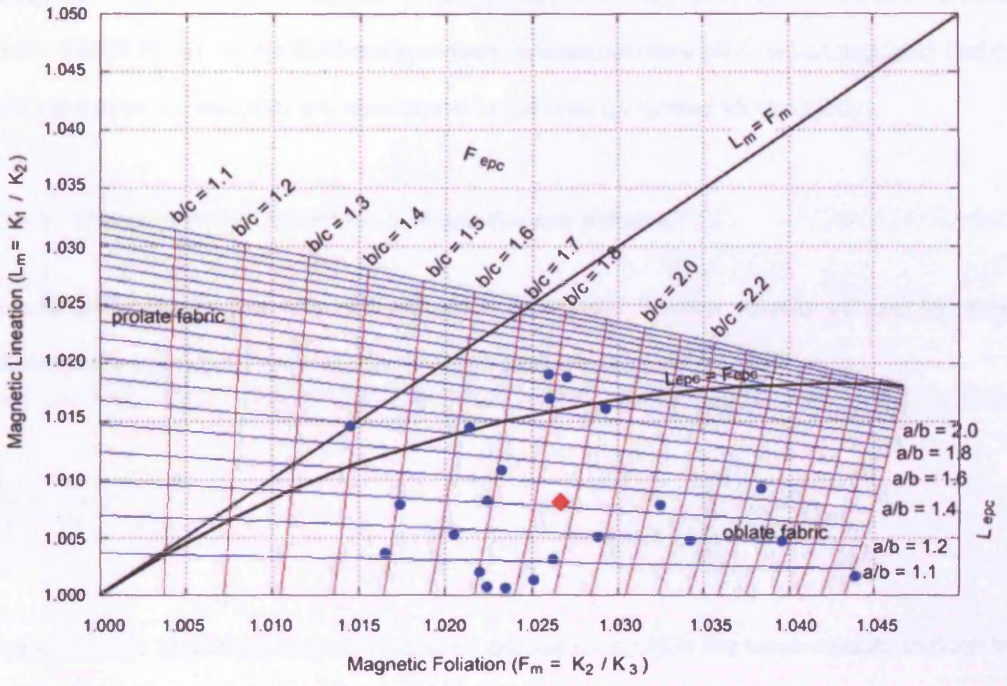


*Fig 10-1. Flinn plots showing the EPC applied to pAMS data using a ferrofluid concentration of 5%. Red diamond denotes the average.*

The graph shows a grid of constant ellipsoid geometry ratios ($L_{epc}$ = a/b and $F_{epc}$ = b/c) representing the equivalent pore to which the plotted pAMS data points relate. The average lineation and foliation is represented by the red diamond, and corresponds to an oblate equivalent pore fabric of a/b = 1.32 and b/c = 1.86. To return a value of anisotropy from the EPC, the ratio a/c (analogous to $K_{max}/K_{min}$) is given by a/c = a/b x b/c = 2.46. This equivalent pore anisotropy of 246% is at great odds with the anisotropies derived from velocity measurements (~6%) and directly from pAMS (~3.5%). The same issue was encountered by Benson (2004), and motivated a study (Jones et al., 2006) to test the accuracy of the EPC by using synthetic void-space of controlled dimensions saturated with ferrofluids of controlled concentrations. They found that the EPC accurately models void-space geometry only when high concentrations of ferrofluid are used as the saturating medium. In this study, as is the standard in pAMS measurements on high porosity rocks, a diluted ferrofluid of low concentration (5%) is used so as not to overload the sensitive susceptibility bridge used to

make the measurements. Jones et al. (2006) conclude that the threshold ferrofluid concentration for which the EPC works reliably is approximately 50%, which suggests that the EPC cannot be applied with any confidence to the data generated for this study.

### 10.1.3 Effects of Water Saturation on P and S-wave Velocity

It is tempting to analyse the 18% increase in average P-wave velocity caused by water-saturation by using the time average equation proposed by Wyllie (1958):

$$\frac{1}{Vt} = \frac{\phi}{Vf} + \frac{1-\phi}{Vm}$$

where $Vt$ is the bulk wave-velocity through a porous rock, $Vf$ is the wave-velocity through the saturating fluid, $Vm$ is the velocity through the rock forming mineral and $\phi$ is the rock porosity.

The relationship above assumes that the bulk velocity through a porous rock is the sum of the travel time through the rock matrix and through the pore-fluid. Water is a stiffer fluid than air, and therefore P-waves are transmitted faster in water than air. This results in a water saturated rock having a greater bulk P-wave velocity than a dry (air saturated) rock. Taking the P-wave velocity through water at ambient pressure and temperature as 1482.3 m/s (Lubbers and Graaff, 1998), Wyllie's equation returns a velocity of 4118 m/s for the solid component of Diemelstadt sandstone. This theoretical prediction is lower than the typical P-wave velocity range of 5480 – 5950 m/s reported for sandstone mineral phases (Mavko et al., 1998). This discrepancy can be explained by considering the seismic ray theory assumptions behind the time average equation; Mavko et al. (1998) note that the total transit time can only be expressed as the sum of each phase's transit time when the wavelength is small relative to the rock's grain and pore size and when the rock's pores and grains are arranged as homogeneous layers perpendicular to the ray path. Neither of these assumptions are valid,

and therefore the applicability of this method is questionable. Furthermore, the time average approach is best suited to measurements made at high effective pressure (not ambient conditions, as is the case here), because a very small porosity fraction at low pressure has a compliance that may have a very large (disproportionate) effect on velocity. This compliance is removed under high pressure conditions, allowing a more accurate correlation between porosity and velocity.

There is no significant deviation in S-wave velocities as a result of water-saturation, which is consistent with the theory that fluids cannot support any shear stress. Therefore in the relationship:

$$V_s = \sqrt{\frac{\mu}{\rho}}$$

where $V_s$ is S-wave velocity, $\mu$ is the shear modulus and $\rho$ the density of the medium, when the medium is a fluid, the shear modulus reduces to zero and S-waves are not transmitted through the pore-space, resulting in the S-wave velocity being the same through dry and saturated rock.

If one considers anisotropic pores being filled with a stiffer isotropic fluid, such as is the case when water replaces air as the saturating fluid, then the P-wave velocity anisotropy will be reduced. In the same way, it can be imagined that if the anisotropic pores were filled with the matrix material, then there would be no velocity anisotropy at all (Louis et al., 2003). The pAMS and velocity data both suggest an oblate, and therefore anisotropic, pore-fabric. This is supported by the reduction in P-wave anisotropy observed when the samples are saturated with water (P-wave anisotropy falls by up to 55% upon saturation with water).

Plotting the variation between dry and water saturated P-wave velocities as a function of azimuth (figure 10-2) reveals that the maximum velocity differences are observed in directions sub-parallel to the z-axis, at around 0° and 180° azimuth. In the xy plane, the variation between dry and saturated P-wave velocity remains essentially constant as a function of azimuth. This suggests that the xy plane is quasi-isotropic, which is not unexpected since this is the bedding plane.

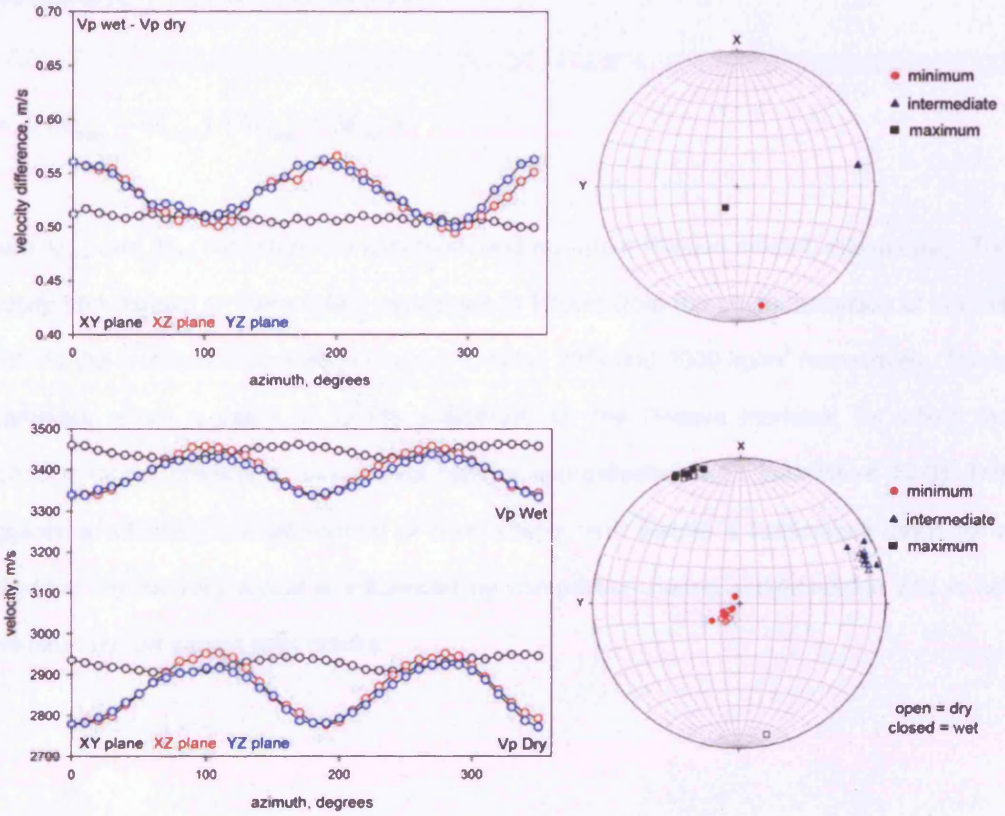


*Fig 10-2. Variation of P-wave velocity, as a function of azimuth, between dry and water saturated cores of Diemelstadt sandstone with stereonet showing principal directions (top). Original P-wave data for dry and saturated cores, with stereonet showing principal directions (bottom).*

### 10.1.4 Kachanov Model

The Kachanov (1993) inclusion model, as applied by Louis et. al (2003) and Baud et al. (2005), can be used to estimate the pore aspect ratio of a material from measurements of the

anisotropy of the P-wave modulus and the porosity of the material (figure 10-3). The Kachanov model was developed for dry inclusions, so it is applied to the dry P-wave velocity data.

The P-wave modulus ($M$) is defined as $M = \rho Vp^2$, where $\rho$ is the bulk density, and $Vp$ the P-wave velocity. By treating all dry azimuthal velocity data in this way, the anisotropy of the P-wave modulus, $\gamma$, is then calculated as:

$$\gamma = 2(M_{\max} - M_{\min})/(M_{\max} + M_{\min})$$

where $M_{max}$ and $M_{min}$ represent the maximum and minimum P-wave moduli, respectively. The porosity and density of Diemelstadt sandstone is known from the characterisation of sample cores via the methods described in chapter 5, being 23% and 2000 kg/m$^3$ respectively. These parameters return a value of 12.7% anisotropy for the P-wave modulus, for which the Kachanov model predicts a pore-aspect ratio of approximately 0.83 (see figure 10-3). This suggests a relatively low anisotropy of pore shape, and seems a reasonable value for a sandstone whose void space is influenced by compaction during sedimentation and is not dominated by low aspect ratio cracks.

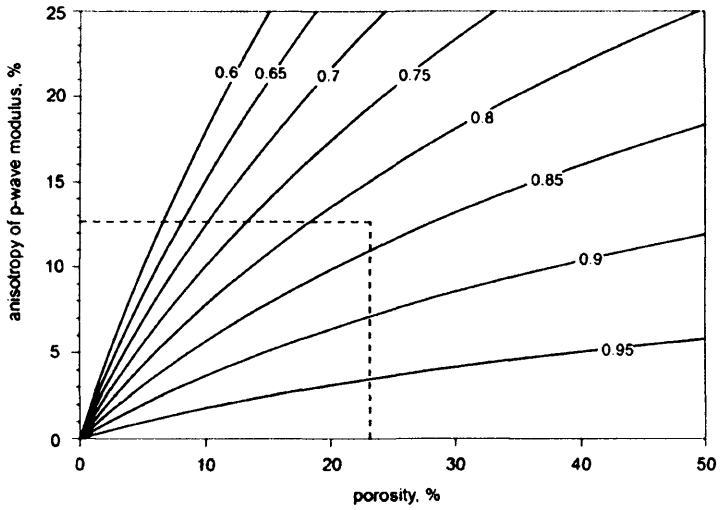


*Fig 10-3. Kachanov model showing anisotropy of p-wave modulus as a function of porosity. The numbered curves indicate different pore aspect-ratios. Diemelstadt sandstone falls between 0.8 and 0.85.*

### 10.1.5 Insights from Elevated Hydrostatic Measurements

The ambient pressure measurements of anisotropy, discussed in the previous sections, allows measurements along samples cored in the z, y and x-axes to be considered as measurements in the minimum, intermediate and maximum directions of anisotropy, respectively. Based on this, experiments under hydrostatic conditions were used to characterise anisotropy in terms of both elastic wave velocities and permeability.

Results show that the anisotropy of Diemelstadt sandstone is preserved until at least 250 MPa hydrostatic pressure. Under increasing hydrostatic pressure, Diemelstadt sandstone shows no significant change in permeability along the x, y and z-axes, despite the monotonic porosity reduction that occurs over the same pressure range. This suggests that the permeability, or connectivity, of Diemelstadt sandstone is not controlled by microcracks, which typically close when subjected to relatively modest pressures (Gueguen and Palciauskas, 1994), but by more equant pores which are not closed by the application of isotropic pressure. The

essentially constant values of permeability in the three orthogonal direction result in the anisotropy of permeability also being essentially constant, at around 40%.

Under increasing hydrostatic pressure, elastic wave velocities increase at a decreasing rate. This is most pronounced during the initial 60 MPa increase in pressure. This is a typically observed trend, and can be attributed to the preferential closure of low aspect ratio pores under the influence of relatively low pressure; as the material stiffens, successive increases in effective pressure result in diminishing velocity increases. Azimuthal velocity measurements indicate greater compliance in the z-direction and a stiffer material in the xy-plane. Axial wave velocities measured under increasing hydrostatic pressure are entirely consistent with this observation, with the greatest percentage increase occurring in the z-direction (increase of 17% for P-wave, 14% for S-wave) and approximately equal percentage increases in the x and y-directions (12% for P-wave, 11% for S-wave). This results in a decrease in velocity anisotropy as a function of increasing hydrostatic pressure. The combination of grain and sample size ensures that at least 10 grain diameters per wavelength are present during elastic wave measurements. This ensures that the advancing wavefront sees the rock as a single homogeneous medium rather than as a collection of individual rock grains whose preferred crystallographic orientation may influence measurements of seismic anisotropy.

### 10.1.4 Conclusions

Although there are difficulties in relating the pAMS data to the theoretically predicted equivalent pore geometry, there is good agreement on the principal directions of pore-fabric anisotropy derived from both pAMS and wave velocity measurements. Both measurements show a minimum principal direction oriented sub-parallel to the z-axis, with the maximum and intermediate directions being distributed in the xy-plane relative to the general co-ordinate frame used in this study. Wave velocity data show a clear distinction between maximum and intermediate directions, whereas pAMS data show intermediate and maximum directions that scatter broadly along the same plane. Initially there appears to be an inconsistency between

the pAMS and wave velocity data. The pAMS data show a minimum void-space direction normal to the bedding plane and a maximum and intermediate void-space direction in the plane parallel to bedding. Since velocity is much reduced by the presence of void space, the pAMS data imply that the maximum wave velocity direction should be normal to the bedding plane. However, the velocity data show that the fast direction is parallel to the bedding plane. This can be explained by considering the idealised organisation of void-space within a sedimentary rock, where grains have been deposited by a current such that their long axes are parallel to flow direction with porosity arising from the packing arrangement of grains (fig 10-4).

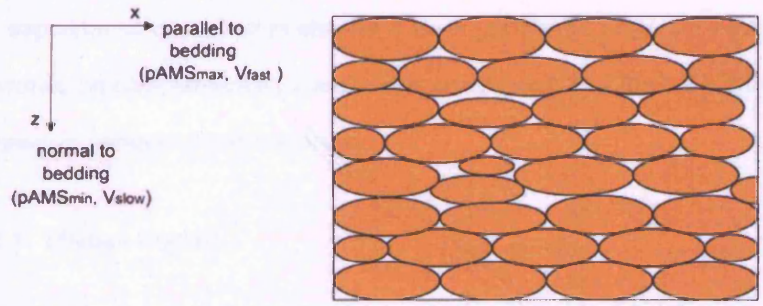


*Fig 10-4. Schematic diagram showing the grain / porosity distribution for a transversely isotropic rock in cross-section.*

This situation leads to an anisotropic distribution of grain contacts, with more grain-pore and grain-grain interfaces encountered per unit distance in the direction normal to bedding than the direction parallel to bedding, resulting in a lower material stiffness in the direction normal to bedding relative to the direction parallel to bedding. This directly influences wave velocities, as they are strongly dependent on elastic properties, and results in the fast direction coinciding with the stiffer, parallel to bedding plane.

Permeability, $k$, and elastic wave velocity, $V$, measurements at elevated hydrostatic pressure show that along x, y and z-axis cores the relationships $k_x > k_y > k_z$ and $V_x > V_y > V_z$ exist,

which is to be expected since pAMS and radial velocity measurements have revealed the x, y and z directions to be the maximum, intermediate and minimum principal directions. The positive correlation observed between magnitudes and directions from measurements of permeability, pAMS and velocity is in agreement with similar comparative studies made using these techniques (Louis et al., 2003; Benson et al., 2003). The confirmation of anisotropy directions by independent techniques provides confidence that the x and z coring directions used for triaxial experiments are appropriate for investigating the influence of anisotropy on compactive deformation.

## 10.2 Influence of Anisotropy on Deformation

The experiments described in chapter 8 were performed under a range of effective confining pressures, on complementary z and x-axis cores, such that the transition between dilatant and compactive behaviour was traversed.

### 10.2.1 Dilatant Regime

Pore volumometry shows that under relatively low effective pressure, the action of differential stress initially results in compactive deformation. Further deformation results in C', the onset of shear-induced dilation, reflecting a transition from predominantly compactive mechanisms to predominantly dilatant mechanisms. Results show that in the dilatant regime there is no obvious difference in sample strength as a function of orientation, although the sample strength in both orientations is positively correlated with effective pressure (fig 10-5).

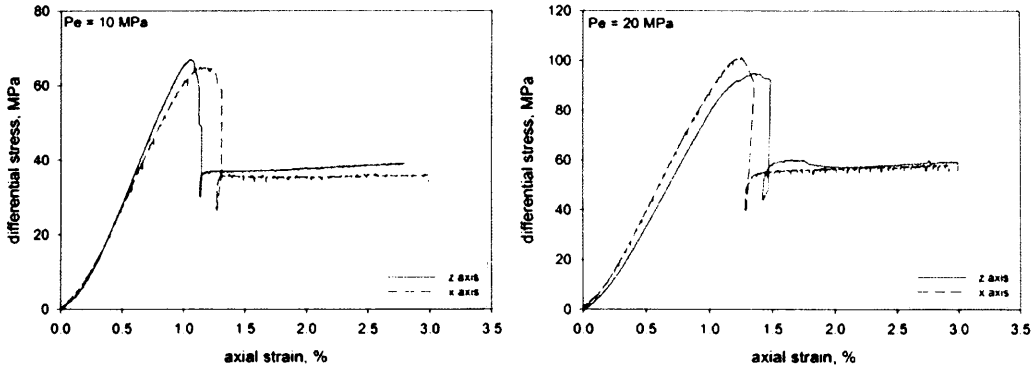


*Fig 10-5. Comparison between the stress-strain curves of z and x-axis samples of Diemelstadt in the dilatant regime at 10 MPa (left) and 20 MPa (right) effective pressure.*

While Diemelstadt sandstone shows no apparent dependency of brittle strength on sample orientation, previous workers (Baud et al., 2005) found that samples of Rothbach sandstone deformed normal to bedding (cf. z-axis) in the brittle regime showed a consistently greater mechanical strength than those cored parallel to bedding (cf. x-axis). Similar results are also reported for Adamswiller sandstone (Gatelier et al., 2002). Both of these sandstones are from the Vosges region of France, and show directional alignment of mica in the bedding plane, which may control the strength of the material. However, not all data in the literature shows this trend; Dunn et al. (1973) observe that for Kayenta sandstone and Cutler sandstone, samples are stronger when deformed parallel to bedding, although the same study reports the opposite trend for Navajo sandstone (fig 10-6). Baud et al. (2005) note that a micromechanical model to explain these differences in brittle strength requires more detailed mechanical and microstructural data.

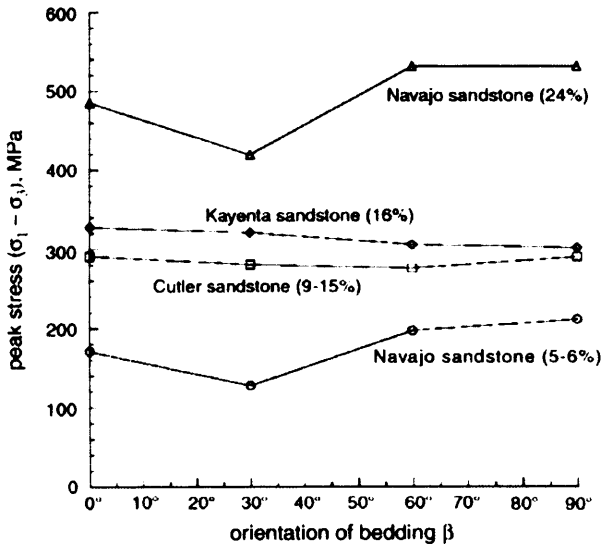


*Fig 10-6. Data from Dunn et al. (1973) showing peak stress as a function of bedding angle to $\sigma_1$ for various sandstones with porosities indicated. From Baud et al., 2005.*

### 10.2.2 Transition to Compaction

As effective pressure is increased, deformation makes a transition from the shear-induced dilation regime to the shear-enhanced compaction regime, and a distinct trend in strength anisotropy begins to emerge; with x-axis samples consistently stronger than their z-axis counterparts. These results are shown in figure 10-7 with the data from both sample orientations plotted on the same axes. The yield stresses from these experiments, and those in the dilatant regime (C' and C*), were discerned in chapter 8, and are plotted in PQ space in figure 10-8.

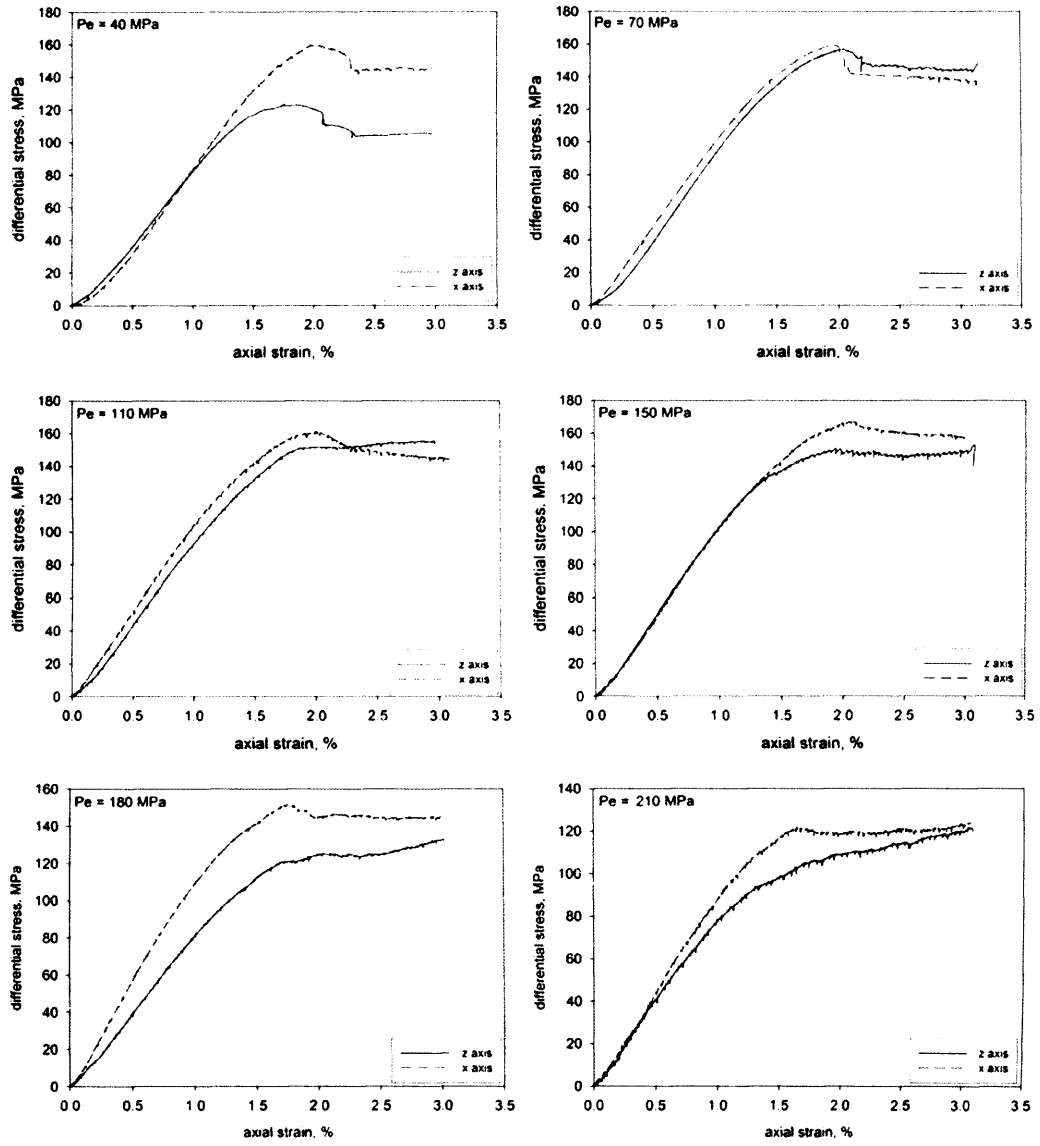


*Fig 10-7. Comparison between the stress-strain curves of z and x-axis samples in the compactive regime at Pe conditions in the 40 – 150 MPa range.*

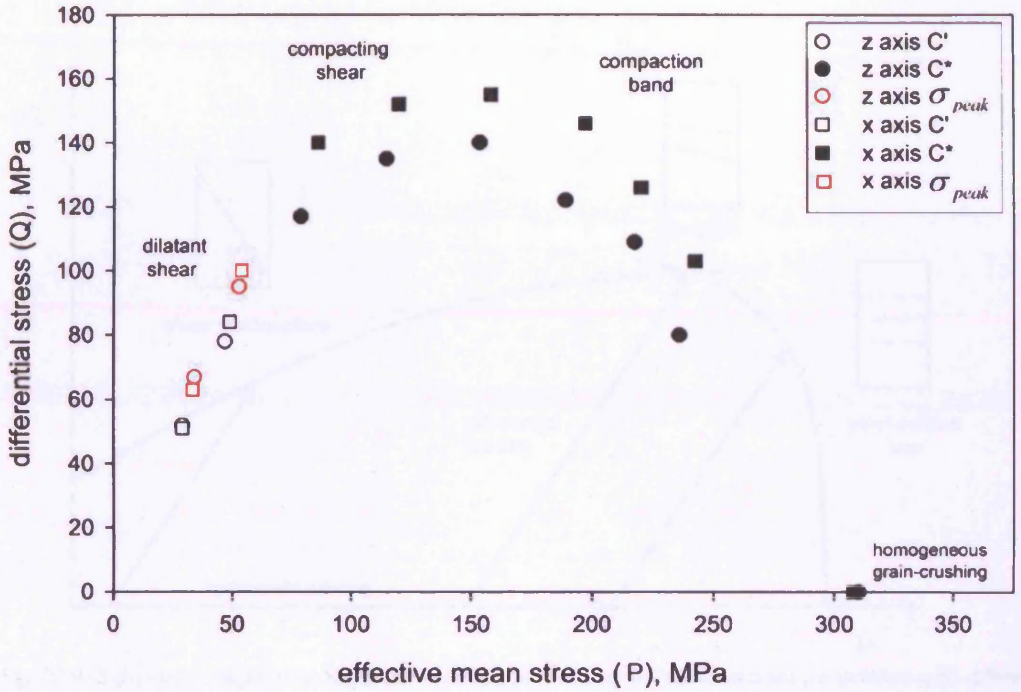


*Fig 10-8. Stress states plotted in PQ space at peak stress (red symbols) and yield (black symbols) in the dilatant (open symbols) and compactive (closed symbols) regimes. The associated deformation styles are also noted.*

In the dilatant faulting regime (Pe = 10 – 20 MPa) the peak stresses are also plotted, which define the Mohr-Coulomb failure envelope. The dilatant regime occupies a relatively small proportion of PQ space which is typical of porous sandstones (Wong et al., 1997). Samples deformed at effective pressures of 70 and 110 MPa show a transitional failure mode, developing compacting shear bands oriented at high angles to $\sigma_1$. The yield points within both the dilatant and transitional regimes show a positive correlation between P and Q, whereas the yield points that represent conditions where only compaction bands *sensu stricto* are observed, show a negative correlation between P and Q. If we consider the two yield-surface model proposed by Issen (2002), then the loading path that results in a sample failing by a transitional mode, involving high angle to $\sigma_1$ compacting shear bands, can be conceptualised as intersecting the region of stress space where the two yield surfaces meet.

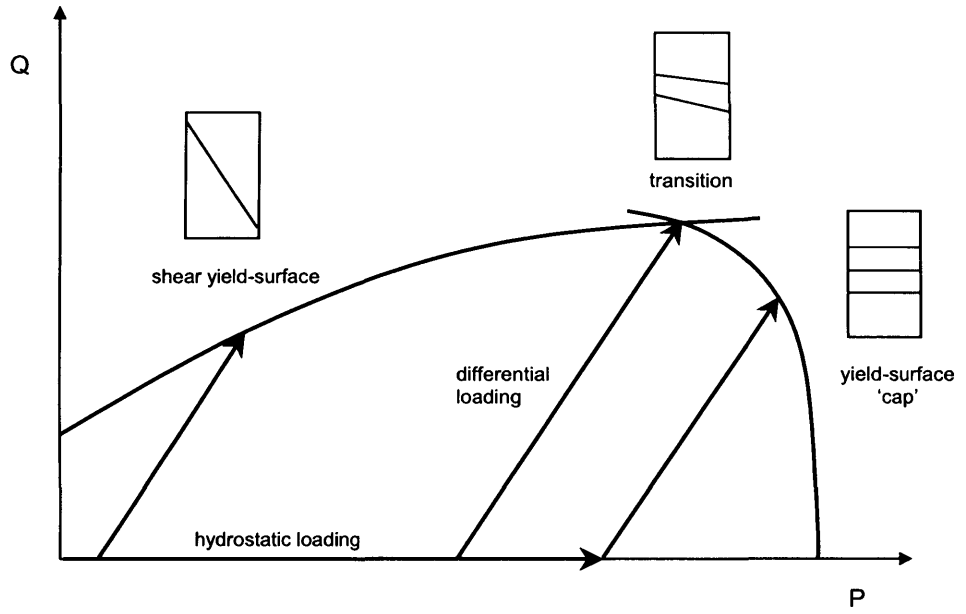


*Fig 10-9. Schematic diagram showing how loading paths lead to failure modes associated with different regions of the two yield-surface model proposed by Issen (2002).*

It is clear from the data that in the compactive regime x-axis samples have greater strength than z-axis samples, and therefore it is perhaps not surprising that the transition between shear localisation and compaction localisation occurs at different stress conditions for the two orientations. This is best illustrated by the samples deformed under 110 MPa effective pressure, where the x-axis sample fails by a transitional mode, whereas the z-axis sample, deformed under the same conditions, fails by the development of discrete compaction bands (see figure 8-7 ). This difference in the style of failure results from the loading paths of the respective samples intersecting different regions of the failure envelope; the loading path of the z-axis sample cuts the cap-surface whereas the loading path of the x-axis sample coincides with the region of stress space where the competing mechanisms of shear localisation and compaction localisation are more evenly balanced.

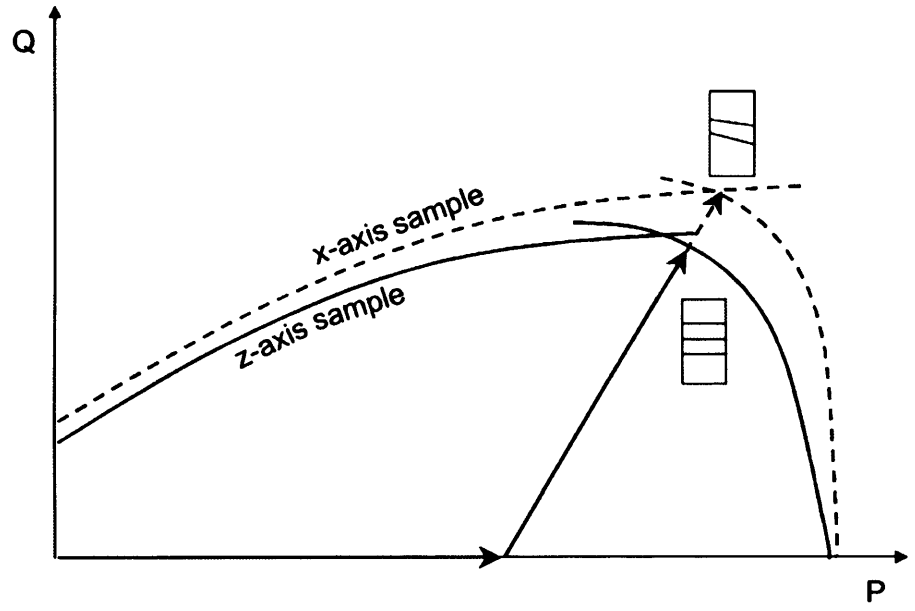


*Fig 10-10. Schematic showing how a Diemelstadt sandstone (stronger in the x-axis) may show different failure modes as a function of sample orientation during deformation under the same conditions (cf. samples deformed at Pe = 110 MPa). The same loading path intersects different regions of the failure envelope.*

Microstructural observations (Wong et al., 2001) show that in the transitional regime strain localisation is partitioned between at least two mechanisms; axial microcracks and grain crushing. These two processes operating in isolation would result in shear localisation and compaction localisation respectively, but it is the fact that the transition zone involves both mechanisms that results in the 'mixed mode' of deformation observed in samples deformed in the Pe = 70 – 110 MPa range.

### 10.2.3 Comparison with Previous Work

The only published work to date which examines compactive deformation in differently oriented samples is that of Wong et al. (1997) and Baud et al. (2005), who both deformed samples of Rothbach sandstone cored normal and parallel to bedding. They report that samples deformed normal to bedding are consistently stronger than those deformed parallel

to bedding samples (fig 10-11), and attribute the difference to Rothbach sandstone being preferentially cemented in the plane parallel to bedding. Post-deformation microstructural observations on the Rothbach samples revealed that while samples deformed normal to bedding showed discrete compaction bands, the damage in parallel to bedding samples was more homogeneously distributed in a fashion similar to that of diffuse compaction bands.

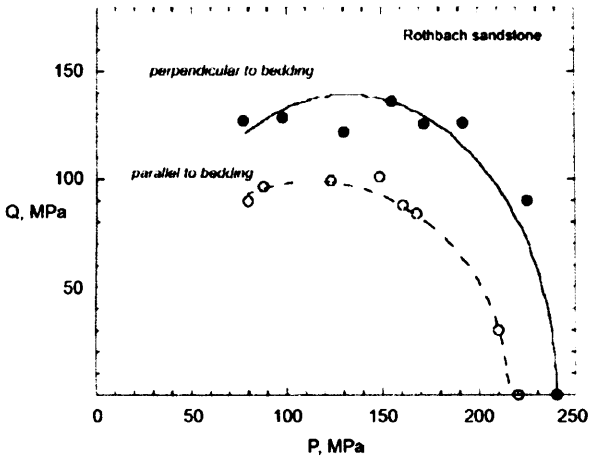


*Fig 10-11. The onset of shear-enhanced compaction in oriented samples of Rothbach sandstone (from Baud et al., 2005).*

Diemelstadt sandstone, on the other hand, shows the opposite trend, with samples deformed parallel to bedding showing greater strength than those deformed normal to bedding. There appears to be an important difference between the styles of compaction bands observed in parallel to bedding samples of Rothbach and Diemelstadt. Whereas the damage in Rothbach sandstone deformed parallel to bedding is reported as being somewhat homogeneously distributed, and not in the form of compaction bands extending fully across the sample, we find that the compaction bands in Diemelstadt sandstone are discrete and do extend across the entire width of the sample (figure 8-16). The relatively high content of clay and feldspar (~28%) in Rothbach sandstone may provide the necessary strain relief to retard the growth of compaction bands.

As noted in section 8.3, the morphology of compaction bands in Diemelstadt sandstone varies as a function of sample orientation, with the samples deformed parallel to bedding developing compaction bands that, while discrete, show greater tortuosity than the discrete compaction bands observed in samples deformed normal to bedding. If the energy required to develop a compaction band is proportional to the number of grains involved in compaction band growth through intragranular cracking and pore-collapse, then it seems logical that it would be more energetically favourable for a planar compaction band to develop than a tortuous compaction band of longer trace. This assumption is consistent with the greater stress values observed at C* in samples deformed parallel to bedding which then go on to develop the more tortuous style of compaction band. The implication of this is that the xy plane, or bedding plane, of Diemelstadt sandstone represents a plane of weakness relative to the orthogonal plane that compaction bands traverse during deformation parallel to bedding. Propagating compaction bands will follow the path of least resistance and, if the xy plane is weak and essentially isotropic, compaction bands induced in this plane, by deformation of z-axis samples, would therefore be expected to exhibit a planar trace.

### 10.2.4 Bifurcation Analysis

As discussed in chapter 4, the bifurcation approach to strain localisation (Rudnicki and Rice, 1975) attempts to constrain the mechanical conditions for which deformation bands of particular orientations can occur. They use a constitutive framework whereby the yield envelope and inelastic volume change are characterised by the pressure sensitivity parameter $\mu$, and the dilatancy factor $\beta$, respectively. Previous work (Wong et al., 1997, 2001; Baud et al. 2006) has extracted values of $\mu$ and $\beta$ from experimental data where the associated deformation mode is known, allowing experimentally derived bifurcation parameters to be used to test the accuracy of the theoretical constraints on compaction band localisation. For triaxial data, the pressure sensitivity parameter is inferred from the slope at the yield stress points by the relationship $\mu = (dQ/dP)/\sqrt{3}$, and the dilatancy factor is

given as $\beta = -\sqrt{3}\left(d\varepsilon_V^P / d\varepsilon_L^P\right)/\left(3 - d\varepsilon_V^P / d\varepsilon_L^P\right)$, where $d\varepsilon_V^P / d\varepsilon_L^P$ denotes the ratio between increments of plastic volumetric and axial strains. Assuming $d\varepsilon_V^P \approx d\phi^P$ (Wong et al., 1997), $\beta$ can be written as $\beta = -\sqrt{3}\left(d\phi^P / d\varepsilon_L^P\right)/\left(3 - d\phi^P / d\varepsilon_L^P\right)$, where $d\phi^P / d\varepsilon_L^P$ denotes the ratio between increments of porosity change and axial strain. Applying these relationships to the data shown in figure 10-8, gives experimental values of $\mu$ and $\beta$ associated with different failure modes. This shows that $\mu$ > 0 in the brittle regime, corresponding to the positive slope of peak stress and C' with increasing effective pressure; $\mu$ ~ 0 in the transitional regime where the failure envelope is more or less parallel to the P axis; and $\mu$ < 0 in the compaction band regime, corresponding to the downward limb of the failure envelope which culminates at conditions sufficient to induce P*. For the dilatancy factor, $\beta$ > 0 in the brittle regime, $\beta$ ~ 0 in the transitional regime, reflecting the more or less equal balance between dilatant and compactive mechanisms, and $\beta$ < 0 in the compaction bands regime (see figure 10-13).

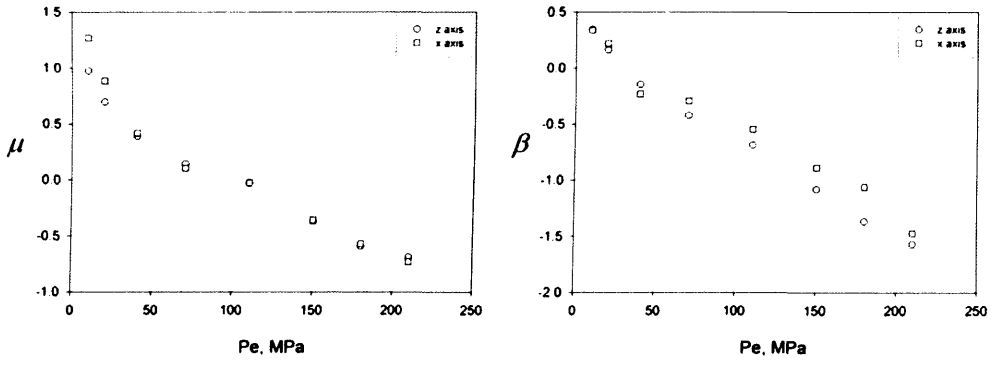


*Fig 10-12. Bifurcation parameters $\mu$ and $\beta$ at the stress states at brittle failure and C*, as shown in PQ space in figure 10-8.*

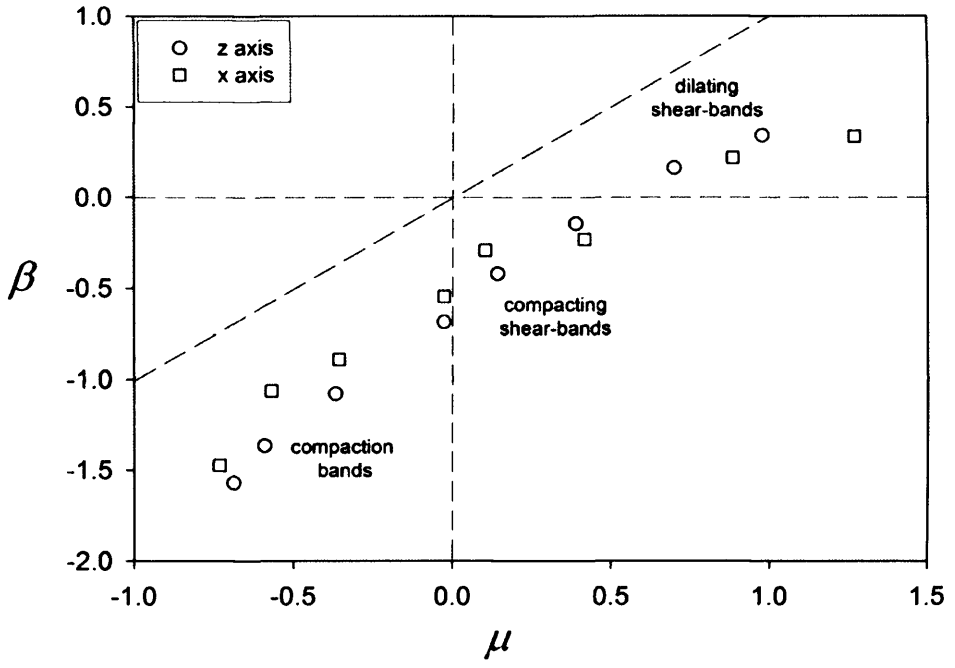


*Fig 10-13. Bifurcation parameters $\mu$ and $\beta$ for z and x-axis orientations of Diemelstadt sandstone. Failure modes are noted.*

Plotting these values in $\mu\beta$ space (figure 10-13) shows that, in the brittle-dilatant regime, $\mu$ and $\beta$ > 0, with $\beta$ decreasing systematically as effective pressure increases and dilatancy is suppressed. Conditions of $\mu > 0$ and $\beta < 0$ exist in the transitional regime, where compacting shear bands are observed, and conditions of $\mu < 0$ and $\beta < 0$ exist in the compaction band regime. These results show that although there is a qualitative agreement between the experimental data and the predictions of strain localisation (decreasing $\mu$ and $\beta$ during the transition from dilating shear band to compaction band), the quantitative predictions are not consistent with the experimental data. This is shown by the fact that the data points do not obey the normality condition ($\mu = \beta$, diagonal line in figure 10-13), which is assumed by many constitutive models (Baud et al., 2006).

## 10.3 Porosity and Permeability

### 10.3.1 Hydrostatic Porosity Reduction Leading to P*

Although hydrostatic measurements of porosity change were included in the contemporaneous measurements of permeability and elastic wave velocities presented in chapter 6, the apparatus used to perform these experiments was not able to reach the necessary pressure conditions to induce P*. Therefore, the value of P* was measured in the triaxial vessel which can also operate in a hydrostatic mode, and is capable of reaching an isostatic confining pressure of 400 MPa.

During initial hydrostatic loading, porosity reduction is non-linear during the initial ~50 MPa effective pressure, after which porosity reduction shows an approximately linear decrease, reflecting a poroelastic response. This trend is maintained until about 310 MPa, at which point grain crushing leads to pore collapse and a rapid acceleration in porosity reduction, a stress state termed P*. The value of P* was found to be independent of sample orientation, which is to be expected since when measuring P*, the stress exerted on a sample is isotropic. The Hertzian model of Zhang et al. (1990 a) suggests that P* is largely controlled by porosity and grain size, with low porosity and small grain size promoting higher values of P*. Experimental observations generally support this suggestion, as shown in the compilation of data presented by Wong et al. (1997) (Table 10-1).

| Material | $r$, mm | $\phi$ | P*, MPa |
|---|---|---|---|
| Adamswiller sandstone | 0.09 | 0.226 | 190 |
| Rothbach sandstone | 0.228 | 0.199 | 240 |
| Lance sandstone | 0.125 | 0.085 | 300 |
| Kayenta sandstone | 0.15 | 0.21 | 300 |
| Fontainebleau | 0.188 | 0.136 | 350 |
| Darley Dale sandstone | 0.167 | 0.145 | 360 |
| Berea sandstone | 0.13 | 0.07 | 380 |

*Table 10-1. A selection of experimental data showing the values of P* for materials of differing porosity ($\phi$) and grain radius (r). (Data as compiled by Wong et al., 1997).*

Figure 10-14 shows that the measured value of P* for Diemelstadt sandstone is consistent with previously the published data, and follows the trend captured by the model of Zhang et al. (1990) which predicts that $P^* \propto (\phi r)^n$. When plotted as a log-log of the product of porosity and grain radius against P*, the data follow an approximately linear form of slope -3/2.

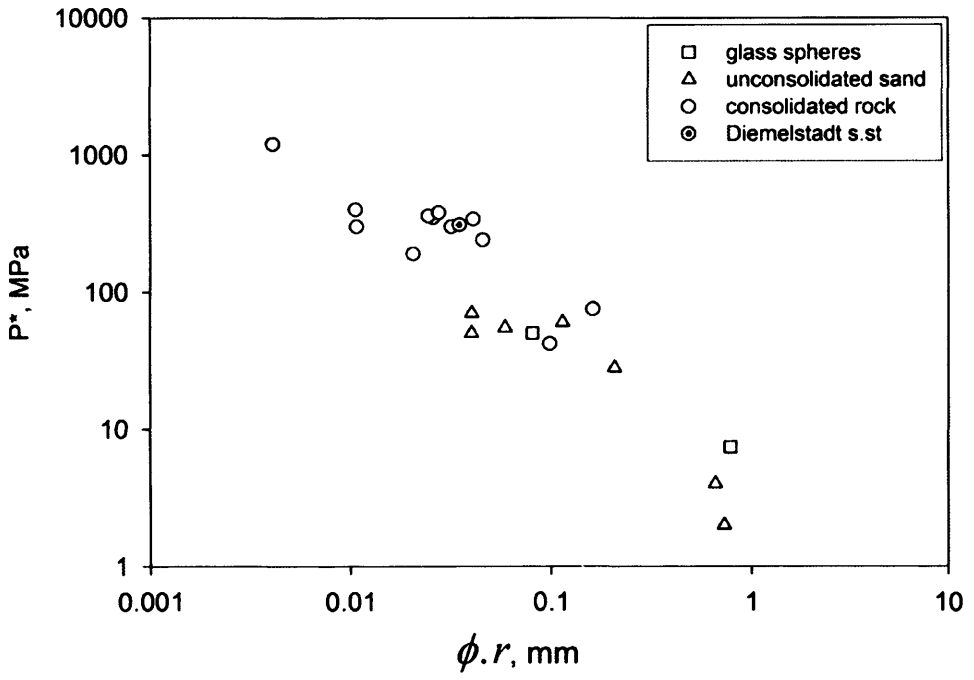


*Fig 10-14. P* as a function of the product of material porosity and grain radius for a range of material including Diemelstadt sandstone. (Data, except for that of Diemelstadt, taken from Wong et al., 1997).*

The correlation of data shown in figure 10-14 suggests that despite being simple, requiring just two parameters to return an approximate value of P*, the model of Zhang et al. (1990) can provide a first order approximation of the grain crushing pressure of rocks without the need to appeal to more sophisticated models which factor in additional complexities.

### 10.3.2 Porosity Evolution Under Triaxial Stress

The evolution of porosity during triaxial loading is shown in figures 8-8 and 8-9 and shown with reference to the complete hydrostat in figure 8-11 The data are consistent with previous work (Curran and Carroll, 1979; Wong et al., 1992) in showing that porosity evolution under hydrostatic and deviatoric stress follow different paths. Whereas increasing hydrostatic stress always results in a porosity reduction, approximately linear up until P*, the action of deviatoric stress leads to either dilatancy and a porosity increase at low effective pressure (10 and 20 MPa) or compaction and a porosity reduction at intermediate and high Pe (> 40 MPa). In triaxial experiments, hydrostatic and non-hydrostatic loading are coupled, and any deviation from the hydrostat implies that the porosity evolution is being controlled by the deviatoric component of stress, which results in a net behaviour of either shear-induced dilation (C') or shear-enhanced compaction (C*).

As discussed in the previous section, hydrostatic loading results in a poroelastic response of the sample which clearly contributes to pre-C* porosity reduction, as demonstrated by the hydrostatic curves. However, post-C* porosity reduction accelerates significantly, with microstructural observations suggesting that this phase of porosity reduction is primarily the result of pore collapse associated with the growth of discrete compaction bands (figure 8-18). Outside the intensely localised damage within compaction bands, there is generally no further brittle deformation to the rock, and porosity remains intact. These observations are consistent with other microstructural work (e.g. Baud et al., 2004) on discrete compaction bands, and contrast with studies on diffuse compaction bands (Olsson and Holcomb, 2000) which report that pervasive compaction fronts move axially though the test material resulting in porosity reduction being homogenously distributed throughout the sample.

### 10.3.3 Permeability Evolution Under Triaxial Stress

The results presented earlier in this study show that, up until 250 MPa, there is no significant influence of hydrostatic stress on permeability. However, during triaxial loading, permeability is reduced substantially, by up to four orders of magnitude.

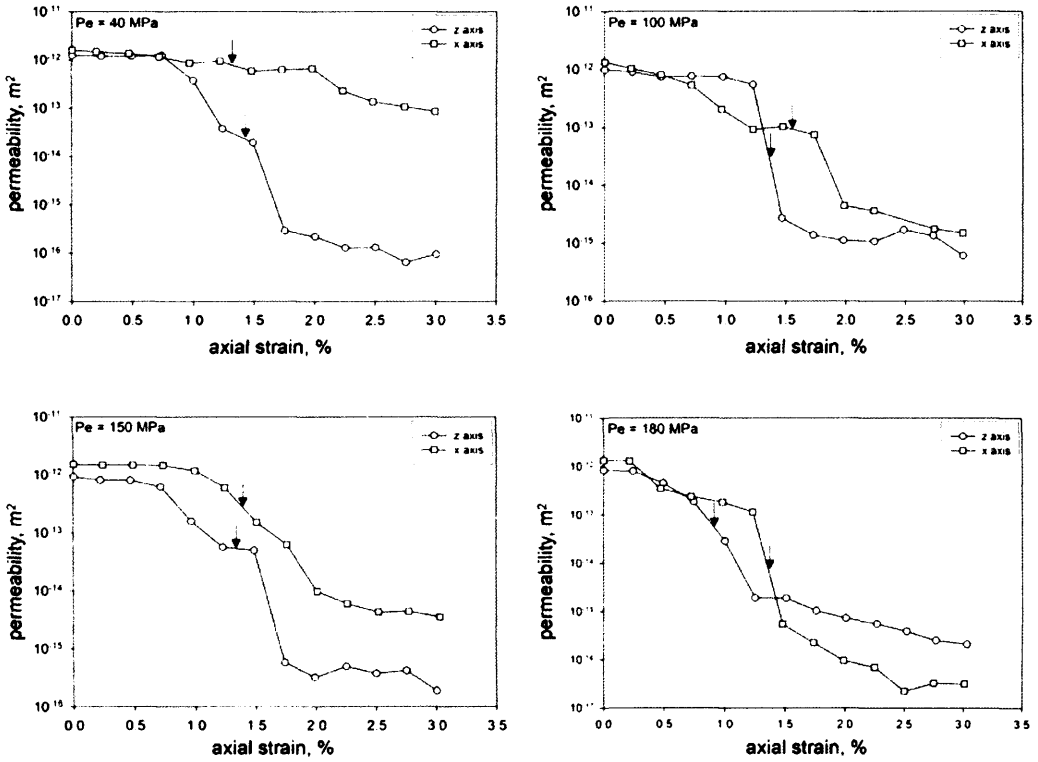


*Fig 10-15. Comparative plots of z and x-axis samples showing the evolution of permeability during deformation in the brittle faulting regime (Pe = 40 MPa), transitional regime (Pe = 100 MPa) and compaction band regime (Pe = 150 and 180 MPa). Black arrows indicate C*.*

From previous tests, we have seen that deformation at Pe = 40 MPa results in net-compactive brittle behaviour, as opposed to dilatant brittle behaviour, with the development of a through-going fault. The compactive nature of this deformation is evidenced by pore-volumometry data (C* is observed rather than C') and also by the reduction in permeability seen during deformation. It is striking that during deformation at Pe = 40 MPa the z-axis sample shows much greater permeability reduction than the equivalent x-axis sample, being three orders of

magnitude less permeable post-C*. Examining the permeability curve in relation to the stress-strain curve of the x-axis sample deformed at Pe = 40 MPa shows that permeability reduction is not really significant until after the dynamic stress drop associated with the formation of the fault, significantly after C*. Therefore, it seems reasonable to assume that sliding on the fault is the primary control on reducing permeability in this example. This has previously been reported during the brittle deformation of porous sandstone (Zhu and Wong, 1997) where sliding on a fault plane is likely to form a gouge which becomes progressively comminuted, resulting in a more efficient packing of grains and the formation of a fault seal. It should be noted that the influence of a fault as either a barrier or conduit to flow depends on the permeability contrast between the structure and the host material, with a porous material such as Diemelstadt likely to develop faults that block flow whereas in compact rocks, the opposite is often true (e.g. Brace et al., 1968).

The earlier, more substantial and more rapid permeability reduction observed in the z-axis sample deformed at Pe = 40 MPa suggests a more significant compactive element to the deformation. Since the z-axis samples are weaker, it seems reasonable to assume that they enter the compaction dominated regime at pressure conditions insufficient to induce similar behaviour in x-axis samples. This idea is represented in figure 10-16, where fitted lines represent the failure envelope for shear localisation. It can be seen that for x-axis samples, the linear nature of the envelope extends further into PQ space than for z-axis samples, suggesting an earlier transition into the compactive-shear regime for z-axis samples. For the x-axis sample, shearing without a significant compactive component, may explain the different extents of permeability evolution that are observed along the 40 MPa loading path.

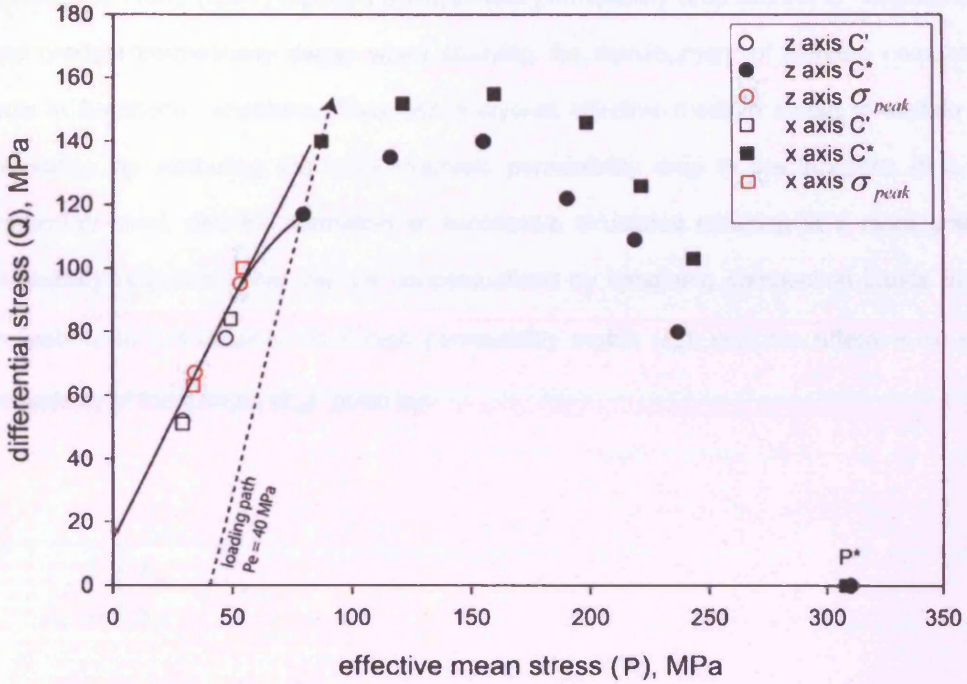


*Fig 10-16. The envelopes fitted to peak stress points show a more extensive linear pressure dependency for x-axis samples than z-axis samples. This suggests that along the loading path illustrated (dotted line), z-axis samples undergo a greater amount of inelastic deformation.*

During deformation at higher effective pressures, the permeability evolution of x and z-axis samples show reductions of similar magnitudes. However, one clear distinction between sample orientations is that z-axis permeability is reduced over a smaller axial strain range, this being particularly evident from the data where Pe = 100 MPa. This observation seems to be in harmony with the greater strength observed for x-axis samples, since if permeability reduction is to be attributed to compaction bands (or compacting shear bands when Pe <100 MPa) then a greater mechanical resistance to compaction band inception would result in a more gradual decay in bulk permeability. Having said this, permeability reduction in neither x nor z-axis samples could accurately be described as gradual *per se*, since both, at stages, demonstrate reductions of over an order of magnitude between sequential measurements.

Vajdova and Wong (2004) reported a large initial permeability drop around C* followed by a more gradual permeability decay when studying the development of discrete compaction bands in Bentheim sandstone. They use a layered effective medium model to explain this observation by attributing the initial dramatic permeability drop to the inception of a first compaction band, and the formation of successive structures resulting in a more gradual permeability reduction. This can be conceptualised by imagining compaction bands of low permeability ($k_{cb}$) embedded in a high permeability matrix ($k_m$); with the effective, or bulk, permeability of the sample ($k_{eff}$) given by:

$$k_{eff} = \frac{k_m}{\left(n\frac{l}{L}\right)\left(\frac{k_m}{k_{cb}} - 1\right) + 1}$$

where $n$ is the number of compaction bands and $l/L$ is the ratio of the width of a compaction band ($l$) to the sample length ($L$).

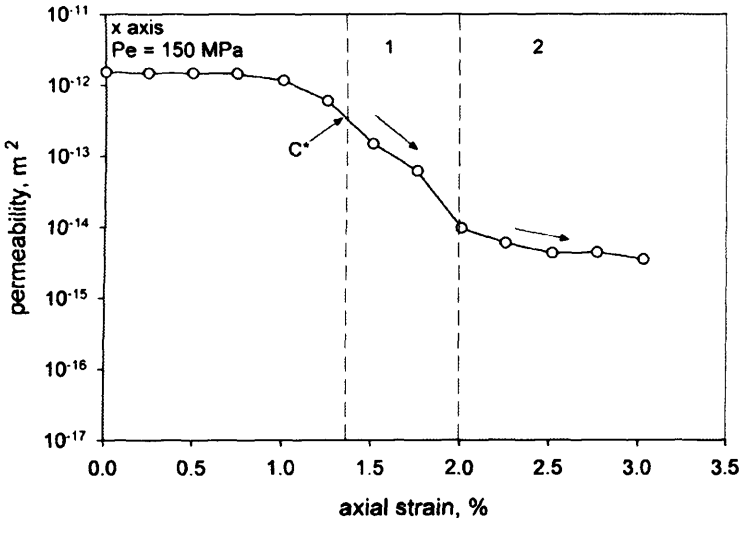


*Fig 10-17. Data illustrating the rapid permeability drop following C* (regime 1), and the subsequent more gradual permeability decrease (regime 2).*

Although we lack the microstructural data necessary to determine the number of compaction bands present at the point of each permeability measurement, the relationship above demonstrates a permeability evolution as a function of an increasing population of compaction bands, $n$, which is in qualitative agreement with the evolution of permeability post C* in our samples.

It is noteworthy that significant permeability reductions are observed in both orientations prior to C*. This is interesting because the traditional definition of C* is given as the point where deviatoric stress causes deviation from the hydrostat, which implicitly means that up until the point of C* the deviatoric component of stress should not have any mechanical influence beyond that already exerted by the hydrostatic component of stress. Given that C* is associated with brittle processes (Wong et al., 1992; Menendez et al., 1996), the pre-C* permeability reduction must be the result of a poroelastic response to the deviatoric stress. With this in mind, it is hard to reconcile the notion that triaxial deformation pre-C* is equal to hydrostatic deformation because during hydrostatic loading we do not observe any appreciable permeability reduction. A possible explanation for this is that C* actually occurs earlier than the picks taken from the permeability curves, which may be the case since the nature of these particular experiments precluded the application of AE in constraining C*. This was so because in order to make permeability measurements, it was necessary to stop the deformation process, allow some time for the system to equilibrate before taking the measurement, and then re-start the deformation process once the measurement had been taken. This stop-start of the loading process results in a similar stop-start AE pattern, which obscures the inflection in hit rate that would otherwise be useful in constraining C*.

### 10.4 Compaction Band Propagation

Previous work has used AE locations to map the accumulation of damage associated with discrete compaction bands (Fortin et al., 2006), and to measure the rate of advance of the compaction front of diffuse compaction bands as it moves axially through the host material

(Olsson and Holcomb, 2000). However, until now AE locations have not been used to capture the propagation of discrete compaction bands as they traverse a sample. Vajdova and Wong (2003) inferred the velocity of compaction band propagation by inducing such structures in notched samples of Bentheim sandstone and considering the duration of AE surges presumed to be associated with compaction localisation. They conclude that the propagation of a compaction band is roughly two orders of magnitude greater than the axial displacement rate.

The results presented in chapter 9 show that compaction bands in z-axis samples propagate on average at less than 0.1 $mm.s^{-1}$. The axial strain rate during these tests was $10^{-5}$ $s^{-1}$, which corresponds to a piston displacement velocity of 0.001 $mm.s^{-1}$. Therefore, the velocity of compaction band propagation is approximately two orders of magnitude greater than the axial displacement velocity, a result which is in excellent agreement with the inferred compaction band propagation velocity of Vajdova and Wong (2003). The velocity of compaction band propagation is measured to be much slower than other damage mechanisms (3 $mm.s^{-1}$ for the slow failure of Etna Basalt, a material with significant pre-existing damage, was recorded by Benson et al., 2007), which is not in agreement with earlier suggestions that if compaction band propagation actually occurs, it is almost instantaneous (Rudnicki and Sternlof, 2005).

### 10.4.1 Scale of Cracking

The seismic b-value characterizes the magnitude-frequency distribution of AE events. If the magnitude of an individual AE event is related to the increment of crack growth producing it, then any change in the b-value during deformation is an indicator of a change in the scale of cracking (Main et al., 1989; Meredith et al., 1990). Here, we observe a relatively high and constant b-value of around 1.6 during compaction band nucleation and growth, suggesting that localised compactive deformation is characterised by small scale cracking that does not change in dimension during propagation. This is consistent with intragranular cracking and pore collapse as the dominant deformation mechanism, and with the observation of a slow

'grain-by-grain' propagation velocity. These observations are in marked contrast to the b-value minimum commonly observed during dynamic failure and localization on a shear fault (Meredith et al., 1990).

Seismic b-values recorded for the x-axis sample are relatively steady, although they do show more variation than those recorded for the z-axis sample. Whereas the z-axis sample developed a compaction band normal to $\sigma_1$, the x-axis sample showed transitional behaviour (fig 10-10) and developed a compacting shear band oriented at a high angle to $\sigma_1$. Since transitional deformation is inherently mixed-mode, the greater variation observed in seismic b-value may be the result of competing mechanisms operating during strain localisation. Mechanical heterogeneity in the direction of damage propagation in z-axis samples may also contribute to the b-value variability.

### 10.4.2 Application to Permeability Data

If the permeability reduction discussed in previous sections is the result of compaction bands propagating across the sample and creating a low porosity/low permeability barrier to flow, then it should be possible to correlate the observed rate of permeability reduction to the measured rate of compaction band growth. The major phase of permeability reduction occurs over a 0.25% axial strain increment, which corresponds to a period of about 250 seconds. According to the data presented in chapter 9, compaction band growth is initially relatively rapid, proceeding at between 0.1 and 0.2 $mm.s^{-1}$ before slowing down considerably by between a factor of 2 – 6. If the rate of permeability reduction is assumed to be proportional to the rate at which a compaction band traverses, and hence isolates from flow, the sample's cross-section, then we would expect to see an initially rapid permeability reduction followed by a more gradual decay. This is the general trend observed in the data of figure 10-15. However, while compaction bands were measured to traverse the sample cross-section over a ~400 second time window, the major phase of permeability reduction was recorded over a

250 second window. This may result from more than one compaction band developing contemporaneously, a phenomenon observed in section 9.1.3 where two spatially discrete compaction bands are seen to develop more or less in parallel. Microstructural work by previous workers (Baud et al., 2004; Vajdova and Wong, 2004) has shown that during the growth of multiple compaction bands, the structures may intersect one another. Therefore, if several compaction bands are growing and interacting during a given period, the resulting impact on bulk permeability cannot be adequately explained in terms of the growth of a single isolated structure.

### 10.4.3 Comparison with Network Models

The network model of Katsman et al. (2005), discussed in section 4.2.2, has some interesting parallels with our experimental observations.

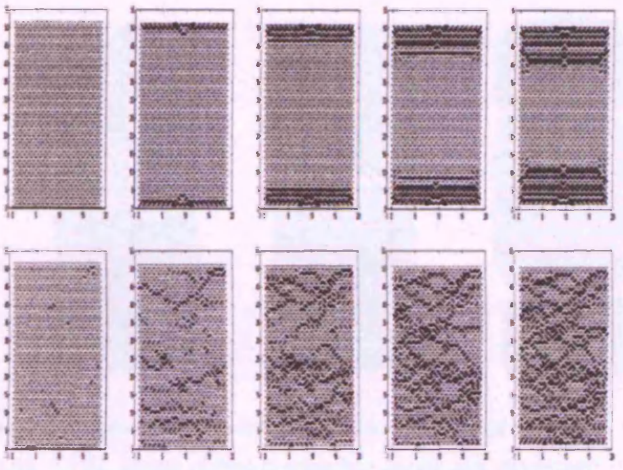

*Fig 10-18. Network model predicting different compaction band morphologies with increasing strain for a homogeneous system (top) and a disordered, or heterogeneous system (bottom). From Katsman et al., 2005.*

When modelling a homogeneous medium, they predict that discrete compaction bands will develop by propagating from the specimen boundary. When disorder, or heterogeneity, is introduced to the system, the style of compaction band is predicted to become increasingly diffuse, with damage nucleating in the specimen interior rather than at the specimen boundary

(figure 10-18). Katsman et al. (2005) describe their disordered system as predicting diffuse compaction bands, although strictly speaking, since they clearly show structures intercalated with undamaged material, they would more accurately be described as tortuous discrete compaction bands. The simulation show in figure 10-18 shows a striking similarity to the compaction band morphologies observed in this study (figure 10-19).

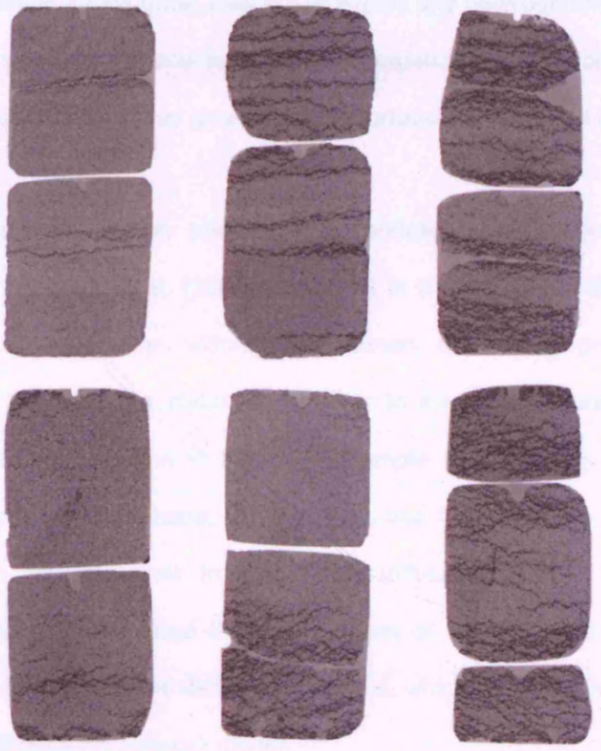

*Fig 10-19. Differences in compaction band morphology during progressive strain in Diemelstadt sandstone (1.5%, 3.0%, 4.5%). Image shows compaction bands that developed in the isotropic bedding plane (top) and compaction bands that developed normal to the isotropic bedding plane (bottom).*

Compaction bands that develop in an isotropic xy plane (the bedding plane) show a relatively straight trace, whereas those that develop in a plane orthogonal to the xy plane show a significantly more tortuous trace. The key to the similarities between the simulated compaction bands and the real compaction bands appears to the isotropy of the xy plane in Diemelstadt sandstone. Within planes parallel to bedding in a sedimentary rock, we can imagine that there

is little heterogeneity because presumably deposition across the area of this plane occurs more or less contemporaneously, and therefore under the same conditions. Successive xy planes that are deposited sequentially over long periods of time, however, may show differences between each other as a result of the transient conditions that operate over geological time scales. This situation would result in disorder, or a juxtapositioning of material properties, in the direction normal to bedding, and relative homogeneity in the planes parallel to bedding. As compaction bands grow, they would exploit any heterogeneities in the direction of their propagation, so as to develop in the most energetically favourable fashion (path of least resistance). This behaviour may give rise to the tortuosities observed in figure 10-19.

A further similarity can be drawn between the modelled compaction bands and the experimental results. Katsman et al. (2005) show that in the case of a disordered system, compaction bands nucleate at sites within the specimen, rather than propagating from a specimen boundary. This appears stylistically similar to the observations made from AE locations on compaction localisation in the x-axis sample (section 9.2). Here, instead of observing a distinct propagation phase, as was the case for the z-axis sample, damage localisation appears to 'organise' itself, from an initially diffuse cloud of AE events to a more defined band. It could be speculated that this pattern of AE locations results from the interaction of damage sites within the deforming material, which would be in basic agreement with the predictions made by the network model.

### 10.4.4 Size Effects

For this study, we also conducted a series of parallel experiments on much smaller samples of Diemelstadt sandstone. These were performed at the Université Louis Pasteur, in Strasbourg with Dr. Patrick Baud. The samples used in this part of the work were cored from the same block of material as our UCL experiments, although they were 40 mm long and 20 mm in diameter and therefore an order of magnitude less in volume than the samples deformed at UCL. Since the aspect ratio of the Strasbourg samples is 2:1, and the aspect

ratio of the UCL samples is 2.5:1, some experiments were also performed at UCL on samples 80 mm long and 40 mm wide. The yield points from these experiments are plotted in PQ space in figure 10-20.

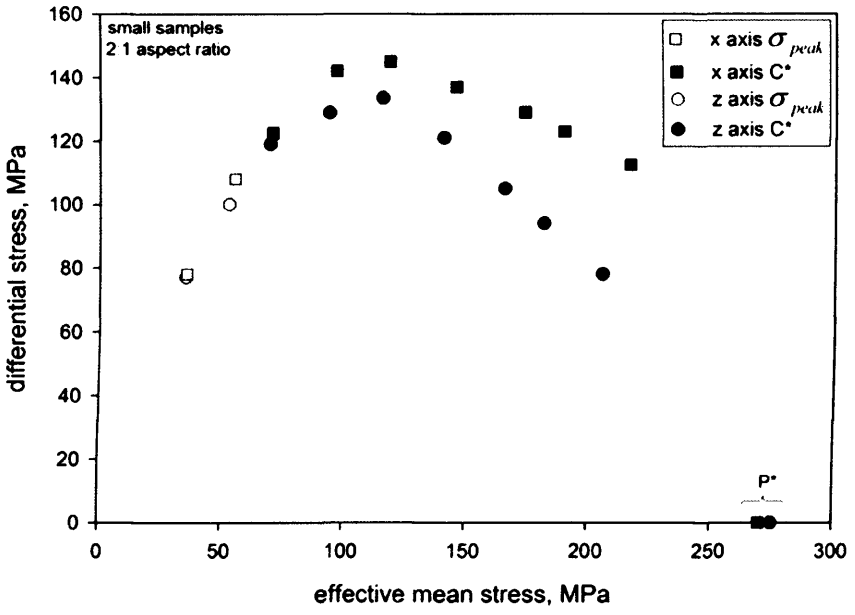


*Fig 10-20. Stress states at peak stress and C* for small samples of Diemelstadt sandstone (40 mm x 20 mm).*

Qualitatively, the same general trend is observed as for the large 2.5:1 aspect ratio samples; the x-axis samples are consistently stronger except under the lowest effective pressure where the strength is the same. At higher effective pressures, the difference in strength becomes more apparent, with the downward limbs of the envelopes following an almost linear trend. The two envelopes converge at P*, with almost identical grain crushing pressures observed between sample orientation. In figure 10-21, the data from the small samples is plotted with the data of the large samples of 2:1 aspect ratio, and the large samples of 2.5:1 aspect ratio.

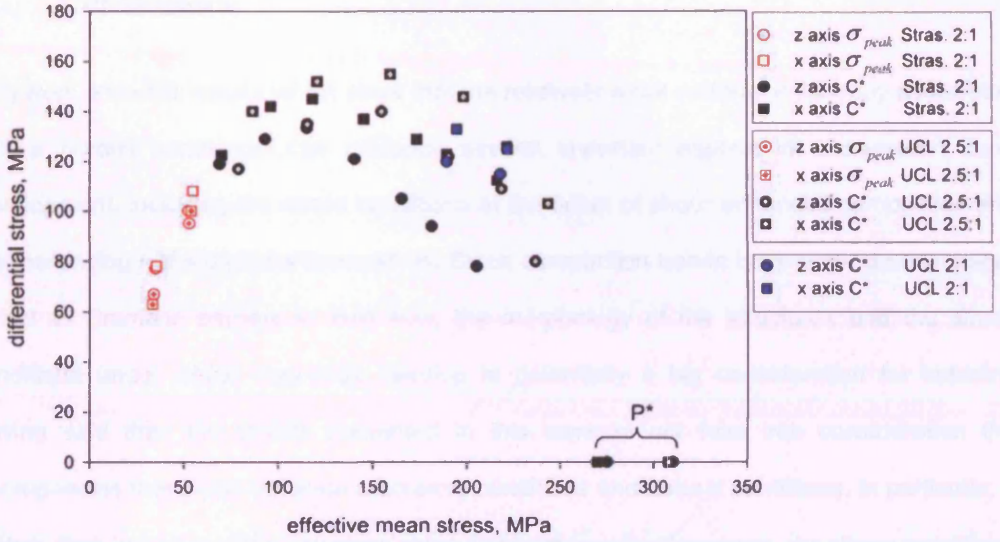


*Fig 10-21. Synthesis plot showing critical stress conditions for a range of Diemelstadt sandstone sample sizes and geometries.*

The results above show some interesting features. In the dilatant regime, small samples (Stras. 2:1) appear stronger than large samples, which is a typically observed trend, since large samples tend to contain more flaws about which stress can concentrate to cause failure. However, in the compactive regime, the smaller samples appear weaker than larger samples. It appears that the influence of sample aspect ratio does not explain this trend reversal, since large 2:1 samples are still stronger than the smaller 2:1 samples. In the compactive regime, large 2:1 samples appear to be of more or less equal strength as the large 2.5:1 samples, which suggests that aspect ratio does not play a significant role in material strength during the development of compaction bands. However, in an extreme situation, the influence of edge effects would presumably come into play. A final observation is that the stress states at P* appear to be influenced by sample size, on one hand this confirms the suitability of P* as a scaling parameter (e.g. Cuss et al., 2003), since the lower value of P* correlates well with the observations of lower C* in the small samples; but on the other hand, the hydrostatic grain crushing pressure of a given material would be expected to independent of sample size. This data-set needs to be expanded before anything conclusive can be said.

# 11 Conclusions

This work presents results which show that the relatively weak material anisotropy associated with a porous sandstone can influence several important aspects of compaction band development, including the stress conditions at the onset of shear-enhanced compaction and the morphology of structures themselves. Since compaction bands have been demonstrated to act as dramatic barriers to fluid flow, the morphology of the structures and the stress conditions under which they may develop is potentially a big consideration for industry. Having said this, the results presented in this work to not take into consideration the discrepancies that exists between laboratory conditions and natural conditions. In particular, it is likely that, by virtue of the low strain rates that exist in natural systems, the stress conditions necessary for the development of compaction bands in nature are substantially lower than those reported in this work. The implication of this is that compaction bands may be more pervasive, or more viable, in a wider variety of geological scenarios than the experimental stress conditions suggest.

Data presented in this work show that discrete compaction bands can be almost pervasive through a material after a relatively modest amount of strain (e.g. figure 10-19). This is an interesting point to note since in geological settings large amounts of strain may accumulate and there is data to suggest (Vajdova et al., 2004) that the number of compaction bands increases linearly with increasing plastic strain. Therefore, high-strain events could result in a commensurately large number, or thick zone, of compaction bands. For Darcian flow, the thickness of a compaction band and the permeability of a compaction band are the key parameters controlling flow; so although individually compaction bands may be thin the cumulative thickness of a zone of compaction bands may be considerably greater. Numerical simulations on deformation bands (Matthai et al., 1998) have shown that in a reservoir context, a large number of structures are required to significantly influence fluid flow. In light of the experimental evidence, this condition seems tenable for compaction bands.

## 11.1 Future Work

In this study, the influence of anisotropy has been examined by deforming samples in two orthogonal directions, however in the brittle regime many studies on compact and porous rocks have been undertaken which systematically investigate the influence of bedding orientation on strength by coring samples at angular increments to bedding. To complete the picture, it would seem that there is a need for this type of study in the brittle-ductile regime and would be particularly useful in fleshing out the scarce data that exist on the influence of anisotropy on compactive deformation.

Laboratory produced compaction bands are taken as being the equivalent structures to those observed in nature, however there are some important differences between the two types of structure which have not yet been addressed. Perhaps most striking difference is the positive relief of field structures, which suggests a resistance to weathering and erosion that appears inconsistent with the delicate and friable nature laboratory induced compaction bands. One possible explanation for the field structures' positive relief is that the process of intense compaction results in a denser and therefore more resilient material, another explanation is that the fracturing of grains during localised compaction provides an increased area of reactive surfaces which, especially when combined with the geothermal influence that exists at depth, may result in a faster rate of chemical reaction leading preferential cementation within the compaction band. Laboratory studies to date have exclusively used distilled water as the saturating pore-fluid, which is an unrealistic assumption for natural systems where multiphases are often the norm. Therefore, a potential future line of research focused on the influence of fluid-rock interactions seems like a relevant direction to pursue – particularly so in light of the slow compaction band propagation revealed by this study, which, in nature, is likely to be even more significant as result of the much lower strain rates that operate. Coupled with this is the influence of temperature on deformation, particularly when the mechanisms being simulated occur at depth and are subject to the prevailing geothermal gradient. Both of these

lines of enquiry are realistic, given that triaxial deformation apparatus is flexible in allowing devices such as furnaces and pore-fluid separators to be appended.

## References

Aki, K. (1965), Maximum likelihood estimate of the parameter b in the formula log N = a – bm and it's confidence limits, *Bull. Earthquake Res. Inst. Tokoyo Uni., 43*, 237 – 239.

Baud, P., Schubnel, A., Wong, T-f., 2000. Dilatancy, compaction and failure mode in Solnhofen limestone. *J. Geophys. Res., 105,* 19289 – 19303.

Baud, P., Klein, E., Wong, T-f, 2004. Compaction localization in porous sandstones: spatial evolution of damage and acoustic emission activity. *J. Struct. Geol., 26,* 603 – 624.

Baud, P., Laurent, L., David, C., Rawling, G. C., Wong, T-f., 2005. Effects of bedding and foliation on mechanical anisotropy, damage evolution and failure mode. In: Bruhn, D., Burlini, L. (eds) High-strain zones: structures and physical properties. *Geological Society of London Special Publications, 245,* pp. 223 – 249.

Baud, P., Vajdova, V., Wong, T-f., 2006. Shear-enhanced compaction and strain localization: inelastic deformation and constitutive modeling of four porous sandstones. *J. Geophys. Res., 111,* B12, B12401.

Bear, J., 1988. *Dynamics of fluids in porous media.* American Elsevier, New York. 764 pp.

Bear, J., 1979. *Hydraulics of groundwater.* McGraw-Hill, New York. 569 pp.

Benson, P. M., Meredith, P. G., Platzman, E. S., 2003. Relating pore fabric geometry to elastic and permeability geometry in Crab Orchard sandstone: a laboratory study using magnetic ferrofluid. *Geophys. Res. Lett., 30(19),* 1976, doi:10.1029/2003GL017929.

Benson, P. M., 2004. Experimental study of void space, permeability and elastic anisotropy in crustal rock under ambient and hydrostatic pressure, Ph.D Thesis. University of London.

Benson, P. M., Thompson, B. D., Meredith, P. G., Vinciguerra, S., Young, R. P., 2007. Imaging slow failure in triaxially deformed Etna basalt using 3D acoustic-emission location and x-ray computed tomography. *Geophys. Res. Lett., 34,* L03303, doi:10.1029/2006GL028721.

Bessinger, B. A., Liu, Z., Cook., N. G. W., Myer, L. R., 1997. A new fracturing mechanism for granular media, *Geophys. Res. Lett., 24,* 2605 – 2608.

Boitnott, G.N., and Scholz, C.H., 1990. Direct measurements of the effective stress law: Deformation of joints subject to pore and confining pressures. *J. Geophys. Res., 95,* 19279-19298.

Brace, W. F., Paulding, B. W., Scholz, C., 1966. Dilatancy in the fracture of crystalline rocks. *J. Geophys. Res., 71,* 3939 – 3953.

Brace, W. F., Walsh, J. B., Frangos, W. T., 1968. Permeability of granite under high pressure. *J. Geophys. Res., 73,* 2225 – 2236.

Byrant, S., Blunt, M. J., 1992. Prediction of relative permeability in simple porous media. *Phys. Rev. A., 46,* (4), 2004 – 2011.

Clint, O. C., 1999. Electric potential changes and elastic emissions generated by fracture and fluid flow during triaxial rock deformation. Ph.D Thesis, University of London.

Costin, L. S., 1987. Time-dependent deformation and failure. In: Atkinson, B. K., (ed) *Fracture mechanics of rock.* Academic Press, London. pp 167 – 215.

Collinson, D. W., 1983. *Methods in rock magnetism and palaeomagnetism.* Chapman and Hall, London. 503 pp.

Curran, J. H., Carroll, M. M., 1979. Shear stress enhancement of void compaction, *J. Geophys. Res., 84,* 1105 – 1112.

Cuss, R. J., Rutter, E. H., Holloway, R. F., 2003. The application of critical state soil mechanics to the mechanical behaviour of porous sandstones. *Int. J. Rock Mech. Min. Sci., 40,* 847 – 862.

Digby, P. J., Murrell, S. A. F., 1975. The role of shear stress concentrations in the initiation of brittle fracture in bodies containing closed cracks. *Bull. Seismol. Soc. Am., 65,* 1163 – 1171.

DiGiovanni, A. A., Fredrich, J. T., Holcomb, D. J., Olsson, W. A., 2000. Micromechanics of compaction in an analogue reservoir sandstone. In: *Proc. 4th North Am. Rock Mech. Symp.*, pp 1153 – 1160.

Du Bernard, X., Eichhubl, P., Aydin, A., 2002. Dilation bands: a new form of localized failure in granular media. *Geophys. Res. Lett., 29,* 2176 – 2179.

Dullien, F., 1979. Porous media: fluid transport and pore structure. Academic Press. 396 pp.

Dunn, D. E., La Fountain, L. J., Jackson, R. E., 1973. Porosity dependence and mechanism of brittle fracture in sandstone. *J. Geophys. Res., 78,* 2403 – 2417.

England, W. A., Mackenzie, A. S., Mann, D. M., Quigley, T. M., 1987. The movement and entrapment of petroleum fluids in the subsurface. *J. Geol. Soc. Lond., 144,* 327-347

Eshelby, J. D., 1957. The determination of the elastic field of an ellipsoidal inclusion and related problems, *Proc. R. Soc. London, Ser. A, 241,* 376 – 396.

Eshelby, J. D., 1959. The elastic field outside an ellipsoidal inclusion, *Proc. R. Soc. London, Ser. A, 252,* 561 – 569.

Fetter, C. W., 2001. *Applied hydrogeology*, Prentice-Hall, UK. 598 pp.

Fletcher, R. C., Pollard, D. D., 1981. Anticrack model for pressure solution surfaces, *Geology, 9,* 419 – 424.

Flinn, D., 1962. On folding during 3D progressive deformation. *Quarterly Journal of the Geological Society of London, 188,* 385 – 428.

Fortin, J., Baud, P., Wong, T-f., 2003. Mechanical compaction of Diemelstadt sandstone: from compacting shear bands to pure compaction bands. *Geophysical Research Abstracts, 5,* 06522, 2003.

Fortin J., Schubnel, A., Gueguen Y., 2005. Elastic wave velocities and permeability evolution during compaction of sandstone. *Int. J. Rock Mech., 42,* 873–889.

Fortin, J., Stanchits, S., Dresen, G., Gueguen. Y., 2006. Acoustic emission and velocities associated with the formation of compaction bands in sandstone, *J Geophys. Res., 111,* B10203, doi:10.1029/2005JB003854.

Freeze, R. A., Cherry., J. A., 1979. *Groundwater.* Prentice-Hall, Englewood Cliffs, New Jersey. 604 pp.

Gatelier, N., Pellet, F., Loret, B., 2002. Mechanical damage of an anisotropic porous rock in cyclic triaxial tests. *Int. J. Rock Mech. Min, 39,* 335 – 354.

Geuguen, Y., Dienes, J., 1989. Transport properties of rocks from statistics and percolation, *Mathematical Geology, 21,* 1 – 13.

Geuguen, Y., Palciauskas, V., 1994. *Introduction to the physics of rocks.* Princeton University Press, Princeton, New Jersey, 294 pp.

Griffith, A. A., 1924. The theory of rupture. In: Biezeno, C. G., Burgers, J. M., (eds), *Proc. 1st Int. Cong. Appl. Mech.* Delft: Tec. Boelhandel en Drukkerji. pp 56 – 63.

Haimson, B.C., Herrick, C.G., 1986. Borehole breakouts - A new tool for estimating in situ stress. In: Stephansson, O., (ed) *Rock stress and rock stress measurements,* Centek Publishers, Stockholm, pp. 271 – 280.

Haimson, B. C., Song, I., 1997. Laboratory study of borehole breakouts in two Berea sandstones reveals dramatically different failure mechanisms, *Eos Trans. AGU, 78* (46), F710.

Haimson, B. C., Song, I., 1998. Borehole breakouts in Berea sandstone: Two porosity-dependent distinct shapes and mechanisms of formation. In: *SPE/ISRM Rock Mechanics in Petroleum Engineering,* Soc. Pet. Eng., Richardson, Tex. pp. 229 – 238.

Handin, J. R. V., Hager, M., Friedman, M., Feather, J. N., 1963. Experimental deformation of sedimentary rock under confining pressure: Pore pressure effects. *AAPG Bull., 47,* 717 – 755.

Hirth, G., Tullis, J., 1994. The brittle-ductile transition in experimentally deformed quartz aggregates. *J. Geophys. Res., 99,* 11731 – 11748.

Holcomb, D. J., 1993. General theory of the Kaiser effect, *Int. J. Rock Mech. Min, 30,* 929 – 935.

Holcomb, D. J., Olsson, W. A., 2003. Compaction localization and fluid flow, *J. Geophys. Res., 108* (B6), 2290, doi:10.1029/2001JB000813.

Horii, D., Nemat-Nasser, S., 1985. Brittle failure in compression: Splitting, faulting and brittle-ductile transition. *Philos. Trans. R. Soc. Lond. Ser. A, 319,* 337 – 374.

Hrouda, F., Hanak, J., Terzijski, I., 2000. The magnetic and pore fabrics of extruded and pressed ceramic models. *Geophys. J. Int., 142,* 941 – 947.

Issen, K. A., Rudnicki, J. W., 2000. Conditions for compaction bands in porous rock, *J. Geophys. Res., 105,* 21529 – 21536.

Issen, K. A., 2002. The influence of constitutive models on localization conditions for porous rock. *Eng. Frac. Mech., 69,* 1891 – 1906.

Ingebritsen, S. E., Sanford, W. E., 1999. *Groundwater in geologic processes.* Cambridge University Press, UK. 341 pp.

Jelinek, V., 1978. Statistical processing of anisotropy of magnetic susceptibility measured on groups of specimens. *Studia. Geoph. Geod., 22,* 50 – 62.

Jaeger, J. C., Cook., 1979. N. G. W., *Fundamentals of Rock Mechanics,* Chapman and Hall, London, UK. 593 pp.

Jones, C., Meredith, P. G., 1998. An experimental study of elastic wave propagation anisotropy and permeability anisotropy in an illitic shale. Presented at Eurock 98.

Jones, S., Benson, P., Meredith, P. G., 2006. Pore fabric anisotropy: testing the equivalent pore concept using magnetic measurements on synthetic voids of known geometry. *Geophys. J. Int.*, 166, 485 – 492.

Kachanov, M., 1993. Elastic solids with many cracks and related problems. *Advances in applied geophysics, 30,* 259 – 445.

Katsman, R., Aharonov, E., Scher, H., 2005. Numerical simulations of compaction bands in high-porosity sedimentary rocks. *Mech. Mater., 37,* 143 – 162.

Katsman, R., Aharonov, E., Scher, H., 2006 a. A numerical study on localized volume reduction in elastic media: some insights on the mechanics of anticracks, *J. Geophys. Res., 111,* B03204, doi:10.1029/2004JB003607.

Katsman, R., Aharonov, E., Scher, H., 2006 b. Localised compaction in rocks: Eshelby's inclusion and the spring network model, *Geophys. Res. Lett., 33,* L10311, doi:1029/2005GL025628.

Klein, E., Baud, P., Reuschle, T., Wong, T-f., 2001. Mechanical behaviour and failure mode of Bentheim sandstone under triaxial compression. *Phys. Chem. Earth A 26,* 21 – 25.

Lajtai, E. Z., Brittle fracture in compression, 1974. *Int. J. Fract. 10,* 525 – 536.

Lockner, D., 1993. The role of acoustic emission in the study of rock. *Int. J. Rock Mech. Min., 30,* 883 – 900.

Lockner, D., Byerlee, J. D., Kuksenko, V., Ponomarev, A., Sidorin, A., 1992. Observations of quasi-static fault growth from acoustic emissions. In: Evans, B., Wong, T-f. (eds) *Fault Mechanics and Transport Properties of Rocks,* International Geophysics Series. Academic Press, London, pp 3 – 32.

Louis, L., David, C., Robion, P., 2003. Comparison of the behaviour of undeformed sandstones under dry and wet conditions. *Tectonophysics, 370,* 193 – 212.

Lubbers, J., Graaff. R., 1998. A simple and accurate formula for the sound velocity in water, *Ultrasound Med. Biol., 24,* 1065-1068.

Main, I. G., Meredith, P. G., Jones, C., 1989. A reinterpretation of the precursory seismic b-value anomaly from fracture mechanics, *Geophys. J. Int., 107,* 353 – 362.

Mair, K., Main, I., Elphick, S., 2000. Sequential growth of deformation bands in the laboratory, *J. Struct. Geol., 22,* 25 – 42.

Mair, K., Elphick, S., Main., 2002. Influence of confining pressure on the mechanical and structural evolution of laboratory deformation bands, *Geophys. Res. Lett., 29,* 10.1029/2001GL013964.

Matthai, S. K., Aydin, A., Pollard, D. D., 1998. Numerical simulations of departures from radial drawdown in faulted sandstone reservoir with joints and deformation bands. In: Jones, G. Fisher, Q. J., Knipe, R. J. (eds) *Faulting, Fault Sealing and Fluid Flow in Hydrocarbon Reservoirs. Geol. Soc. Lond. Special Publications, 147.* pp. 157 – 192.

Mavko, G., Mukerji, T., Dvorkin, J., 1998. *The rock physics handbook*, Cambridge University Press, UK, 329 pp.

McClintock, F. A., Walsh, J. B., 1962. Friction on Griffith cracks in rocks under pressure. In: *Proc. 4th U.S. Nat. Congr. Appl. Mech.*: New York, Am. Soc. Mech. Eng. II. pp 1015 – 1021.

McGarr, A.M., and Gay, N.C., 1978. State of stress in the Earth's crust: *Annual Review of Earth and Planetary Sciences, v. 6,* 405 – 436.

Menendez, B., Zhu., W., Wong, T-f, 1996. Micromechanics of brittle faulting and cataclastic flow in Berea sandstone. *J. Struct. Geol., 18,* 1 – 16.

Meredith, P. G., Main, I., Jones., C. J., 1990. Temporal variations in seismicity during quasi-static and dynamic rock failure. *Tectonophysics, 175,* 249 – 268.

Meredith, P. G., Boon, S. A., Vinciguerra, S., 2005. Creep: Long-term time-dependent rock deformation in a deep-sea laboratory in the Ionian sea: a pilot study. Geophysical Research Abstracts, 7, 06491, 2005.

Mollema, P. N., Antonellini, M. A. 1996. Compaction bands: a structural analog for anti-mode 1 cracks in aeolian sandstone, *Tectonophysics, 267,* 209 – 228.

Murrell, S. A. F., 1963. A criterion for brittle fracture of rocks and concrete under triaxial stress, and the effects of pore pressure on the criterion. In: Fairhurst, C., (ed) *Rock mechanics. 5th Symp. Rock Mechanics.* Pergamon Press, Oxford. pp 563 – 577.

Murrell, S. A. F., 1964. The theory of the propagation of elliptical Griffith cracks under various conditions of plane strain or plane stress. *Br. J. Appl. Phys., 15,* 1195 – 1223.

Nur, A., Byerlee, J.D., 1971. An exact effective stress law for elastic deformation of rock with fluids. *J. Geophys. Res., 76,* 6414 – 6419.

Olsson, W. A., 1999. Theoretical and experimental investigation of compaction bands in porous rock. *J. Geophys. Res.,* 104, 7219 – 7228.

Olsson, W. A., Holcomb, D. J., 2000. Compaction localization in porous rock. *Geophys. Res. Lett., 27,* 3537 – 3540.

Olsson, W. A., 2001. Quasi-static propagation of compaction fronts in porous rock. *Mech. Mater., 33,* 659 – 668.

Olsson, W. A., Holcomb, D. J, Rudnicki, J. W., 2002. Compaction localization in porous sandstone: implications for reservoir mechanics. *Oil & Gas Science and Technology – Rev., 57,* 591 – 599.

Osborn, J. A., 1945. Demagnetising factors of the general ellipsoid. *Phys. Rev., 67,* 345 – 357.

Paterson, M.S., Wong, T-f., 2005. *Experimental rock deformation – the brittle field.* Springer, New York. 347pp.

Pfleiderer, S., Halls, H. C., 1990. Magnetic susceptibility of rocks saturated with ferrofluid: a new method to study pore fabric? *Phys. Earth Planet In., 65,* 158 – 164.

Price, N. J., 1975. Rates of deformation, *J. Geol. Soc. Lond., 131,* pp. 553 – 575.

Ranalli, G., 1995. *Rheology of the earth.* Chapman and Hall, UK. 413 pp.

Rasolofosaon, P. N. J., Zinszner, B. E., 2002. Comparison between permeability anisotropy and elastic anisotropy of reservoir rocks. *Geophysics, 67,* 230 – 240.

Read, M. D., Ayling, M. R., Meredith, P. G., Murrell., S. A. F., 1995. Microcracking during triaxial deformation of porous rocks monitored by changes in rock physical properties. II. Pore volumometry and acoustic emission measurements on water saturated rocks. *Tectonophysics, 245,* 223 – 236.

Rudnicki, J. W., 2002. Compaction bands in porous rock. In: Labuz, J., Drescher, A. (eds) *Bifurcations and instabilities in geomechanics. Proceedings of the international workshop on bifurcation and instability,*. Swets & Zeitlinger, Minnesota, pp 29 – 39.

Rudnicki, J. W., 2006. Models for compaction band propagation, submitted to *Geological Society of London*.

Rudnicki, J. W., Rice, J. R., 1975. Conditions for the localization of deformation in pressure sensitive dilatant materials. *J. Mech. Phys. Solids, 23,* 371 – 394.

Rudnicki, J. W., Sternlof, K., 2005. Energy release model of compaction band propagation. *Geophys. Res. Lett., 32,* L16303, doi:10.1029/2005GL023602

Sammonds, P. R., Ayling, M. R., Meredith, P. G., Murrell, S. A. F., Jones, C., 1989. A laboratory investigation of acoustic emissions and elastic wave velocity changes during rock failure under triaxial stresses. In: Maury and Fourmaintraux (eds), *Rock at great depth – rock mechanics and rock physics at great depth*, Balkema, Rotterdam, 1, 233 – 240.

Sammonds, P. R., Meredith, P. G., Main. I., 1992. Role of pore fluids in the generation of seismic precursors to failure. *Nature, 359,* 228 – 230.

Scholz, C. H., 1968. The frequency-magnitude relation of microfracturing in rock and its relation to earthquakes. *Bull. Seismol. Soc. Am., 58,* 399 – 415.

Scholz, C.H. 2002. *The mechanics of earthquakes and faulting*, 2nd edition. Cambridge University Press. 471pp.

Sibson, R.H., 1986. Earthquakes and rock deformation in crustal fault zone, *Ann. Rev. Earth Planet. Sci, 14,* 149 – 175.

Smith, R., 2007. Forecasting volcanic eruptions from fracture mechanics. Ph.D Thesis, University of London.

Sternlof, K., Pollard, D., 2001. Deformation bands as linear elastic fractures: progress in theory and observation. *Eos Transactions American Geophysical Union 82* (47), F1222.

Sternlof, K., Chapin, J., Pollard, D.D., Durlofsky, L.J., 2004. Effective permeability in sandstones containing deformation band arrays, *AAPG Bulletin, 88,* 1315 – 1329.

Sternlof, K. R., Rudnicki, J. W., Pollard, D. D., 2005. Anticrack inclusion model for compaction bands in sandstone, *J. Geophys. Res.,* 110, B11403, doi: 10.1029/2005JB003764.
Tarling, D.H., Hrouda, F., 1993. *The magnetic anisotropy of rocks*. Chapman and Hall. 232 pp.

Tembe, S., Vajdova, V., Wong, T-f., Zhu, W., 2006, Initiation and propagation of strain localization in circumferentially notched samples of two porous sandstones, *J. Geophys. Res., 111,* B02409, doi:10.1029/2005JB003611.

Terzaghi, K., 1936. The shear resistance of saturated soils and the angle between the planes of shear. In: *Proceedings of the international conference on soil mechanics and foundation engineering, vol 1.* Havard University Press, Cambridge, Mass., pp. 54-56

Thompson, B. D., 2006. Acoustic emission investigation of fracture and fault mechanics in the laboratory. Ph.D Thesis, University of Liverpool.

Tullis, J., Yund, R., 1992. The brittle-ductile transition in feldspar aggregates: an experimental study. In: Evans, B., Wong, T-f. (eds) *Fault mechanics and transport properties of rocks.* International Geophysics Series. Academic Press, London, pp 89 – 117.

Vajdova, V., Wong, T-f., 2003. Incremental propagation of discrete compaction bands: Acoustic emission and microstructural observations on circumferentially notched samples of Bentheim, *J. Geophys. Res., 30,* 14, 1775, doi:10.1029/2003GL017750.

Vajdova, V., Baud, P., Wong, T-f., 2004. Permeability evolution during localized deformation in Bentheim sandstone. *J. Geophys. Res., 109,* B10406, doi:10.1029/2003JB002942.

von Kármán, T., 1911. Festigkeitsversuche unter allseitigem Druck. Z Verein deutsch Ing 55:1749 – 1757.

Wang, B. S., Y. Chen, Wong, T-f., 2006. A discrete element model for the development of compaction localization in granular rock, submitted, *J. Geophys. Res.*

Wilson, M., 1993. Plate moving mechanisms: constraints and controversies, *J. Geol. Soc., 150*: pp 923 – 926.

Winograd, I. J., 1971. Hydrogeology of ash-flow tuff: a preliminary statement. *Water Resour. Res., 7,* 994 – 1006.

Wong, T-f., Baud, P., Klein, E., 2001. Localized failure modes in a compactant porous rock, *Geophys. Res. Lett., 28,* 2521 – 2524.

Wong, T-f., David, C., Zhu, W., 1997. The transition from brittle faulting to cataclastic flow in porous sandstone: mechanical deformation. *J. Geophys. Res., 102,* 3009 – 3025.

Wong, T-f., Szeto, H., Zhang J., 1992. Effect of loading path and porosity on the failure mode of porous rock. *Appl. Mech. Rev., 45,* 281 – 293.

Wu, X. Y., Baud, P., Wong, T-f., 2000. Micromechanics of compressive failure and spatial evolution of anisotropic damage in Darley Dale sandstone, *Int. J. Rock Mech. Min. Sci., 37,* 143 – 160.

Wyllie, M. R. J., Gregory, A. R., Gardner, L. W., 1958. An experimental investigation of factors affecting elastic wave velocities in porous media. *Geophysics, 23,* 459 – 493.

Young, Bowes, 2002. Ultrasonic giga-recorder for seismic and rock fracture mechanics research.

Zhang, J., Wong, T-f., Davis, D. M., 1990. Micromechanics of pressure-induced grain crushing in porous rocks, *J. Geophys. Res., 95,* 341 – 352.

Zhu. W., Wong. T-f., 1997. The transition from brittle faulting to cataclastic flow: permeability evolution. *J. Geophys. Res., 102,* 3027 – 3041.

Zimmerman, R. W., 1991. Compressibility of sandstones. Developments in Geoscience, 29. Elsevier, New York. 173 pp.

Zoback, M.L., 1992. First and second order patterns of stress in the lithosphere: The world stress map project, *J. Geophys. Res., 97,* 11703 – 11728.

Zoback, M.L., Magee, M., 1991. Stress magnitudes in the crust: constraints from stress orientation and relative magnitude data. In: Whitmarsh, R.B., Bott, M.H.P., Fairhead, J.B. and Kusznir, N.J. (eds) *Tectonic stress in the lithosphere. Philosophical transactions of the Royal Society, London,* pp. 181 – 194.

Zoback, M.L., Mastin, L., Barton, C., 1986. In-situ stress measurements in deep boreholes using hydraulic fracturing, wellbore breakouts, and Stoneley-wave polarization. In: Stephansson, O., (ed) *Rock stress and rock stress measurements*, Cenek Publishers, pp. 289 – 299.

| Sample | mAMS Data, principal susceptibilities (degrees) | | | | | | |
|---|---|---|---|---|---|---|---|
| | Bulk susc. | Minimum | | Intermediate | | Maximum | |
| | ($10^{-6}$SI) | Trend | Plunge | Trend | Plunge | Trend | Plunge |
| 1 | 11.04 | 180 | 81 | 0 | 9 | 90 | 0 |
| 2 | 5.52 | 291 | 11 | 66 | 74 | 199 | 11 |
| 3 | 7.61 | 114 | 63 | 336 | 21 | 240 | 17 |
| 4 | 12.76 | 218 | 55 | 45 | 35 | 313 | 3 |
| 5 | 9.35 | 234 | 80 | 24 | 9 | 115 | 5 |
| 6 | 16.8 | 241 | 18 | 132 | 46 | 346 | 39 |
| 7 | 8.19 | 90 | 0 | 0 | 90 | 0 | 0 |
| 8 | 14.66 | 215 | 45 | 98 | 25 | 349 | 35 |
| 9 | 14.04 | 205 | 71 | 308 | 4 | 39 | 18 |
| 10 | 8.25 | 148 | 34 | 336 | 56 | 240 | 4 |
| 11 | 11.96 | 290 | 60 | 27 | 4 | 120 | 30 |
| 12 | 16.96 | 12 | 44 | 180 | 45 | 276 | 6 |
| 13 | 17.48 | 262 | 66 | 123 | 18 | 28 | 15 |
| 14 | 13.98 | 205 | 84 | 333 | 4 | 63 | 4 |
| 15 | 16.9 | 214 | 48 | 357 | 36 | 101 | 19 |
| 16 | 16.04 | 245 | 83 | 7 | 4 | 98 | 6 |
| 17 | 11.96 | 338 | 81 | 239 | 1 | 149 | 9 |
| 18 | 11.1 | 217 | 63 | 111 | 8 | 18 | 25 |
| 19 | 16.96 | 15 | 74 | 208 | 15 | 117 | 3 |
| 20 | 11.99 | 209 | 54 | 309 | 8 | 45 | 35 |
| 21 | 11.78 | 192 | 80 | 27 | 10 | 297 | 3 |
| 22 | 18.86 | 354 | 69 | 131 | 16 | 225 | 13 |

| Sample | tAMS Data, principal susceptibilities (degrees) | | | | | | |
|---|---|---|---|---|---|---|---|
| | Bulk susc. | Minimum | | Intermediate | | Maximum | |
| | ($10^{-6}$SI) | Trend | Plunge | Trend | Plunge | Trend | Plunge |
| 1 | 19390 | 174 | 86 | 42 | 3 | 312 | 3 |
| 2 | 19040 | 129 | 87 | 273 | 2 | 3 | 2 |
| 3 | 20102 | 268 | 83 | 134 | 5 | 43 | 5 |
| 4 | 19630 | 178 | 82 | 77 | 1 | 347 | 7 |
| 5 | 19280 | 190 | 81 | 92 | 1 | 2 | 9 |
| 6 | 20850 | 178 | 80 | 355 | 10 | 85 | 1 |
| 7 | 18960 | 216 | 86 | 56 | 4 | 326 | 1 |
| 8 | 19220 | 153 | 81 | 265 | 3 | 355 | 8 |
| 9 | 18980 | 143 | 87 | 293 | 3 | 23 | 2 |
| 10 | 19040 | 151 | 83 | 4 | 6 | 274 | 4 |
| 11 | 19440 | 253 | 85 | 88 | 5 | 358 | 1 |
| 12 | 20180 | 241 | 75 | 38 | 14 | 129 | 6 |
| 13 | 20880 | 214 | 85 | 2 | 4 | 92 | 3 |
| 14 | 20240 | 330 | 89 | 193 | 1 | 103 | 1 |
| 15 | 19820 | 241 | 80 | 355 | 4 | 86 | 9 |
| 16 | 20540 | 291 | 83 | 131 | 6 | 41 | 2 |
| 17 | 19750 | 155 | 88 | 3 | 2 | 273 | 1 |
| 18 | 20670 | 252 | 84 | 81 | 6 | 351 | 1 |
| 19 | 20350 | 254 | 73 | 149 | 5 | 57 | 16 |
| 20 | 20640 | 213 | 85 | 337 | 3 | 67 | 4 |
| 21 | 20380 | 229 | 75 | 37 | 15 | 128 | 3 |
| 22 | 21170 | 250 | 80 | 48 | 9 | 139 | 3 |

| Sample | mAMS, anisotropy parameters | | | | | |
|---|---|---|---|---|---|---|
| | Principal Susceptibilities, normalised to bulk susceptibility | | | | | |
| | Minimum | Intermediate | Maximum | F | L | A, % |
| 1 | 11.0400 | 0.9682 | 1.0101 | 1.0217 | 1.0433 | 5.4 |
| 2 | 5.5200 | 0.9723 | 1.0068 | 1.0209 | 1.0355 | 4.9 |
| 3 | 7.6100 | 0.9715 | 1.0018 | 1.0267 | 1.0312 | 5.5 |
| 4 | 12.7600 | 0.9769 | 0.9980 | 1.0251 | 1.0216 | 4.8 |
| 5 | 9.3500 | 0.9750 | 0.9994 | 1.0256 | 1.0250 | 5.1 |
| 6 | 16.8000 | 0.9690 | 1.0089 | 1.0221 | 1.0412 | 5.3 |
| 7 | 8.1900 | 0.9606 | 1.0113 | 1.0281 | 1.0528 | 6.8 |
| 8 | 14.6600 | 0.9668 | 1.0012 | 1.0320 | 1.0356 | 6.5 |
| 9 | 14.0400 | 0.9745 | 0.9931 | 1.0324 | 1.0191 | 5.8 |
| 10 | 8.2500 | 0.9714 | 1.0094 | 1.0192 | 1.0391 | 4.8 |
| 11 | 11.9600 | 0.9781 | 1.0092 | 1.0127 | 1.0318 | 3.5 |
| 12 | 16.9600 | 0.9637 | 1.0087 | 1.0276 | 1.0467 | 6.4 |
| 13 | 17.4800 | 0.9777 | 0.9949 | 1.0274 | 1.0176 | 5.0 |
| 14 | 13.9800 | 0.9531 | 1.0220 | 1.0249 | 1.0723 | 7.2 |
| 15 | 16.9000 | 0.9837 | 1.0015 | 1.0148 | 1.0181 | 3.1 |
| 16 | 16.0400 | 0.9729 | 1.0071 | 1.0200 | 1.0352 | 4.7 |
| 17 | 11.9600 | 0.9393 | 1.0215 | 1.0392 | 1.0875 | 10.0 |
| 18 | 11.1000 | 0.9654 | 1.0056 | 1.0290 | 1.0416 | 6.4 |
| 19 | 16.9600 | 0.9533 | 1.0171 | 1.0296 | 1.0669 | 7.6 |
| 20 | 11.9900 | 0.9686 | 1.0094 | 1.0220 | 1.0421 | 5.3 |
| 21 | 11.7800 | 0.9655 | 1.0055 | 1.0290 | 1.0414 | 6.3 |
| 22 | 18.8600 | 0.9677 | 1.0079 | 1.0244 | 1.0415 | 5.7 |

| Sample | tAMS, anisotropy parameters | | | | | |
|---|---|---|---|---|---|---|
| | Principal Susceptibilities, normalised to bulk susceptibility | | | | | |
| | Minimum | Intermediate | Maximum | F | L | A, % |
| 1 | 0.9860 | 1.0032 | 1.0108 | 1.0175 | 1.0076 | 2.5 |
| 2 | 0.9762 | 1.0026 | 1.0212 | 1.0271 | 1.0186 | 4.5 |
| 3 | 0.9818 | 1.0076 | 1.0106 | 1.0263 | 1.0029 | 2.9 |
| 4 | 0.9762 | 1.0096 | 1.0142 | 1.0342 | 1.0046 | 3.8 |
| 5 | 0.9728 | 1.0113 | 1.0159 | 1.0396 | 1.0045 | 4.3 |
| 6 | 0.9768 | 1.0022 | 1.0210 | 1.0260 | 1.0188 | 4.4 |
| 7 | 0.9856 | 1.0000 | 1.0144 | 1.0146 | 1.0144 | 2.9 |
| 8 | 0.9831 | 1.0079 | 1.0090 | 1.0252 | 1.0012 | 2.6 |
| 9 | 0.9844 | 1.0076 | 1.0081 | 1.0236 | 1.0005 | 2.4 |
| 10 | 0.9795 | 1.0078 | 1.0127 | 1.0289 | 1.0049 | 3.3 |
| 11 | 0.9849 | 1.0066 | 1.0085 | 1.0221 | 1.0018 | 2.4 |
| 12 | 0.9812 | 1.0023 | 1.0165 | 1.0215 | 1.0142 | 3.5 |
| 13 | 0.9711 | 1.0137 | 1.0152 | 1.0439 | 1.0015 | 4.4 |
| 14 | 0.9850 | 1.0072 | 1.0078 | 1.0225 | 1.0006 | 2.3 |
| 15 | 0.9812 | 1.0041 | 1.0147 | 1.0233 | 1.0106 | 3.4 |
| 16 | 0.9763 | 1.0080 | 1.0157 | 1.0325 | 1.0076 | 3.9 |
| 17 | 0.9848 | 1.0051 | 1.0101 | 1.0206 | 1.0051 | 2.5 |
| 18 | 0.9879 | 1.0043 | 1.0078 | 1.0166 | 1.0035 | 2.0 |
| 19 | 0.9774 | 1.0029 | 1.0197 | 1.0261 | 1.0168 | 4.2 |
| 20 | 0.9721 | 1.0094 | 1.0185 | 1.0384 | 1.0090 | 4.6 |
| 21 | 0.9756 | 1.0042 | 1.0202 | 1.0293 | 1.0159 | 4.5 |
| 22 | 0.9826 | 1.0047 | 1.0127 | 1.0225 | 1.0080 | 3.0 |

| vP, dry | x-axis / YZ plane velocities, m/s | | | | | |
|---|---|---|---|---|---|---|
| Angle | X1 | X2 | X3 | X4 | X5 | X6 |
| 0 | 2777 | 2772 | 2785 | 2775 | 2785 | 2777 |
| 10 | 2781 | 2774 | 2790 | 2777 | 2785 | 2779 |
| 20 | 2799 | 2785 | 2807 | 2785 | 2793 | 2800 |
| 30 | 2810 | 2805 | 2819 | 2810 | 2801 | 2811 |
| 40 | 2827 | 2832 | 2837 | 2836 | 2823 | 2832 |
| 50 | 2852 | 2849 | 2857 | 2860 | 2844 | 2855 |
| 60 | 2878 | 2877 | 2886 | 2884 | 2879 | 2875 |
| 70 | 2892 | 2897 | 2891 | 2894 | 2892 | 2886 |
| 80 | 2903 | 2904 | 2909 | 2897 | 2909 | 2899 |
| 90 | 2909 | 2910 | 2915 | 2914 | 2919 | 2909 |
| 100 | 2913 | 2912 | 2909 | 2927 | 2914 | 2920 |
| 110 | 2916 | 2911 | 2907 | 2925 | 2910 | 2930 |
| 120 | 2906 | 2905 | 2906 | 2905 | 2901 | 2913 |
| 130 | 2893 | 2896 | 2895 | 2892 | 2891 | 2896 |
| 140 | 2870 | 2864 | 2866 | 2868 | 2867 | 2867 |
| 150 | 2847 | 2863 | 2844 | 2846 | 2841 | 2847 |
| 160 | 2810 | 2819 | 2815 | 2811 | 2815 | 2815 |
| 170 | 2784 | 2788 | 2784 | 2786 | 2796 | 2783 |
| 180 | 2777 | 2773 | 2771 | 2776 | 2786 | 2769 |
| 190 | 2787 | 2783 | 2771 | 2785 | 2786 | 2773 |
| 200 | 2789 | 2794 | 2786 | 2795 | 2792 | 2795 |
| 210 | 2809 | 2805 | 2805 | 2806 | 2807 | 2807 |
| 220 | 2821 | 2824 | 2826 | 2836 | 2826 | 2822 |
| 230 | 2855 | 2857 | 2850 | 2858 | 2853 | 2849 |
| 240 | 2873 | 2875 | 2886 | 2873 | 2879 | 2868 |
| 250 | 2894 | 2896 | 2903 | 2893 | 2904 | 2880 |
| 260 | 2912 | 2910 | 2918 | 2909 | 2917 | 2907 |
| 270 | 2927 | 2921 | 2932 | 2922 | 2922 | 2914 |
| 280 | 2926 | 2918 | 2936 | 2922 | 2922 | 2914 |
| 290 | 2924 | 2925 | 2935 | 2916 | 2922 | 2924 |
| 300 | 2915 | 2908 | 2916 | 2904 | 2904 | 2909 |
| 310 | 2893 | 2888 | 2888 | 2892 | 2876 | 2886 |
| 320 | 2855 | 2856 | 2851 | 2844 | 2854 | 2849 |
| 330 | 2817 | 2821 | 2818 | 2821 | 2829 | 2816 |
| 340 | 2775 | 2773 | 2808 | 2786 | 2791 | 2787 |
| 350 | 2774 | 2762 | 2773 | 2782 | 2763 | 2774 |

| vP, dry | y-axis / XZ plane velocities, m/s | | | | | |
|---|---|---|---|---|---|---|
| Angle | Y1 | Y2 | Y3 | Y4 | Y5 | Y6 |
| 0 | 2779 | 2779 | 2773 | 2783 | 2775 | 2780 |
| 10 | 2782 | 2782 | 2777 | 2784 | 2785 | 2787 |
| 20 | 2786 | 2784 | 2779 | 2795 | 2794 | 2788 |
| 30 | 2800 | 2791 | 2797 | 2807 | 2800 | 2796 |
| 40 | 2829 | 2827 | 2830 | 2828 | 2821 | 2822 |
| 50 | 2851 | 2859 | 2856 | 2853 | 2840 | 2854 |
| 60 | 2880 | 2875 | 2882 | 2890 | 2878 | 2881 |
| 70 | 2901 | 2904 | 2904 | 2910 | 2905 | 2903 |
| 80 | 2929 | 2925 | 2926 | 2936 | 2940 | 2935 |
| 90 | 2938 | 2935 | 2938 | 2946 | 2949 | 2949 |
| 100 | 2952 | 2944 | 2944 | 2958 | 2963 | 2954 |
| 110 | 2952 | 2942 | 2949 | 2960 | 2963 | 2954 |
| 120 | 2932 | 2929 | 2942 | 2959 | 2955 | 2931 |
| 130 | 2908 | 2909 | 2918 | 2924 | 2923 | 2914 |
| 140 | 2881 | 2886 | 2879 | 2874 | 2883 | 2883 |
| 150 | 2842 | 2852 | 2839 | 2842 | 2839 | 2854 |
| 160 | 2831 | 2826 | 2828 | 2817 | 2811 | 2831 |
| 170 | 2808 | 2803 | 2809 | 2810 | 2803 | 2805 |
| 180 | 2778 | 2779 | 2785 | 2785 | 2788 | 2774 |
| 190 | 2776 | 2775 | 2785 | 2772 | 2784 | 2774 |
| 200 | 2783 | 2777 | 2800 | 2774 | 2800 | 2772 |
| 210 | 2807 | 2799 | 2832 | 2797 | 2832 | 2803 |
| 220 | 2830 | 2833 | 2863 | 2824 | 2865 | 2830 |
| 230 | 2859 | 2869 | 2889 | 2852 | 2892 | 2859 |
| 240 | 2884 | 2884 | 2917 | 2891 | 2923 | 2889 |
| 250 | 2911 | 2917 | 2933 | 2916 | 2942 | 2914 |
| 260 | 2929 | 2930 | 2946 | 2937 | 2951 | 2924 |
| 270 | 2947 | 2940 | 2959 | 2945 | 2961 | 2940 |
| 280 | 2958 | 2955 | 2942 | 2958 | 2953 | 2944 |
| 290 | 2949 | 2953 | 2935 | 2955 | 2931 | 2946 |
| 300 | 2930 | 2927 | 2900 | 2931 | 2902 | 2935 |
| 310 | 2900 | 2903 | 2879 | 2898 | 2868 | 2908 |
| 320 | 2875 | 2877 | 2845 | 2872 | 2833 | 2873 |
| 330 | 2841 | 2854 | 2807 | 2840 | 2810 | 2832 |
| 340 | 2809 | 2824 | 2783 | 2820 | 2783 | 2814 |
| 350 | 2789 | 2789 | 2795 | 2807 | 2788 | 2784 |

| vP, dry | z-axis / XY plane velcoties, m/s | | | | | |
|---|---|---|---|---|---|---|
| Angle | Z1 | Z2 | Z3 | Z4 | Z5 | Z6 |
| 0 | 2926 | 2949 | 2932 | 2937 | 2939 | 2927 |
| 10 | 2919 | 2934 | 2925 | 2930 | 2930 | 2933 |
| 20 | 2916 | 2915 | 2927 | 2921 | 2923 | 2928 |
| 30 | 2913 | 2913 | 2923 | 2920 | 2922 | 2915 |
| 40 | 2918 | 2911 | 2919 | 2911 | 2911 | 2918 |
| 50 | 2898 | 2907 | 2915 | 2908 | 2914 | 2917 |
| 60 | 2897 | 2904 | 2901 | 2909 | 2912 | 2908 |
| 70 | 2896 | 2915 | 2905 | 2904 | 2907 | 2905 |
| 80 | 2898 | 2899 | 2907 | 2910 | 2906 | 2899 |
| 90 | 2905 | 2905 | 2916 | 2900 | 2906 | 2908 |
| 100 | 2919 | 2913 | 2919 | 2904 | 2905 | 2916 |
| 110 | 2924 | 2921 | 2923 | 2913 | 2914 | 2918 |
| 120 | 2914 | 2921 | 2927 | 2919 | 2931 | 2919 |
| 130 | 2936 | 2922 | 2934 | 2928 | 2934 | 2925 |
| 140 | 2935 | 2925 | 2928 | 2938 | 2943 | 2938 |
| 150 | 2938 | 2935 | 2936 | 2941 | 2942 | 2943 |
| 160 | 2938 | 2944 | 2941 | 2942 | 2941 | 2951 |
| 170 | 2938 | 2952 | 2936 | 2939 | 2939 | 2942 |
| 180 | 2939 | 2949 | 2933 | 2939 | 2935 | 2937 |
| 190 | 2938 | 2937 | 2939 | 2935 | 2929 | 2930 |
| 200 | 2926 | 2923 | 2931 | 2935 | 2927 | 2929 |
| 210 | 2914 | 2908 | 2934 | 2928 | 2927 | 2914 |
| 220 | 2914 | 2900 | 2911 | 2919 | 2923 | 2903 |
| 230 | 2900 | 2906 | 2907 | 2915 | 2918 | 2909 |
| 240 | 2906 | 2903 | 2906 | 2908 | 2911 | 2913 |
| 250 | 2905 | 2906 | 2912 | 2906 | 2903 | 2915 |
| 260 | 2918 | 2910 | 2916 | 2912 | 2922 | 2924 |
| 270 | 2926 | 2921 | 2922 | 2918 | 2916 | 2932 |
| 280 | 2934 | 2927 | 2920 | 2930 | 2924 | 2941 |
| 290 | 2939 | 2931 | 2938 | 2934 | 2926 | 2949 |
| 300 | 2941 | 2932 | 2945 | 2938 | 2930 | 2947 |
| 310 | 2937 | 2930 | 2934 | 2938 | 2934 | 2952 |
| 320 | 2945 | 2938 | 2936 | 2950 | 2945 | 2954 |
| 330 | 2946 | 2950 | 2952 | 2951 | 2944 | 2951 |
| 340 | 2946 | 2956 | 2948 | 2951 | 2942 | 2950 |
| 350 | 2932 | 2958 | 2945 | 2946 | 2939 | 2952 |

| vSa, dry | x-axis / YZ plane velocities, m/s | | | | | |
|---|---|---|---|---|---|---|
| Angle | X1 | X2 | X3 | X4 | X5 | X6 |
| 0 | 1862 | 1858 | 1859 | 1853 | 1843 | 1866 |
| 10 | 1867 | 1862 | 1873 | 1857 | 1859 | 1867 |
| 20 | 1875 | 1870 | 1884 | 1869 | 1870 | 1874 |
| 30 | 1877 | 1881 | 1880 | 1879 | 1883 | 1891 |
| 40 | 1885 | 1891 | 1896 | 1896 | 1892 | 1905 |
| 50 | 1897 | 1900 | 1902 | 1906 | 1908 | 1910 |
| 60 | 1906 | 1911 | 1914 | 1924 | 1918 | 1920 |
| 70 | 1919 | 1921 | 1922 | 1930 | 1934 | 1936 |
| 80 | 1935 | 1930 | 1934 | 1947 | 1946 | 1947 |
| 90 | 1954 | 1943 | 1939 | 1951 | 1954 | 1953 |
| 100 | 1952 | 1943 | 1951 | 1947 | 1953 | 1938 |
| 110 | 1935 | 1935 | 1926 | 1932 | 1940 | 1924 |
| 120 | 1927 | 1932 | 1937 | 1924 | 1924 | 1904 |
| 130 | 1915 | 1910 | 1909 | 1909 | 1910 | 1889 |
| 140 | 1903 | 1896 | 1913 | 1894 | 1891 | 1878 |
| 150 | 1874 | 1882 | 1876 | 1861 | 1871 | 1862 |
| 160 | 1862 | 1870 | 1862 | 1851 | 1852 | 1861 |
| 170 | 1870 | 1860 | 1867 | 1845 | 1847 | 1853 |
| 180 | 1859 | 1856 | 1858 | 1841 | 1846 | 1853 |
| 190 | 1852 | 1849 | 1854 | 1839 | 1848 | 1862 |
| 200 | 1852 | 1857 | 1857 | 1850 | 1848 | 1882 |
| 210 | 1858 | 1862 | 1866 | 1866 | 1853 | 1887 |
| 220 | 1872 | 1870 | 1882 | 1878 | 1870 | 1896 |
| 230 | 1884 | 1882 | 1895 | 1892 | 1881 | 1911 |
| 240 | 1900 | 1891 | 1904 | 1901 | 1899 | 1916 |
| 250 | 1917 | 1912 | 1917 | 1915 | 1917 | 1929 |
| 260 | 1930 | 1922 | 1933 | 1933 | 1933 | 1948 |
| 270 | 1955 | 1947 | 1955 | 1947 | 1952 | 1948 |
| 280 | 1948 | 1950 | 1949 | 1947 | 1955 | 1948 |
| 290 | 1953 | 1953 | 1950 | 1947 | 1952 | 1940 |
| 300 | 1942 | 1943 | 1944 | 1938 | 1940 | 1925 |
| 310 | 1923 | 1926 | 1930 | 1922 | 1917 | 1897 |
| 320 | 1906 | 1913 | 1912 | 1896 | 1894 | 1881 |
| 330 | 1886 | 1890 | 1900 | 1874 | 1879 | 1875 |
| 340 | 1874 | 1874 | 1880 | 1853 | 1862 | 1857 |
| 350 | 1862 | 1849 | 1871 | 1844 | 1853 | 1860 |

| vSa, dry | y-axis / XZ plane velocities, m/s | | | | | |
|---|---|---|---|---|---|---|
| Angle | Y1 | Y2 | Y3 | Y4 | Y5 | Y6 |
| 0 | 1857 | 1857 | 1856 | 1872 | 1866 | 1863 |
| 10 | 1864 | 1866 | 1862 | 1863 | 1868 | 1870 |
| 20 | 1872 | 1874 | 1872 | 1870 | 1870 | 1877 |
| 30 | 1879 | 1884 | 1885 | 1882 | 1871 | 1883 |
| 40 | 1889 | 1891 | 1900 | 1883 | 1882 | 1883 |
| 50 | 1896 | 1907 | 1909 | 1896 | 1896 | 1896 |
| 60 | 1913 | 1917 | 1925 | 1909 | 1904 | 1916 |
| 70 | 1938 | 1938 | 1949 | 1935 | 1930 | 1943 |
| 80 | 1964 | 1956 | 1966 | 1953 | 1951 | 1964 |
| 90 | 1960 | 1963 | 1964 | 1959 | 1960 | 1961 |
| 100 | 1949 | 1963 | 1946 | 1947 | 1950 | 1942 |
| 110 | 1943 | 1943 | 1926 | 1939 | 1943 | 1938 |
| 120 | 1928 | 1934 | 1913 | 1926 | 1942 | 1923 |
| 130 | 1923 | 1929 | 1907 | 1919 | 1936 | 1930 |
| 140 | 1912 | 1911 | 1892 | 1909 | 1914 | 1907 |
| 150 | 1896 | 1898 | 1886 | 1901 | 1895 | 1886 |
| 160 | 1880 | 1880 | 1866 | 1866 | 1868 | 1879 |
| 170 | 1875 | 1875 | 1855 | 1874 | 1861 | 1870 |
| 180 | 1854 | 1862 | 1858 | 1855 | 1853 | 1853 |
| 190 | 1853 | 1862 | 1857 | 1853 | 1853 | 1849 |
| 200 | 1849 | 1859 | 1855 | 1850 | 1850 | 1845 |
| 210 | 1858 | 1869 | 1865 | 1857 | 1849 | 1847 |
| 220 | 1871 | 1861 | 1867 | 1870 | 1862 | 1860 |
| 230 | 1892 | 1872 | 1883 | 1882 | 1873 | 1868 |
| 240 | 1902 | 1888 | 1896 | 1891 | 1893 | 1882 |
| 250 | 1911 | 1900 | 1920 | 1903 | 1902 | 1896 |
| 260 | 1964 | 1916 | 1960 | 1920 | 1912 | 1917 |
| 270 | 1960 | 1941 | 1949 | 1960 | 1959 | 1933 |
| 280 | 1960 | 1957 | 1952 | 1958 | 1964 | 1961 |
| 290 | 1951 | 1959 | 1954 | 1960 | 1968 | 1963 |
| 300 | 1923 | 1951 | 1926 | 1949 | 1956 | 1943 |
| 310 | 1898 | 1928 | 1900 | 1917 | 1927 | 1921 |
| 320 | 1877 | 1897 | 1884 | 1903 | 1913 | 1902 |
| 330 | 1856 | 1885 | 1866 | 1883 | 1881 | 1880 |
| 340 | 1862 | 1864 | 1850 | 1854 | 1870 | 1858 |
| 350 | 1860 | 1852 | 1848 | 1856 | 1878 | 1845 |

| vSa, dry | z-axis / XY plane velcoties, m/s | | | | | |
|---|---|---|---|---|---|---|
| Angle | Z1 | Z2 | Z3 | Z4 | Z5 | Z6 |
| 0 | 1963 | 1969 | 1964 | 1964 | 1970 | 1954 |
| 10 | 1967 | 1968 | 1971 | 1966 | 1967 | 1965 |
| 20 | 1964 | 1965 | 1965 | 1963 | 1960 | 1968 |
| 30 | 1959 | 1961 | 1962 | 1964 | 1952 | 1960 |
| 40 | 1964 | 1960 | 1967 | 1956 | 1962 | 1955 |
| 50 | 1959 | 1959 | 1967 | 1955 | 1966 | 1955 |
| 60 | 1964 | 1964 | 1963 | 1957 | 1961 | 1967 |
| 70 | 1959 | 1957 | 1958 | 1955 | 1963 | 1960 |
| 80 | 1957 | 1955 | 1963 | 1960 | 1964 | 1952 |
| 90 | 1957 | 1955 | 1963 | 1956 | 1955 | 1955 |
| 100 | 1955 | 1952 | 1953 | 1954 | 1949 | 1959 |
| 110 | 1960 | 1964 | 1961 | 1960 | 1964 | 1960 |
| 120 | 1962 | 1962 | 1960 | 1961 | 1964 | 1957 |
| 130 | 1965 | 1960 | 1961 | 1960 | 1967 | 1957 |
| 140 | 1965 | 1963 | 1968 | 1963 | 1967 | 1960 |
| 150 | 1963 | 1961 | 1960 | 1963 | 1964 | 1964 |
| 160 | 1960 | 1961 | 1960 | 1960 | 1960 | 1960 |
| 170 | 1957 | 1959 | 1960 | 1957 | 1956 | 1956 |
| 180 | 1960 | 1964 | 1962 | 1956 | 1959 | 1961 |
| 190 | 1959 | 1960 | 1958 | 1954 | 1959 | 1960 |
| 200 | 1956 | 1960 | 1955 | 1955 | 1958 | 1961 |
| 210 | 1953 | 1953 | 1952 | 1955 | 1956 | 1959 |
| 220 | 1958 | 1946 | 1956 | 1956 | 1961 | 1954 |
| 230 | 1958 | 1954 | 1951 | 1959 | 1963 | 1955 |
| 240 | 1963 | 1957 | 1960 | 1962 | 1963 | 1961 |
| 250 | 1955 | 1955 | 1949 | 1958 | 1956 | 1964 |
| 260 | 1959 | 1958 | 1958 | 1956 | 1957 | 1968 |
| 270 | 1969 | 1965 | 1957 | 1960 | 1964 | 1968 |
| 280 | 1967 | 1963 | 1965 | 1961 | 1963 | 1969 |
| 290 | 1967 | 1968 | 1967 | 1966 | 1969 | 1971 |
| 300 | 1968 | 1967 | 1970 | 1965 | 1969 | 1965 |
| 310 | 1968 | 1970 | 1969 | 1964 | 1969 | 1960 |
| 320 | 1967 | 1972 | 1968 | 1967 | 1968 | 1958 |
| 330 | 1964 | 1966 | 1968 | 1970 | 1965 | 1955 |
| 340 | 1962 | 1961 | 1961 | 1966 | 1963 | 1955 |
| 350 | 1963 | 1960 | 1960 | 1963 | 1948 | 1952 |

| vSb, dry | x-axis / YZ plane velocities, m/s | | | | | |
|---|---|---|---|---|---|---|
| Angle | X1 | X2 | X3 | X4 | X5 | X6 |
| 0 | 1865 | 1862 | 1865 | 1865 | 1862 | 1851 |
| 10 | 1870 | 1869 | 1864 | 1874 | 1869 | 1864 |
| 20 | 1884 | 1879 | 1885 | 1885 | 1880 | 1866 |
| 30 | 1882 | 1887 | 1881 | 1892 | 1883 | 1879 |
| 40 | 1905 | 1899 | 1902 | 1903 | 1899 | 1892 |
| 50 | 1912 | 1910 | 1897 | 1910 | 1905 | 1902 |
| 60 | 1921 | 1923 | 1921 | 1917 | 1917 | 1920 |
| 70 | 1935 | 1935 | 1933 | 1932 | 1926 | 1930 |
| 80 | 1939 | 1938 | 1934 | 1939 | 1934 | 1934 |
| 90 | 1944 | 1948 | 1947 | 1948 | 1943 | 1945 |
| 100 | 1942 | 1948 | 1945 | 1951 | 1944 | 1941 |
| 110 | 1933 | 1935 | 1934 | 1954 | 1929 | 1930 |
| 120 | 1921 | 1916 | 1911 | 1936 | 1937 | 1920 |
| 130 | 1906 | 1908 | 1914 | 1902 | 1906 | 1907 |
| 140 | 1885 | 1890 | 1882 | 1885 | 1896 | 1907 |
| 150 | 1868 | 1867 | 1862 | 1864 | 1875 | 1874 |
| 160 | 1859 | 1857 | 1853 | 1852 | 1859 | 1859 |
| 170 | 1851 | 1854 | 1847 | 1849 | 1856 | 1853 |
| 180 | 1848 | 1853 | 1854 | 1853 | 1853 | 1856 |
| 190 | 1849 | 1853 | 1857 | 1854 | 1843 | 1857 |
| 200 | 1857 | 1857 | 1866 | 1861 | 1858 | 1865 |
| 210 | 1879 | 1869 | 1880 | 1881 | 1869 | 1880 |
| 220 | 1893 | 1883 | 1891 | 1891 | 1881 | 1885 |
| 230 | 1904 | 1899 | 1903 | 1901 | 1878 | 1887 |
| 240 | 1918 | 1908 | 1917 | 1917 | 1904 | 1900 |
| 250 | 1930 | 1925 | 1935 | 1939 | 1910 | 1914 |
| 260 | 1946 | 1945 | 1949 | 1946 | 1922 | 1930 |
| 270 | 1949 | 1955 | 1949 | 1950 | 1929 | 1950 |
| 280 | 1948 | 1959 | 1944 | 1954 | 1951 | 1936 |
| 290 | 1942 | 1950 | 1937 | 1948 | 1938 | 1947 |
| 300 | 1931 | 1934 | 1923 | 1939 | 1934 | 1926 |
| 310 | 1919 | 1921 | 1909 | 1925 | 1917 | 1917 |
| 320 | 1896 | 1908 | 1897 | 1911 | 1899 | 1895 |
| 330 | 1882 | 1890 | 1883 | 1882 | 1877 | 1880 |
| 340 | 1867 | 1871 | 1868 | 1863 | 1857 | 1855 |
| 350 | 1863 | 1870 | 1855 | 1863 | 1846 | 1866 |

| vSb, dry | y-axis / XZ plane velocities, m/s | | | | | |
|---|---|---|---|---|---|---|
| Angle | Y1 | Y2 | Y3 | Y4 | Y5 | Y6 |
| 0 | 1853 | 1852 | 1855 | 1855 | 1855 | 1862 |
| 10 | 1858 | 1854 | 1857 | 1850 | 1857 | 1863 |
| 20 | 1859 | 1862 | 1866 | 1865 | 1869 | 1881 |
| 30 | 1872 | 1873 | 1873 | 1866 | 1874 | 1884 |
| 40 | 1893 | 1887 | 1890 | 1891 | 1895 | 1889 |
| 50 | 1908 | 1907 | 1909 | 1901 | 1913 | 1901 |
| 60 | 1931 | 1928 | 1920 | 1926 | 1922 | 1926 |
| 70 | 1947 | 1942 | 1936 | 1931 | 1939 | 1943 |
| 80 | 1950 | 1952 | 1951 | 1952 | 1955 | 1951 |
| 90 | 1950 | 1950 | 1960 | 1947 | 1952 | 1947 |
| 100 | 1947 | 1945 | 1960 | 1955 | 1946 | 1947 |
| 110 | 1930 | 1926 | 1937 | 1951 | 1935 | 1930 |
| 120 | 1914 | 1915 | 1917 | 1921 | 1918 | 1913 |
| 130 | 1908 | 1903 | 1896 | 1906 | 1902 | 1900 |
| 140 | 1900 | 1899 | 1892 | 1898 | 1888 | 1882 |
| 150 | 1879 | 1877 | 1876 | 1885 | 1874 | 1870 |
| 160 | 1872 | 1874 | 1862 | 1876 | 1866 | 1859 |
| 170 | 1867 | 1868 | 1858 | 1870 | 1859 | 1853 |
| 180 | 1854 | 1848 | 1848 | 1858 | 1858 | 1847 |
| 190 | 1857 | 1850 | 1842 | 1853 | 1854 | 1857 |
| 200 | 1849 | 1845 | 1842 | 1843 | 1858 | 1846 |
| 210 | 1854 | 1856 | 1852 | 1848 | 1851 | 1855 |
| 220 | 1869 | 1872 | 1864 | 1858 | 1874 | 1869 |
| 230 | 1884 | 1885 | 1874 | 1854 | 1882 | 1879 |
| 240 | 1896 | 1903 | 1893 | 1892 | 1903 | 1898 |
| 250 | 1909 | 1901 | 1915 | 1901 | 1910 | 1912 |
| 260 | 1921 | 1919 | 1921 | 1914 | 1921 | 1920 |
| 270 | 1951 | 1956 | 1947 | 1952 | 1938 | 1943 |
| 280 | 1947 | 1940 | 1958 | 1951 | 1955 | 1954 |
| 290 | 1947 | 1941 | 1957 | 1957 | 1948 | 1965 |
| 300 | 1950 | 1953 | 1953 | 1952 | 1938 | 1965 |
| 310 | 1926 | 1925 | 1930 | 1922 | 1921 | 1928 |
| 320 | 1912 | 1911 | 1906 | 1900 | 1907 | 1916 |
| 330 | 1889 | 1890 | 1884 | 1879 | 1879 | 1904 |
| 340 | 1870 | 1868 | 1861 | 1866 | 1862 | 1909 |
| 350 | 1851 | 1858 | 1858 | 1843 | 1848 | 1867 |

| vSb, dry | z-axis / XY plane velcoties, m/s | | | | | |
|---|---|---|---|---|---|---|
| Angle | Z1 | Z2 | Z3 | Z4 | Z5 | Z6 |
| 0 | 1962 | 1965 | 1972 | 1962 | 1961 | 1970 |
| 10 | 1963 | 1966 | 1968 | 1962 | 1957 | 1958 |
| 20 | 1956 | 1963 | 1963 | 1957 | 1950 | 1958 |
| 30 | 1951 | 1956 | 1959 | 1955 | 1951 | 1954 |
| 40 | 1947 | 1954 | 1953 | 1950 | 1951 | 1951 |
| 50 | 1945 | 1951 | 1943 | 1946 | 1947 | 1945 |
| 60 | 1945 | 1950 | 1943 | 1942 | 1946 | 1943 |
| 70 | 1941 | 1943 | 1938 | 1939 | 1937 | 1939 |
| 80 | 1955 | 1942 | 1943 | 1942 | 1938 | 1943 |
| 90 | 1954 | 1951 | 1952 | 1944 | 1943 | 1944 |
| 100 | 1952 | 1951 | 1951 | 1948 | 1950 | 1951 |
| 110 | 1953 | 1954 | 1956 | 1952 | 1953 | 1959 |
| 120 | 1955 | 1953 | 1964 | 1954 | 1951 | 1959 |
| 130 | 1955 | 1959 | 1964 | 1956 | 1958 | 1965 |
| 140 | 1960 | 1958 | 1962 | 1959 | 1956 | 1955 |
| 150 | 1962 | 1951 | 1963 | 1962 | 1960 | 1951 |
| 160 | 1962 | 1957 | 1961 | 1965 | 1964 | 1964 |
| 170 | 1960 | 1956 | 1960 | 1961 | 1961 | 1953 |
| 180 | 1957 | 1950 | 1959 | 1956 | 1958 | 1958 |
| 190 | 1955 | 1950 | 1957 | 1954 | 1955 | 1952 |
| 200 | 1951 | 1951 | 1953 | 1951 | 1951 | 1949 |
| 210 | 1948 | 1951 | 1950 | 1948 | 1947 | 1943 |
| 220 | 1943 | 1947 | 1950 | 1945 | 1947 | 1942 |
| 230 | 1944 | 1941 | 1945 | 1945 | 1945 | 1947 |
| 240 | 1946 | 1946 | 1946 | 1947 | 1939 | 1944 |
| 250 | 1945 | 1943 | 1951 | 1947 | 1939 | 1947 |
| 260 | 1951 | 1951 | 1958 | 1950 | 1957 | 1948 |
| 270 | 1951 | 1956 | 1960 | 1953 | 1958 | 1955 |
| 280 | 1958 | 1958 | 1954 | 1956 | 1951 | 1958 |
| 290 | 1958 | 1959 | 1954 | 1958 | 1961 | 1955 |
| 300 | 1960 | 1962 | 1954 | 1959 | 1954 | 1959 |
| 310 | 1961 | 1964 | 1955 | 1961 | 1966 | 1960 |
| 320 | 1961 | 1964 | 1956 | 1964 | 1969 | 1964 |
| 330 | 1960 | 1964 | 1951 | 1963 | 1961 | 1962 |
| 340 | 1964 | 1957 | 1951 | 1964 | 1960 | 1956 |
| 350 | 1961 | 1955 | 1953 | 1963 | 1967 | 1952 |

| vP, sat | x-axis / YZ plane velocities, m/s | | | | | |
|---|---|---|---|---|---|---|
| Angle | X1 | X2 | X3 | X4 | X5 | X6 |
| 0 | 3342 | 3340 | 3333 | 3337 | 3345 | 3337 |
| 10 | 3338 | 3335 | 3338 | 3338 | 3338 | 3342 |
| 20 | 3351 | 3352 | 3345 | 3347 | 3357 | 3354 |
| 30 | 3354 | 3362 | 3356 | 3355 | 3366 | 3362 |
| 40 | 3370 | 3367 | 3366 | 3369 | 3367 | 3377 |
| 50 | 3381 | 3371 | 3382 | 3385 | 3386 | 3394 |
| 60 | 3400 | 3381 | 3400 | 3402 | 3411 | 3408 |
| 70 | 3414 | 3409 | 3412 | 3416 | 3412 | 3422 |
| 80 | 3429 | 3413 | 3417 | 3424 | 3422 | 3431 |
| 90 | 3434 | 3419 | 3414 | 3422 | 3423 | 3430 |
| 100 | 3427 | 3421 | 3419 | 3427 | 3431 | 3422 |
| 110 | 3432 | 3427 | 3425 | 3425 | 3426 | 3434 |
| 120 | 3418 | 3417 | 3425 | 3419 | 3430 | 3429 |
| 130 | 3424 | 3408 | 3410 | 3410 | 3420 | 3409 |
| 140 | 3424 | 3397 | 3393 | 3395 | 3400 | 3393 |
| 150 | 3407 | 3383 | 3353 | 3386 | 3391 | 3382 |
| 160 | 3387 | 3359 | 3333 | 3363 | 3363 | 3362 |
| 170 | 3366 | 3346 | 3335 | 3337 | 3341 | 3340 |
| 180 | 3349 | 3335 | 3348 | 3335 | 3340 | 3342 |
| 190 | 3338 | 3341 | 3352 | 3336 | 3345 | 3348 |
| 200 | 3340 | 3347 | 3360 | 3342 | 3345 | 3359 |
| 210 | 3347 | 3357 | 3367 | 3351 | 3354 | 3375 |
| 220 | 3354 | 3364 | 3385 | 3363 | 3366 | 3378 |
| 230 | 3363 | 3395 | 3405 | 3386 | 3390 | 3394 |
| 240 | 3392 | 3402 | 3417 | 3397 | 3404 | 3409 |
| 250 | 3405 | 3417 | 3429 | 3414 | 3424 | 3424 |
| 260 | 3410 | 3427 | 3428 | 3417 | 3435 | 3433 |
| 270 | 3425 | 3431 | 3424 | 3424 | 3432 | 3434 |
| 280 | 3428 | 3426 | 3429 | 3426 | 3425 | 3430 |
| 290 | 3426 | 3433 | 3419 | 3425 | 3422 | 3420 |
| 300 | 3421 | 3424 | 3410 | 3416 | 3418 | 3418 |
| 310 | 3419 | 3409 | 3381 | 3410 | 3405 | 3405 |
| 320 | 3407 | 3383 | 3357 | 3393 | 3393 | 3383 |
| 330 | 3387 | 3358 | 3337 | 3373 | 3366 | 3365 |
| 340 | 3367 | 3348 | 3328 | 3347 | 3345 | 3334 |
| 350 | 3342 | 3345 | 3325 | 3338 | 3326 | 3330 |

| vP, sat | y-axis / XZ plane velocities, m/s | | | | | |
|---|---|---|---|---|---|---|
| Angle | Y1 | Y2 | Y3 | Y4 | Y5 | Y6 |
| 0 | 3335 | 3345 | 3340 | 3339 | 3335 | 3337 |
| 10 | 3340 | 3342 | 3340 | 3333 | 3336 | 3345 |
| 20 | 3335 | 3344 | 3339 | 3343 | 3342 | 3341 |
| 30 | 3350 | 3357 | 3355 | 3354 | 3345 | 3352 |
| 40 | 3378 | 3371 | 3378 | 3365 | 3357 | 3370 |
| 50 | 3388 | 3390 | 3385 | 3395 | 3363 | 3383 |
| 60 | 3403 | 3408 | 3406 | 3396 | 3379 | 3402 |
| 70 | 3423 | 3426 | 3424 | 3423 | 3391 | 3422 |
| 80 | 3446 | 3438 | 3443 | 3446 | 3405 | 3448 |
| 90 | 3454 | 3450 | 3451 | 3458 | 3424 | 3455 |
| 100 | 3465 | 3461 | 3462 | 3454 | 3434 | 3465 |
| 110 | 3453 | 3454 | 3462 | 3445 | 3453 | 3456 |
| 120 | 3444 | 3450 | 3453 | 3424 | 3460 | 3448 |
| 130 | 3425 | 3424 | 3439 | 3414 | 3462 | 3443 |
| 140 | 3409 | 3414 | 3405 | 3397 | 3448 | 3420 |
| 150 | 3378 | 3391 | 3377 | 3380 | 3401 | 3389 |
| 160 | 3370 | 3367 | 3376 | 3350 | 3376 | 3377 |
| 170 | 3354 | 3354 | 3350 | 3335 | 3360 | 3347 |
| 180 | 3338 | 3342 | 3335 | 3344 | 3340 | 3328 |
| 190 | 3331 | 3344 | 3335 | 3333 | 3354 | 3331 |
| 200 | 3337 | 3354 | 3352 | 3340 | 3371 | 3348 |
| 210 | 3354 | 3376 | 3370 | 3350 | 3391 | 3371 |
| 220 | 3368 | 3396 | 3398 | 3376 | 3415 | 3393 |
| 230 | 3393 | 3415 | 3409 | 3395 | 3427 | 3417 |
| 240 | 3414 | 3431 | 3426 | 3416 | 3439 | 3436 |
| 250 | 3433 | 3441 | 3440 | 3434 | 3449 | 3446 |
| 260 | 3441 | 3448 | 3450 | 3443 | 3460 | 3448 |
| 270 | 3447 | 3456 | 3462 | 3451 | 3462 | 3447 |
| 280 | 3458 | 3453 | 3458 | 3458 | 3441 | 3439 |
| 290 | 3455 | 3442 | 3441 | 3448 | 3426 | 3422 |
| 300 | 3443 | 3425 | 3417 | 3435 | 3414 | 3402 |
| 310 | 3419 | 3405 | 3400 | 3418 | 3388 | 3386 |
| 320 | 3400 | 3382 | 3379 | 3400 | 3371 | 3359 |
| 330 | 3373 | 3364 | 3359 | 3371 | 3343 | 3340 |
| 340 | 3354 | 3346 | 3347 | 3351 | 3346 | 3343 |
| 350 | 3338 | 3341 | 3349 | 3340 | 3350 | 3340 |

| vP, sat | z-axis / XY plane velcoties, m/s | | | | | |
|---|---|---|---|---|---|---|
| Angle | Z1 | Z2 | Z3 | Z4 | Z5 | Z6 |
| 0 | 3460 | 3449 | 3468 | 3462 | 3465 | 3454 |
| 10 | 3448 | 3453 | 3465 | 3468 | 3460 | 3456 |
| 20 | 3444 | 3446 | 3456 | 3454 | 3442 | 3443 |
| 30 | 3440 | 3443 | 3442 | 3446 | 3440 | 3437 |
| 40 | 3436 | 3435 | 3438 | 3432 | 3439 | 3433 |
| 50 | 3438 | 3429 | 3436 | 3431 | 3438 | 3427 |
| 60 | 3431 | 3426 | 3435 | 3430 | 3434 | 3426 |
| 70 | 3430 | 3421 | 3430 | 3421 | 3428 | 3425 |
| 80 | 3432 | 3421 | 3429 | 3426 | 3428 | 3427 |
| 90 | 3431 | 3429 | 3432 | 3430 | 3436 | 3424 |
| 100 | 3443 | 3437 | 3434 | 3436 | 3438 | 3431 |
| 110 | 3446 | 3437 | 3442 | 3441 | 3444 | 3439 |
| 120 | 3450 | 3443 | 3451 | 3437 | 3439 | 3448 |
| 130 | 3454 | 3445 | 3459 | 3439 | 3443 | 3452 |
| 140 | 3462 | 3455 | 3463 | 3445 | 3439 | 3458 |
| 150 | 3457 | 3465 | 3465 | 3451 | 3441 | 3456 |
| 160 | 3451 | 3464 | 3458 | 3458 | 3452 | 3463 |
| 170 | 3448 | 3461 | 3470 | 3459 | 3459 | 3471 |
| 180 | 3457 | 3460 | 3461 | 3445 | 3464 | 3463 |
| 190 | 3448 | 3455 | 3466 | 3440 | 3464 | 3461 |
| 200 | 3440 | 3446 | 3453 | 3437 | 3452 | 3454 |
| 210 | 3435 | 3446 | 3457 | 3430 | 3442 | 3438 |
| 220 | 3427 | 3439 | 3450 | 3423 | 3435 | 3437 |
| 230 | 3424 | 3432 | 3439 | 3426 | 3421 | 3434 |
| 240 | 3422 | 3427 | 3433 | 3430 | 3431 | 3433 |
| 250 | 3422 | 3431 | 3431 | 3433 | 3423 | 3431 |
| 260 | 3436 | 3435 | 3438 | 3427 | 3428 | 3437 |
| 270 | 3440 | 3440 | 3439 | 3444 | 3444 | 3445 |
| 280 | 3448 | 3444 | 3446 | 3454 | 3450 | 3452 |
| 290 | 3460 | 3444 | 3450 | 3455 | 3456 | 3455 |
| 300 | 3466 | 3449 | 3447 | 3459 | 3457 | 3461 |
| 310 | 3468 | 3453 | 3449 | 3455 | 3457 | 3461 |
| 320 | 3474 | 3467 | 3457 | 3458 | 3457 | 3459 |
| 330 | 3470 | 3460 | 3462 | 3462 | 3457 | 3458 |
| 340 | 3465 | 3459 | 3470 | 3450 | 3461 | 3457 |
| 350 | 3457 | 3455 | 3464 | 3442 | 3459 | 3465 |

| vSa, sat | x-axis / YZ plane velocities, m/s | | | | | |
|---|---|---|---|---|---|---|
| Angle | X1 | X2 | X3 | X4 | X5 | X6 |
| 0 | 1759 | 1756 | 1745 | 1777 | 1779 | 1753 |
| 10 | 1768 | 1764 | 1762 | 1770 | 1779 | 1766 |
| 20 | 1777 | 1771 | 1762 | 1779 | 1774 | 1773 |
| 30 | 1776 | 1773 | 1782 | 1781 | 1774 | 1770 |
| 40 | 1791 | 1786 | 1779 | 1788 | 1783 | 1784 |
| 50 | 1797 | 1796 | 1807 | 1799 | 1789 | 1800 |
| 60 | 1804 | 1800 | 1801 | 1810 | 1800 | 1829 |
| 70 | 1826 | 1821 | 1826 | 1822 | 1821 | 1847 |
| 80 | 1838 | 1830 | 1849 | 1836 | 1837 | 1863 |
| 90 | 1855 | 1851 | 1862 | 1846 | 1864 | 1844 |
| 100 | 1854 | 1840 | 1855 | 1855 | 1860 | 1830 |
| 110 | 1838 | 1843 | 1850 | 1855 | 1851 | 1814 |
| 120 | 1820 | 1821 | 1829 | 1849 | 1820 | 1800 |
| 130 | 1804 | 1801 | 1831 | 1840 | 1810 | 1773 |
| 140 | 1782 | 1803 | 1806 | 1817 | 1805 | 1762 |
| 150 | 1774 | 1777 | 1806 | 1799 | 1774 | 1751 |
| 160 | 1770 | 1774 | 1778 | 1780 | 1780 | 1750 |
| 170 | 1770 | 1770 | 1765 | 1779 | 1758 | 1762 |
| 180 | 1771 | 1756 | 1760 | 1766 | 1749 | 1746 |
| 190 | 1766 | 1755 | 1755 | 1757 | 1745 | 1766 |
| 200 | 1759 | 1756 | 1743 | 1752 | 1751 | 1780 |
| 210 | 1759 | 1766 | 1758 | 1749 | 1766 | 1804 |
| 220 | 1778 | 1780 | 1765 | 1750 | 1768 | 1808 |
| 230 | 1785 | 1786 | 1785 | 1761 | 1780 | 1824 |
| 240 | 1799 | 1802 | 1796 | 1774 | 1789 | 1836 |
| 250 | 1806 | 1803 | 1793 | 1787 | 1819 | 1843 |
| 260 | 1822 | 1826 | 1813 | 1804 | 1827 | 1835 |
| 270 | 1852 | 1847 | 1842 | 1821 | 1835 | 1847 |
| 280 | 1852 | 1860 | 1840 | 1845 | 1843 | 1851 |
| 290 | 1847 | 1873 | 1836 | 1858 | 1844 | 1831 |
| 300 | 1843 | 1851 | 1829 | 1848 | 1841 | 1809 |
| 310 | 1827 | 1836 | 1817 | 1833 | 1821 | 1788 |
| 320 | 1818 | 1813 | 1806 | 1824 | 1813 | 1768 |
| 330 | 1805 | 1779 | 1796 | 1799 | 1777 | 1753 |
| 340 | 1784 | 1770 | 1778 | 1788 | 1782 | 1745 |
| 350 | 1771 | 1753 | 1769 | 1779 | 1765 | 1742 |

| vSa, sat | y-axis / XZ plane velocities, m/s | | | | | |
|---|---|---|---|---|---|---|
| Angle | Y1 | Y2 | Y3 | Y4 | Y5 | Y6 |
| 0 | 1756 | 1774 | 1766 | 1769 | 1765 | 1772 |
| 10 | 1774 | 1764 | 1766 | 1762 | 1773 | 1755 |
| 20 | 1771 | 1768 | 1766 | 1770 | 1762 | 1769 |
| 30 | 1777 | 1783 | 1783 | 1779 | 1779 | 1775 |
| 40 | 1801 | 1795 | 1783 | 1804 | 1788 | 1793 |
| 50 | 1795 | 1803 | 1804 | 1812 | 1804 | 1788 |
| 60 | 1821 | 1807 | 1810 | 1821 | 1813 | 1813 |
| 70 | 1832 | 1824 | 1821 | 1836 | 1821 | 1824 |
| 80 | 1838 | 1867 | 1830 | 1851 | 1839 | 1841 |
| 90 | 1837 | 1873 | 1838 | 1851 | 1860 | 1830 |
| 100 | 1855 | 1856 | 1860 | 1843 | 1860 | 1851 |
| 110 | 1863 | 1846 | 1844 | 1826 | 1856 | 1838 |
| 120 | 1834 | 1825 | 1830 | 1810 | 1848 | 1828 |
| 130 | 1831 | 1812 | 1817 | 1791 | 1843 | 1826 |
| 140 | 1830 | 1801 | 1803 | 1768 | 1827 | 1815 |
| 150 | 1809 | 1805 | 1785 | 1774 | 1804 | 1802 |
| 160 | 1793 | 1774 | 1776 | 1758 | 1796 | 1779 |
| 170 | 1772 | 1777 | 1779 | 1754 | 1783 | 1763 |
| 180 | 1780 | 1758 | 1775 | 1759 | 1763 | 1756 |
| 190 | 1769 | 1745 | 1762 | 1757 | 1756 | 1752 |
| 200 | 1755 | 1756 | 1760 | 1748 | 1753 | 1743 |
| 210 | 1769 | 1749 | 1753 | 1751 | 1760 | 1741 |
| 220 | 1776 | 1763 | 1757 | 1768 | 1779 | 1755 |
| 230 | 1772 | 1777 | 1780 | 1791 | 1788 | 1775 |
| 240 | 1774 | 1804 | 1808 | 1813 | 1788 | 1807 |
| 250 | 1795 | 1813 | 1812 | 1816 | 1802 | 1810 |
| 260 | 1817 | 1819 | 1840 | 1826 | 1804 | 1827 |
| 270 | 1825 | 1840 | 1855 | 1847 | 1830 | 1856 |
| 280 | 1851 | 1863 | 1842 | 1842 | 1863 | 1844 |
| 290 | 1861 | 1852 | 1831 | 1849 | 1870 | 1842 |
| 300 | 1848 | 1842 | 1820 | 1843 | 1862 | 1836 |
| 310 | 1855 | 1824 | 1803 | 1832 | 1858 | 1819 |
| 320 | 1837 | 1803 | 1783 | 1811 | 1851 | 1801 |
| 330 | 1803 | 1784 | 1780 | 1804 | 1822 | 1772 |
| 340 | 1795 | 1782 | 1774 | 1788 | 1792 | 1767 |
| 350 | 1775 | 1766 | 1772 | 1780 | 1783 | 1770 |

| vSa, sat | z-axis / XY plane velcoties, m/s | | | | | |
|---|---|---|---|---|---|---|
| Angle | Z1 | Z2 | Z3 | Z4 | Z5 | Z6 |
| 0 | 1864 | 1869 | 1869 | 1853 | 1868 | 1869 |
| 10 | 1857 | 1865 | 1864 | 1864 | 1867 | 1867 |
| 20 | 1864 | 1868 | 1850 | 1865 | 1867 | 1866 |
| 30 | 1856 | 1859 | 1850 | 1857 | 1860 | 1855 |
| 40 | 1858 | 1856 | 1855 | 1856 | 1862 | 1849 |
| 50 | 1848 | 1848 | 1843 | 1850 | 1859 | 1847 |
| 60 | 1847 | 1840 | 1841 | 1842 | 1855 | 1847 |
| 70 | 1849 | 1837 | 1843 | 1838 | 1847 | 1849 |
| 80 | 1845 | 1847 | 1850 | 1848 | 1843 | 1843 |
| 90 | 1851 | 1851 | 1838 | 1856 | 1852 | 1851 |
| 100 | 1851 | 1853 | 1849 | 1864 | 1857 | 1856 |
| 110 | 1851 | 1863 | 1855 | 1865 | 1868 | 1854 |
| 120 | 1860 | 1856 | 1855 | 1864 | 1863 | 1854 |
| 130 | 1851 | 1857 | 1855 | 1868 | 1861 | 1857 |
| 140 | 1854 | 1860 | 1860 | 1870 | 1852 | 1860 |
| 150 | 1860 | 1850 | 1860 | 1862 | 1858 | 1860 |
| 160 | 1854 | 1862 | 1859 | 1860 | 1856 | 1854 |
| 170 | 1860 | 1860 | 1847 | 1857 | 1852 | 1851 |
| 180 | 1862 | 1855 | 1853 | 1849 | 1844 | 1858 |
| 190 | 1858 | 1858 | 1853 | 1847 | 1846 | 1864 |
| 200 | 1857 | 1855 | 1850 | 1855 | 1853 | 1860 |
| 210 | 1853 | 1848 | 1851 | 1846 | 1851 | 1849 |
| 220 | 1851 | 1862 | 1849 | 1846 | 1849 | 1852 |
| 230 | 1853 | 1847 | 1847 | 1848 | 1850 | 1847 |
| 240 | 1851 | 1848 | 1845 | 1847 | 1853 | 1847 |
| 250 | 1851 | 1854 | 1847 | 1858 | 1855 | 1853 |
| 260 | 1864 | 1860 | 1857 | 1861 | 1863 | 1857 |
| 270 | 1868 | 1860 | 1862 | 1858 | 1868 | 1861 |
| 280 | 1869 | 1864 | 1865 | 1862 | 1858 | 1861 |
| 290 | 1864 | 1860 | 1867 | 1864 | 1862 | 1864 |
| 300 | 1872 | 1862 | 1865 | 1864 | 1865 | 1866 |
| 310 | 1867 | 1868 | 1865 | 1865 | 1859 | 1866 |
| 320 | 1864 | 1864 | 1862 | 1858 | 1857 | 1861 |
| 330 | 1866 | 1856 | 1858 | 1857 | 1855 | 1856 |
| 340 | 1869 | 1851 | 1855 | 1857 | 1854 | 1855 |
| 350 | 1855 | 1850 | 1866 | 1853 | 1856 | 1863 |

| vSb, sat | x-axis / YZ plane velocities, m/s | | | | | |
|---|---|---|---|---|---|---|
| Angle | X1 | X2 | X3 | X4 | X5 | X6 |
| 0 | 1765 | 1752 | 1771 | 1768 | 1758 | 1745 |
| 10 | 1761 | 1767 | 1770 | 1756 | 1764 | 1764 |
| 20 | 1778 | 1781 | 1775 | 1766 | 1757 | 1776 |
| 30 | 1784 | 1779 | 1779 | 1774 | 1777 | 1779 |
| 40 | 1806 | 1795 | 1786 | 1792 | 1790 | 1810 |
| 50 | 1808 | 1809 | 1792 | 1797 | 1793 | 1815 |
| 60 | 1822 | 1818 | 1805 | 1798 | 1808 | 1827 |
| 70 | 1834 | 1834 | 1838 | 1811 | 1806 | 1843 |
| 80 | 1834 | 1834 | 1838 | 1831 | 1838 | 1838 |
| 90 | 1844 | 1844 | 1847 | 1835 | 1846 | 1837 |
| 100 | 1848 | 1850 | 1847 | 1843 | 1839 | 1837 |
| 110 | 1839 | 1855 | 1848 | 1845 | 1840 | 1826 |
| 120 | 1831 | 1823 | 1839 | 1855 | 1818 | 1811 |
| 130 | 1830 | 1803 | 1833 | 1832 | 1798 | 1800 |
| 140 | 1796 | 1795 | 1806 | 1809 | 1809 | 1785 |
| 150 | 1766 | 1773 | 1783 | 1783 | 1772 | 1774 |
| 160 | 1757 | 1753 | 1771 | 1767 | 1766 | 1757 |
| 170 | 1758 | 1756 | 1754 | 1755 | 1768 | 1753 |
| 180 | 1752 | 1747 | 1751 | 1753 | 1750 | 1753 |
| 190 | 1757 | 1762 | 1750 | 1743 | 1753 | 1749 |
| 200 | 1757 | 1754 | 1758 | 1742 | 1746 | 1762 |
| 210 | 1771 | 1779 | 1775 | 1741 | 1748 | 1786 |
| 220 | 1796 | 1772 | 1791 | 1749 | 1758 | 1796 |
| 230 | 1805 | 1804 | 1800 | 1761 | 1766 | 1800 |
| 240 | 1820 | 1817 | 1813 | 1779 | 1796 | 1806 |
| 250 | 1833 | 1834 | 1824 | 1788 | 1811 | 1827 |
| 260 | 1847 | 1843 | 1834 | 1820 | 1827 | 1843 |
| 270 | 1860 | 1845 | 1850 | 1842 | 1851 | 1856 |
| 280 | 1845 | 1852 | 1854 | 1847 | 1851 | 1847 |
| 290 | 1853 | 1851 | 1864 | 1848 | 1851 | 1838 |
| 300 | 1847 | 1832 | 1864 | 1852 | 1845 | 1826 |
| 310 | 1831 | 1815 | 1849 | 1855 | 1839 | 1814 |
| 320 | 1796 | 1803 | 1826 | 1846 | 1821 | 1800 |
| 330 | 1777 | 1789 | 1810 | 1811 | 1802 | 1780 |
| 340 | 1758 | 1781 | 1787 | 1786 | 1787 | 1763 |
| 350 | 1763 | 1779 | 1777 | 1775 | 1777 | 1753 |

| vSb, sat | y-axis / XZ plane velocities, m/s | | | | | |
|---|---|---|---|---|---|---|
| Angle | Y1 | Y2 | Y3 | Y4 | Y5 | Y6 |
| 0 | 1763 | 1757 | 1761 | 1779 | 1753 | 1774 |
| 10 | 1755 | 1757 | 1767 | 1773 | 1760 | 1770 |
| 20 | 1773 | 1766 | 1765 | 1779 | 1767 | 1771 |
| 30 | 1774 | 1777 | 1784 | 1790 | 1772 | 1774 |
| 40 | 1784 | 1800 | 1793 | 1804 | 1808 | 1791 |
| 50 | 1806 | 1791 | 1816 | 1821 | 1791 | 1800 |
| 60 | 1828 | 1814 | 1819 | 1828 | 1818 | 1821 |
| 70 | 1852 | 1825 | 1838 | 1841 | 1828 | 1846 |
| 80 | 1862 | 1849 | 1839 | 1851 | 1845 | 1852 |
| 90 | 1855 | 1840 | 1844 | 1830 | 1851 | 1845 |
| 100 | 1850 | 1845 | 1840 | 1837 | 1836 | 1834 |
| 110 | 1847 | 1829 | 1826 | 1821 | 1832 | 1825 |
| 120 | 1832 | 1816 | 1806 | 1816 | 1826 | 1808 |
| 130 | 1838 | 1817 | 1791 | 1793 | 1813 | 1790 |
| 140 | 1803 | 1813 | 1780 | 1787 | 1804 | 1774 |
| 150 | 1787 | 1813 | 1764 | 1769 | 1781 | 1760 |
| 160 | 1779 | 1798 | 1747 | 1754 | 1764 | 1752 |
| 170 | 1777 | 1776 | 1746 | 1748 | 1762 | 1749 |
| 180 | 1754 | 1769 | 1754 | 1753 | 1754 | 1758 |
| 190 | 1754 | 1756 | 1743 | 1760 | 1752 | 1770 |
| 200 | 1754 | 1749 | 1767 | 1765 | 1753 | 1776 |
| 210 | 1749 | 1750 | 1786 | 1769 | 1758 | 1789 |
| 220 | 1757 | 1759 | 1799 | 1787 | 1779 | 1800 |
| 230 | 1771 | 1774 | 1799 | 1796 | 1797 | 1815 |
| 240 | 1772 | 1792 | 1817 | 1813 | 1811 | 1821 |
| 250 | 1802 | 1794 | 1835 | 1828 | 1845 | 1840 |
| 260 | 1804 | 1807 | 1850 | 1838 | 1848 | 1851 |
| 270 | 1821 | 1843 | 1855 | 1850 | 1846 | 1857 |
| 280 | 1859 | 1847 | 1844 | 1842 | 1845 | 1860 |
| 290 | 1860 | 1856 | 1833 | 1862 | 1845 | 1837 |
| 300 | 1841 | 1855 | 1821 | 1830 | 1821 | 1823 |
| 310 | 1857 | 1861 | 1817 | 1819 | 1802 | 1817 |
| 320 | 1823 | 1826 | 1808 | 1809 | 1787 | 1800 |
| 330 | 1813 | 1813 | 1780 | 1794 | 1777 | 1787 |
| 340 | 1784 | 1795 | 1770 | 1766 | 1769 | 1778 |
| 350 | 1781 | 1772 | 1770 | 1757 | 1776 | 1770 |

| vSb, sat | z-axis / XY plane velcoties, m/s | | | | | |
|---|---|---|---|---|---|---|
| Angle | Z1 | Z2 | Z3 | Z4 | Z5 | Z6 |
| 0 | 1868 | 1867 | 1873 | 1851 | 1870 | 1868 |
| 10 | 1861 | 1860 | 1869 | 1863 | 1865 | 1865 |
| 20 | 1861 | 1856 | 1866 | 1863 | 1858 | 1863 |
| 30 | 1855 | 1859 | 1854 | 1852 | 1855 | 1858 |
| 40 | 1854 | 1855 | 1855 | 1851 | 1844 | 1851 |
| 50 | 1845 | 1860 | 1860 | 1852 | 1852 | 1847 |
| 60 | 1844 | 1853 | 1852 | 1843 | 1842 | 1843 |
| 70 | 1833 | 1847 | 1849 | 1842 | 1845 | 1837 |
| 80 | 1847 | 1843 | 1846 | 1851 | 1845 | 1837 |
| 90 | 1842 | 1847 | 1847 | 1857 | 1848 | 1845 |
| 100 | 1850 | 1856 | 1849 | 1859 | 1851 | 1845 |
| 110 | 1856 | 1864 | 1854 | 1856 | 1859 | 1850 |
| 120 | 1864 | 1864 | 1855 | 1856 | 1858 | 1852 |
| 130 | 1871 | 1858 | 1855 | 1861 | 1857 | 1850 |
| 140 | 1862 | 1855 | 1860 | 1859 | 1854 | 1855 |
| 150 | 1865 | 1854 | 1860 | 1860 | 1857 | 1855 |
| 160 | 1859 | 1857 | 1855 | 1864 | 1853 | 1851 |
| 170 | 1858 | 1860 | 1861 | 1857 | 1860 | 1858 |
| 180 | 1851 | 1860 | 1853 | 1852 | 1855 | 1855 |
| 190 | 1856 | 1860 | 1853 | 1852 | 1851 | 1847 |
| 200 | 1857 | 1849 | 1846 | 1852 | 1848 | 1847 |
| 210 | 1862 | 1834 | 1852 | 1855 | 1844 | 1850 |
| 220 | 1855 | 1848 | 1852 | 1854 | 1851 | 1849 |
| 230 | 1848 | 1847 | 1847 | 1852 | 1844 | 1844 |
| 240 | 1847 | 1851 | 1850 | 1847 | 1844 | 1849 |
| 250 | 1852 | 1851 | 1847 | 1847 | 1849 | 1849 |
| 260 | 1842 | 1859 | 1849 | 1845 | 1852 | 1843 |
| 270 | 1857 | 1864 | 1857 | 1851 | 1852 | 1850 |
| 280 | 1862 | 1866 | 1867 | 1854 | 1852 | 1860 |
| 290 | 1864 | 1858 | 1861 | 1855 | 1860 | 1860 |
| 300 | 1857 | 1862 | 1864 | 1857 | 1864 | 1863 |
| 310 | 1856 | 1866 | 1864 | 1859 | 1857 | 1860 |
| 320 | 1862 | 1865 | 1863 | 1855 | 1855 | 1855 |
| 330 | 1860 | 1865 | 1865 | 1851 | 1860 | 1855 |
| 340 | 1860 | 1863 | 1865 | 1856 | 1868 | 1862 |
| 350 | 1865 | 1858 | 1871 | 1859 | 1869 | 1855 |

| x-axis-1 | | | | |
|---|---|---|---|---|
| Pe | Elastic Wave Velocity, m/s | | Porosity | Permeability |
| (MPa) | p-wave | s-wave | (%) | ($m^2$) |
| 6.1 | 3577 | 1943 | 23.30 | 1.42440E-12 |
| 10.4 | 3645 | 1971 | 23.17 | 1.39159E-12 |
| 15.5 | 3714 | 1994 | 22.99 | 1.41215E-12 |
| 20.9 | 3747 | 2005 | 22.82 | 1.38459E-12 |
| 30.4 | 3784 | 2014 | 22.63 | 1.42352E-12 |
| 40.9 | 3830 | 2028 | 22.48 | 1.39990E-12 |
| 50.5 | 3864 | 2043 | 22.35 | 1.38590E-12 |
| 60.2 | 3887 | 2045 | 22.22 | 1.39771E-12 |
| 70.7 | 3889 | 2055 | 22.12 | 1.37147E-12 |
| 80.5 | 3919 | 2061 | 22.01 | 1.40996E-12 |
| 91.2 | 3928 | 2074 | 21.91 | 1.39115E-12 |
| 101.2 | 3943 | 2081 | 21.85 | 1.38634E-12 |
| 110.6 | 3967 | 2085 | 21.73 | 1.39421E-12 |
| 120.7 | 3982 | 2090 | 21.65 | 1.40252E-12 |
| 131.2 | 3984 | 2093 | 21.55 | 1.41302E-12 |
| 141.7 | 3993 | 2096 | 21.43 | 1.39028E-12 |
| 150.6 | 4000 | 2102 | 21.37 | 1.41259E-12 |
| 161.2 | 4006 | 2104 | 21.27 | 1.42483E-12 |
| 172.4 | 4011 | 2104 | 21.19 | 1.39334E-12 |
| 180.4 | 4013 | 2107 | 21.11 | 1.40296E-12 |
| 190.5 | 4015 | 2110 | 20.99 | 1.37934E-12 |
| 200.3 | 4021 | 2112 | 20.89 | 1.40821E-12 |
| 210.6 | 4026 | 2116 | 20.81 | 1.38372E-12 |
| 220.4 | 4031 | 2117 | 20.73 | 1.40690E-12 |
| 230.5 | 4031 | 2118 | 20.67 | 1.41040E-12 |
| 240.5 | 4030 | 2119 | 20.60 | 1.39946E-12 |
| 250.1 | 4030 | 2120 | 20.55 | 1.38415E-12 |

| x-axis-2 | | | | |
|---|---|---|---|---|
| Pe | Elastic Wave Velocity, m/s | | Porosity | Permeability |
| (MPa) | p-wave | s-wave | (%) | ($m^2$) |
| 5.4 | 3574 | 1904 | 22.95 | 1.40734E-12 |
| 10.3 | 3642 | 1973 | 22.87 | 1.40340E-12 |
| 15.2 | 3715 | 1977 | 22.68 | 1.40121E-12 |
| 20.3 | 3753 | 1992 | 22.51 | 1.40865E-12 |
| 30.4 | 3791 | 2007 | 22.33 | 1.39159E-12 |
| 41.5 | 3829 | 2034 | 22.18 | 1.40952E-12 |
| 51.1 | 3876 | 2060 | 22.06 | 1.39553E-12 |
| 60.5 | 3889 | 2075 | 21.93 | 1.39509E-12 |
| 70.2 | 3912 | 2084 | 21.83 | 1.38240E-12 |
| 80.3 | 3920 | 2091 | 21.73 | 1.39115E-12 |
| 90.5 | 3941 | 2105 | 21.63 | 1.38109E-12 |
| 100.6 | 3950 | 2119 | 21.57 | 1.38634E-12 |
| 111.0 | 3984 | 2127 | 21.45 | 1.39378E-12 |
| 121.0 | 3994 | 2130 | 21.37 | 1.38896E-12 |
| 133.1 | 3999 | 2136 | 21.27 | 1.38503E-12 |
| 141.2 | 4014 | 2139 | 21.16 | 1.39640E-12 |
| 151.3 | 4013 | 2137 | 21.10 | 1.38153E-12 |
| 160.5 | 4022 | 2141 | 21.01 | 1.38765E-12 |
| 170.2 | 4026 | 2146 | 20.93 | 1.38765E-12 |
| 180.5 | 4026 | 2146 | 20.84 | 1.38022E-12 |
| 190.5 | 4026 | 2146 | 20.72 | 1.39071E-12 |
| 200.9 | 4038 | 2150 | 20.63 | 1.37672E-12 |
| 210.3 | 4044 | 2157 | 20.54 | 1.38590E-12 |
| 220.6 | 4053 | 2157 | 20.47 | 1.38328E-12 |
| 230.2 | 4053 | 2157 | 20.41 | 1.37978E-12 |
| 240.5 | 4053 | 2165 | 20.34 | 1.38328E-12 |
| 250.3 | 4059 | 2163 | 20.29 | 1.39290E-12 |

| | y-axis-1 | | | |
|---|---|---|---|---|
| Pe | Elastic Wave Velocity, m/s | | Porosity | Permeability |
| (MPa) | p-wave | s-wave | (%) | ($m^2$) |
| 5.4 | 3535 | 1931 | 23.14 | 1.28513E-12 |
| 10.2 | 3599 | 1957 | 23.03 | 1.29717E-12 |
| 15.6 | 3675 | 1971 | 22.84 | 1.28825E-12 |
| 20.3 | 3710 | 1998 | 22.67 | 1.30482E-12 |
| 30.6 | 3745 | 2009 | 22.51 | 1.32398E-12 |
| 40.1 | 3786 | 2027 | 22.34 | 1.33679E-12 |
| 50.5 | 3810 | 2042 | 22.23 | 1.31944E-12 |
| 60.7 | 3827 | 2055 | 22.06 | 1.30279E-12 |
| 70.6 | 3839 | 2056 | 21.98 | 1.30713E-12 |
| 80.5 | 3862 | 2058 | 21.86 | 1.31899E-12 |
| 91.1 | 3875 | 2069 | 21.73 | 1.31081E-12 |
| 100.5 | 3880 | 2081 | 21.71 | 1.33160E-12 |
| 110.6 | 3909 | 2087 | 21.59 | 1.32250E-12 |
| 120.3 | 3928 | 2100 | 21.47 | 1.32042E-12 |
| 130.7 | 3934 | 2101 | 21.41 | 1.35052E-12 |
| 140.8 | 3940 | 2107 | 21.33 | 1.31207E-12 |
| 151.2 | 3946 | 2111 | 21.19 | 1.29828E-12 |
| 160.3 | 3951 | 2117 | 21.14 | 1.37495E-12 |
| 170.2 | 3955 | 2121 | 21.06 | 1.33838E-12 |
| 180.3 | 3960 | 2128 | 20.94 | 1.32537E-12 |
| 190.7 | 3962 | 2128 | 20.86 | 1.28140E-12 |
| 200.2 | 3964 | 2131 | 20.76 | 1.31697E-12 |
| 210.4 | 3967 | 2132 | 20.67 | 1.32620E-12 |
| 220.9 | 3970 | 2132 | 20.60 | 1.35516E-12 |
| 231.3 | 3971 | 2133 | 20.54 | 1.33580E-12 |
| 240.2 | 3971 | 2135 | 20.47 | 1.28637E-12 |
| 251.2 | 3971 | 2134 | 20.39 | 1.33284E-12 |

| | y-axis-2 | | | |
|---|---|---|---|---|
| Pe | Elastic Wave Velocity, m/s | | Porosity | Permeability |
| (MPa) | p-wave | s-wave | (%) | ($m^2$) |
| 5.6 | 3502 | 1917 | 23.46 | 1.34040E-12 |
| 10.2 | 3555 | 1944 | 23.34 | 1.30191E-12 |
| 15.4 | 3630 | 1961 | 23.20 | 1.30181E-12 |
| 20.4 | 3655 | 1969 | 23.03 | 1.30379E-12 |
| 30.5 | 3700 | 1995 | 22.74 | 1.22476E-12 |
| 41.1 | 3729 | 2012 | 22.55 | 1.27127E-12 |
| 51.0 | 3761 | 2025 | 22.38 | 1.29311E-12 |
| 60.4 | 3784 | 2047 | 22.27 | 1.32330E-12 |
| 70.5 | 3794 | 2053 | 22.14 | 1.33333E-12 |
| 80.5 | 3815 | 2068 | 22.02 | 1.31226E-12 |
| 91.0 | 3829 | 2079 | 21.89 | 1.30473E-12 |
| 100.6 | 3843 | 2081 | 21.79 | 1.31997E-12 |
| 110.6 | 3864 | 2089 | 21.67 | 1.25405E-12 |
| 120.6 | 3878 | 2100 | 21.58 | 1.27373E-12 |
| 131.4 | 3888 | 2103 | 21.48 | 1.26747E-12 |
| 141.5 | 3892 | 2109 | 21.43 | 1.31398E-12 |
| 151.2 | 3896 | 2105 | 21.36 | 1.34408E-12 |
| 160.6 | 3909 | 2109 | 21.25 | 1.28917E-12 |
| 170.9 | 3909 | 2124 | 21.14 | 1.31293E-12 |
| 180.5 | 3915 | 2121 | 21.02 | 1.28601E-12 |
| 190.6 | 3923 | 2125 | 20.92 | 1.31900E-12 |
| 200.6 | 3923 | 2121 | 20.84 | 1.30890E-12 |
| 210.4 | 3932 | 2129 | 20.78 | 1.30379E-12 |
| 220.5 | 3936 | 2136 | 20.66 | 1.26991E-12 |
| 230.6 | 3936 | 2134 | 20.60 | 1.30562E-12 |
| 240.5 | 3940 | 2134 | 20.56 | 1.27555E-12 |
| 250.5 | 3944 | 2138 | 20.46 | 1.22620E-12 |

| z-axis-1 | | | | |
|---|---|---|---|---|
| Pe | Elastic Wave Velocity, m/s | | Porosity | Permeability |
| (MPa) | p-wave | s-wave | (%) | ($m^2$) |
| 5.3 | 3265 | 1797 | 23.10 | 9.35556E-13 |
| 10.5 | 3345 | 1821 | 22.98 | 9.01398E-13 |
| 15.3 | 3412 | 1837 | 22.84 | 9.28462E-13 |
| 20.4 | 3468 | 1871 | 22.72 | 8.73704E-13 |
| 30.3 | 3505 | 1897 | 22.57 | 8.55980E-13 |
| 40.6 | 3559 | 1914 | 22.45 | 8.11542E-13 |
| 50.3 | 3587 | 1925 | 22.34 | 8.93570E-13 |
| 60.7 | 3620 | 1941 | 22.23 | 8.68573E-13 |
| 70.1 | 3669 | 1952 | 22.15 | 8.53582E-13 |
| 80.1 | 3694 | 1959 | 22.05 | 8.94726E-13 |
| 90.3 | 3707 | 1968 | 21.96 | 8.39054E-13 |
| 100.9 | 3722 | 1990 | 21.87 | 8.67376E-13 |
| 111.3 | 3751 | 1994 | 21.78 | 8.84341E-13 |
| 121.1 | 3757 | 2002 | 21.71 | 8.56937E-13 |
| 133.8 | 3769 | 2013 | 21.61 | 8.46952E-13 |
| 140.5 | 3778 | 2016 | 21.53 | 8.67053E-13 |
| 150.7 | 3781 | 2021 | 21.43 | 8.30052E-13 |
| 160.8 | 3796 | 2023 | 21.34 | 8.64891E-13 |
| 170.2 | 3798 | 2025 | 21.27 | 8.43050E-13 |
| 180.3 | 3803 | 2026 | 21.15 | 8.78218E-13 |
| 190.5 | 3807 | 2028 | 21.05 | 8.83749E-13 |
| 200.5 | 3807 | 2029 | 20.96 | 8.47728E-13 |
| 210.3 | 3810 | 2030 | 20.84 | 8.77422E-13 |
| 220.9 | 3810 | 2030 | 20.78 | 9.06249E-13 |
| 230.3 | 3811 | 2035 | 20.69 | 8.52381E-13 |
| 240.2 | 3815 | 2038 | 20.61 | 8.18601E-13 |
| 250.2 | 3814 | 2039 | 20.52 | 8.68349E-13 |

| z-axis-2 | | | | |
|---|---|---|---|---|
| Pe | Elastic Wave Velocity, m/s | | Porosity | Permeability |
| (MPa) | p-wave | s-wave | (%) | ($m^2$) |
| 5.4 | 3217 | 1767 | 23.38 | 9.65948E-13 |
| 10.0 | 3304 | 1788 | 23.26 | 9.67909E-13 |
| 15.1 | 3357 | 1813 | 23.12 | 9.43771E-13 |
| 20.1 | 3430 | 1845 | 23.00 | 9.83504E-13 |
| 30.4 | 3483 | 1870 | 22.85 | 9.50212E-13 |
| 42.3 | 3542 | 1881 | 22.66 | 9.85913E-13 |
| 51.9 | 3546 | 1900 | 22.55 | 9.41251E-13 |
| 60.2 | 3580 | 1912 | 22.44 | 9.61844E-13 |
| 70.2 | 3624 | 1927 | 22.35 | 9.89761E-13 |
| 80.5 | 3664 | 1942 | 22.25 | 9.41854E-13 |
| 90.6 | 3677 | 1945 | 22.16 | 9.62457E-13 |
| 100.2 | 3693 | 1953 | 22.06 | 9.82106E-13 |
| 110.6 | 3715 | 1972 | 21.93 | 9.66169E-13 |
| 120.9 | 3715 | 1979 | 21.85 | 9.37930E-13 |
| 132.4 | 3726 | 1985 | 21.75 | 9.69876E-13 |
| 141.9 | 3734 | 1990 | 21.67 | 9.90478E-13 |
| 151.9 | 3738 | 1992 | 21.58 | 1.01242E-12 |
| 160.2 | 3756 | 1996 | 21.48 | 9.88742E-13 |
| 170.2 | 3762 | 1992 | 21.41 | 9.56806E-13 |
| 180.7 | 3762 | 2001 | 21.29 | 9.26216E-13 |
| 190.5 | 3762 | 1997 | 21.25 | 9.56412E-13 |
| 201.3 | 3756 | 2001 | 21.11 | 9.79694E-13 |
| 210.2 | 3770 | 2003 | 21.06 | 9.49206E-13 |
| 220.3 | 3768 | 2012 | 20.99 | 9.34103E-13 |
| 230.1 | 3776 | 2014 | 20.87 | 9.56598E-13 |
| 240.7 | 3772 | 2021 | 20.75 | 9.99055E-13 |
| 250.3 | 3770 | 2023 | 20.68 | 9.93176E-13 |

```
% Program to generate b values from a time: amplitude data file
% Load the input data file, which contains time in seconds in
column 1
% and amplitude in dB in column 6
load HT2604A.dat
time=HT2604A(:,1);
Amp=HT2604A(:,6);
A0=47;
% user inputs
Namps=input ('enter the no. of amplitude values you want to use to
determine each b value: ');
Ngap=input ('enter the no. of AE events you want between each b
value calculation: ');
% removes amplitudes less than threshold and
% finds no of b values that will be calculated
% (note Nbval is one less than no to be calculated)
A_ind=find(Amp>A0);
A_gtA0=Amp(A_ind);
T=time(A_ind);
NAE=length(A_gtA0);
Nbval=fix(NAE/Ngap-Namps/Ngap);
% calculates b and a value using Aki's maximum likelihood method
j=0;
for i=0:Nbval
    j=j+1;
    amps=A_gtA0((1+i*Ngap):(Namps+i*Ngap));
    Amean=mean(amps);
    b_val(j)=(4.3429/(Amean-A0));
    B_V2(j)=(8.6858/(Amean-A0));
    aval(j)=((b_val(j)*A0*0.1)+(log10(Namps)));
    tb(j)=T(Namps+i*Ngap);
    %calculates the standard error of meanAmp
    %then calculates the standard error of b from this
    %using method in Shi and Bolt, 1982
    Adiffs2=(amps-Amean).^2;
    S2A=sum(Adiffs2)/(Namps*(Namps-1));
    stdEmA(j)=S2A^0.5;
    stdEb(j)=2.3*(b_val(j)^2)*stdEmA(j);
    % calculates difference between calculated distribuiton and
actual data
    % as used in Wiemer and Wyss (2000)
```

```
    % to determine the minimum magnitude of completeness
    logN=aval(j)-0.1*b_val(j).*amps;
    N=10.^logN;
    count=1:Namps;
    N2=[sort(N)]';
    diffs=sqrt((N2-count).^2);
    perc_err(j)=100*mean(diffs)/mean(N2);
end
% this section saves the data in a file containing
% time, b value, a value, std error of mean amp, std error of b, %
error of f-M distribution
results=[tb;B_V2;aval;stdEmA;stdEb;perc_err]'
Asort=sort(A_gtA0);
count=[NAE:-1:1];
save temp.dat results /ascii
```

Epore lookup charts:

```
Ksus=0.1;
%%bc=1.2;
%loop start
%N=0;
I=0;
ab = 1.0001:0.1:3;  lab  =length(ab);
bc = 1.0001:0.1:3;   lbc = length(bc);
%%for (N=0:1:4)
%%Counter=0;
%%ab=1.2;
%%bc=bc+(N/10);
Lnew = zeros(lab,lbc); Fnew = zeros(lab,lbc);
figure
%%    while (Counter<100)
for ii = 1:lbc
    for jj = 1:lab
%%    for I = 1:100
%%    I=(N*100)+(Counter+1);
%%    [L F P] = EPore(ab, bc, Ksus);
      [Lnew(jj,ii), Fnew(jj,ii)] = Epore(ab(jj),bc(ii),Ksus);
%%    Lnew(I)=L; Fnew(I)=F; Pnew(I)=P;
%%    abnew(I)=ab; bcnew(I)=bc;
%%    ab=ab+0.01;
%%    [bc];
%%    Counter=Counter+1;
    end
    plot(Fnew(:,ii),Lnew(:,ii),'r-'), hold on
    axis([1 1.05 1 1.05])
%N=N+1;
%bc=bc+0.1
end
for jj = 1:lab
   plot(Fnew(jj,:),Lnew(jj,:),'b-'), hold on
%  axis([1 1.02 1 1.02])
end
%[XL]=X(:,1); [XF]=X(:,2);
%plot(XF,XL,'k*'), hold on
%plot(1.0270,1.0117,'gO'), hold on
%loop end
xlabel('Foliation (=Kint/Kmin)'), ylabel('Lineation (=Kmax/Kint)'),
grid on
%%LT=Lnew'; FT=Fnew'; PT=Pnew'; abT=abnew'; bcT=bcnew';
%%LM=[bcT abT LT FT PT];
%save L.txt LM -ascii
```

Epore anisotropy parameters L, F and P

```
function[L, F, P] = EPore(ab, bc, Ksus)
% set up parameters
% bc=1.1; ab=3.0; Ksus=3.707; %3.34
BA=1/ab; CA=1/(bc/BA);
%CA=0.76604; BA=0.87037;
Ctheta=CA; Cphi=BA;
Stheta=sqrt(1-(CA^2)); Sphi=sqrt(1-(BA^2)); S3theta=(Stheta^3);
Salpha=Sphi/Stheta; S2alpha=(Salpha^2);
```

```
Calpha=sqrt(1-(Salpha^2)); C2alpha=(Calpha^2);
k=Salpha;
theta=acos(CA);
phi=360*(theta/(2*pi));
%[k,m,theta,phi]
[fe,ee]=elit(k,phi);
K=fe; E=ee;
% calculate Na
facA=(Cphi*Ctheta)/(S3theta*S2alpha);
ellipA=(K-E);
Na=facA*ellipA;
% calculate Nb
facB1=(Cphi*Ctheta)/(S3theta*S2alpha*C2alpha);
facB2=C2alpha;
facB3=(S2alpha*Stheta*Ctheta)/Cphi;
Nb=facB1*(E-(facB2*K)-facB3);
% calculate Nc
facC1=(Cphi*Ctheta)/(S3theta*C2alpha);
facC2=(Stheta*Cphi)/Ctheta;
Nc=facC1*(facC2-E);
% output list
%[CA BA]
%[Ctheta Cphi Calpha C2alpha]
%[Stheta S3theta Sphi Salpha S2alpha]
%[Na Nb Nc]
%Na+Nb+Nc
% Calculate ratios L/F/P
L=(1+(Ksus*(Nb)))/(1+(Ksus*(Na)));
F=(1+(Ksus*(Nc)))/(1+(Ksus*(Nb)));
P=(1+(Ksus*(Nc)))/(1+(Ksus*(Na)));
[L F P];
%

%This program is a direct conversion of the corresponding Fortran
program in
%S. Zhang & J. Jin "Computation of Special Functions" (Wiley, 1996).
%online: http://iris-lee3.ece.uiuc.edu/~jjin/routines/routines.html
%
%Converted by f2matlab open source project:
%online: https://sourceforge.net/projects/f2matlab/
% written by Ben Barrowes (barrowes@alum.mit.edu)
%
function [fe,ee]=elit(hk,phi);
%
%       ===================================================
%       Purpose: Compute complete and incomplete elliptic
%                integrals F(k,phi) and E(k,phi)
%       Input  : HK  --- Modulus k ( 0 ó k ó 1 )
%                Phi --- Argument ( in degrees )
%       Output : FE  --- F(k,phi)
%                EE  --- E(k,phi)
%       ===================================================
%
g=0.0d0;
pi=3.14159265358979d0;
a0=1.0d0;
b0=sqrt(1.0d0-hk.*hk);
```

```
d0=(pi./180.0d0).*phi;
r=hk.*hk;
if (hk == 1.0d0&phi == 90.0d0);
fe=1.0d+300;
ee=1.0d0;
elseif (hk == 1.0d0);
fe=log((1.0d0+sin(d0))./cos(d0));
ee=sin(d0);
else;
fac=1.0d0;
for  n=1:40;
a=(a0+b0)./2.0d0;
b=sqrt(a0.*b0);
c=(a0-b0)./2.0d0;
fac=2.0d0.*fac;
r=r+fac.*c.*c;
if (phi ~= 90.0d0);
d=d0+atan((b0./a0).*tan(d0));
g=g+c.*sin(d);
d0=d+pi.*fix(d./pi+.5d0);
end;
a0=a;
b0=b;
if (c < 1.0d-7) break; end;
end;
         ck=pi./(2.0d0.*a);
ce=pi.*(2.0d0-r)./(4.0d0.*a);
if (phi == 90.0d0);
fe=ck;
ee=ce;
else;
fe=d./(fac.*a);
ee=fe.*ce./ck+g;
end;
end;
```

```
TQ=Q';
TQQ=TQ*Q;
ITTQ=inv(TQQ);
TQW=TQ*W;
P=ITTQ*TQW
x=ones(3,3);
x(1,1)=P(1);
x(2,2)=P(2);
x(3,3)=P(3);
x(1,2)=P(4)/2;
x(2,1)=P(4)/2;
x(1,3)=P(5)/2;
x(3,1)=P(5)/2;
x(2,3)=P(6)/2;
x(3,2)=P(6)/2;
[eigvec,eigval]=eig(x)
L=x*eigvec;
R=eigvec*eigval;
L-R;
```